X-ray multiphoton ionization dynamics: Quantum-state-resolved calculations and machine-learning approach

Dissertation
zur Erlangung des Doktorgrades
an der Fakultät für Mathematik, Informatik und Naturwissenschaften
Fachbereich Physik
der Universität Hamburg

vorgelegt von
Laura Budewig

Hamburg
2024

Gutachter/innen der Dissertation:	Prof. Dr. Robin Santra Prof. Dr. Nina Rohringer
Zusammensetzung der Prüfungskommission:	Prof. Dr. Daniela Pfannkuche Prof. Dr. Robin Santra Prof. Dr. Nina Rohringer Dr. Michael Meyer Dr. Sang-Kil Son
Vorsitzende/r der Prüfungskommission:	Prof. Dr. Daniela Pfannkuche
Datum der Disputation:	12.11.2024
Vorsitzender des Fach-Promotionsausschusses PHYSIK:	Prof. Dr. Markus Drescher
Leiter des Fachbereichs PHYSIK:	Prof. Dr. Wolfgang J. Parak
Dekan der Fakultät MIN:	Prof. Dr.-Ing. Norbert Ritter

Abstract

X-ray free-electron lasers (XFELs) offer unique opportunities for unraveling ultrafast dynamics in matter and for imaging biomolecules with almost atomic resolution. For these attractive applications of XFELs, deepening our understanding of the interaction of high-intensity X rays with individual atoms is essential. In a single intense X-ray pulse, atoms are highly ionized by multiple sequences of one-photon ionization events and accompanying decay processes. These X-ray multiphoton ionization dynamics are commonly simulated by a rate-equation approach for electronic configurations. However, the configuration-based rate-equation approach does not include individual quantum states and, thereby, is unsuitable for studying the electron-cloud alignment of the produced atomic ions. It has been well-known that atomic photoionization can align an electron cloud, initially being perfectly spherically symmetric. But it is not clear how the alignment of the electron cloud evolves during X-ray multiphoton ionization dynamics. However, such a study requires a computationally expensive description of individual quantum states and quantum-state-resolved atomic transitions and includes solving rate equations in a generally extremely large space of states. In this thesis, I present a comprehensive framework for quantum-state-resolved calculations of X-ray multiphoton ionization dynamics of atoms and apply machine learning for handling the high computational cost.

To this end, a quantum-state-resolved electronic-structure framework for isolated atoms and atomic ions is introduced in the first part of the thesis. This framework uses first-order many-body perturbation theory, which improves accuracy of transition energies. In addition, I employ quantum-state-resolved electronic-structure calculations to study how much the electron cloud of argon ions can be aligned through a single X-ray-induced atomic transition. A nonnegligible degree of alignment is observed.

Combining the quantum-state-resolved electronic-structure framework with a Monte Carlo rate-equation method in a follow-up study enables me to calculate quantum-state-resolved X-ray multiphoton ionization dynamics. Results for neon

atoms demonstrate that state-resolved calculations provide similar charge-state distributions, but more precise information about resonant excitations and electron and photon spectra than the common configuration-based calculations. Moreover, calculated time-resolved spectra of electrons and photons present detailed insight into ultrafast dynamics of state-resolved X-ray multiphoton ionization. However, performing such state-resolved calculations for atoms much heavier than neon is very costly due to extremely time-consuming state-resolved calculations of a very large number of atomic transition parameters.

Because of this limitation, I next present a strategy that embeds machine-learning models for predicting atomic transition parameters into the state-resolved calculation of X-ray multiphoton ionization dynamics. As potential machine-learning models, I discuss feedforward neural networks and random forest regressors, which exhibit a similarly acceptable, but limited accuracy. In addition, fully calculated and machine-learning-based charge-state distributions and electron and photon spectra are compared for argon atoms. The comparison demonstrates that the machine-learning strategy works in principle and that the performance, in terms of charge-state distributions and electron and photon spectra, is good.

Lastly, I apply the state-resolved X-ray multiphoton ionization dynamics calculations to explore the possibility to align the electron cloud of argon ions through a linearly polarized XFEL pulse. The induced X-ray multiphoton ionization dynamics generate ions in a wide range of charge states with nonzero orbital- and spin-angular momentum. While the electron-cloud alignment is suppressed with progressing ionization dynamics when averaging over all individual quantum states, the simulations clearly demonstrate nonnegligible electron-cloud alignment for orbital-angular-momentum- and charge-resolved states.

Overall, this thesis contributes to a deeper understanding of the interaction of XFEL pulses with atoms by providing more accurate state-resolved information, complemented by insight into electron-cloud alignment dynamics. It also establishes a first step toward computationally efficient calculations of X-ray multiphoton ionization dynamics for easily examining a variety of atoms and XFEL beam parameters in the future.

Zusammenfassung

Freie-Elektronen-Röntgenlaser (XFELs) bieten einzigartige Möglichkeiten, ultraschnelle Dynamiken in Materie zu entschlüsseln und Biomoleküle mit nahezu atomarer Auflösung abzubilden. Für diese attraktiven Anwendungen von XFELs ist ein vertieftes Verständnis von der Wechselwirkung hochintensiver Röntgenstrahlung mit individuellen Atomen essenziell. In einem einzelnen intensiven Röntgenlaserpuls entstehen stark ionisierte Atome durch mehrere Sequenzen von Photonionisationen und begleitender Zerfallsprozesse. Diese röntgeninduzierten Vielphotonenionisierungsdynamiken werden gewöhnlich mit einem Ratengleichungsansatz für Elektronenkonfigurationen simuliert. Jedoch berücksichtigt der konfigurationsbasierte Ratengleichungsansatz keine individuellen Quantenzustände und ist somit zur Studie der Elektronenhüllenausrichtung der produzierten atomaren Ionen ungeeignet. Es ist bekannt, dass durch atomare Photoionisation eine anfänglich perfekt sphärisch symmetrische Elektronenhülle ausgerichtet werden kann. Allerdings ist unklar, wie sich die Ausrichtung der Elektronenhülle während der röntgeninduzierten Vielphotonenionisierungsdynamiken entwickelt. Jedoch bedarf eine solche Studie eine rechenintensive Beschreibung einzelner Quantenzustände sowie quantenzustandsaufgelöster atomarer Übergänge und erfordert die Lösung von Ratengleichungen in einem im Allgemeinen extrem großen Zustandsraum. In dieser Arbeit präsentiere ich ausführliche quantenzustandsaufgelöste Berechnungen der röntgeninduzierten Vielphotonenionisierungsdynamiken von Atomen und wende maschinelles Lernen zur Bewältigung des hohen Rechenaufwands an.

Dafür wird im ersten Teil der Arbeit ein Framework zur quantenzustandsaufgelösten Elektronenstrukturberechnung von isolierten Atomen und atomaren Ionen eingeführt. Dieses Framework verwendet erste Ordnung Vielteilchenstörungstheorie, wodurch die Genauigkeit der Übergangsenergien verbessert wird. Des Weiteren wende ich die quantenzustandsaufgelösten Elektronenstrukturberechnungen an, um zu untersuchen, wie stark die Elektronenhülle von Argonionen durch einen einzigen röntgeninduzierten Prozess ausgerichtet werden kann. Ein nicht zu vernachlässigender Grad an Ausrichtung wird beobachtet.

Die quantenzustandsaufgelösten Elektronenstrukturberechnungen kombiniere ich in einer Folgestudie mit einer Monte Carlo Ratengleichungsmethode, was quantenzustandsaufgelöste Berechnungen von röntgeninduzierten Vielphotonenionisierungsdynamiken ermöglicht. Ergebnisse für Neonatome zeigen, dass die zustandsaufgelösten Berechnungen ähnliche Ladungszustandsverteilungen aber präzisere Informationen über resonante Anregungen sowie Elektronen- und Photonenspektren liefern als die gewöhnlichen konfigurationsbasierten Berechnungen. Zudem bieten zeitaufgelöste Berechnungen von Elektronen- und Photonenspektren detaillierte Einblicke in die ultraschnelle Dynamik der zustandsaufgelösten Vielphotonenionisation. Jedoch sind solche zustandsaufgelösten Berechnungen für wesentlich schwere Atome als Neon sehr aufwendig, extrem zeitaufwändiger zustandsaufgelöster Berechnungen einer riesigen Anzahl an atomaren Übergangsparameten wegen.

Aufgrund dieser Einschränkung bringe ich als nächstes eine Strategie vor, welche Modelle des maschinellen Lernens zur Vorhersage atomarer Übergangsparameter in die zustandsaufgelöste Berechnung der röntgeninduzierten Vielphotonenionisierungsdynamiken einbettet. Als mögliche Modelle diskutiere ich Neuronale Netze und Random-Forest-Regressoren, welche eine ähnlich akzeptable aber begrenzte Genauigkeit aufweisen. Weiterhin werden vollständig berechnete und auf maschinellem Lernen basierte Ladungszustandsverteilungen sowie Elektronen- und Photonenspektren für Argonatome verglichen. Der Vergleich zeigt, dass die Strategie des maschinellen Lernens prinzipiell funktioniert und dass die Leistung bezüglich Ladungszustandsverteilungen sowie Elektronen- und Photonenspektren gut ist.

Abschließend wende ich die zustandsaufgelösten Berechnungen der Vielphotonenionisierungsdynamiken an, um zu untersuchen, inwieweit die Elektronenhülle von Argonionen durch einen linear polarisierten XFEL-Puls ausgerichtet wird. Die induzierten Vielphotonenionisierungsdynamiken produzieren Ionen in verschiedensten Ladungszuständen mit von Null verschiedenen Bahn- und Spindrehimpuls. Während bei einer Mittelung über alle einzelnen Quantenzustände die Elektronenhüllenausrichtung mit fortschreitender Ionisierungsdynamik gehemmt wird, zeigen die Simulationen eindeutig eine nicht zu vernachlässigende Elektronenhüllenausrichtung für Zustände, die nach Bahndrehimpuls und Ladung aufgelöst sind.

Insgesamt trägt diese Arbeit zu einem tieferen Verständnis von der Wechselwirkung von XFEL-Pulsen mit Atomen bei, indem sie genauere quantenzustandsaufgelöste Informationen liefert, die durch Einblicke in die Ausrichtungsdynamik der Elektronenhüllen ergänzt werden. Sie stellt auch einen ersten Schritt zu effizienten Berechnungen der Vielphotonenionisierungsdynamiken dar, um zukünftig eine Vielzahl von Atomen und XFEL-Strahlparametern besser untersuchen zu können.

Contents

List of Publications

- L. Budewig, S.-K. Son, and R. Santra, Theoretical investigation of orbital alignment of x-ray-ionized atoms in exotic electronic configurations, Phys. Rev. A **105**, 033111 (2022)
- L. Budewig, S.-K. Son, and R. Santra, State-resolved ionization dynamics of a neon atom induced by x-ray free-electron-laser pulses, Phys. Rev. A **107**, 013102 (2023)
- L. Budewig, S.-K. Son, Z. Jurek, M. M. Abdullah, M. Tropmann-Frick, and R. Santra, X-ray-induced atomic transitions via machine learning: A computational investigation, Phys. Rev. Research **6**, 013265 (2024)
- L. Budewig, S.-K. Son, and R. Santra, Electron-cloud alignment dynamics induced by an intense X-ray free-electron laser pulse: a case study on atomic argon, Commun. Phys. **7**, 363 (2024)

Chapter 1

Introduction

X-ray free-electron lasers (XFELs) [1–5], developed during the past two decades, offer highly attractive and exciting opportunities for determining the structure and dynamics of matter on atomic length and time scales [6–10]. But they also confront scientists with new challenges. XFELs provide ultraintense ($\sim 10^{12}$ photons per pulse) and ultrashort (~ 10 femtoseconds) X-ray pulses [9, 11] with a peak brightness that is much larger than for synchrotrons. This enormous peak brightness enables to unravel the three-dimensional structure of complex biomolecules with almost atomic resolution [6, 7, 12–17] using serial femtosecond crystallography [14, 15] and single-particle imaging [12, 13] experiments. These experiments employ micro- and nanocrystals and eventually individual single molecules and, therefore, make it possible to study biomolecules that cannot be crystallized. However, the inevitably high intensity of X-ray photons unavoidably damages the electronic structure of the investigated molecule and, as a consequence, the molecule undergoes structural disintegration. This radiation damage [18–23] clearly limits the attractive applications of XFELs. Electronic-structure damage predominantly results from the interaction of X rays with the individual atoms of the molecules [20].

Therefore, deepening our understanding of the interaction of high-intensity X rays with atoms is crucial. When an atom is exposed to an intense X-ray pulse, it absorbs more than one X-ray photon via sequences of one-photon ionization events taking mostly place in inner shells [24, 25]. Accompanying decay processes via Auger-Meitner decay and/or X-ray fluorescence [24, 26] refill the produced inner-shell holes and, thus, enable further inner-shell photoionization. As a result of these so-called X-ray multiphoton ionization dynamics [24], the atom becomes very highly ionized within a single X-ray pulse [25–30]. This is indeed a serious electronic-structure modification. X-ray multiphoton ionization dynamics are commonly simulated by solving a coupled set of rate equations [25, 31, 32] describing the time-dependent

populations of the electronic configurations visited during the X-ray multiphoton ionization dynamics. This configuration-based rate-equation approach has already been widely used and successfully applied for interpreting and designing many XFEL experiments [25, 27–47]. Its first validation was for neon atoms [25, 31], studied in the first experiments at the Linac Coherent Light Source (LCLS) in California, United States of America [1, 48]. Follow-up studies for neon have demonstrated the importance of including shake-off effects [34, 49], direct nonsequential two-photon ionization in excited neon ions [34, 50], and resonant photoabsorption transitions at certain X-ray photon energies [35]. Furthermore, X-ray multiphoton ionization dynamics in heavier atoms [26–30, 33] and molecules [36–39, 51] have been explored and also for other atoms than neon relevant resonant photoabsorption transitions have been found [27, 28, 40–44]. Frustrated absorption [39], also called intensity-induced X-ray transparency [25], is yet another interesting and investigated phenomenon [25, 39, 41]. It considers the suppression of X-ray multiphoton ionization dynamics by shorter X-ray pulse durations due to hollow-atom formation and reduction of decay processes [24]. Typically, the studies on X-ray multiphoton ionization dynamics measure the ions produced by the X-ray pulse [25–30, 34, 35, 40–42, 49] as well as electron spectra [26, 41, 51, 52] and photon spectra [26, 28, 49, 51]. However, studying the electron-cloud alignment of the produced ions can deliver complementary information.

Photoionization generally induces an alignment of the electron cloud of the produced ions with nonzero orbital-angular momentum [53–60] due to different ionization probabilities for different orbital-angular-momentum projection states. This alignment manifests itself in a spatial reshaping of the electron cloud [61] even if initially the electron cloud is perfectly spherically symmetric for closed-shell atoms. Comparably strong alignments have been encountered in strong-field ionized [62, 63] and resonantly excited [64] atoms. Recently, a nonnegligible alignment has theoretically been demonstrated for krypton ions up to Kr^{3+} produced by extreme ultraviolet (XUV) pulses [65]. This study focused on single ionization events and did not include previous ionization sequences. For sequential double and triple ionizations driven by XUV pulses, photoelectron angular distributions have been investigated [66–70]. Photoelectrons already display a fundamental anisotropy in their angular distribution when being emitted from an unaligned atom [71–73]. But when they are emitted from an aligned ion, this fundamental anisotropy is modified [66]. As a consequence of electron-cloud alignment, also emitted Auger-Meitner electrons and fluorescence photons are anisotropically distributed [60, 74–78]. Fluorescence photons are also polarized [74, 79, 80]. On the one hand, anisotropies in the angular distribution of emitted electrons and photons make electron-cloud align-

ment experimentally accessible [56–58, 78, 80]. On the other hand, angle-resolved spectroscopy experiments [67, 69, 81, 82] may profit from theoretical knowledge of electron-cloud alignment and the resulting anisotropies in the angular distribution of emitted electrons and photons. However, it is not clear how the electron-cloud alignment evolves during X-ray multiphoton ionization dynamics and how it will be measurable in XFEL experiments.

Addressing these questions requires to consider individual quantum states during the X-ray multiphoton ionization dynamics, which are not captured by the common configuration-based rate-equation approach. Therefore, a state-resolved rate-equation approach is necessary, whose basis is a quantum-state-resolved description of atomic ions and X-ray-induced atomic transitions. A state-resolved rate-equation approach is not only crucial for exploring electron-cloud alignment, but also interesting for investigating how ion, electron, and photon spectra profit from a more precise state-resolved description. To solve rate equations that describe time-dependent quantum state populations, it is necessary to include all possible electronic quantum states that may be formed by removing zero, one, or more electrons from the ground state of the neutral atom. The corresponding number of involved quantum states goes far beyond the number of involved electronic configurations, which is already very large for heavy atoms [40]. Consequently, apart from very light atoms like neon, solving state-resolved rate equations in an extremely large space of states will be unavoidable. A way to efficiently perform huge-sized rate-equation calculations is the Monte Carlo rate-equation method [26, 29], applied for heavy atoms in the configuration-based approach. However, even with such a Monte Carlo rate-equation method, computationally expensive, first-principle calculations of a huge number of state-resolved atomic transition parameters are necessary in the state-resolved rate-equation approach. This limits its potential applications to light atoms and to XFEL beam parameter scans with only a very few selected scanning points.

Therefore, it is natural to ask whether this critical challenge of high computational effort might be addressed by applying a suitable machine-learning strategy. Dating back to the 1950s [83, 84], machine learning, deep learning included, has recently become really popular. It is nowadays applied in almost all areas of modern life [84, 85] ranging from private media usage [86–89] to industry [90–93] and healthcare [94–99]. Its increasing popularity mainly results from the development of very powerful computers and from the massive amount of data, now being available. Machine learning efficiently processes large amounts of data by recognizing useful patterns in the data and by applying the learned patterns to tasks like prediction [83, 84], classification [83, 84], image and speech recognition [100–103], and natural language processing [104, 105]. With that, machine learning is also well-

suited for supporting natural science in various ways [106–108]. The prototype example is the application to protein structure predictions with atomic accuracy [109]. Other important applications of machine learning include the prediction of X-ray absorption spectra [110–113], the identification of phase transitions in condensed matter [114], the characterization and calibration of laser pulses [115–118], as well as its use in electronic-structure theory [119–124], just to name a few (for more see, e.g., Refs. [106, 107] and references therein). One high-impact role that machine learning has been playing in electronic-structure theory so far is in speeding up the construction of potential energy surfaces [125–128]. A recent review about the progress of machine learning in the context of potential energy surfaces can be found in Ref. [129]. Furthermore, an interesting approach is to reduce the high computational effort in configuration interaction calculations by preselecting only the most important configurations via machine-learning models [130, 131]. However, machine learning has not been applied yet for handling extremely large numbers of atomic transition parameters, required in huge-sized rate-equation calculations.

To sum up, the most important questions that have arisen are:

- Is it possible to develop a state-resolved rate-equation approach for describing X-ray multiphoton ionization dynamics, and in which way does it extend our current understanding?
- Can machine learning help to make the state-resolved rate-equation calculations computationally efficient?
- How is the electron cloud of atoms aligned through an ultraintense and ultrafast X-ray pulse generated by XFELs?

In this thesis, I address these questions by extending the *ab initio* electronic-structure and ionization dynamics toolkit XATOM [20, 132]. XATOM simulates X-ray multiphoton ionization dynamics of atoms based on the configuration-based rate-equation approach. The underlying electronic-structure calculations are performed using the Hartree-Fock-Slater approximation [133], being one of the simplest and most efficient first-principle electronic-structure methods. There are, of course, more accurate but computationally more expensive electronic-structure methods [134, 135]. However, computational efficiency is crucial for XATOM because even the number of electronic configurations involved in the configuration-based rate-equation approach is extremely large for heavy atoms [40]. In my prior master thesis [136], XATOM has already been extended by a quantum-state-resolved electronic-structure framework, which is based on first-order many-body perturbation theory and which improves the accuracy of transition energies.

Thesis outline

In this cumulative dissertation, I theoretically study state-resolved X-ray multiphoton ionization dynamics of atoms based on a developed state-resolved Monte Carlo rate-equation implementation in XATOM. The theoretical concepts used in this thesis are reviewed in Chapter 2. My scientific contributions are the topic of Chapter 3. In particular, Sec. 3.1 introduces the quantum-state-resolved electronic-structure framework. It delivers the basis for the state-resolved Monte Carlo rate-equation implementation, presented in Sec. 3.2. I consider how the high computational cost of this state-resolved Monte Carlo rate-equation implementation can be tackled by a machine-learning strategy in Sec. 3.3, while I apply it to explore electron-cloud alignment dynamics during an intense linearly polarized X-ray pulse in Sec. 3.4. The thesis finishes with a conclusion and future perspectives in Chapter 4.

Chapter 2

Theoretical Framework

This chapter provides a general introduction to the theoretical framework into which this thesis is embedded. The theories on which each individual scientific contribution is essentially based are discussed in separate sections according to the order of the scientific publications in Chapter 3.

2.1 Electronic-structure calculations

To simulate X-ray multiphoton ionization dynamics, a suitable electronic-structure framework is necessary for efficiently describing atoms, atomic ions, and X-ray-induced transitions between them. This section outlines the theory of electronic-structure calculations based on more detailed discussions in Refs. [136–138]. Throughout this and the following sections, atomic units, i.e., $m = |e| = \hbar = 1$ and $c = 1/\alpha$ are employed, where α is the fine-structure constant.

2.1.1 The Hamiltonian and its solutions

The fundamental Hamiltonian The problem to solve is that of N nonrelativistically treated electrons in an isolated atom or ion of nuclear charge Z. According to the Born-Oppenheimer approximation [139, 140] the nucleus is assumed to be at rest (position zero) and the focus is on the electrons only. They are described by the following electronic Hamiltonian [140]

$$\hat{H}_{\text{matter}} = \sum_{i=1}^{N} \left\{ -\frac{1}{2}\nabla_i^2 - \frac{Z}{|\boldsymbol{x}_i|} \right\} + \frac{1}{2} \sum_{\substack{i,j \\ i \neq j}}^{N} \frac{1}{|\boldsymbol{x}_i - \boldsymbol{x}_j|} \tag{2.1}$$

with $\boldsymbol{x}_i$ being the position vector of an electron in the atom or ion. $\hat{H}_{\text{matter}}$ contains a kinetic energy term, an attractive electron-nucleus interaction term, and a repulsive electron-electron interaction term for each electron. Due to the latter term, finding exact solutions to $\hat{H}_{\text{matter}}$ is impossible (when $N > 1$).

For this reason, a common approach is to decompose $\hat{H}_{\text{matter}}$ into a mean-field Hamiltonian $\hat{H}_{\text{MF}}$ and a residual electron-electron interaction $\hat{V}_{\text{res}}$ via

$$\hat{H}_{\text{matter}} = \hat{H}_{\text{MF}} + \hat{V}_{\text{res}}. \tag{2.2}$$

$\hat{H}_{\text{MF}}$ approximates the electron-electron interaction term by a mean-field potential $\hat{V}_{\text{MF}}$, which individually acts on the electrons (i.e., $\sum_i$ only). Each electron can be thought of as being in an effective potential formed by the nucleus and all other electrons. The part of the full electron-electron interaction that is not captured by $\hat{V}_{\text{MF}}$ is contained in $\hat{V}_{\text{res}}$. In this way, the problem is reduced to finding solutions to $\hat{H}_{\text{MF}}$ only. A suitable mean-field Hamiltonian has a good balance between minimum computational effort to solve the equations and maximum possible impact of the electron-electron interaction.

The Hartree-Fock-Slater Hamiltonian A very simple but efficient choice for $\hat{H}_{\text{MF}}$ is the Hartree-Fock-Slater (HFS) Hamiltonian $\hat{H}_{\text{HFS}}$ [133]. It is given by

$$\hat{H}_{\text{HFS}} = \sum_{i=1}^{N} \left\{ -\frac{1}{2}\nabla_i^2 + \hat{V}_{\text{HFS}}(\boldsymbol{x}_i) \right\}, \tag{2.3a}$$

with

$$\hat{V}_{\text{HFS}}(\boldsymbol{x}_i) = -\frac{Z}{|\boldsymbol{x}_i|} + \int d^3x_j \frac{\rho(\boldsymbol{x}_j)}{|\boldsymbol{x}_i - \boldsymbol{x}_j|} - \frac{3}{2}\left[\frac{3}{\pi}\rho(\boldsymbol{x}_i)\right]^{\frac{1}{3}}, \tag{2.3b}$$

where $\rho(\boldsymbol{x})$ is the local electron density.

The one-electron solutions of $\hat{H}_{\text{HFS}}$ are the so-called spin orbitals φ_q with spin-orbital energies ε_q. They solve the effective one-electron HFS equation

$$\left[-\frac{1}{2}\nabla^2 + \hat{V}_{\text{HFS}}(\boldsymbol{x}) \right] \varphi_q(\boldsymbol{x}) = \varepsilon_q \varphi_q(\boldsymbol{x}). \tag{2.4}$$

For bound spin orbitals ($\varepsilon_q < 0$), the spin-orbital index q consists of a set of four quantum numbers: the principal quantum number n_q, the orbital-angular momentum l_q, and the orbital- and spin-angular-momentum projections m_{l_q} and m_{s_q}. For unbound spin orbitals ($\varepsilon_q \geq 0$), n_q is replaced by the spin-orbital energy ε_q. In this way, φ_q decomposes into a radial part, an angular part given by a spherical harmonic

$Y_{l_q}^{m_{l_q}}$, and a spin part, such that

$$\varphi_q(\boldsymbol{x}) = \frac{u_{\xi_q,l_q}(r)}{r} Y_{l_q}^{m_{l_q}}(\theta,\phi) \begin{pmatrix} \delta_{m_{s_q},\frac{1}{2}} \\ \delta_{m_{s_q},-\frac{1}{2}} \end{pmatrix}, \tag{2.5}$$

with $\xi_q = n_q$ for $\varepsilon_q < 0$ and $\xi_q = \varepsilon_q$ for $\varepsilon_q \geq 0$. As a consequence of the decomposition of φ_q, the problem of solving N effective one-electron HFS equations [Eq. (2.4)] reduces to radial HFS equations for the subshells occupied in the atom or ion. For each subshell, characterized by n and l quantum numbers, a bound radial orbital $u_{n,l}$ needs to be calculated via a radial HFS equation. The orbital energy ε_{nl} is shared by all φ_q that belong to the subshell nl. When eventually desired, some unbound radial orbitals $u_{\varepsilon,l}$ for certain electron energies $\varepsilon \geq 0$ are calculated via radial HFS equations as well.

Note that the electron density is given by $\rho(\boldsymbol{x}) = \sum_{q=1}^{N} \varphi_q^\dagger(\boldsymbol{x})\varphi_q(\boldsymbol{x})$ and, thus, $\hat{V}_{\mathrm{HFS}}$ [Eq. (2.3b)] depends already on its solutions φ_q. Therefore, the radial HFS equations have to be solved in a self-consistent way. Consequently, each atomic species and each electronic configuration has its own radial orbitals and orbital energies, which need to be recalculated when considering a new atomic species or electronic configuration. (For more detail about numerically solving the self-consistent HFS equations, the reader is referred to Refs. [20, 132]).

The antisymmetrized product of the one-electron solutions build up the N-electron solutions of $\hat{H}_{\mathrm{HFS}}$ [141]. These so-called electronic Fock states $|\Phi_\alpha\rangle$ are expressed as

$$|\Phi_\alpha\rangle = \prod_{q=1}^{\infty} |n_q^\alpha\rangle. \tag{2.6}$$

Here, n_q^α is the occupation of the spin orbital φ_q in the Fock state with index α. It is restricted to $n_q^\alpha \in \{0,1\}$ due to the Pauli exclusion principle and its sum is restricted by $\sum_{q=1}^{\infty} n_q^\alpha = N$. The energy of a Fock state is determined by

$$E_\alpha = \sum_{n,l} N_{nl}\varepsilon_{nl} \tag{2.7}$$

with the subshell nl being occupied by N_{nl} electrons. (When unbound spin orbitals with energy ε are involved, they are added as well with $N_{nl} = 1$ and $\varepsilon_{nl} = \varepsilon$.)

Beyond the Hartree-Fock-Slater Hamiltonian The HFS approximation can be improved through first-order many-body perturbation theory [140, 142]. The basis for perturbation theory is the decomposition of $\hat{H}_{\mathrm{matter}}$ in Eq. (2.2). In this way, $\hat{H}_{\mathrm{HFS}}$ is the unperturbed Hamiltonian, the Fock states $|\Phi_\alpha\rangle$—the N-electron

solutions of $\hat{H}_{\mathrm{HFS}}$—are the unperturbed zeroth-order states, and $\hat{V}_{\mathrm{res}}$ is the perturbation. Because the Fock states belonging to the same electronic configuration share the same energy [Eq. (2.7)], degenerate first-order many-body perturbation theory is employed. The objective of degenerate perturbation theory is the creation of the matrix representation $\left\langle \Phi_\alpha \middle| \hat{H}_{\mathrm{matter}} \middle| \Phi_\beta \right\rangle$ in the degenerate subspace of Fock states belonging to the electronic configuration of interest. Diagonalizing the resulting matrix yields improved first-order-corrected energies and linear combinations of Fock states, which generally provide a better description of the electronic states.

2.1.2 X-ray-induced atomic transitions

Having at hand electronic states for atoms and ions, we discuss the transitions induced in an atom or ion by interaction with X rays. The nucleus is too heavy to noticeably interact with X rays and, as before, the focus is on the electrons only [138]. Before describing the interaction between X rays and electrons, let us ask why this interaction is of interest at all. There are two main reasons for probing atoms or generally matter with X rays: (i) Their photon energy ranges from a few hundred electron volt (eV) for soft X rays to several kilo electron volt (keV) for hard X rays [138]. Because K($1s$)-shell binding energies range from 24.6 eV for helium ($Z = 2$) to 34.6 keV for xenon ($Z = 54$) [143], a single X-ray photon can ionize an inner-shell electron for most atoms. As a consequence of inner-shell photoionization, more complex ionization dynamics in atoms, including ultrafast decay processes, can be probed with X rays than with less energetical photons, which can ionize only outer valence shells. (ii) The photon energy E_{ph} in keV is related to a wavelength λ_{ph} in ångstrom (Å) via [144]

$$\lambda_{\mathrm{ph}}[\text{Å}] = \frac{12.4}{E_{\mathrm{ph}}[\mathrm{keV}]}. \tag{2.8}$$

Due to the inverse proportionality, the large X-ray photon energies result in very short wavelengths of just a few Å. Therefore, X rays principally permit imaging of objects with almost or even atomic resolution. With that said, let us now describe the interaction between X rays and electrons and the resulting X-ray-induced atomic transitions in a more detailed fashion.

Photon-electron interaction Hamiltonian When neglecting relativistic effects, photons (more general than X rays) and electrons are coupled by the following interaction Hamiltonian [138]

$$\hat{H}_{\mathrm{int}} = \alpha \sum_{p,q} \hat{c}_p^\dagger \hat{c}_q \left\langle \varphi_p \middle| \hat{A}(\boldsymbol{x}) \cdot \frac{\nabla}{\imath} \middle| \varphi_q \right\rangle + \frac{\alpha^2}{2} \sum_{p,q} \hat{c}_p^\dagger \hat{c}_q \left\langle \varphi_p \middle| \hat{A}^2(\boldsymbol{x}) \middle| \varphi_q \right\rangle, \tag{2.9a}$$

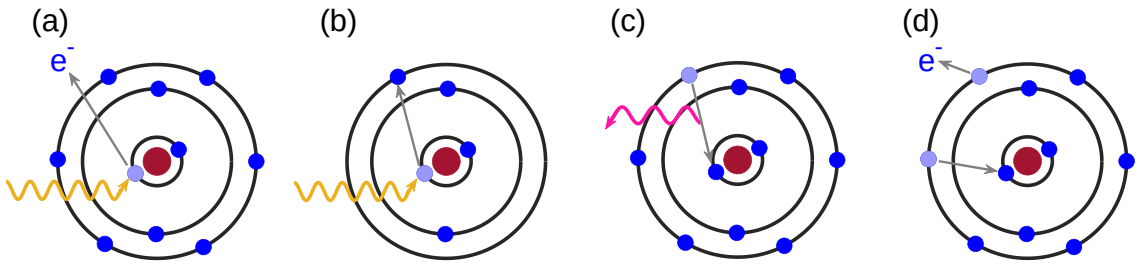

Figure 2.1: Diagrams of X-ray-induced atomic transitions considered in the present thesis. (a) Photoionization, (b) resonant photoabsorption, (c) fluorescence, and (d) Auger-Meitner decay.

with the vector-potential operator

$$\hat{A}(\boldsymbol{x}) = \sqrt{\frac{2\pi}{V\alpha^2}} \sum_{\boldsymbol{k},\lambda} \frac{1}{\sqrt{\omega_{\boldsymbol{k}}}} \left\{ \hat{a}_{\boldsymbol{k},\lambda} \epsilon_{\boldsymbol{k},\lambda} e^{\imath \boldsymbol{k}\cdot\boldsymbol{x}} + \hat{a}^{\dagger}_{\boldsymbol{k},\lambda} \epsilon^{*}_{\boldsymbol{k},\lambda} e^{-\imath \boldsymbol{k}\cdot\boldsymbol{x}} \right\} . \tag{2.9b}$$

Here, V is the quantization volume of the photon field. Note that $\hat{H}_{\text{int}}$ [Eq. (2.9a)] and $\hat{A}(\boldsymbol{x})$ [Eq. (2.9b)] are written in the formalism of second quantization with respect to both photons and electrons because it is one of the simplest formalisms for describing X-ray-induced transitions. To this end, we introduce creation and annihilation operators, $\hat{c}^{\dagger}_{p}$ and $\hat{c}_{q}$, for the electrons, associated with the spin orbitals φ_p and φ_q, respectively. Because electrons are fermions, $\hat{c}^{\dagger}_{p}$ and $\hat{c}_{q}$ are anticommutating operators [138, 141, 145, 146]. Similarly, for the photons, we introduce creation and annihilation operators, $\hat{a}^{\dagger}_{\boldsymbol{k},\lambda}$ and $\hat{a}_{\boldsymbol{k},\lambda}$. They are associated with a photon in the photon mode characterized by a wave vector $\boldsymbol{k}$, a polarization vector $\epsilon_{\boldsymbol{k},\lambda}$ ($\lambda = 1, 2$), and an energy $\omega_{\boldsymbol{k}} = \frac{|\boldsymbol{k}|}{\alpha}$ (in atomic units). But because photons are bosons, $\hat{a}^{\dagger}_{\boldsymbol{k},\lambda}$ and $\hat{a}_{\boldsymbol{k},\lambda}$ are commutating operators [138, 146, 147]. (For a deeper insight into the formalism of second quantization, the reader is referred to Refs. [137, 138, 141, 145, 147, 148].) It should be pointed out that only one part of $\hat{H}_{\text{int}}$ [Eq. (2.9a)] and $\hat{A}(\boldsymbol{x})$ [Eq. (2.9b)] is actively involved in an X-ray-induced atomic transition. The specific part involved depends on the X-ray-induced transition under consideration.

Four X-ray-induced atomic transitions are of special importance for the present thesis. These X-ray-induced atomic transitions are depicted in Fig. 2.1 and briefly discussed in the following.

Photoionization Photoionization [Fig. 2.1(a)] describes the process in which an atom or ion absorbs a single X-ray photon, while it ejects one of its bound electron into the continuum [24, 136, 138, 149]. The atom or ion becomes (further) ionized. This process is driven by the $\hat{A} \cdot \frac{\nabla}{\imath}$ term of $\hat{H}_{\text{int}}$ [Eq. (2.9a)], describing a

one-photon and one-electron process and involves the $\hat{a}_{\boldsymbol{k},\lambda}$ term of $\hat{A}(\boldsymbol{x})$ [Eq. (2.9b)], corresponding to photon annihilation. Because the energy is conserved during photoionization, the energy of the ejected photoelectron is $\varepsilon = \omega_{\boldsymbol{k}_{\text{in}}} + E_i^N - E_f^{N-1}$, which has to be > 0 for a continuum state. Here, $\omega_{\boldsymbol{k}_{\text{in}}}$ is the energy of the absorbed X-ray photon. E_i^N and E_f^{N-1} are the energies of the initial (index i) and final (index f) electronic states of N and $N-1$ electrons, respectively. For a transition between two specific initial and final states, the threshold energy $E_f^{N-1} - E_i^N$ determines the minimum energy $\omega_{\boldsymbol{k}_{\text{in}}}$ that is necessary for this photoionization transition to be energetically allowed [138]. If the X-ray photon energy is sufficiently large to ionize inner-shell electrons, inner-shell photoionization is, generally, much more likely than valence-shell photoionization [20, 24].

Resonant photoabsorption When $\omega_{\boldsymbol{k}_{\text{in}}}$ is smaller than the threshold energy, resonant photoabsorption [Fig. 2.1(b)] can take place. Resonant photoabsorption is similar to photoionization. But an electron is transferred into an energetically higher-lying orbital in a partially occupied or empty subshell instead of the continuum. Therefore, it stays bound ($\varepsilon < 0$). Owing to the energy conservation, only a very few selected transitions are possible at all for a given sharp $\omega_{\boldsymbol{k}_{\text{in}}}$. This strong restriction is, generally, softened by considering an energy distribution around $\omega_{\boldsymbol{k}_{\text{in}}}$ [40].

Fluorescence Photoionization and resonant photoabsorption generate ions in excited electronic states of high energy. As a consequence, these ions partly relax by giving off their excess energy through spontaneous emission of a photon of energy ω_F [24, 136, 138, 150]. The photon emission is accompanied by the refilling of a hole by an electron from an energetically higher-lying orbital. This process is called fluorescence [Fig. 2.1(c)]. For inner-shell holes, $\omega_F = E_i^N - E_f^N$, generally, lies in the X-ray photon energy region (more than a few hundred eV). In this case, the process is also called X-ray fluorescence. Likewise to photoionization, fluorescence is driven by the $\hat{A} \cdot \frac{\nabla}{\imath}$ term of $\hat{H}_{\text{int}}$ [Eq. (2.9a)]. But because a photon is created not annihilated, the $\hat{a}^\dagger_{\boldsymbol{k},\lambda}$ term of $\hat{A}(\boldsymbol{x})$ [Eq. (2.9b)] is involved.

Auger-Meitner decay Especially for atoms with low nuclear charge Z, like neon ($Z = 10$) or argon ($Z = 18$), the relaxation is dominated by Auger-Meitner decay [24, 136, 138, 150]. In Auger-Meitner decay [Fig. 2.1(d)], the ion relaxes via emission of an electron of energy $\varepsilon = E_i^N - E_f^{N-1} > 0$ into the continuum, while another bound electron refills a hole in an energetically lower-lying orbital. In contrast to the previous X-ray-induced transitions, Auger-Meitner decay is purely electronic,

without any photon being directly involved. Therefore, the photon-electron interaction Hamiltonian [Eq. (2.9a)] cannot serve as $\hat{H}_{\mathrm{int}}$. Instead, the electron-electron Coulomb interaction mediates the Auger-Meitner decay and, thus, in the mean-field approximation (Sec. 2.1.1), it is $\hat{H}_{\mathrm{int}} = \hat{V}_{\mathrm{res}}$ [136, 138].

Other X-ray-induced atomic transitions There are, of course, further possible X-ray-induced atomic transitions [24, 132]. Photoionization also occurs via direct nonsequential multiphoton ionization [34, 50], where several X-ray photons are simultaneously absorbed. This process involves artificial intermediate electronic states that cannot be resonantly populated. However, for X rays, direct nonsequential multiphoton ionization is clearly a very weak process compared to one-photon ionization. To first order in $\hat{H}_{\mathrm{int}}$, elastic and inelastic X-ray scattering [138, 151–153] is mediated by the $\hat{A}^2$ term of $\hat{H}_{\mathrm{int}}$ [Eq. (2.9a)]. Whereas elastic X-ray scattering only affects the X-ray photons, but leaves the bound electrons unaffected, bound electrons can be excited by inelastic X-ray scattering. But scattering probabilities are more than one order of magnitude smaller than photoionization probabilities for photon energies ≤ 10 keV [154]. Furthermore, photons may not only be spontaneously emitted by fluorescence, but are also generated by stimulated emission [24]. Stimulated emission leads to coherent effects like Rabi flopping [155–160], which are, however, minor effects for a stochastic ensemble of X-ray pulses based on the self-amplified spontaneous emission principle [155–157]. Note that in an atomic gas, stimulated emission can be driven by X-ray fluorescence photons emitted from ions produced first by an X-ray pulse. When the X-ray pulse propagates through an elongated atomic gas and produces more atoms in excited states, stimulated emission is exponentially amplified. This amplification of stimulated emission results in an atomic X-ray lasers [161, 162], but is beyond the scope of this work, which focuses on isolated atoms. Moreover, double photoionization and double Auger-Meitner decay via shake-off and knockout mechanisms [163–165] lead to the emission of several electrons and are known to be nonnegligible processes [34, 49, 62, 165]. But describing these higher-order many-body processes requires a higher-level description of electronic states, including electron-electron correlation effects. None of these further X-ray-induced atomic transitions is included in the present thesis. For the sake of computational efficiency of the generally cumbersome X-ray multiphoton ionization dynamics calculations (Sec. 2.2), the focus is only on the most relevant and easy to calculate X-ray-induced atomic transitions, which are given in Fig. 2.1.

Transition rate Next, we consider the probability $P_{I\to F}$ that an atom or ion initially in state $|I\rangle$ undergoes a specific X-ray-induced atomic transition into a

final state $|F\rangle$. To calculate $P_{I\to F}$ for a transition, time-dependent perturbation theory [138] is applied using

$$\hat{H} = \hat{H}_{\text{matter}} + \hat{H}_{\text{ph}} + \hat{H}_{\text{int}}. \tag{2.10}$$

Here, $\hat{H}_{\text{matter}}$ is the approximated electronic Hamiltonian (Sec. 2.1.1) and $\hat{H}_{\text{ph}} = \sum_{\boldsymbol{k},\lambda} \omega_{\boldsymbol{k}} \hat{a}^\dagger_{\boldsymbol{k},\lambda} \hat{a}_{\boldsymbol{k},\lambda}$ is the photonic Hamiltonian (ignoring the zero point energy). Together they form the unperturbed Hamiltonian $\hat{H}_0 = \hat{H}_{\text{matter}} + \hat{H}_{\text{ph}}$, whereas the underlying interaction Hamiltonian $\hat{H}_{\text{int}}$ is the perturbation. Although the X-ray-induced interaction is actually not a small perturbation for high-intensity X rays [24], this assumption sufficiently and efficiently describes X-ray-induced atomic transition for X-ray multiphoton ionization dynamics (Sec. 2.2).

The initial state $|I\rangle = |\Psi_i^N\rangle|N_{\text{ph}}^{\text{in}}\rangle$ consists of the N-electron state $|\Psi_i^N\rangle$ and the pure photonic state $|N_{\text{ph}}^{\text{in}}\rangle$. $|\Psi_i^N\rangle$ is an eigenstate of the approximated $\hat{H}_{\text{matter}}$ with energy E_i^N, e.g., an electronic Fock state or an improved state (Sec. 2.1.1)—but its exact specification does not matter here. $|N_{\text{ph}}^{\text{in}}\rangle$ describes the incoming photon state with $N_{\text{ph}}^{\text{in}}$ photons in the mode with $\boldsymbol{k}_{\text{in}}$ and $\epsilon_{\boldsymbol{k}_{\text{in}},\lambda_{\text{in}}}$ and is an eigenstate of $\hat{H}_{\text{ph}}$ with energy $E_{\text{ph}}^{\text{in}} = N_{\text{ph}}^{\text{in}} \omega_{\boldsymbol{k}_{\text{in}}}$. Consequently, $|I\rangle$ is an eigenstate of $\hat{H}_0$ with energy $E_I = E_i^N + E_{\text{ph}}^{\text{in}}$.

Initially in $|I\rangle$, the state $|\Psi(t)\rangle_{\text{int}}$ evolves in time due to the X-ray-induced interaction. In the interaction picture [166], employed here, the time evolution is solely caused by $\hat{H}_{\text{int}}$. This means that the time factor $e^{-\imath \hat{H}_0 t}$ is eliminated. Thus, $|\Psi(t)\rangle_{\text{int}}$ evolves according to the following equation of motion [138, 166]

$$\imath \frac{\partial}{\partial t} |\Psi(t)\rangle_{\text{int}} = e^{\imath \hat{H}_0 t} \hat{H}_{\text{int}} e^{-\epsilon|t|} e^{-\imath \hat{H}_0 t} |\Psi(t)\rangle_{\text{int}}, \tag{2.11}$$

with $\epsilon > 0$ ensuring that $\frac{\partial}{\partial t}|\Psi(t)\rangle_{\text{int}} = 0$ for $t \to \pm\infty$. Integrating Eq. (2.11) from $-\infty$ to some final time t_f and inserting the initial condition $\lim_{t\to-\infty} |\Psi(t)\rangle_{\text{int}} = |I\rangle$ yields the recursive formula

$$\begin{aligned} |\Psi(t_f)\rangle_{\text{int}} = |I\rangle &- \imath \int_{-\infty}^{t_f} dt e^{\imath \hat{H}_0 t} \hat{H}_{\text{int}} e^{-\epsilon|t|} e^{-\imath \hat{H}_0 t} |I\rangle \\ &- \int_{-\infty}^{t_f} dt \int_{-\infty}^{t} dt' e^{\imath \hat{H}_0 t} \hat{H}_{\text{int}} e^{-\epsilon|t|} e^{-\imath \hat{H}_0 t} e^{\imath \hat{H}_0 t'} \hat{H}_{\text{int}} e^{-\epsilon|t'|} e^{-\imath \hat{H}_0 t'} |I\rangle \\ &+ \cdots, \end{aligned} \tag{2.12}$$

where $\cdots$ refers to terms with three and more time integrals.

To obtain the transition probability $P_{I\to F}$ for reaching a final state $|F\rangle$ in the

end of the interaction, t_f is set to ∞ [141], so that

$$P_{I\to F} = |\langle F|\Psi(t_f \to \infty)\rangle_{\text{int}}|^2. \tag{2.13}$$

Note that the final state $|F\rangle$ with energy E_F is defined similar to $|I\rangle$, and so are the subsequently introduced intermediate states $|M\rangle$ with energies E_M. Employing Eq. (2.12), assumming orthonormality of states, inserting $1 = \sum_M |M\rangle\langle M|$, and utilizing the definition of the delta distribution, $P_{I\to F}$ is expressed by the recursive formula

$$\begin{aligned} P_{I\to F} = \Big|2\pi\delta(E_F - E_I)\Big\{&\left\langle F\left|\hat{H}_{\text{int}}\right|I\right\rangle \\ &+ \sum_M \frac{1}{E_I - E_M + \imath\epsilon}\left\langle F\left|\hat{H}_{\text{int}}\right|M\right\rangle\left\langle M\left|\hat{H}_{\text{int}}\right|I\right\rangle \\ &+ \sum_{M,M',\cdots}\cdots\Big\}\Big|^2. \end{aligned} \tag{2.14}$$

Here, $\cdots$ refers to terms summing over two and more intermediate states $|M\rangle$. Note that $|\delta(x)|^2 = \delta(x)\frac{dt}{2\pi}$ [138] for some time interval dt. Thus, the transition rate (the transition probability per unit time) is given by

$$\begin{aligned} \Gamma_{I\to F} = 2\pi\delta(E_F - E_I)\Big\{&\left|\left\langle F\left|\hat{H}_{\text{int}}\right|I\right\rangle\right. \\ &+ \sum_M \frac{1}{E_I - E_M + \imath\epsilon}\left\langle F\left|\hat{H}_{\text{int}}\right|M\right\rangle\left\langle M\left|\hat{H}_{\text{int}}\right|I\right\rangle \\ &+ \sum_{M,M',\cdots}\cdots\Big|^2\Big\}. \end{aligned} \tag{2.15}$$

In first-order time-dependent perturbation theory, this simplifies to

$$\Gamma_{I\to F} = 2\pi\delta(E_F - E_I)\left|\left\langle F\left|\hat{H}_{\text{int}}\right|I\right\rangle\right|^2. \tag{2.16}$$

The delta distribution guarantees the energy conservation during the X-ray-induced atomic transition. It can be eliminated by integrating over the continuum of final energy states.

Cross section For photoionization and photoabsorption, the transition rate $\Gamma_{I\to F}$ depends on the number of incoming photons. In these cases, it is, therefore, useful to employ a quantity independent of the number of incoming photons. A convenient

quantity, closely related to $\Gamma_{I\to F}$, is the cross section

$$\sigma_{I\to F} = \frac{\Gamma_{I\to F}}{J_{\mathrm{ph}}}, \tag{2.17}$$

where J_{ph} is the photon flux (the number of photons per unit time and unit area) [138].

Having at hand the formulae of Eqs. (2.15) and (2.17), we can describe all basic X-ray-induced atomic transitions discussed above. For an X-ray-induced atomic transition of interest, just the corresponding interaction Hamiltonian $\hat{H}_{\mathrm{int}}$ and the electronic states $|\Psi^N\rangle$ need to be specified and the corresponding transition rate $\Gamma_{I\to F}$ can be calculated following Eqs. (2.15), (2.16), or (2.17). Because this is straightforward and corresponding calculations are performed in Refs. [136, 138], detailed calculations are not shown here.

2.1.3 Conclusion and outlook

In this section, the HFS approximation for describing the electronic structure of atoms and atomic ions has been briefly sketched. For an atom or atomic ion in a specific electronic configuration, radial HFS calculations deliver a bound radial orbital $u_{n,l}$ with energy $\varepsilon_{n,l}$ for each involved subshell nl and eventually unbound radial orbitals $u_{\varepsilon,l}$ with energies ε when desired. The HFS approximation is sensible when very simple and efficient electronic-structure calculations are required. This is the case when simulating X-ray multiphoton ionization dynamics, which include large numbers of different electronic configurations and, hence, individual HFS calculations (see Sec. 2.2). The basic X-ray-induced atomic transitions critical for X-ray multiphoton ionization dynamics (see Sec. 2.2) have also been briefly discussed. General formulae for calculating transition rates and cross sections have been presented, which allow us to obtain transition rates and cross sections for all basic X-ray-induced atomic transitions.

However, the simple HFS-based electronic-structure calculations [20, 49] are limited in the following way. They focus on electronic configurations, so that more detailed electronic quantum states are not accessible. Moreover, they only provide zeroth-order energies and averaged subshell cross sections and transition rates. But individual quantum-state-resolved cross sections and transition rates are necessary for studying electron-cloud alignment. Therefore, first-order many-body perturbation theory is applied to improve the HFS-based electronic-structure calculations. Improved quantum-state-resolved electronic-structure calculations, including the calculation of individual quantum-state-resolved cross sections and transition

rates, have been performed in a prior master thesis of the author [136] and are also the subject of Sec. 3.1.

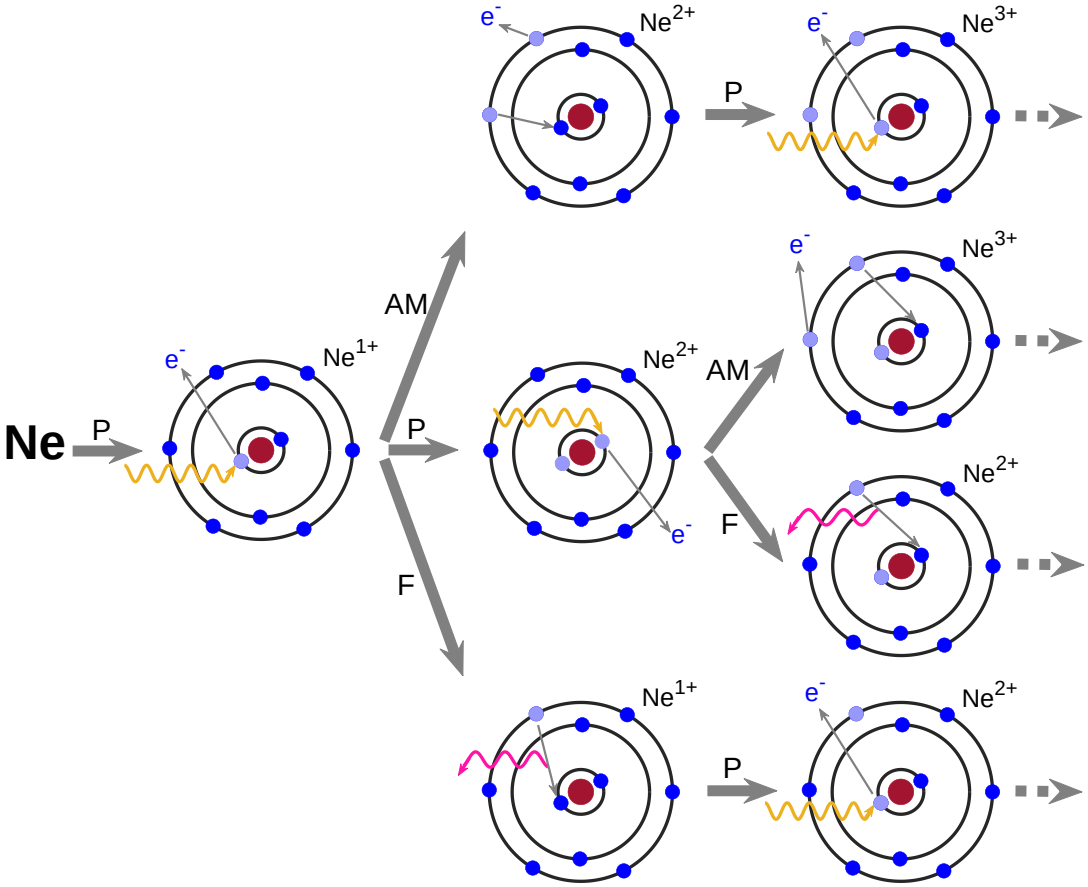

Figure 2.2: X-ray multiphoton ionization dynamics. For neon (Ne), the first few possible sequences of inner-shell photoionization (P), Auger-Meitner decay (AM), and X-ray fluorescence (F) are depicted. For simplicity, valence-shell photoionization, which is unlikely, and Auger-Meitner decay involving the 2*s*-shell are neglected.

2.2 X-ray multiphoton ionization dynamics

When an atom is exposed to an X-ray pulse, it may absorb an X-ray photon predominantly via one-photon ionization of the inner shell. Inner-shell photoionization is accompanied by one or multiple decay processes via Auger-Meitner decay and/or X-ray fluorescence, refilling inner-shell holes. For an intense X-ray pulse, the extremely large number of X-ray photons enables the sequential absorption of multiple X-ray photons, which competes with the accompanying decay processes (Fig. 2.2). As a consequence of the sequences of one-photon ionization events accompanied by Auger-Meitner decay and X-ray fluorescence, high atomic charge states are formed within a single X-ray pulse. These atomic ionization dynamics driven by high-intensity X rays are called X-ray multiphoton ionization dynamics [24]. Note that at specific X-ray photon energies also resonant photoabsorption of some intermediate ions notably contribute to the X-ray multiphoton ionization dynamics (see Refs. [25, 35]

for studies on neon).

To quantify what is an intense X-ray pulse, the X-ray fluence F (the number of incoming X-ray photons per X-ray pulse and unit area) is a useful quantity [24]. Next to the total photoionization cross section σ, the probability that an atom undergoes one-photon ionization depends on F. An atom is ionized with almost unit probability at the saturation fluence [24]

$$F_{\mathrm{sat}} = \frac{1}{\sigma}. \tag{2.18}$$

For $F > F_{\mathrm{sat}}$, the probability that the produced ions undergo further one-photon ionization within the same X-ray pulse is very large. This is the X-ray multiphoton ionization dynamics regime. To give an example, for argon at an X-ray photon energy of 5 keV, it is $\sigma \approx 2.8 \times 10^{-2}$ Mb (Megabarn) (calculated with the implementation presented in Sec. 3.1). This corresponds to $F_{\mathrm{sat}} \approx 3 \times 10^{11}$ photons/μm^2. X-ray fluences in the order of 10^{11}–10^{12} photons/μm^2 are routinely achieved by X-ray free-electron lasers [1, 2, 4, 11]. As a consequence, X-ray multiphoton ionization dynamics have attracted attention with the recent advent of X-ray free-electron lasers around the world [1–5]. In this section, a method for simulating X-ray multiphoton ionization dynamics is presented.

2.2.1 Rate-equation approach

X-ray multiphoton ionization dynamics can be simulated by a rate-equation approach [20, 24, 31, 32]. The rate-equation approach described in this section excludes resonant photoabsorption, which can, however, be easily included. Moreover, we only consider the states of the bound electrons in the ions formed during X-ray multiphoton ionization dynamics. In particular, we are interested in the time-resolved population probability $P_I(t)$ of the bound-electron states I formed. However, the unbound photoelectrons and Auger-Meitner electrons are immediately neglected after emission. With that also their interaction with each other and with the bound electrons is neglected. Without the restriction to bound electrons, simulating X-ray multiphoton ionization dynamics would be extremely challenging [24].

Configuration-based approach A common approach is to define the states I by the electronic configurations $1s^{N_{1s}}2s^{N_{2s}}2p^{N_{2p}}3s^{N_{3s}}3p^{N_{3p}}\cdots$. Here, $N_j \leq 4l_j + 2$ is the occupation number of the jth subshell with orbital-angular momentum l_j. This approach is the focus of this section, but rate equations work fairly similarly for other definitions of I. The configuration-based rate-equation approach is illustrated

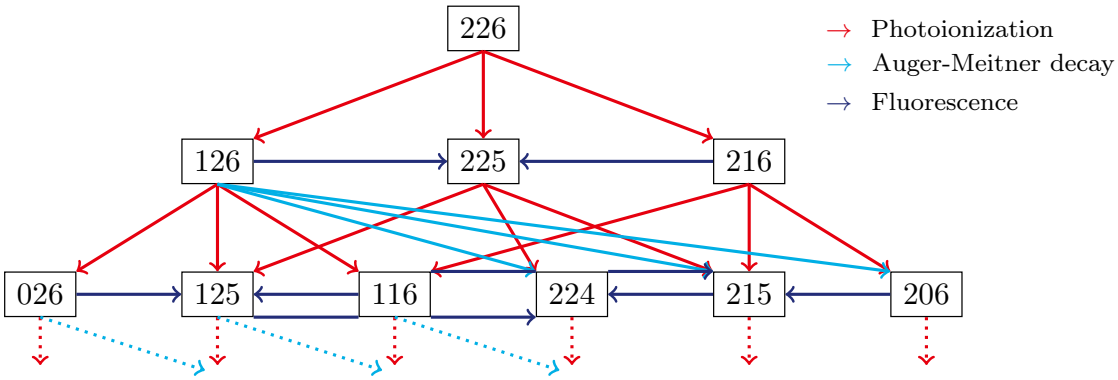

Figure 2.3: Configuration-based rate-equation approach at the example of neon. Nodes represent all possible electronic configurations $1s^{N_{1s}}2s^{N_{2s}}2p^{N_{2p}}$, labeled by $N_{1s}N_{2s}N_{2p}$, that may be formed by removing zero, one, or two electrons from neutral neon (226). Electronic configurations are connected by X-ray-induced atomic transitions via either photonionization (red arrows), Auger-Meitner decay (cyan arrows), or fluorescence (blue arrows). For simplicity, electronic configurations with more than two removed electrons are not shown. A complete graph is presented in Ref. [49].

for neon (ground state electronic configuration $1s^22s^22p^6$) in Fig. 2.3. For a given atomic species, we construct all possible electronic configurations I that may be formed by removing zero, one, two, or up to $N_{\max}$ electrons from the neutral ground state electronic configuration of Z electrons. $N_{\max} \leq Z$ is the maximum number of electrons that can be ionized via sequences of one-photon ionization events, including eventually resonant photoabsorption, at a given X-ray photon energy. For each involved electronic configuration I, individual HFS calculations have to be performed (Sec. 2.1.1). Based on them, all possible subshell photoionization and eventually resonant photoabsorption cross sections $\sigma_{I\to I'}$ as well as subshell transition rates $\Gamma^{\mathrm{AM}}_{I\to I'}$ for Auger-Meitner decay and $\Gamma^{\mathrm{F}}_{I\to I'}$ for fluoresecence are calculated (Sec. 2.1.2). The calculated cross sections and transition rates among all electronic configurations involved (arrows in Fig. 2.3) serve as input parameters to the rate equations.

Rate equations Before the X-ray pulse, the atom is in the neutral ground state electronic configuration I_0, so that $P_{I_0} = 1$. During the X-ray pulse, the atom undergoes one-photon ionization into a singly ionized electronic configuration I_1 with transition rate $\Gamma_{I_0\to I_1} = \sigma_{I_0\to I_1} J_{\mathrm{ph}}(t)$ [Eq. (2.17)]. The time evolution is completely mediated by the photon flux $J_{\mathrm{ph}}(t)$, describing the temporal X-ray pulse shape.

Hence, the time evolution of $P_{I_0}(t)$ is described by the rate equation

$$\frac{dP_{I_0}(t)}{dt} = -\sum_{I_1} \sigma_{I_0 \to I_1} J_{\mathrm{ph}}(t) P_{I_0}(t), \tag{2.19}$$

where the sum is over all possible I_1 (arrows pointing away from I_0, i.e., 226, in Fig. 2.3). The time evolution of the population probability $P_{I_1}(t)$ of a produced singly ionized electronic configuration I_1 is described by the rate equation

$$\frac{dP_{I_1}(t)}{dt} = \sigma_{I_0 \to I_1} J_{\mathrm{ph}}(t) P_{I_0}(t) - \left\{ \sum_{I_2} [\sigma_{I_1 \to I_2} J_{\mathrm{ph}}(t) + \Gamma^{\mathrm{AM}}_{I_1 \to I_2}] + \sum_{I_1' \neq I_1} \Gamma^{\mathrm{F}}_{I_1 \to I_1'} \right\} P_{I_1}(t). \tag{2.20}$$

On the one hand, the population of I_1 grows (positive sign) due to the ionization of the neutral atom (arrows pointing toward I_1 in Fig. 2.3). On the other hand, it dwindles (negative sign) due to a subsequent ionization or decay process (arrows pointing away from I_1 in Fig. 2.3). It results either in a doubly ionized electronic configuration I_2 or in another singly ionized electronic configuration I_1' for fluorescence. In the same manner, we proceed for all higher ionized electronic configurations. Generalization of Eq. (2.20) yields the following rate equation for describing the time evolution of the population probability $P_I(t)$ of an electronic configuration I

$$\frac{dP_I(t)}{dt} = \sum_{I' \neq I} \left[\Gamma_{I' \to I} P_{I'}(t) - \Gamma_{I \to I'} P_I(t) \right]. \tag{2.21}$$

Setting up a rate equation via Eq. (2.21) for each electronic configuration I involved in the X-ray multiphoton ionization dynamics results in a set of coupled, first-order differential equations, which can be numerically solved [20].

Number of coupled rate equations The number of coupled rate equations to be solved is equal to the number of electronic configurations I involved in the X-ray multiphoton ionization dynamics. Note that each subshell j can be occupied by $N_j = 0, \ldots, N_j^{\max}$ electrons, where $N_j^{\max} \leq 4l_j + 2$ is the occupation number of the neutral ground state electronic configuration. Hence, the number of all possible electronic configurations involved is evaluated by [40]

$$N_{\mathrm{config}} = \prod_j (N_j^{\max} + 1). \tag{2.22}$$

Here, the product is over all subshells j being accessible via sequences of one-photon ionization events at a given X-ray photon energy. No resonant photoabsorption

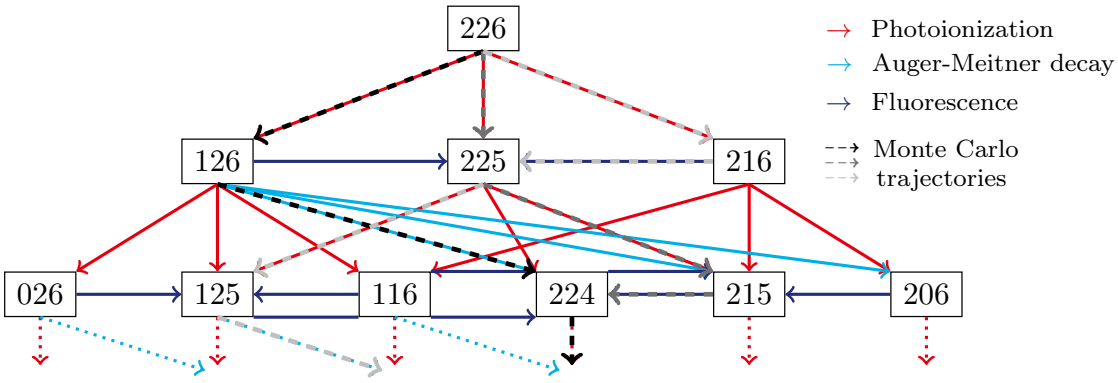

Figure 2.4: Monte Carlo method for indirectly solving the rate equations by stochastically sampling possible ionization trajectories. Three different Monte Carlo trajectories are visualized by dashed arrows. For more details see Fig. 2.3.

is assumed to be available. For the case that all subshells are accessible, N_{config} as a function of the nuclear charge Z is shown in Sec. 3.2. For example, for neon ($1s^2 2s^2 2p^6$), it is $N_{\text{config}} = 3^2 \times 7 = 63$, for argon ($1s^2 2s^2 2p^6 3s^2 3p^6$), it is $N_{\text{config}} = 3^3 \times 7^2 = 1323$, whereas for xenon ($1s^2 2s^2 2p^6 3s^2 3p^6 3d^{10} 4s^2 4p^6 4d^{10} 5s^2 5p^6$), it is $N_{\text{config}} = 3^5 \times 7^4 \times 11^2 = 70596603$. As can be seen by this example, for heavy atoms, the number of electronic configurations involved and, thus, the number of coupled rate equations to be solved is impracticably large. The number of X-ray-induced atomic processes among the electronic configurations that have to be considered is even much larger than the number of electronic configurations involved (≈ 5 times larger for neon [49] and ≈ 40 times larger for xenon [26]). Moreover, the number of rate equations explodes when resonant photoabsorption transitions are included [40, 43].

2.2.2 Monte Carlo on-the-fly rate-equation method

Solving huge-sized rate equations directly is a tough task. To this end, huge-sized rate equations are more efficiently solved via a Monte Carlo on-the-fly rate-equation method [26, 29]. In the Monte Carlo method, the population probabilities $P_I(t)$ are obtained by stochastically sampling possible Monte Carlo trajectories, as sketched in Fig. 2.4. A Monte Carlo trajectory corresponds to a specific time-resolved ionization pathway, i.e., sequence of repeated one-photon ionization events, Auger-Meitner decays, and fluorescence, that an initially neutral atom may undergo in time during the X-ray multiphoton ionization dynamics. The Monte Carlo trajectory ends in a final electronic configuration when no further processes are possible because either the X-ray pulse is over and all decays are completed or all accessible electrons are ionized. Note that, generally, a huge number of different Monte Carlo trajectories is

possible and that different Monte Carlo trajectories may visit the same intermediate electronic configuration or may end in the same final electronic configuration. The probability of propagating in time along a certain ionization pathway depends on the underlying transition probabilities from electronic configurations I to I' at time t. It is given by

$$P_{I\to I'}(t) = \begin{cases} \sigma_{I\to I'} J_{\mathrm{ph}}(t)\Delta t & \text{for photoionization and photoabsorption,} \\ \Gamma_{I\to I'}\Delta t & \text{for Auger-Meitner decay and fluorescence.} \end{cases} \tag{2.23}$$

Here, Δt is the time step utilized in the simulation for the time propagation, i.e., $t \to t + \Delta t$ (for more details, see Ref. [26] and Sec. 3.2).

The required cross sections $\sigma_{I\to I'}$ and transition rates $\Gamma_{I\to I'}$ are calculated on-the-fly [29]. When an electronic configuration I is visited during a Monte Carlo trajectory, $\sigma_{I\to I'}$ and $\Gamma_{I\to I'}$ are calculated for all possible X-ray-induced atomic transitions from the given I to all reachable I' (i.e., all arrows pointing away from node I in Fig. 2.4). For Monte Carlo trajectories sampled sequentially in time, it is useful to store the calculated $\sigma_{I\to I'}$ and $\Gamma_{I\to I'}$. Then, they can be directly reused for following Monte Carlo trajectories. In this way, only those $\sigma_{I\to I'}$ and $\Gamma_{I\to I'}$ are calculated that are really needed in the Monte Carlo sampling. Therefore, when only a part of all electronic configurations is visited, the on-the-fly method is more efficient than the precalculation of all possible $\sigma_{I\to I'}$ and $\Gamma_{I\to I'}$ [26] as performed in the direct rate-equation approach (Sec. 2.2.1).

After running a sufficiently large number of Monte Carlo trajectories, $P_I(t)$ is approximated by the average over all sampled Monte Carlo trajectories. Each Monte Carlo trajectory visits a certain I at time t with either unit or zero probability. It should be stressed here, that keeping track of a very large number of all I is impractical. Accordingly, an alternative way is to directly consider more processed quantities like charge-state distributions or electron and photon spectra during the Monte Carlo sampling [26].

In contrast to the direct rate-equation approach (Sec. 2.2.1), the Monte Carlo rate-equation method involves some statistical uncertainty caused by the finite number of samples of Monte Carlo trajectories. The estimated statistical error ϵ for population probabilities P of e.g., electronic configurations I or charge states q is obtained via [167]

$$\epsilon = \sqrt{\frac{P(1-P)}{N_{\mathrm{traj}} - 1}}. \tag{2.24}$$

It depends on the inverse of N_{traj}, the number of Monte Carlo trajectories sampled. Therefore, the desired level of accuracy determines what value for N_{traj} is referred

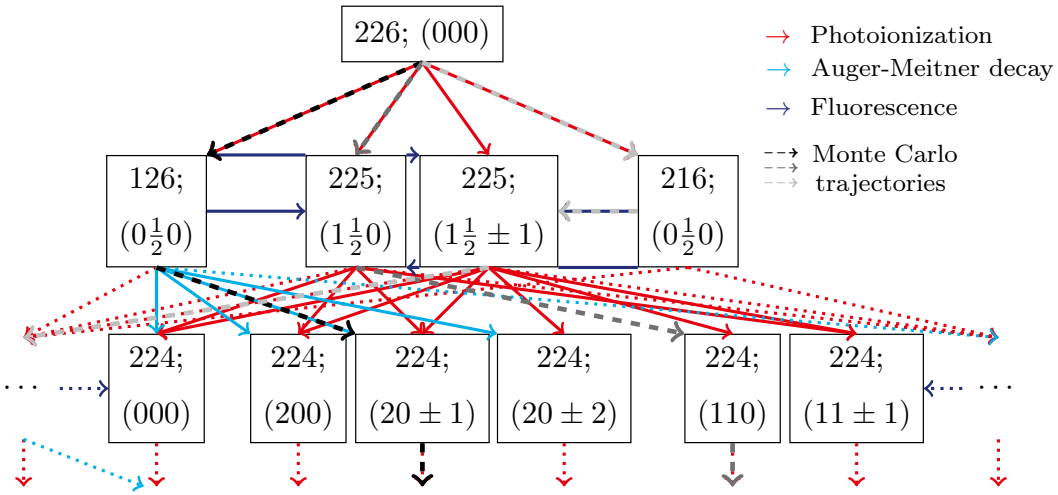

Figure 2.5: State-resolved Monte Carlo rate-equation method. Nodes represent individual quantum states, defined by an electronic configuration $N_{1s}N_{2s}N_{2p}$ and additional quantum numbers LSM_L. For more details on the figure and on the individual quantum states, see Figs. 2.3 and 2.4 and Secs. 3.1 and 3.2, respectively.

to as sufficiently large. For instance, for a statistical error in the order of 0.01 (1%), around 1000 Monte Carlo trajectories are required, whereas a statistical error in the order of 0.001 (0.1%) corresponds to around 100000 Monte Carlo trajectories. Note that statistical errors for quantities other than population probabilities like spectra or alignment parameters cannot be simply estimated by Eq. (2.24). Instead, other methods like bootstrapping [167] have to be applied. The Monte Carlo on-the-fly rate-equation method is most efficient in the cases where N_{traj}, required for the desired level of accuracy, is much smaller than the total number of all possible Monte Carlo trajectories and, consequently, only a fraction of all $P_I(t)$ is involved in the calculations.

2.2.3 Conclusion and outlook

In this section, the configuration-based rate-equation approach for simulating X-ray multiphoton ionization dynamics has been presented. The set of coupled rate equations is solved either directly or via a more efficient Monte Carlo on-the-fly method when the number of rate equations is very huge. The presented rate-equation approach does not include higher-order many-body processes like double photoionization and double Auger-Meitner decay [163–165]. But these processes nonnegligibly affect the charge-state distribution of the ions produced by the X-ray multiphoton ionization dynamics [34, 49]. Taking this into account, the configuration-based rate-equation approach has already been widely and successfully applied for describing X-ray multiphoton ionization dynamics and for interpreting and designing X-ray

free-electron laser experiments [25–35, 40–45, 49].

However, the configuration-based approach cannot capture individual quantum states. Considering individual quantum states would provide complementary information about the X-ray multiphoton ionization dynamics, electron-cloud alignment dynamics included. To this end, in Sec. 3.2 a state-resolved Monte Carlo on-the-fly rate-equation method is developed. The fundamental idea of the state-resolved approach is illustrated in Fig. 2.5. It is quite similar to the configuration-based approach. But individual quantum states, as defined in Sec. 3.1, are used for the bound-electron states I instead of the electronic configurations. As can be seen from comparing Fig. 2.5 and Fig. 2.4, the use of individual quantum states incredibly increases the number of coupled rate equations to be solved. For example, the number of coupled rate equations in the configuration-based approach is 1323 for argon (Sec. 2.2.1), whereas it is 262144 in the state-resolved approach (Sec. 3.2). Consequently, solving state-resolved rate equations for most atoms is even challenging with the Monte Carlo on-the-fly method. Addressing this challenge by applying a machine-learning strategy is the objective of Sec. 3.3.

2.3 Machine learning and neural networks

This section introduces the concepts of machine learning with a focus on neural networks. Its content is mainly based on Refs. [83, 168].

The key idea of machine learning is that a computer algorithm learns its own knowledge by recognizing patters in a given set of data and that its learning performance improves with experience by increasing time and/or amount of data [169]. The learned knowledge is then used to predict properties of never-seen data with a certain accuracy. But machine learning does not provide entirely certain rules in contrast to conventional physical equations based on well-known assumptions. A famous form of machine learning is deep learning [83]. Deep learning is concerned with computer algorithms that learn better suited and high-level representations of the given data by hierarchically building more abstract representations out of simpler ones.

To build a machine-learning model for predicting properties of interest, commonly the following parts are combined:

- a dataset and
- a machine-learning algorithm, including
- a training procedure based on a loss function and
- a regularization.

Potential machine-learning algorithms are supported vector machines [170, 171], kernel machines [172, 173], decision trees [174], and feedforward neural networks [175, 176]—the quintessential example of deep learning. Using feedforward neural networks as an example, the parts of the machine-learning model are described in what follows.

2.3.1 A dataset

Features and labels A dataset D consists of a set of N_D samples. The samples are drawn ideally randomly and independently from the data distribution being of interest for the machine-learning problem at hand. Each sample (index $i = 1, \ldots, N_D$) is represented by a vector $\boldsymbol{x}^{(i)}$, characterizing the sample by a set of features $x_\mu^{(i)}$. To each feature vector $\boldsymbol{x}^{(i)}$ corresponds a label vector $\boldsymbol{y}^{(i)}$, consisting of the variable(s) that should be predicted. In a supervised regression problem, this implies that the machine-learning algorithm is supposed to learn the mapping function $f : \boldsymbol{x} \to \boldsymbol{y}$ between features and label(s). But also unsupervised (no $\boldsymbol{y}$) and/or classification problems are typical in machine learning [83, 177].

Training, validation, and test set The dataset D is divided into a large training set (commonly $\approx 80\%$ of D) and smaller validation and test sets. On the training set, the machine-learning algorithm is run to learn the mapping function f from the training data. The validation set is employed for evaluating and optimizing the performance of the resulting machine-learning model. According to its performance on the validation data, the machine-learning algorithm is adapted and retrained several times until the performance is sufficient. Finally, the test set serves as the ultimate judge of the performance of the final machine-learning model. The size of the training set has an important impact on the performance of the machine-learning algorithm and model. On the one hand, training on a larger set generally results in better predictions on new data not in the training set. On the other hand, training on a smaller set is clearly more computationally efficient.

Data preparation Even though neural networks are supposed to learn suitable representations out of the raw features, some kind of data preparation is usually still crucial. Most important is the normalization of features and label(s), widely performed via Z-score normalization [178]

$$\tilde{z}_\mu^{(i)} = \frac{z_\mu^{(i)} - \bar{z}_\mu}{\Delta_{z_\mu}}. \tag{2.25}$$

Here, $z_\mu^{(i)}$ is the μth feature or label of the ith sample and $\tilde{z}_\mu^{(i)}$ is its normalized value. Furthermore, $\bar{z}_\mu$ and Δ_{z_μ} are the mean and standard deviation, respectively, of the μth feature or label with respect to the training set of N_Tr samples. Hence, it is

$$\bar{z}_\mu = \frac{1}{N_\mathrm{Tr}} \sum_{i=1}^{N_\mathrm{Tr}} z_\mu^{(i)} \quad \text{and} \quad \Delta_{z_\mu}^2 = \frac{1}{N_\mathrm{Tr}} \sum_{i=1}^{N_\mathrm{Tr}} \left(z_\mu^{(i)} - \bar{z}_\mu \right)^2. \tag{2.26}$$

Consequently, the normalized features and label(s) form a distribution with zero mean and unit standard deviation. Scaling features is generally helpful to obtain features that are all equally important during training (unless a very important or unimportant feature should be emphasized). Z-score normalization is particularly beneficial to accelerate the training procedure. Elements of the neural network like activation functions or weight initialization (see Secs. 2.3.2 and 2.3.3) are developed for such a normalized distribution. Therefore, providing directly normalized data to the neural network avoids that an appropriate scaling and shifting has to be learned in a first step. However, if a label y_μ covers several orders of magnitude, a logarithmic scaling, $\tilde{y}_\mu^{(i)} = \log_{10}\left(y_\mu^{(i)}\right)$, is also well suited. In this way, all samples are treated equally during training despite different label orders.

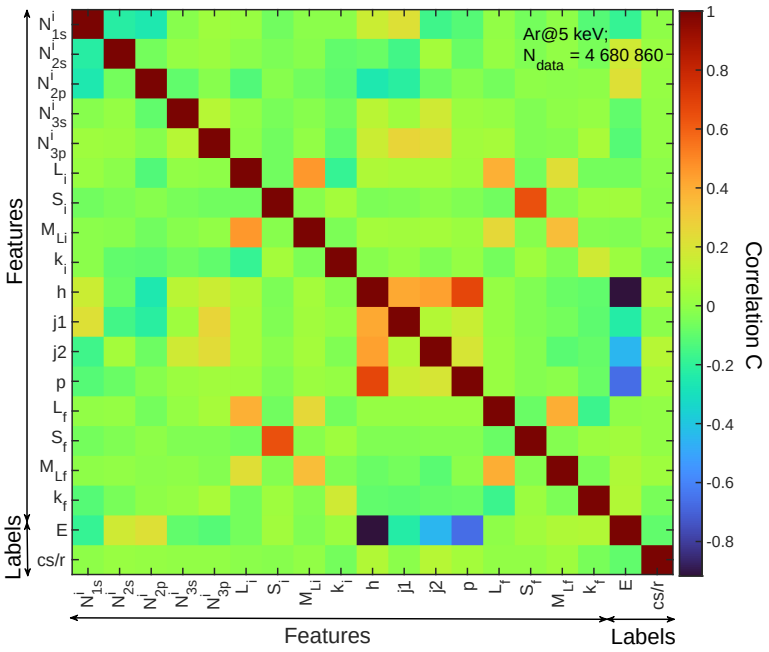

Figure 2.6: Pearson's correlation matrix. The underlying dataset is explained in Sec. 3.3.

Correlation matrix The relationship between two features or feature and label (generalized variables z_μ and z_λ) is measured by the covariance

$$\mathrm{Cov}(z_\mu, z_\lambda) = \frac{1}{N_D} \sum_{i=1}^{N_D} \left[\left(z_\mu^{(i)} - \bar{z}_\mu \right) \left(z_\lambda^{(i)} - \bar{z}_\lambda \right) \right]. \tag{2.27}$$

Note that D can also be only the training set or any other subset of interest. Normalizing the covariance by the standard derivations Δ_{z_μ} and Δ_{z_λ} for both variables yields Pearson's correlation matrix [179]

$$C(z_\mu, z_\lambda) = \frac{\mathrm{Cov}(z_\mu, z_\lambda)}{\Delta_{z_\mu} \Delta_{z_\lambda}}. \tag{2.28}$$

For Z-score normalization on D, correlation and covariance are exactly equal.

Figure 2.6 presents an example of a Pearson's correlation matrix for the machine-learning problem discussed in Sec. 3.3. As can be seen, a correlation matrix is always symmetric with unit diagonal elements. Two variables z_μ and z_λ are perfectly positively or negatively correlated when $C(z_\mu, z_\lambda) = 1$ or $C(z_\mu, z_\lambda) = -1$, respectively, and are uncorrelated when $C(z_\mu, z_\lambda) = 0$. Two correlated features are dependent in the way that when one feature changes, the other feature changes simultaneously either in the same ($C > 0$) or opposite ($C < 0$) direction. Training is more efficient for uncorrelated features [178] because the optimization of a weight can be per-

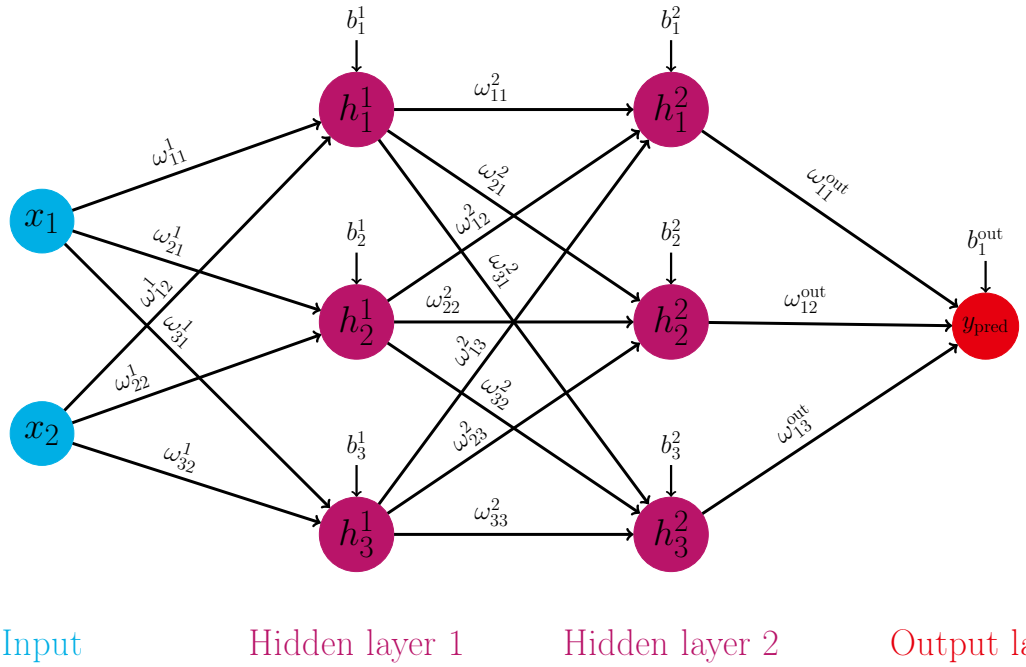

Figure 2.7: Fully connected feedforward neural network with two features x_μ as input, two hidden layers ($j = 1, 2$) each with three units h^j_λ, and a single output y_{pred}. Units of neighboring layers are connected by weights $w^j_{\lambda\mu}$ and each unit is activated by a bias b^j_λ.

formed independently of other weights (see Sec. 2.3.3 for optimization). Moreover, the correlation between feature and label determines how important this individual feature is for the prediction. However, this does not necessarily imply that a feature that is weakly correlated with the label is negligible. Nonetheless, the weaker features and label are correlated the tougher is the machine-learning task. In the present example, just using the few strongly correlated features for predicting the E label is clearly not sufficient. But as discussed in Sec. 3.3, predicting the E label is much simpler than predicting the cs/r label, which is much less correlated with the features.

2.3.2 Neural network

Neural networks [83, 175, 176] are the central tool of deep learning. An example of a very small fully connected feedforward neural network is sketched in Fig. 2.7. It consists of units (also called neurons or nodes) that are organized in layers. The input to the neural network is a given feature vector $\boldsymbol{x}$ taken from the dataset of interest (i.e., training, validation, or test set or real-world data). The output layer returns a prediction $\boldsymbol{y}_{\text{pred}}$ for the label vector $\boldsymbol{y}$. In between there are N_L hidden layers, whose units are not directly determined by the training data and whose

task is to transform $\boldsymbol{x}$ into higher-level representations $\boldsymbol{h}^j$ $(j = 1, \ldots, N_L)$ [180]. The connection of neighboring layers is represented by a set of weight matrices $\{\boldsymbol{W}^j\}_{j=1,\ldots,N_L+1}$ and a set of bias vectors $\{\boldsymbol{b}^j\}_{j=1,\ldots,N_L+1}$ determines how easily each unit is activated[1]. Because each unit is connected to all units in the neighboring layers, the neural network is called fully connected.

Accordingly, the prediction $\boldsymbol{y}_{\text{pred}}$ is obtained via a chain of different functions $f(\boldsymbol{x}, \{\boldsymbol{W}^j\}, \{\boldsymbol{b}^j\}) = f^{\text{out}}(f^{N_L}(f^{N_L-1}(\ldots f^1(\boldsymbol{x}, \boldsymbol{W}^1, \boldsymbol{b}^1))))$. Based on the input $\boldsymbol{x}$, the unit h_λ^1 of the first hidden layer is calculated via

$$h_\lambda^1 = f^1(\boldsymbol{x}, \boldsymbol{W}^1, \boldsymbol{b}^1)_\lambda = \sigma\left(b_\lambda^1 + \sum_\mu w_{\lambda\mu}^1 x_\mu\right). \tag{2.29}$$

Here, x_μ, $w_{\lambda\mu}^1$, and b_λ^1 are the elements of $\boldsymbol{x}$, $\boldsymbol{W}^1$, and $\boldsymbol{b}^1$, respectively. Eq. (2.29) is a simple linear transformation on top of which a nonlinear activation function σ is applied. Using the units h_μ^{j-1} of the previous layer calculated in a previous step, the unit h_λ^j of the jth layer is calculated in a very similar way

$$h_\lambda^j = f^j(\boldsymbol{h}^{j-1}, \boldsymbol{W}^j, \boldsymbol{b}^j)_\lambda = \sigma\left(b_\lambda^j + \sum_\mu w_{\lambda\mu}^j h_\mu^{j-1}\right). \tag{2.30}$$

In this way, the calculation propagates through the layers until the final output $\boldsymbol{y}_{\text{pred}}$ with

$$y_\lambda^{\text{pred}} = f^{\text{out}}(\boldsymbol{h}^{N_L}, \boldsymbol{W}^{\text{out}}, \boldsymbol{b}^{\text{out}})_\lambda = \sigma\left(b_\lambda^{\text{out}} + \sum_\mu w_{\lambda\mu}^{\text{out}} h_\mu^{N_L}\right) \tag{2.31}$$

is reached. For the output layer, whether to apply a nonlinear activation function σ or just a linear transformation depends on the specific output type. As can be seen, each layer is effectively learning a new and more complex representation of the input $\boldsymbol{x}$. Because information flows through the neural network from input $\boldsymbol{x}$ to output $\boldsymbol{y}_{\text{pred}}$ without any connection between nonneighboring layers, the neural network is called feedforward.

When designing a neural network for a specific machine-learning problem, many decisions have to be made. The ideal design decisions depend on the machine-learning problem and, as a consequence, have to be found via experimentation and some "rules of thumb" [83]. The most crucial design decisions together with widely-used recommendations are presented in Fig. 2.8. First, the neural network architecture has to be selected, i.e., above all, the number of hidden layers and of units per layer. The total number of units determines the number of trainable parameters (all

[1] The $(N_L + 1)$th layer is the output layer, also labeled by out.

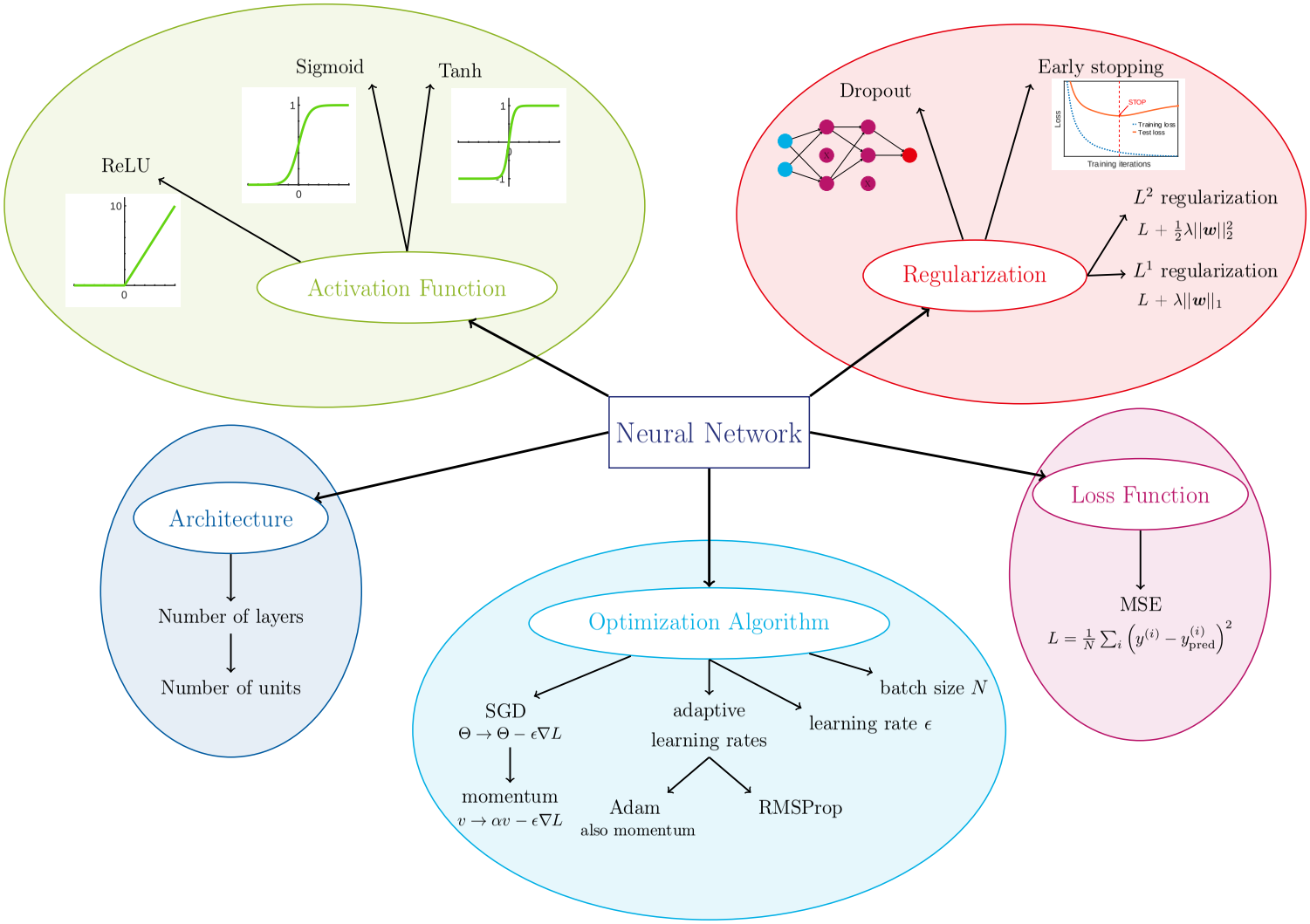

Figure 2.8: Design decisions for a fully connected feedforward neural network. The individual components are described in more detail in the main text. This chart is not complete because there are many more mostly however less common choices.

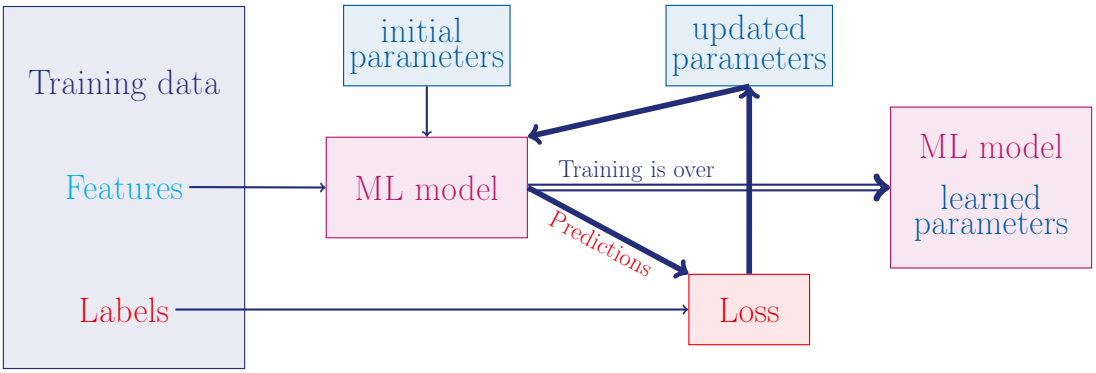

Figure 2.9: Training procedure. Based on the training data, the parameters of the machine-learning (ML) model are updated by iteratively minimizing the average loss. The outcome is a machine-learning model with learned parameters, resulting in a small average loss and, thus, a good function approximation.

$w^i_{\lambda\mu}$ and $b^i_{\lambda,}$) and, therefore, affects the capacity of the neural network. An increased capacity (more units) increases the neural network's ability to fit a wide variety of functions, however, at the expense of reduced computational efficiency. A deeper neural network (more hidden layers) is known to reduce the number of trainable parameters required [181]. There are also other network architectures, based on the fully connected feedforward neural network. Most common are the recurrent neural network [83, 182], which includes feedback connections, and the convolutional neural network [83, 175, 183], which is not fully connected. Second, a nonlinear activation function σ is required for the hidden layers (Fig. 2.8). Nowadays, rectified linear units (ReLU) or variants thereof [175, 184] are recommended, whereas sigmoid or hyperbolic tangent (tanh) chosen before the advent of ReLU can still also perform reasonably well [185]. (The remaining parts of Fig. 2.8 are discussed in the following.)

2.3.3 Training procedure

The goal of training a machine-learning model is to find a suitable set of model parameters (i.e., $\{\boldsymbol{W}^j\}$ and $\{\boldsymbol{b}^j\}$ for the neural network) that results in a good function approximation [i.e., $f(\boldsymbol{x}, \{\boldsymbol{W}^j\}, \{\boldsymbol{b}^j\})$] and, thus, a good performance of the machine-learning model. The training procedure is illustrated in Fig. 2.9. Starting from a machine-learning model with randomly initialized model parameters, predictions $\boldsymbol{y}^{(i)}_{\text{pred}}$ for the feature vectors $\boldsymbol{x}^{(i)}$ in the training set are made. Based on these predictions $\boldsymbol{y}^{(i)}_{\text{pred}}$ and the corresponding labels $\boldsymbol{y}^{(i)}$, the average loss over the training set is calculated. It is commonly very large at the start. Because only the

finite training set is considered instead of the whole underlying data distribution, the average loss is also called empirical risk. Note that if the whole underlying data distribution had been known, it would not have been a machine-learning problem. To minimize the empirical risk, the model parameters are simultaneously updated based on an optimization algorithm. The machine-learning model with the updated model parameters predicts new (hopefully improved) $\boldsymbol{y}^i_{\text{pred}}$. The update procedure is repeated until the desired number of training iterations is over or a stopping criterion is met (see early stopping in Sec. 2.3.4). The resulting machine-learning model with the learning model parameters can then be evaluated on the validation and/or test set and applied on the real-world data of interest. Let us now describe the most important parts of the training procedure in more detail.

Parameter initialization The training procedure starts with the initialization of the model parameters. A good initialization is important because it often leads to faster convergence and avoids getting stuck at points in parameter space with comparably large losses. For neural networks, the initial biases b^j_λ are commonly set to zero, whereas the initial weights $w^j_{\lambda\mu}$ are randomly selected from a uniform or Gaussian distribution. The scale of this distribution is known to clearly affect the training. As a consequence, several parameter initializers with different scales have been proposed. Most important are the Glorot initializer [186] and the He initializer [187] useful for tanh and ReLU activation functions, respectively.

Loss function An important quantity for the training procedure is the average loss, determined by a loss function. For a regression problem, a common choice for the loss function (Fig. 2.8) is the mean squared error (MSE) [175]. Assuming only a single label (i.e., $\boldsymbol{y}^{(i)} = y^{(i)}$), MSE on a dataset D with size N_D is defined as

$$L^{\text{MSE}} = \frac{1}{N_D} \sum_{i=1}^{N_D} \left(y^{(i)} - y^{(i)}_{\text{pred}} \right)^2 . \tag{2.32}$$

Here, $y^{(i)}_{\text{pred}}$ is the prediction made for the ith feature vector in D. During the training procedure, D is indeed the training set, whereas it is the validation or test set during the subsequent evaluation. MSE considers the squared Euclidean distance between label and prediction. Therefore, MSE only works well when labels cover a similar range. When they cover several orders of magnitude, training is only performed on very large labels, whereas small labels are completely overlooked. To avoid this, either a suitable label scaling (Sec. 2.3.1) or another loss function are required. In this case, an alternative but less common loss function is the mean

squared logarithmic error (MSLE)

$$L^{\mathrm{MSLE}} = \frac{1}{N_D} \sum_{i=1}^{N_D} \left(\log_{10} \left[y^{(i)} + \epsilon \right] - \log_{10} \left[y_{\mathrm{pred}}^{(i)} + \epsilon \right] \right)^2 . \tag{2.33}$$

To guarantee numerical stability, a small, tunable constant ϵ is added. MSLE measures by how many orders of magnitude label and prediction differ and, thus, is able to treat small and large label values alike. However, this is at the expense of a lost preference for predicting larger label values more accurately. For classification problems, the cross-entropy [175] is another widely-used loss function. But this work focuses on regression.

Optimization algorithm (for an overview, see Fig. 2.8) The standard first-order optimization algorithm to update the model parameters of a neural network is stochastic gradient descent (SGD) [188]. The SGD algorithm iteratively adapts a model parameter Θ (an $w_{\lambda\mu}^j$ or b_λ^j) by moving it in the direction of the negative gradient $\hat{g}_\Theta$ of the loss function L with respect to that model parameter. The update rule is

$$\Theta \to \Theta - \epsilon \hat{g}_\Theta \quad \text{with} \quad \hat{g}_\Theta = \nabla_\Theta L. \tag{2.34}$$

Here, $\epsilon > 0$ is the learning rate (default $\epsilon = 0.01$). The learning rate ϵ determines the size of each update step and is tuned to a given machine-learning problem. On the one hand, a too small ϵ requires a lot of update steps and, thus, slows down the training procedure. Moreover, the training procedure may get stuck in a local minimum in parameter space with comparably large losses. On the other hand, a too large ϵ very likely overshoots a minimum, which leads to heavy oscillations in the loss curve (i.e., the sequence of the losses at each update step).

So far, this is the same as gradient descent. The difference and the reason why it is called stochastic is the following. In each update step, the loss L is calculated only on a random subset of training data (minibatch) instead of the whole training set [83, 189]. For pure stochasticity, the subset consists only of a single sample. But utilizing a single new sample in each update step is quite noisy and requires a lot of update steps to consider each training sample at least once during training. Therefore often minibatches with several samples are employed. Smaller minibatch sizes introduce more stochasticity to the training procedure, which may serve as a regularization (see Sec. 2.3.4).

Optimization via SGD can be accelerated by adding a momentum term [83, 190]. The momentum term does not only include the gradient calculated at the current update step but also previously calculated gradients. Their contribution is reduced

the more a previously calculated gradient lies in the past with respect to the current update step and is controlled by a tunable parameter α. The update rule is

$$\Theta \to \Theta + v \quad \text{with} \quad v \to \alpha v - \epsilon \hat{g}_\Theta. \tag{2.35}$$

In SGD, the learning rate ϵ is tuned for all model parameters, i.e., all $w^j_{\lambda\mu}$ and b^j_λ, alike. However, optimization can be improved by individually adapting learning rates for different model parameters. Effective approaches for adaptive learning rates are RMSProp [191] and Adam [192]. The latter combines the adaptive learning rates (i.e., RMSProp) with momentum and is known to be fairly robust to the choice of the required tunable parameters.

Back-propagation For neural networks, the gradients $\hat{g}_\Theta$ required in every update step [Eq. (2.34)] are obtained via back-propagation [178, 182] (for a visualization, see Ref. [193]). Back-propagation is preceded by a forward propagation through the neural network with current model parameters—from input $\boldsymbol{x}$ over hidden layers $\boldsymbol{h}^j$ from $j = 1$ to N_L to the output $\boldsymbol{y}_{\text{pred}}$ [Eqs. (2.29)–(2.31)]. The final step in the forward propagation is the calculation of the loss L between $\boldsymbol{y}_{\text{pred}}$ and label $\boldsymbol{y}$. Starting from the loss L, back-propagation passes through the neural network in the opposite direction—from output $\boldsymbol{y}_{\text{pred}}$ over hidden layers $\boldsymbol{h}^j$ from $j = N_L$ to 1 to the input $\boldsymbol{x}$. During back-propagation, gradients are gradually calculated via the chain rule for derivatives for all units h^j_λ, all weights $w^j_{\lambda\mu}$, and all biases b^j_λ. More specifically, the units of the jth hidden layer are calculated based on results for the $(j+1)$th layer via

$$\frac{\partial L}{\partial h^j_\lambda} = \sum_\mu w^{j+1}_{\mu\lambda} \frac{\partial L}{\partial \tilde{h}^{j+1}_\mu}. \tag{2.36}$$

Here, $w^{j+1}_{\mu\lambda}$ is the currently given weight between the jth and $(j+1)$th layers and

$$\frac{\partial L}{\partial \tilde{h}^{j+1}_\mu} = \frac{\partial h^{j+1}_\mu}{\partial \tilde{h}^{j+1}_\mu} \frac{\partial L}{\partial h^{j+1}_\mu} \quad \text{with} \quad h^{j+1}_\mu = \sigma(\tilde{h}^{j+1}_\mu) \tag{2.37}$$

is already known from the preceding back-propagation step on the $(j+1)$th layer. For the N_Lth layer, being the first one in back-propagation, it is

$$\frac{\partial L}{\partial \tilde{h}^{j+1}_\mu} = \frac{\partial L}{\partial \tilde{y}^{\text{pred}}_\mu} = \frac{\partial y^{\text{pred}}_\mu}{\partial \tilde{y}^{\text{pred}}_\mu} \frac{\partial L}{\partial y^{\text{pred}}_\mu} \quad \text{with} \quad y^{\text{pred}}_\mu = \sigma_{\text{out}}(\tilde{y}^{\text{pred}}_\mu). \tag{2.38}$$

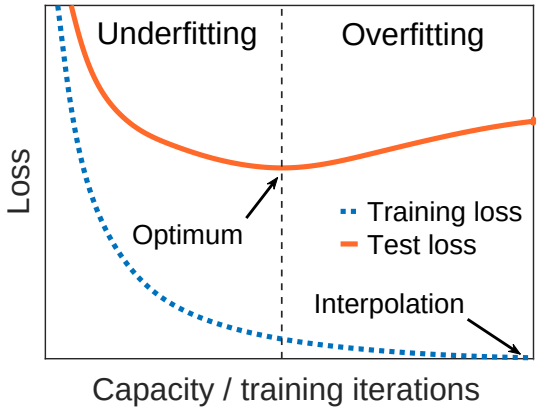

Figure 2.10: Under- and overfitting. Training loss (dotted blue line) and test loss (solid orange line) are shown as a function of the model capacity, here determined by the number of training iterations. The given example is obtained for an unregulated neural network designed for predicting fluorescence rates in Sec. 3.3. Units are omitted for simplicity.

Using the result of Eqs. (2.36) and (2.37), gradients for the weights between the $(j-1)$th and jth layers are calculated via

$$\frac{\partial L}{\partial w^j_{\lambda\mu}} = h^{j-1}_\mu \frac{\partial L}{\partial \tilde{h}^j_\lambda}. \tag{2.39}$$

The units h^{j-1}_μ are well-known from the forward propagation. For the first layer, being the last one in back-propagation, it is $h^{j-1}_\mu = x_\mu$. Similarly, gradients for the biases of the jth layer are given by

$$\frac{\partial L}{\partial b^j_\lambda} = \frac{\partial L}{\partial \tilde{h}^j_\lambda}. \tag{2.40}$$

In each update step, forward and backward propagation are carried out as described above for all samples in the minibatch of training data. Having at hand the averaged gradients with respect to all weights and biases, the model parameters can now be updated via the chosen optimization algorithm.

2.3.4 Regularization

The primary goal of machine learning is to achieve both small training and test losses—not small training losses alone. The critical quantity here is the model capacity, i.e., the ability of the machine-learning algorithm to fit a wide variety of functions [83]. Additionally, the number of training iterations has a similar impact on the losses and is included in the model capacity for simplicity. With more learning

steps, the machine-learning algorithm has a higher chance of learning a good fit of the model parameters. The effect of the model capacity on training and test (or equivalently validation) losses is visualized in Fig. 2.10. The training loss gradually decreases with higher model capacity, whereas the test loss exhibits an asymmetric U-shaped curve. On the one hand, with a too low model capacity, a machine-learning algorithm is unable to learn an accurate description of the training data. As a consequence, both training and test losses are unsuitably large (underfitting). On the other hand, the higher the model capacity, the better the training data are fitted until they are interpolated. In this case, the machine-learning model is adapted to specific and spurious properties of the training data only. Therefore, a too high model capacity results in a large test loss and a large gap between training and test losses (overfitting). The optimal model capacity—leading to a small training loss and a small gap between training and test losses simultaneously—is, however, hard to find.

For this reason, often an actually too high model capacity, resulting in overfitting, is employed and overfitting is prevented by adding a regularization to the machine-learning algorithm. The purpose of regularization is to modify the machine-learning algorithm in such a way that the test loss is reduced but not necessarily the training loss [83]. Different kinds of regularization are common for neural networks (see e.g., Ref. [83] and also Fig. 2.8).

Parameter norm penalty A very common regularization strategy is to add parameter norm penalties $\Omega(\boldsymbol{W}^j)$ for the weights to the loss L. Then, the modified loss, written with an explicit dependence on the model parameters, reads

$$\tilde{L}(\{\boldsymbol{W}^j\},\{\boldsymbol{b}^j\}) = L(\{\boldsymbol{W}^j\},\{\boldsymbol{b}^j\}) + \sum_j \lambda_j \Omega(\boldsymbol{W}^j). \tag{2.41}$$

Here, $\lambda_j \geq 0$ is a tunable parameter determining the strength of the regularization for the jth hidden layer. Minimizing the modified loss $\tilde{L}$ leads to a preference of simpler models. Most important parameter norm penalties are L^2 and L^1 regularizations with $\Omega(\boldsymbol{W}^j) = \frac{1}{2}\sum_\mu ||\boldsymbol{w}_\mu^j||_2^2$ and $\Omega(\boldsymbol{W}^j) = \sum_\mu ||\boldsymbol{w}_\mu^j||_1$, respectively. Here, $\boldsymbol{w}_\mu^j$ is the μth column of $\boldsymbol{W}^j$. The L^2 regularization aims to drive unimportant weights to near zero (but not exactly zero), whereas it barely affects important weights. In contrast, the L^1 regularization encourages unimportant weights to become exactly zero and, thus, results in sparse models.

Early stopping A very simple regularization strategy is early stopping, which handels overfitting due to a too large number of training iterations. Using early

stopping, both training and validation losses are monitored during the training procedure. When the validation loss has not been improved over a certain number of training iterations, the training stops and the model parameters of the update step that has the smallest validation loss are returned.

Dropout A very powerful regularization strategy is dropout [194]. During each update step, nonoutput units along with their connections to other units are dropped out of the neural network with probability $1 - p$. p is a tunable parameter with $0 < p \leq 1$ and is specified individually for each layer. In this way, in each update step a different sparse neural network is trained. But it shares the model parameters with all other sparse neural networks. When training is over, it is averaged over all sparse neural networks by using the full neural network without dropout but with each model parameter being scaled by p. Therefore, dropout is an inexpensive approximation to model averaging, which is a widely-known, well-working strategy for reducing overfitting.

Modern interpolation hypothesis A very modern strategy is to barely or not at all add a regularization to the machine-learning algorithm. The model capacity is instead increased further. This is the "modern" interpolation hypothesis [195]. The idea is that going beyond the point of interpolation results in a test loss that decreases again ideally even beyond the loss at optimal model capacity (double-descent test loss curve). However, reaching this "modern" interpolation region requires to perfectly interpolate training data by using a very high model capacity, a huge number of training iterations included. Concomitantly, this yields a comparably large training time and effort.

2.3.5 Random forest regressor: An alternative machine-learning algorithm

Random forest regressors [180, 196] are a decision-tree-based ensemble method and a powerful alternative to neural networks. An individual decision tree is generally weak because it often performs poor on never-seen data. However, a random forest regressor achieves its power from averaging over hundreds of different decision trees [177]. Apart from model averaging, a random forest regressor is basically based on the same machine-learning parts as previously described for neural networks though indeed each part looks a bit different.

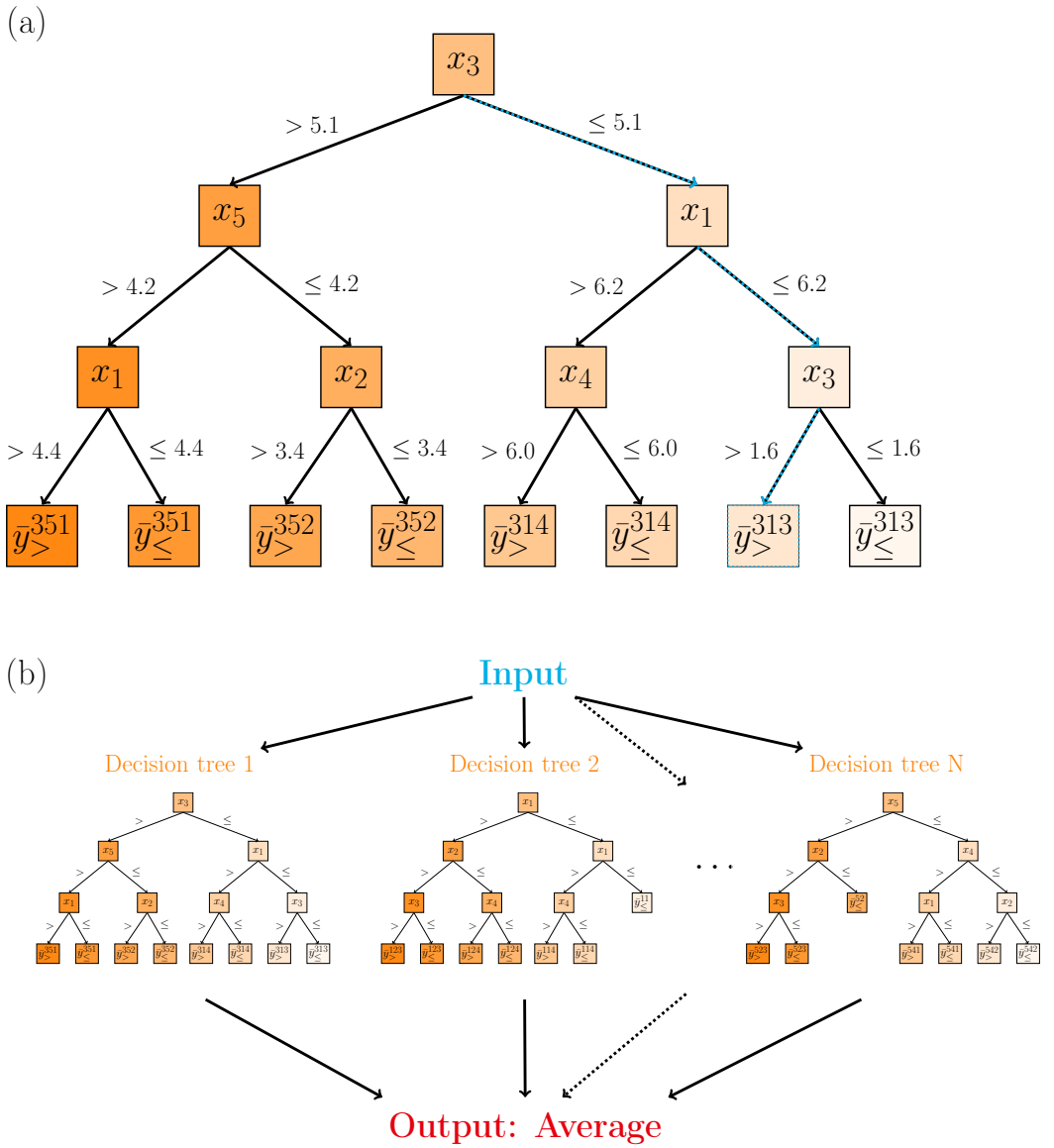

Figure 2.11: (a) An individual decision tree. This example uses five features x_μ [i.e., $\boldsymbol{x} = (x_1, x_2, x_3, x_4, x_5)^T$] and a single output y_{pred}, indicated by the path followed to reach the corresponding output node. A possible path through the decision tree is indicated by the dotted cyan lines. (b) A random forest regressor is built of N decision trees. Note that all decision trees are made up for this occasion, just in case you should wonder about its meaning.

Dataset Normally, no normalization of features is required because the random forest regressor is not distance-based. Nonetheless, scaling of the labels, especially when they cover a wide range, can be useful due to use of a distance-based loss function.

Decision tree and random forest regressor An example of a decision tree [180] is given in Fig. 2.11(a). It consists of hierarchically-ordered nodes, which each represents a feature x_μ of the feature vector $\boldsymbol{x}$. The nodes are connected by branches, which each corresponds to a condition (or decision) for a feature commonly based on relation operators. At the end of each branch is an output node, which returns the prediction y_{pred} for the label y of interest. A prediction for an input $\boldsymbol{x}^{(i)}$ of interest is made via a decision tree by propagating through the decision tree following those branches whose conditions $\boldsymbol{x}^{(i)}$ fulfills [i.e., blue dotted path in Fig. 2.11(a) for $\boldsymbol{x}^{(i)} = (2.2, 6.1, 3.4, 5.6, 3.0)^T$]. The prediction y_{pred} is finally obtained from the output node reached in this way.

A random forest regressor, shown in 2.11(b), is build of N different decision trees (commonly $N = 100$–500). Its output is the average over all predictions y_{pred} made by the individual decision trees.

Training procedure During the training procedure, the individual decision trees are created by hierarchically separating the training data into subsets as follows. For a decision tree, the most important feature x_μ is selected using the training data. Based on a condition (i.e., a threshold value) for this feature, the training data are separated into two subsets, one with those fulfilling the condition ($>$) and the other with those not fulfilling it ($\leq$). The most important feature and the best splitting condition are controlled by a loss function and the aim of minimizing this loss as well as some form of regularization. On the subsets, it is proceeded in the same manner by separating the subsets into smaller subsets based on a splitting condition for a selected feature. This procedure stops at an output node when either the subsets are sufficiently small or the maximum number of branches is reached. The prediction y_{pred} of an output node is determined by the average over the labels of all training data in the final subset for this output node.

Regularization Without any regularization, the individual decision trees in a random forest would look fairly similar and would be very prone to overfitting. Accordingly, also for the random forest regressor some form of regularization is necessary. Possible regularization strategies [196, 197] are to use a limited maximum number of branches, to consider only a randomly selected subset of features at each

split, or to train each individual decision tree only on a minibatch (random subset of training data). Moreover, also a larger number of individual decision trees in a random forest can help to reduce overfitting [198].

2.3.6 Conclusion and outlook

In this section, the basic concepts of machine learning have been explained. But machine learning is a much broader and actively investigated field with a lot more topics not captured in this introduction (for more details, see e.g., Ref. [83]). One of the most central and popular machine-learning algorithms is neural networks, which have been the focus of this section. However, random forest regressors, also briefly discussed here, are a powerful alternative. Whether neural networks, random forest regressors, or any other machine-learning algorithm are the most successful choice depends on the specific machine-learning problem at hand. It is a widely-known statement—the no free lunch theorem [83, 199, 200]—that there is no universally best machine-learning algorithm. Therefore, a machine-learning algorithm, including its special architecture, training procedure, and regularization strategy, has to be selected individually via experimentation and some "rules of thumb" for the specific machine-learning problem at hand.

In Sec. 3.3, the specific machine-learning problem of predicting X-ray-induced atomic transition parameters is investigated. Both neural networks and random forest regressors are employed as machine-learning algorithms and their performances are compared for this specific problem.

2.4 Electron-cloud alignment

Electron clouds of atomic ions produced by photoionization are generally aligned when their orbital-angular momentum is nonzero. This is due to different ionization probabilities for different orbital-angular-momentum projection states. The electron-cloud alignment is also called orbital alignment (Sec. 3.1; ionization of a specific subshell) or ion alignment (Sec. 3.4; average over ions in different energy levels). In this section, electron-cloud alignment is generally discussed using the alignment parameter derived from the density matrix formalism, the spatial shape of the electron cloud of the aligned ions, and the angular distribution of subsequently emitted Auger-Meitner electrons.

2.4.1 Density matrix and state multipoles

Let us consider an ensemble of ions being in various orbital-angular-momentum projection states $|LM_L\rangle$ with projection quantum number $M_L = -L, \ldots, L$. The orbital-angular momentum L is fixed and all ions belong to the same energy level. Thus, apart from M_L, all state features are shared and neglected in the following discussion except L. The states $|LM_L\rangle$ form an orthonormalized basis set, i.e, $\langle LM'_L|LM_L\rangle = \delta_{M'_L,M_L}$. Moreover, ions with different M_L can be regarded as having different shapes and/or orientations of their electron clouds in space [61] (see also Sec. 2.4.4).

Density matrix and operator The ensemble of ions is represented by a $(2L+1)\times(2L+1)$ density matrix $\boldsymbol{\rho}$ [53, 61, 166, 201] with elements $\langle LM'_L\,|\hat{\rho}|\,LM_L\rangle$ and density operator

$$\hat{\rho} = \sum_{M'_L,M_L} \langle LM'_L\,|\hat{\rho}|\,LM_L\rangle\,|LM'_L\rangle\langle LM_L|. \tag{2.42}$$

The off-diagonal elements of $\boldsymbol{\rho}$ describe the coherence between the states with different M_L. For an incoherent superposition of states, $\boldsymbol{\rho}$ is diagonal in $\{|LM_L\rangle\}$ representation. Then, it is

$$\langle LM'_L\,|\hat{\rho}|\,LM_L\rangle = \delta_{M'_L,M_L} P_{M_L}, \tag{2.43}$$

with P_{M_L} being the probability that an ion in the ensemble is in a state with projection quantum number M_L. The corresponding density operator is given by

$$\hat{\rho} = \sum_{M_L} P_{M_L} |LM_L\rangle\langle LM_L|. \tag{2.44}$$

Normalized probabilities, i.e., $\sum_{M_L} P_{M_L} = 1$, correspond to a normalization of $\hat{\rho}$ by its trace, i.e., $\mathrm{tr}(\hat{\rho}) = 1$.

The density operator $\hat{\rho}$ is an important quantity because having at hand $\hat{\rho}$ permits the calculation of the expectation value of any operator $\hat{O}$ of interest via

$$\langle \hat{O} \rangle = \frac{\mathrm{tr}(\hat{\rho}\hat{O})}{\mathrm{tr}(\hat{\rho})}. \tag{2.45}$$

State multipoles and irreducible spherical tensor operators Alternatively to density matrix and operator, the ensemble of ions is equivalently-well described in terms of state multipoles, also known as statistical tensors, and irreducible spherical tensor operators. The introduction of state multipoles is motivated by the expectation values of the orbital-angular-momentum operators $\langle \hat{L}_Q \rangle$ ($Q = 0, \pm 1$), which are proportional to first rank state multipoles [61]. Next to advantages regarding symmetry considerations [61], orientation and alignment parameters can be directly derived from the state multipoles. State multipoles for a definite L are defined as [61, 201, 202]

$$\langle T(L)^\dagger_{KQ} \rangle = \sum_{M'_L, M_L} (-1)^{L-M'_L} \langle LM'_L \,|\hat{\rho}|\, LM_L \rangle \, C(L, L, K; M_L, -M'_L, Q), \tag{2.46}$$

with $C(\cdot)$ denoting a Clebsch-Gordan coefficient [203, 204]. $\langle T(L)^\dagger_{KQ} \rangle$ is a tensor of rank K with $0 \leq K \leq 2L$ and component Q with $|Q| \leq K$. The conditions for K and Q are determined by the triangular conditions for the Clebsch-Gordan coefficient. Consequently, only $\langle T(L)^\dagger_{00} \rangle$ exists for $L = 0$. Note that for the incoherent superposition of states [Eq. (2.43)], the state multipoles for $Q \neq 0$ vanish and those for $Q = 0$ simplify to

$$\langle T(L)^\dagger_{K0} \rangle = \sum_{M_L} (-1)^{L-M_L} P_{M_L} C(L, L, K; M_L, -M_L, 0). \tag{2.47}$$

In addition to the state multipoles, irreducible spherical tensor operators $\hat{T}(L)_{KQ}$ are introduced so that the state multipoles are expectation values of $\hat{T}(L)^\dagger_{KQ}$. Thus, it follows from $\langle T(L)^\dagger_{KQ} \rangle = \mathrm{tr}(\hat{\rho}\hat{T}(L)^\dagger_{KQ})$ [Eq. (2.45)] that [53, 201]

$$\hat{T}(L)_{KQ} = \sum_{M'_L, M_L} (-1)^{L-M'_L} C(L, L, K; M_L, -M'_L, Q) |LM'_L\rangle\langle LM_L|. \tag{2.48}$$

The $\hat{T}(L)_{KQ}$ are orthonormal, i.e., $\mathrm{tr}(\hat{T}(L)^\dagger_{KQ}\hat{T}(L)_{K'Q'}) = \delta_{K,K'}\delta_{Q,Q'}$, and behave under rotation like spherical harmonics [201]. In this way, the density operator

$\hat{\rho}$ is decomposed in terms of $\hat{T}(L)_{KQ}$ with expansion coefficients $\langle T(L)^{\dagger}_{KQ}\rangle$ and reads [53, 201]

$$\hat{\rho} = \sum_{K,Q} \langle T(L)^{\dagger}_{KQ}\rangle \hat{T}(L)_{KQ}. \tag{2.49}$$

This relation is derived from inverting the definition of $\langle T(L)^{\dagger}_{KQ}\rangle$ [Eq. (2.46)], inserting the obtained equation for $\langle LM'_L \,|\hat{\rho}|\, LM_L\rangle$ in terms of $\langle T(L)^{\dagger}_{KQ}\rangle$ into the equation for $\hat{\rho}$ [Eq. (2.42)], and identifying the residual terms with $\hat{T}(L)_{KQ}$ [Eq. (2.48)].

2.4.2 Orientation and alignment parameters

Orientation parameter Important state multipoles are those of first rank because they constitute the orientation vector [61]. For the incoherent superposition of states (with $L > 0$) [Eq. (2.47)], the orientation vector has only a single nonzero component

$$\langle T(L)^{\dagger}_{10} \rangle = \sum_{M_L} (-1)^{L-M_L} P_{M_L} C(L, L, 1; M_L, -M_L, 0). \tag{2.50}$$

Employing Racah's second form given by Eq. (16) in Ref. [203], the Clebsch-Gordan coefficient is calculated as follows

$$\begin{aligned} C(L, L, 1; M_L, -M_L, 0) =& \sqrt{\frac{3(2L-1)!}{(2L+2)!}} \\ & \times \sum_z \frac{(-1)^z (L+M_L)!(L-M_L)!}{z!(2L-1-z)!(L-M_L-z)!^2(1-L+M_L+z)!^2}. \end{aligned} \tag{2.51}$$

The sum over z is restricted to $z = L-M_L-1$ and $z = L-M_L$. Moreover, a factorial $n!$ is expressed as a smaller factorial via recursive application of $n! = n(n-1)!$. In this way, the Clebsch-Gordan coefficient becomes

$$\begin{aligned} C(L, L, 1; M_L, -M_L, 0) =& \sqrt{\frac{3}{(2L+2)(2L+1)2L}} \\ & \times \left\{ (-1)^{L-M_L-1} \frac{(L+M_L)!(L-M_L)!}{(L-M_L-1)!(L+M_L)!} \right. \\ & \left. + (-1)^{L-M_L} \frac{(L+M_L)!(L-M_L)!}{(L-M_L)!(L+M_L-1)!} \right\} \\ =& (-1)^{L-M_L} \frac{1}{2} \sqrt{\frac{3}{(L+1)L(2L+1)}} \{(L+M_L) - (L-M_L)\} \\ =& (-1)^{L-M_L} \sqrt{\frac{3}{(L+1)L(2L+1)}} M_L \end{aligned} \tag{2.52}$$

and, therefore, it is

$$\langle T(L)^{\dagger}_{10} \rangle = \sqrt{\left[\frac{1}{2L+1}\right]\left[\frac{3}{(L+1)L}\right]} \sum_{M_L} M_L P_{M_L}. \tag{2.53}$$

The factor $\sqrt{\frac{1}{2L+1}}$ is equal to $\langle T(L)^{\dagger}_{00}\rangle$, which is also known as the normalization constant. Normalization of $\langle T(L)^{\dagger}_{10}\rangle$ yields the orientation parameter O_{10}, defined as [59]

$$O_{10}(L) = \frac{\langle T(L)^{\dagger}_{10}\rangle}{\langle T(L)^{\dagger}_{00}\rangle} = \sqrt{\frac{3}{(L+1)L}} \sum_{M_L} M_L P_{M_L}. \tag{2.54}$$

The orientation parameter O_{10} is a measure of the direction of the orbital-angular-momentum projection of the ensemble of ions. O_{10} is negative, when ions with $-M_L$ are more populated than those with $+M_L$, and positive, when ions with $+M_L$ are more populated than those with $-M_L$. For $P_{-M_L} = P_{+M_L}$, there is no orientation and, hence, $O_{10} = 0$. Since $\langle T(L)^{\dagger}_{10}\rangle = \langle \hat{L}_z \rangle$, no orbital-angular momentum is transferred to an unoriented ensemble of ions during its production process [61]. For example, an unaligned ensemble of ions is produced by interaction with linearly polarized photons. To break the symmetry in P_{M_L} and, thus, to create an oriented ensemble of ions, circularly polarized photons or magnetic fields are required. Note that O_{10} [Eq. (2.54)] has only been derived by state multipoles and can, in principle, be used for an ensemble of ions produced by any X-ray-induced atomic transition, not only photoionization.

Alignment parameter Most important are the state multipoles of second rank because they constitute the alignment tensor [61]. For the incoherent superposition of states (with $L > 0$) [Eq. (2.47)], the alignment tensor has only a single nonzero component

$$\langle T(L)^{\dagger}_{20} \rangle = \sum_{M_L} (-1)^{L-M_L} P_{M_L} C(L, L, 2; M_L, -M_L, 0). \tag{2.55}$$

In a very similar manner as for $C(L, L, 1; M_L, -M_L, 0)$ [Eqs. (2.51) and (2.52)], the present Clebsch-Gordan coefficient is calculated as follows

$$\begin{aligned}
C(L, L, 2; M_L, -M_L, 0) =& \sqrt{\frac{20(2L-2)!}{(2L+3)!}} \\
& \times \sum_z \frac{(-1)^z 2(L+M_L)!(L-M_L)!}{z!(2L-2-z)!(L-M_L-z)!^2(2-L+M_L+z)!^2} \\
=& \sqrt{\frac{5}{(2L+3)(L+1)(2L+1)L(2L-1)}} \\
& \times \left\{ (-1)^{L-M_L-2} \frac{(L+M_L)!(L-M_L)!}{2(L-M_L-2)!(L+M_L)!} \right. \\
& + (-1)^{L-M_L-1} \frac{2(L+M_L)!(L-M_L)!}{(L-M_L-1)!(L+M_L-1)!} \\
& \left. + (-1)^{L-M_L} \frac{(L+M_L)!(L-M_L)!}{2(L-M_L)!(L+M_L-2)!} \right\} \\
=& (-1)^{L-M_L} \sqrt{\frac{5}{(2L+3)(L+1)(2L+1)L(2L-1)}} \\
& \times \left\{ \frac{(L-M_L)(L-M_L-1)}{2} - 2(L-M_L)(L+M_L) \right. \\
& \left. + \frac{(L+M_L)(L+M_L-1)}{2} \right\} \\
=& (-1)^{L-M_L} \sqrt{\frac{5}{(2L+3)(L+1)(2L+1)L(2L-1)}} \\
& \times \left\{ 3M_L^2 - L(L+1) \right\}.
\end{aligned} \tag{2.56}$$

Hence, the alignment tensor reads

$$\langle T(L)^{\dagger}_{20} \rangle = \sqrt{\left[\frac{1}{2L+1}\right] \left[\frac{5}{(2L+3)(L+1)L(2L-1)}\right]} \sum_{M_L} \left[3M_L^2 - L(L+1)\right] P_{M_L}. \tag{2.57}$$

Table 2.1: Perfect alignment where all ions have the same $|M_L|$, i.e., $P_{|M_L|} = 1$, for different orbital-angular momenta L.

	Alignment parameter A_{20}				
L	$M_L = 0$	$M_L = \|1\|$	$M_L = \|2\|$	$M_L = \|3\|$	$M_L = \|4\|$
1	$-\sqrt{2}$	$\sqrt{1/2}$			
2	$-\sqrt{10/7}$	$-\sqrt{5/14}$	$\sqrt{10/7}$		
3	$-\sqrt{4/3}$	$-\sqrt{3/4}$	0	$\sqrt{25/12}$	
4	$-\sqrt{100/77}$	$-\sqrt{289/308}$	$\sqrt{16/77}$	$\sqrt{7/11}$	$\sqrt{28/11}$

Normalization of $\langle T(L)^\dagger_{20}\rangle$ yields the alignment parameter A_{20}, defined as [59]

$$A_{20}(L) = \frac{\langle T(L)^\dagger_{20}\rangle}{\langle T(L)^\dagger_{00}\rangle} = \sqrt{\frac{5}{(2L+3)(L+1)L(2L-1)}} \sum_{M_L} \left[3M_L^2 - L(L+1)\right] P_{M_L}. \tag{2.58}$$

The alignment parameter A_{20} measures the degree and direction of the alignment of an ensemble of ions regarding its orbital-angular-momentum projection. A_{20} is negative (alignment), when ions with smaller $|M_L|$ are more populated than others, and positive (anti alignment), when ions with larger $|M_L|$ are more populated. $A_{20} = 0$ (no alignment) indicates a uniform distribution, i.e., $P_{M_L} = \frac{1}{2L+1}$, while the larger $|A_{20}|$ the stronger the alignment. The meaning of A_{20} is further elaborated in Sec. 2.4.4 and extreme values of A_{20} are listed in Table 2.1.

2.4.3 Averaged alignment parameter

So far, the alignment parameter has been discussed for an ensemble of ions in the same energy level. Now, let us consider many of these ensembles of ions, labeled with an index j and each described by an alignment parameter $A_{20}^{E_j}(L)$ [Eq. (2.58)]. All ensembles have the same orbital-angular momentum L, but each ensemble belongs to a different energy level E_j. The probability that an ion is in the ensemble belonging to energy level E_j is $P_{E_j}(L)$. In this case, the alignment parameter $A_{20}(L)$ with definite L is the mean or average over all energy levels

$$\begin{aligned} \bar{A}_{20}(L) =& \sum_{E_j} P_{E_j}(L) A_{20}^{E_j}(L) \\ =& f(L) \sum_{M_L} \left[3M_L^2 - L(L+1)\right] \sum_{E_j} P_{M_L}^{E_j} P_{E_j}(L). \end{aligned} \tag{2.59}$$

Here, it is $f(L) = \sqrt{\frac{5}{(2L+3)(L+1)L(2L-1)}}$ and $P_{M_L}^{E_j}$ is the energy-level specific probability of M_L [Eq. (2.43)]. We identify

$$\sum_{E_j} P_{M_L}^{E_j} P_{E_j}(L) = \bar{P}_{M_L}, \tag{2.60}$$

which is the probability that an ion is in a state with projection quantum number M_L regardless of its energy level. In this way, $\bar{A}_{20}(L)$ [Eq. (2.59)] simplifies to

$$\bar{A}_{20}(L) = f(L) \sum_{M_L} \left[3M_L^2 - L(L+1)\right] \bar{P}_{M_L}. \tag{2.61}$$

Note that $\bar{A}_{20}(L)$ has the same form as $A_{20}(L)$ [Eq. (2.58)], just using a probability $\bar{P}_{M_L}$ that is the average over all energy levels. Therefore, it has been demonstrated that the alignment parameter derived in Sec. 2.4.2 is also applicable for multiple ensembles of ions with definite L. Thus, explicitly indexing the average is omitted in what follows, i.e., $\bar{A}_{20}(L) = A_{20}(L)$.

But when $A_{20}(L)$ is an average over ensembles, it has a corresponding width

$$\Delta_{A_{20}}^2(L) = \sum_{E_j} \left[A_{20}^{E_j}(L)\right]^2 P_{E_j}(L) - A_{20}(L)^2. \tag{2.62}$$

This term cannot be simplified very efficiently. All we can do is to introduce

$$\bar{P}_{M_L M_L'} = \sum_{E_j} P_{M_L}^{E_j} P_{M_L'}^{E_j} P_{E_j}(L), \tag{2.63}$$

which can be thought of as the averaged probability of having two ions, one with M_L and the other with M_L'. Then, the width reads

$$\Delta_{A_{20}}^2(L) = f(L)^2 \sum_{M_L, M_L'} \left[3M_L^2 - L(L+1)\right] \left[3{M_L'}^2 - L(L+1)\right] \bar{P}_{M_L M_L'} - A_{20}(L)^2. \tag{2.64}$$

Let us next consider many ensembles of ions that have different orbital-angular momenta L_j. In this case, the alignment parameter is the mean or average over all energy levels

$$\bar{A}_{20} = \sum_{E_j} P_{E_j} A_{20}^{E_j}(L_j), \tag{2.65}$$

with the probability P_{E_j} that an ion is in the energy level E_j with regard to all L. The energy levels are grouped according to their L values and each L value has a probability of P_L that an ion is found in a state with L regardless of the energy level. Thus, it is $P_{E_j} = P_{E_j}(L) P_L$. With Eq. (2.59), the expression for $\bar{A}_{20}$ simplifies

to a mean alignment parameter average over all L

$$\begin{aligned}\bar{A}_{20} &= \sum_L P_L \sum_{E_j} P_{E_j}(L) A_{20}^{E_j}(L) \\ &= \sum_L P_L A_{20}(L).\end{aligned} \tag{2.66}$$

Its width is given by

$$\begin{aligned}\Delta_{A_{20}}^2 &= \sum_{E_j} \left[A_{20}^{E_j}(L_j)\right]^2 P_{E_j} - \bar{A}_{20}^2 \\ &= \sum_L P_L \sum_{E_j} \left[A_{20}^{E_j}(L)\right]^2 P_{E_j}(L) - \bar{A}_{20}^2 \\ &= \sum_L P_L A_{20}(L)^2 - \bar{A}_{20}^2 + \sum_L \Delta_{A_{20}}^2(L) P_L.\end{aligned} \tag{2.67}$$

Note that the width contains two parts. The first two terms determine the width with respect to the average over L and the last term takes into account that each $A_{20}(L)$ already contains a width [Eq. (2.64)].

The averaged orientation parameter can be obtained in a very similar manner and with very similar outcomes and is, therefore, not discussed here.

2.4.4 Spatial shapes of aligned electron clouds

To develop some intuition about electron-cloud alignment, we next discuss the spatial shape of the electron cloud of aligned ions. This part is based mainly on Ref. [61]. As in Secs. 2.4.1 and 2.4.2, we consider an ensemble of ions in an incoherent superposition of states described by the density matrix $\hat{\rho} = \sum_{M_L} P_{M_L} |LM_L\rangle\langle LM_L|$. (But also ensembles of ions in different energy levels can be used as demonstrated in Sec. 2.4.3.) Moreover, the z axis is chosen as the quantization axis.

Each individual state $|LM_L\rangle$ has an electron or charge distribution

$$\varrho_{M_L}(\boldsymbol{r}) = e|\langle \boldsymbol{r}|LM_L\rangle|^2 = e|\Psi_{LM_L}(\boldsymbol{r})|^2. \tag{2.68}$$

The wave function $\Psi_{LM_L}(\boldsymbol{r})$ decomposes into a radial part $R_L(r)$ and an angular part, given by the spherical harmonic $Y_L^{M_L}(\theta, \phi)$. Thus, it is

$$\varrho_{M_L}(\boldsymbol{r}) = e|R_L(r)|^2 |Y_L^{M_L}(\theta, \phi)|^2. \tag{2.69}$$

The average over the individual electron distributions yields the total electron dis-

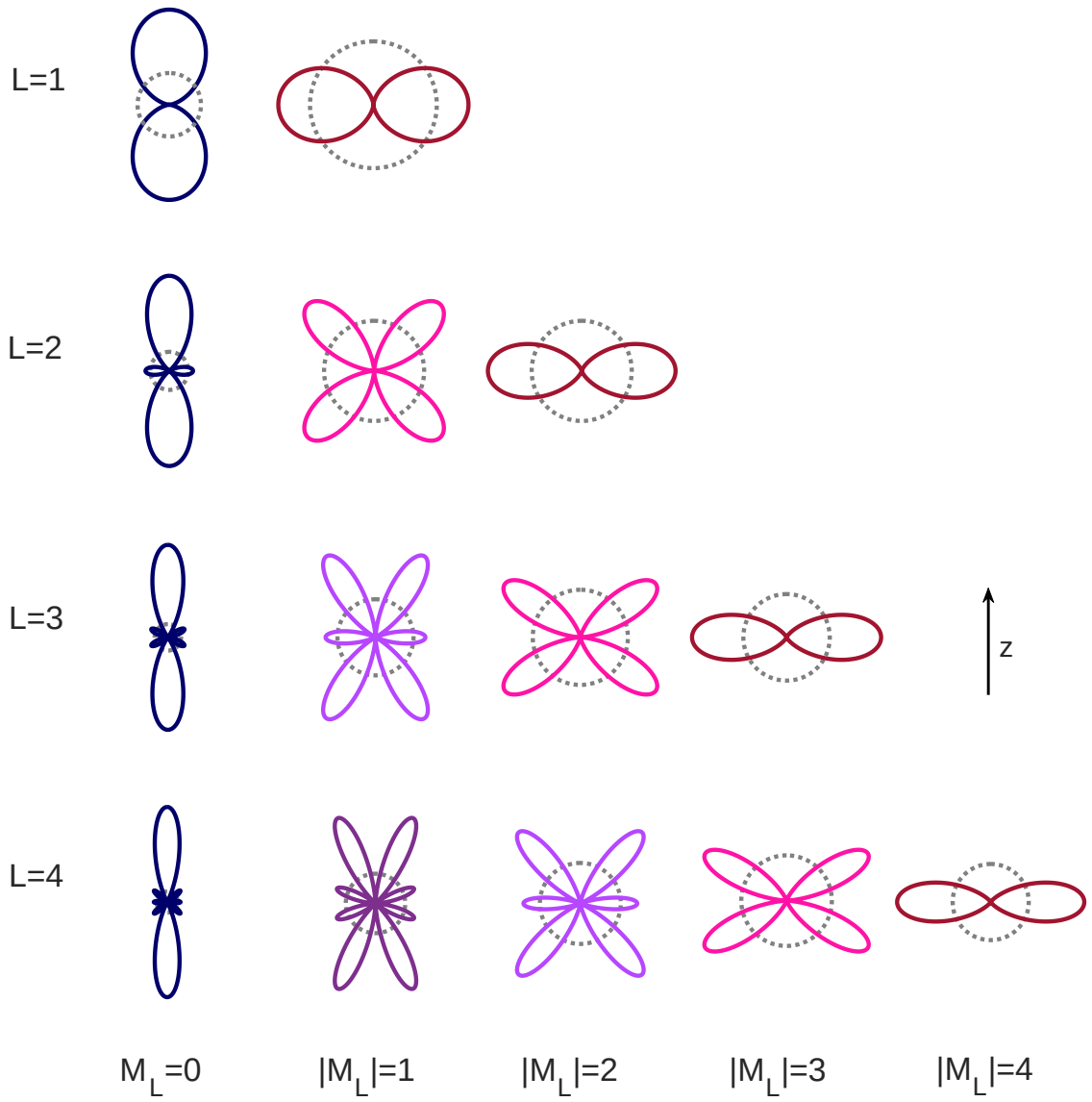

Figure 2.12: Polar diagram of the spatial shape of the electron cloud $|\bar{Y}_L(\theta)|^2$. The special case of perfect alignment, where all ions have the same $|M_L|$ ($P_{|M_L|} = 1$), is considered for different orbital-angular momenta L. The corresponding alignment parameters are given in Table 2.1. The dotted gray circles indicate the unaligned electron cloud with a uniform distribution $P_{M_L} = \frac{1}{2L+1}$. The vertical axis corresponds to the quantization (z) axis.

tribution of the ensemble

$$\begin{aligned}\varrho(\boldsymbol{r}) &= \sum_{M_L=-L}^{L} P_{M_L}\varrho_{M_L}(\boldsymbol{r}) \\ &= e|R_L(r)|^2 \sum_{M_L=-L}^{L} P_{M_L}|Y_L^{M_L}(\theta,\phi)|^2 \\ &= e|R_L(r)|^2|\bar{Y}_L(\theta)|^2.\end{aligned} \tag{2.70}$$

The angular part of the electron distribution

$$|\bar{Y}_L(\theta)|^2 = \sum_{M_L=-L}^{L} P_{M_L}|Y_L^{M_L}(\theta,\phi)|^2 \tag{2.71}$$

is the spatial shape of the electron cloud of the ensemble of ions. Its ϕ-dependence is eliminated by the squaring. Figure 2.12 depicts the spatial shape of the electron cloud for the special case of perfect alignment (Table 2.1), where all ions have the same $|M_L|$. In this case, $|\bar{Y}_L(\theta)|^2$ reduces to a single $|Y_L^{M_L}(\theta,\phi)|^2$. The electron cloud exhibits a peanut-like shape aligned along the quantization axis, when all ions have $M_L = 0$. When all ions have $|M_L| = L$, the peanut-like shaped electron cloud is anti aligned. In between, there are more butterfly-like shapes, which become less aligned along the quantization axis the larger $|M_L|$. An arbitrarily aligned ensemble of ions shows an electron-cloud shape that is averaged over the electron-cloud shapes for a definite L in Fig. 2.12. For an unaligned ensemble of ions (uniform distribution of M_L), the electron cloud is perfectly spherically symmetric.

The spatial shape of the electron cloud $|\bar{Y}_L(\theta)|^2$ is related to the state multipoles $\langle T(L)^\dagger_{KQ}\rangle$ [Eq. (2.46)] and, consequently, the alignment parameter $A_{20}(L)$ [Eq. (2.58)]. This relation is derived in the following. In general, the total electron distribution of the ensemble $\varrho(\boldsymbol{r})$ is given by the coordinate representation of the density matrix [61]

$$\varrho(\boldsymbol{r}) = e\,\langle \boldsymbol{r}\,|\rho|\,\boldsymbol{r}\rangle\,. \tag{2.72}$$

Inserting the general formula for the density matrix [Eq. (2.42)] and $\langle \boldsymbol{r}|LM_L\rangle = \Psi_{LM_L}(\boldsymbol{r}) = R_L(r)Y_L^{M_L}(\theta,\phi)$ into Eq. (2.72) yields

$$\begin{aligned}\varrho(\boldsymbol{r}) =& e\sum_{M'_L,M_L} \langle LM'_L\,|\hat{\rho}|\,LM_L\rangle\,\langle \boldsymbol{r}|LM'_L\rangle\langle \boldsymbol{r}|LM_L\rangle^* \\ =& e|R_L(r)|^2 \sum_{M'_L,M_L} \langle LM'_L\,|\hat{\rho}|\,LM_L\rangle\,Y_L^{M'_L}(\theta,\phi)Y_L^{M_L}(\theta,\phi)^*.\end{aligned} \tag{2.73}$$

As a next step, the inverted relation for the state multipoles $\langle T(L)^\dagger_{KQ}\rangle$

$$\langle LM'_L\,|\hat{\rho}|\,LM_L\rangle = \sum_{K,Q}(-1)^{L-M'_L}C(L,L,K;M_L,-M'_L,Q)\langle T(L)^\dagger_{KQ}\rangle \tag{2.74}$$

and the identity [205]

$$\begin{aligned} Y_L^{M'_L}(\theta,\phi)Y_L^{M_L}(\theta,\phi) = \frac{2L+1}{\sqrt{4\pi}}\sum_{K',Q'}\frac{(-1)^{Q'}}{\sqrt{2K'+1}}C(L,L,K';M_L,-M'_L,Q') \\ \times C(L,L,K';0,0,0)Y_{K'}^{Q'}(\theta,\phi)^* \end{aligned} \tag{2.75}$$

are used. Combining this with the fact that $Y_L^{M_L}(\theta,\phi)^* = (-1)^{M_L}Y_L^{-M_L}(\theta,\phi)$ and $(-1)^{-M'_L+M_L+Q'} = 1$, and with the orthogonality relation for Clebsch-Gordan coefficients, $\sum_{M'_L,M_L} C(L,L,K;M_L,-M'_L,Q)C(L,L,K';M_L,-M'_L,Q') = \delta_{K,K'}\delta_{Q,Q'}$ [203], we obtain for the total electron distribution

$$\varrho(\boldsymbol{r}) = e|R_L(r)|^2(-1)^L\frac{2L+1}{\sqrt{4\pi}}\sum_{K,Q}\frac{\langle T(L)^\dagger_{KQ}\rangle}{\sqrt{2K+1}}C(L,L,K;0,0,0)Y_K^Q(\theta,\phi)^*. \tag{2.76}$$

Note that only even K contribute to the sum owing to the triangular condition for the Clebsch-Gordan coefficients [203]. As a consequence, an orientation ($K = 1$) of the ensemble of ions does not affect the spatial shape of its electron cloud. From Eqs. (2.70) and (2.76), we are now able to derive the spatial shape of the electron cloud $|\bar{Y}_L(\theta)|^2$ in terms of state multipoles $\langle T(L)^\dagger_{KQ}\rangle$ for an incoherent superposition of states ($Q = 0$). Applying $C(L,L,K;0,0,0) = (-1)^L\sqrt{\frac{2K+1}{2L+1}}C(K,L,L;0,0,0)$, the normalization $\langle T(L)^\dagger_{00}\rangle = \sqrt{\frac{1}{2L+1}}$, and the definition of $A_{20}(L)$ [Eq. (2.58)], the spatial shape of the electron cloud separates as follows

$$\begin{aligned} |\bar{Y}_L(\theta)|^2 = \frac{1}{\sqrt{4\pi}}\Bigg\{1 + \sqrt{4\pi}A_{20}(L)C(2,L,L;0,0,0)Y_2^0(\theta) \\ + \sqrt{4\pi}\sum_{K>2}\frac{\langle T(L)^\dagger_{K0}\rangle}{\langle T(L)^\dagger_{00}\rangle}C(K,L,L;0,0,0)Y_K^0(\theta)\Bigg\}. \end{aligned} \tag{2.77}$$

The first term yields a perfectly spherically symmetric electron cloud, whereas the second term reshapes this perfectly spherically symmetric electron cloud according to A_{20}. When $A_{20} < 0$, the shape becomes more pronounced along the quantization axis, while it is reduced in the quantization axis, when $A_{20} > 0$ (see $L = 1$ in Fig. 2.12). For $L > 1$, the spatial shape of the electron cloud is further modified by state multipoles of higher rank.

2.4.5 Angular distribution of Auger-Meitner electrons

Electrons emitted from an aligned ion by Auger-Meitner decay are generally anisotropically distributed in space [60, 74–76]. Here, the resulting angular distribution of Auger-Meitner electrons is discussed following Ref. [201]. We assume that the interaction Hamiltonian does not couple to the spin. Therefore, the spin of both ions and electrons is not of interest and, hence, is summed over in the density matrix formalism (so-called reduced density matrix) [61, 201].

Let us start with the helicity system [166, 201] as coordinate system. In the helicity system, the direction of the Auger-Meitner electron emission is chosen as quantization (z) axis. As a consequence, the orbital-angular-momentum projection m_{l_a} of an Auger-Meitner electron is always zero. Following the density matrix formalism introduced in Sec. 2.4.2, the initial and final system involved in the Auger-Meitner decay are represented by a density matrix. The initial system is given by the ensemble of initial ions, having orbital-angular momentum L_i and being arbitrarily aligned with alignment parameter $A_{20}(L_i)$. The expansion in terms of irreducible spherical tensor operators [Eq. (2.49)] is used for its density matrix, i.e.,

$$\hat{\rho}_i = \sum_{K,Q} \langle T(L_i)^\dagger_{KQ} \rangle \hat{T}(L_i)_{KQ}. \tag{2.78}$$

The final system is given by the ensemble of resulting ions and the emitted Auger-Meitner electrons. Its density matrix is related to the initial density matrix by the transition or interaction operator $\hat{V}$ in the following way [61]

$$\hat{\rho}_f = \hat{V} \hat{\rho}_i \hat{V}^\dagger. \tag{2.79}$$

For Auger-Meitner decay, $\hat{V}$ is the Coulomb operator [206]. A suitable normalization of the final density matrix is by the intensity I of the Auger-Meitner electron emission, so that $\mathrm{tr}(\hat{\rho}_f) = I$. Note that I exhibits no angular-dependence in the helicity system. Utilizing this normalization and Eqs. (2.78) and (2.79), the intensity is expressed in terms of state multipoles $\langle T(L_i)^\dagger_{KQ} \rangle$ for the initial ensemble of ions as follows

$$\begin{aligned} I &= \mathrm{tr}(\hat{\rho}_f) = \mathrm{tr}(\hat{V} \hat{\rho}_i \hat{V}^\dagger) \\ &= \sum_{K,Q} \langle T(L_i)^\dagger_{KQ} \rangle \mathrm{tr}(\hat{V} \hat{T}(L_i)_{KQ} \hat{V}^\dagger). \end{aligned} \tag{2.80}$$

As a next step, an initial system in an incoherent superposition of states is assumed, so that $Q = 0$ (Sec. 2.4.2). Moreover, the unnormalized generalized anisotropy

parameter

$$A(KQ) = \mathrm{tr}(\hat{V}\hat{T}(L_i)_{KQ}\hat{V}^\dagger) \tag{2.81}$$

is introduced. Then, Eq. 2.80 for the intensity reads

$$I = \sum_{K \text{ even}} \langle T(L_i)^\dagger_{K0}\rangle A(K0). \tag{2.82}$$

The sum over K is restricted to even values because of the symmetry relation $A(KQ) = (-1)^K A(K-Q)$ [207].

However, when performing an experiment we are, of course, interested in the laboratory (lab) system. Therefore, the state multipoles are transformed from the helicity system to the lab system via reduced rotation matrices $d^{(K)}_{Q'Q}(\theta)$ [166, 201, 208]. For $Q = Q' = 0$, the reduced rotation matrix is given by a Legendre polynomial $P_K(\cos\theta)$ [208] and the transformation is

$$\langle T(L_i)^\dagger_{K0}\rangle = \langle T(L_i)^\dagger_{K0}\rangle_{\mathrm{lab}} P_K(\cos\theta). \tag{2.83}$$

θ is the angle between the quantization (z) axes in the helicity system—the direction of Auger-Meitner electron emission—and the lab system—e.g., the polarization direction of the ionizing photon beam. The generalized anisotropy parameter $A(K0)$ is not transformed and remains in the helicity system. As a result of the transformation, the intensity becomes angle-dependent and is given by

$$I(\theta) = \sum_{K \text{ even}} \langle T(L_i)^\dagger_{K0}\rangle_{\mathrm{lab}} A(K0) P_K(\cos\theta). \tag{2.84}$$

This equation describes the angular distribution of emitted Auger-Meitner electrons. I only depends on the polar angle θ. Therefore, Auger-Meitner electrons are anisotropically emitted with respect to θ, but isotropically emitted with respect to the azimuthal angle ϕ. The total intensity I_0 is obtained by summing up all emitted Auger-Meitner electrons independent of their direction of emission, so that

$$\begin{aligned} I_0 &= \int_0^{2\pi} d\phi \int_0^{\pi} d\theta \ \sin\theta \ I(\theta) \\ &= 2\pi \sum_{K \text{ even}} \langle T(L_i)^\dagger_{K0}\rangle_{\mathrm{lab}} A(K0) \int_0^{\pi} d\theta \ \sin\theta \ P_K(\cos\theta) \\ &= 2\pi \sum_{K \text{ even}} \langle T(L_i)^\dagger_{K0}\rangle_{\mathrm{lab}} A(K0) \int_{-1}^{1} dx \ P_K(x) \\ &= 4\pi \langle T(L_i)^\dagger_{00}\rangle_{\mathrm{lab}} A(00). \end{aligned} \tag{2.85}$$

$\langle T(L_i)^\dagger_{00}\rangle_{\text{lab}}$ and $A(00)$ can be thought of as normalizations. Accordingly, we define the normalized anisotropy parameter

$$\alpha_K = \frac{A(K0)}{A(00)} \tag{2.86}$$

and a generalized form of the alignment parameter

$$A_{K0} = \frac{\langle T(L_i)^\dagger_{K0}\rangle_{\text{lab}}}{\langle T(L_i)^\dagger_{00}\rangle_{\text{lab}}}, \tag{2.87}$$

which is equal to Eq. (2.58) for $K = 2$. In this way, the angular distribution of emitted Auger Meitner electrons is expressed as

$$I(\theta) = \frac{I_0}{4\pi}\left\{1 + \sum_{\substack{K\geq 2\\ \text{even}}} \alpha_K A_{K0} P_K(\cos\theta)\right\}. \tag{2.88}$$

There are a few points worthy of note regarding this equation. The sum over K is restricted by $K \leq 2L_i$ owing to the Clebsch-Gordan coefficient in $\langle T(L_i)^\dagger_{K0}\rangle_{\text{lab}}$ [Eq. (2.46)]. Thus, in general, not only A_{20}, but also higher A_{K0} contribute to the sum unless $L_i = 1$. Moreover, the angular distribution of emitted Auger-Meitner electrons has a similar form as the spatial shape of the electron cloud of an aligned ion [Eq. (2.77)]. The first term yields an isotropic angular distribution, whereas the second term reshapes it. This reshaping depends on both the alignment of the initial ion produced in a primary ionization step (A_{K0}) and the dynamics of the subsequent Auger-Meitner decay (α_K). It is possible to express α_K [Eq. (2.86)] explicitly in terms of summations over quantum numbers, Clebsch-Gordan coefficients, and reduced transition matrix elements [201, 207, 209–211]. But this is beyond the scope of this introduction into the theoretical framework of electron-cloud alignment and is not necessary to understand the scientific contributions in Chapter 3.

Here, the angular distribution of emitted Auger-Meitner electrons is illustrated by means of an example. Let us consider Auger-Meitner decays that involve only a single continuum wave for the Auger-Meitner electron with orbital-angular momentum l_a. Examples are $L_{2,3}M_1M_1$ or $L_1L_{2,3}M_1$ Auger-Meitner decays or those resulting in ions with final orbital-angular momentum $L_f = 0$. In these special cases, the anisotropy parameter α_K becomes independent of the reduced transition matrix elements and simplifies to a purely analytic expression [75, 76, 201, 209]

$$\alpha_K = (-1)^{L_i+L_f}\sqrt{2L_i+1}(2l_a+1)C(l_a,l_a,K;0,0,0)\begin{Bmatrix} l_a & l_a & K \\ L_i & L_i & L_f \end{Bmatrix}. \tag{2.89}$$

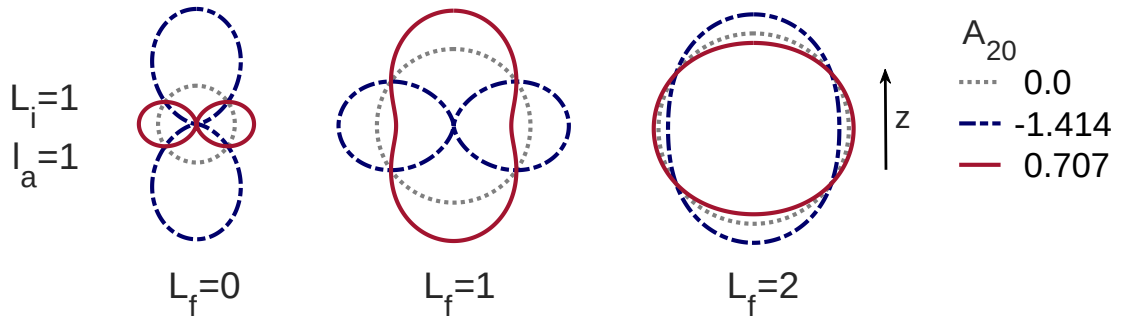

Figure 2.13: Polar diagram of the angular distribution of emitted Auger-Meitner electrons $I(\theta)$. The initial ion, having orbital-angular momentum $L_i = 1$, is either unaligned ($A_{20} = 0$), perfectly aligned ($A_{20} = -\sqrt{2} \approx -0.141$), or perfectly anti aligned ($A_{20} = 1/\sqrt{2} \approx 0.707$). The emitted Auger Meitner electrons are assumed to be in a single continuum wave with orbital-angular momentum $l_a = 1$. Different orbital-angular momenta L_f for the resulting final ion are discussed. The vertical axis corresponds to the quantization (z) axis in the laboratory system.

Here, $\{\cdot\}$ is a $6j$ symbol [204] and $K \leq 2l_a$ due to the triangular condition for the Clebsch-Gordan coefficient [203]. As a consequence of the latter, it is

$$I(\theta) = \frac{I_0}{4\pi} \{1 + \alpha_2 A_{20} P_2(\cos\theta)\} \text{ for } l_a = 1 \text{ or } L_i = 1. \tag{2.90}$$

In these two special cases, the angular distribution of emitted Auger-Meitner electrons gives direct access to the alignment parameter A_{20} for the initial ion. For perfectly aligned or anti aligned ions with $L_i = 1$, exemplary angular distribution of emitted Auger-Meitner electrons with $l_a = 1$ are presented in Fig. 2.13. As can be seen, for $L_f = 0$, the shapes of the angular distribution look fairly similar to the spatial shapes of the electron cloud of the initial ion, shown in Fig. 2.12. For $L_f = 1$, the angular distributions are rotated by $\pi/2$ due to the sign factor of α_2 [Eq. (2.89)]. For $L_f = 2$, reshaping of the isotropic angular distribution is clearly reduced, which is related to much smaller values for α_2. When the initial ion is unaligned, the angular distribution is always perfectly isotropic.

2.4.6 Conclusion and outlook

In this section, a general introduction into electron-cloud alignment has been given with a focus on the alignment parameter for its describtion, on the spatial shape of aligned electron clouds, and on the anisotropic emission of Auger-Meitner electrons from aligned ions. Anisotropies in the angular distribution of Auger-Meitner electrons are one possibility to make electron-cloud alignment experimentally acces-

sible [58, 75, 76]. Others are anisotropies in the angular distribution of fluorescence photons or their polarization [74, 78–80] as well as modifications in the photoelectron angular distribution [66]. But because photoelectrons emitted from unaligned ions already display an anisotropy [71–73], the latter is less useful. Both electron-cloud alignment and angular distribution of Auger-Meitner electrons have already been extensively explored theoretically and/or experimentally for a variety of singly ionized atoms [54–58, 60, 64, 74, 80, 212–214]. Also the alignment of strong-field ionized atoms has been studied [62, 63].

However, it is not clear how the electron-cloud alignment evolves during X-ray multiphoton ionization dynamics (see Refs. [65, 66] for work in this direction, though they employ XUV pulses). Answering this question is the aim of Sec. 3.1 and especially Sec. 3.4.

Chapter 3

Scientific Contributions

Having introduced the theoretical framework relevant for this thesis, I present all my scientific contributions in this chapter. An overview is given in Fig. 3.1.

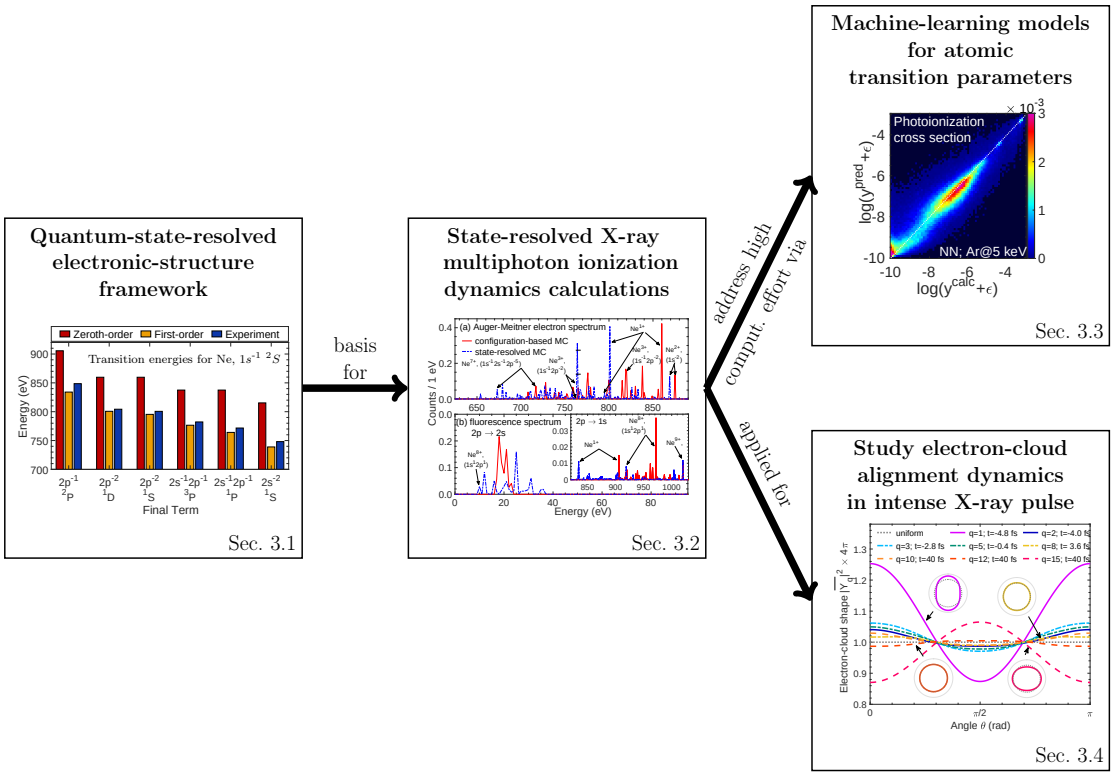

Figure 3.1: Graphical overview of my scientific contributions. For details, the reader is referred to the corresponding sections.

3.1 Theoretical investigation of orbital alignment of X-ray-ionized atoms in exotic electronic configurations

The first publication presents a nonrelativistic quantum-state-resolved electronic-structure framework for isolated atoms and atomic ions. This framework improves the accuracy of calculated transition energies and enables to investigate orbital alignment generated by an X-ray-induced transition. It also provides the basis for the subsequent studies of state-resolved X-ray multiphoton ionization dynamics (Secs. 3.2–3.4).

The underlying project was predominantly already performed as part of my master thesis, which was jointly supervised by Dr. S.-K. Son and Professor Dr. R. Santra. In particular, I embedded an improved quantum-state-resolved electronic-structure description based on first-order many-body perturbation theory into the XATOM toolkit [20, 132, 215]. During my doctoral project, I used the alignment parameter to investigate orbital alignment of X-ray-ionized atoms and wrote the manuscript with inputs from all authors.

Theoretical investigation of orbital alignment of x-ray-ionized atoms in exotic electronic configurations

Laura Budewig,[1,2] Sang-Kil Son,[1,3] and Robin Santra[1,2,3]

[1]*Center for Free-Electron Laser Science CFEL, Deutsches Elektronen-Synchrotron DESY, Notkestrasse 85, 22607 Hamburg, Germany*

[2]*Department of Physics, Universität Hamburg, Notkestrasse 9-11, 22607 Hamburg, Germany*

[3]*The Hamburg Centre for Ultrafast Imaging, Luruper Chaussee 149, 22761 Hamburg, Germany*

(Received 30 September 2021; revised 11 January 2022; accepted 8 March 2022; published 29 March 2022)

We theoretically study orbital alignment in x-ray-ionized atoms and ions, based on improved electronic-structure calculations starting from the Hartree-Fock-Slater model. We employ first-order many-body perturbation theory to improve the Hartree-Fock-Slater calculations and show that the use of first-order-corrected energies yields significantly better transition energies than originally obtained. The improved electronic-structure calculations enable us also to compute individual state-to-state cross sections and transition rates and, thus, to investigate orbital alignment induced by linearly polarized x rays. To explore the orbital alignment of transiently formed ions after photoionization, we discuss alignment parameters and ratios of individual state-resolved photoionization cross sections for initially neutral argon and two exotic electronic configurations that may be formed during x-ray multiphoton ionization dynamics induced by x-ray free-electron lasers. We also present how the orbital alignment is affected by Auger-Meitner decay and demonstrate how it evolves during a sequence of one photoionization and one Auger-Meitner decay. Our present work establishes a step toward investigation of orbital alignment in atomic ionization driven by high-intensity x rays.

DOI: 10.1103/PhysRevA.105.033111

I. INTRODUCTION

The development of x-ray free-electron lasers (XFELs) around the world [1–5] has enabled scientists to study a variety of new fields in structural biology [6–9], ultrafast x-ray atomic and molecular physics [10–13], as well as dense matter physics [14], owing to ultra-intense and ultrashort x-ray radiation with an unprecedentedly high brilliance [15]. Prototype examples of the excellent opportunities of XFELs are serial femtosecond crystallography [16] and single-particle imaging experiments [17,18], which permit structure determination with almost atomic resolution [19–23].

Accurate theoretical simulations in combination with experimental studies [24–29] have shown that extremely highly ionized atomic ions can be produced during interaction with ultra-intense and ultrashort x-ray pulses. In general, an x-ray photon is absorbed by an inner-shell electron, which is followed by a decay process via Auger-Meitner decay or x-ray fluorescence [30]. Further photoionization with accompanying decay cascades lead to very highly charged states of atoms [24–28] or molecules [29], which is called x-ray multiphoton ionization [31]. In the molecular case, the sample undergoes structural disintegration, which limits the resolution achievable in x-ray imaging experiments [32–35].

On the other hand, it has been well known for a long time that ions produced by single photoionization commonly exhibit an alignment [36–39] due to different ionization probabilities of ions with different projection quantum numbers. A theoretical treatment of alignment, including a description of parameters to quantify the alignment and orientation, can be found in Refs. [40–42]. More recently, orbital alignment has, for instance, been explored for single photoionization of initially closed-shell atoms and cations with respect to spin-orbit coupling [43,44] and for strong-field ionized atoms [45,46].

As a consequence of these aspects, orbital alignment during x-ray multiphoton ionization has become a topic of interest, which remains relatively unexplored. It addresses not only the orbital alignment of the highly charged ions produced in the end of multiple sequences of photoabsorption and accompanying relaxation events, but also how the alignment changes during the x-ray multiphoton ionization dynamics. A first critical step in this research direction is to develop a suitable atomic structure framework that provides individual *LS* eigenstates as well as individual state-to-state cross sections and transition rates for each angular momentum projection M_L. In a later step, this framework can then be embedded in an ionization dynamics calculation, so that individual states can also be captured during x-ray multiphoton ionization dynamics.

In this work, we present such a first step by extending the *ab initio* electronic-structure toolkit XATOM [35,47]. XATOM is a useful and successful tool [24–26,28] for simulating x-ray-induced atomic processes and ionization dynamics of neutral atoms, atomic ions, and ions embedded in a plasma [48,49]. Based on a Hartree-Fock-Slater (HFS) calculation of orbitals and orbital energies, subshell photoionization cross sections and fluorescence and Auger-Meitner group rates [35] can be computed, among other things [50–53]. These quantities are employed to determine the ionization

dynamics by solving a set of coupled rate equations [31], either directly [35] or via more efficient Monte Carlo algorithms for heavy atoms [24,54]. Since, especially for heavy atoms, an extremely huge number of electronic configurations are involved in the ionization dynamics, computational efficiency is critical. For instance, for xenon atoms, this number can be estimated to be $\sim 2.6 \times 10^{68}$ when relativistic and resonant effects are included [25]. Therefore, the XATOM toolkit uses HFS, one of the simplest and most efficient first-principles electronic-structure methods. Even though there are other more accurate atomic structure toolkits (see, e.g., [55]), improving the XATOM toolkit is of critical relevance for investigations in x-ray-induced ionization dynamics. Computational efficiency becomes even more crucial for solving state-resolved rate equations. In this case, the number of individual electronic states involved in the ionization dynamics goes far beyond the number of involved electronic configurations.

We extend the XATOM toolkit [35,47,56] by incorporating an improved electronic-structure description, based on the first-order many-body perturbation theory. This permits the computation of first-order-corrected energies and a set of zeroth-order *LS* eigenstates, for arbitrary electronic configurations. Moreover, individual state-to-state photoionization cross sections and transition rates are calculated, based on our new implementation. A detailed comparison with experimental results available in the literature shows that the extended XATOM toolkit delivers significantly improved transition energies in contrast to the original version. The knowledge of individual state-to-state cross sections enables us to study orbital alignment of ions produced by single photoionization. We focus on the orbital alignment of transiently formed ions resulting from photoionization of a neutral argon atom and some exotic electronic configurations of argon by linearly polarized x rays. An important remark here is that these ions can be viewed as examples of species appearing in x-ray multiphoton ionization of neutral atoms. It would be possible to observe them experimentally with ultrafast XFEL pulses by using a transient absorption experiment with two-color x rays, similar to that employed in Ref. [45]. Using the individual state-to-state transition rates, we investigate any change of orbital alignment after fluorescence and Auger-Meitner decay. Combining state-to-state cross sections and rates, we examine the orbital alignment after one x-ray-induced ionization process, i.e., a sequence comprising a photoionization event and a subsequent relaxation event. Understanding of the orbital alignment of this x-ray single-photon ionization will be a building block to explore and explain the orbital alignment occurring during x-ray multiphoton ionization dynamics induced by interaction with intense XFEL pulses.

The paper is organized as follows. In Sec. II, we briefly present the theoretical framework of our implementation in XATOM and discuss quantities to quantify the alignment. The validation of our implementation is the topic of Sec. III. Orbital alignment in initially neutral Ar, Ar^+ $(2p^{-1})$, and Ar^{2+} $(2p^{-2})$ is studied in Sec. IV. We also briefly address the orbital alignment caused by x-ray-induced ionization including relaxation in this section. We conclude with a summary and future perspectives in Sec. V.

II. THEORETICAL DETAILS

The aim of this section is to outline the theoretical framework. In particular, we start with the HFS Hamiltonian, whose solutions are already present in the XATOM toolkit [56]. Then we develop a method to determine first-order-corrected energies and a new set of eigenstates by employing first-order degenerate perturbation theory. These improved electronic-structure calculations are implemented as an extension of the XATOM toolkit [56] and are further utilized to calculate individual state-to-state cross sections and transition rates. Throughout this paper, atomic units, i.e., $m = |e| = \hbar = 1$ and $c = 1/\alpha$, are used, where α is the fine-structure constant.

A. The Hamiltonian

The Hamiltonian describing N nonrelativistic electrons in an atom can be separated into the HFS Hamiltonian $\hat{H}^{\mathrm{HFS}}$ and the residual electron-electron interaction $\hat{V}_{\mathrm{res}}$, defined by the full two-electron interactions minus the HFS mean field [see Eq. (6)],

$$\hat{H}_{\mathrm{matter}} = \hat{H}^{\mathrm{HFS}} + \hat{V}_{\mathrm{res}}. \tag{1}$$

The one-electron solutions of the HFS Hamiltonian are the so-called spin orbitals φ_q and spin-orbital energies ε_q, respectively [30]. Consequently, we solve the following effective one-electron equation:

$$\left[-\tfrac{1}{2}\nabla^2 + \hat{V}^{\mathrm{HFS}}(\vec{x})\right]\varphi_q(\vec{x}) = \varepsilon_q \varphi_q(\vec{x}). \tag{2}$$

Here, $\hat{V}^{\mathrm{HFS}}$ is the Hartree-Fock-Slater mean field [57],

$$\hat{V}^{\mathrm{HFS}}(\vec{x}) = -\frac{Z}{|\vec{x}|} + \int d^3x' \frac{\rho(\vec{x}')}{|\vec{x} - \vec{x}'|} - \frac{3}{2}\left[\frac{3}{\pi}\rho(\vec{x})\right]^{\frac{1}{3}}, \tag{3}$$

with the local electron density $\rho(\vec{x})$ and the nuclear charge Z. A more extensive description of how to numerically solve Eq. (2) within the XATOM toolkit can be found in, e.g., Refs. [35,47]. In the context of this paper, it is only worth mentioning that the spin orbitals can be decomposed into a radial part, a spherical harmonic, and a spin part [35],

$$\varphi_q(\vec{x}) = \frac{u_{\xi_q, l_q}(r)}{r} Y_{l_q}^{m_{l_q}}(\Omega) \begin{pmatrix} \delta_{m_{s_q}, \frac{1}{2}} \\ \delta_{m_{s_q}, -\frac{1}{2}} \end{pmatrix}. \tag{4}$$

Accordingly, the index q refers to a set of four quantum numbers $(\xi_q, l_q, m_{l_q}, m_{s_q})$ (with $\xi_q = n_q$ for bound spin orbitals, i.e., $\varepsilon_q < 0$, and $\xi_q = \varepsilon_q$ for unbound spin orbitals, i.e., $\varepsilon_q \geqslant 0$). Note that spin orbitals belonging to the same subshell, i.e., the same n and l quantum numbers, share the same orbital energy, denoted as ε_{nl}.

Introducing anticommutating creation and annihilation operators, $\hat{c}_q^\dagger$ and $\hat{c}_q$, associated with the spin orbitals [30,58], the two parts of Eq. (1) can be expressed as

$$\hat{H}^{\mathrm{HFS}} = \sum_q \varepsilon_q \hat{c}_q^\dagger \hat{c}_q \tag{5}$$

and

$$\hat{V}_{\mathrm{res}} = -\sum_{p,q} V_{pq}^{\mathrm{HFS}} \hat{c}_p^\dagger \hat{c}_q + \frac{1}{2}\sum_{p,q,r,s} v_{pqrs} \hat{c}_p^\dagger \hat{c}_q^\dagger \hat{c}_s \hat{c}_r. \tag{6}$$

In these expressions, the summations run over all spin orbitals. Furthermore,

$$V_{pq}^{\mathrm{HFS}} = \int d^3x\, \varphi_p^\dagger(\vec{x}) \hat{V}^{\mathrm{HFS}}(\vec{x}) \varphi_q(\vec{x}) \tag{7}$$

is a mean-field matrix element and

$$v_{pqrs} = \int\int d^3x\, d^3x'\, \varphi_p^\dagger(\vec{x}) \varphi_q^\dagger(\vec{x}') \frac{1}{|\vec{x} - \vec{x}'|} \varphi_r(\vec{x}) \varphi_s(\vec{x}') \tag{8}$$

is a two-electron Coulomb matrix element.

Having at hand the one-electron eigenstates, the N-electron eigenstates of $\hat{H}^{\mathrm{HFS}}$ are then formed by an antisymmetrized product [58]. Known as electronic Fock states, these multiorbital states read

$$|\Phi_\alpha\rangle = \left| \prod_{q=1}^{\infty} n_q^\alpha \right\rangle = \prod_{q=1}^{\infty} (\hat{c}_q^\dagger)^{n_q^\alpha} |0\rangle, \tag{9}$$

where $|0\rangle$ is the vacuum and the occupation number $n_q^\alpha \in \{0, 1\}$ is restricted by $\sum_{q=1}^{\infty} n_q^\alpha = N$. The energy of a Fock state is

$$E_\alpha = \sum_{q=1}^{\infty} n_q^\alpha \varepsilon_q = \sum_{n,l} N_{nl} \varepsilon_{nl}, \tag{10}$$

with the latter summation running over all subshells, occupied by N_{nl} electrons. Note that the Fock states are only eigenstates of $\hat{H}^{\mathrm{HFS}}$, but not of $\hat{H}_{\mathrm{matter}}$.

B. Improved electronic-structure calculations

In order to obtain approximate solutions of $\hat{H}_{\mathrm{matter}}$, we employ first-order time-independent degenerate perturbation theory [59,60]. Regarding $\hat{H}_{\mathrm{matter}}$ in Eq. (1), $\hat{H}^{\mathrm{HFS}}$ is treated as the unperturbed Hamiltonian, the well-known Fock states $|\Phi_\alpha\rangle$ as the unperturbed zeroth-order states, and $\hat{V}_{\mathrm{res}}$ as the perturbation. Since the Fock states belonging to the same electronic configuration share the same energy with respect to $\hat{H}^{\mathrm{HFS}}$ [see Eq. (10)], degenerate perturbation theory has to be applied.

Here the method implemented to determine the first-order-corrected energy eigenvalues of $\hat{H}_{\mathrm{matter}}$ and a new set of zeroth-order eigenstates by employing first-order degenerate perturbation theory is briefly sketched. In particular, we assume that an arbitrary electronic configuration is given for the atom or ion for which we want to find the solutions. Then an application of degenerate perturbation theory requires the following steps.

(i) *Find the set of Fock states belonging to the given electronic configuration and make subsets according to (M_S, M_L).* It is useful to group the Fock states $|\Phi_\alpha\rangle$ into subsets according to the total spin projection, $M_S^\alpha = \sum_q n_q^\alpha m_{s_q}$, and the projection of the total angular momentum operator, $M_L^\alpha = \sum_q n_q^\alpha m_{l_q}$. Therefore, from now on, a Fock state is expressed as $|\Phi_\gamma^{M_S;M_L}\rangle$, with its projection quantum numbers as upper labels and with a lower index γ that runs from 1 to the number of Fock states with M_S and M_L. Then, for each subset $\{|\Phi_\gamma^{M_S;M_L}\rangle\}$, the Fock states are separately determined as strings of occupation numbers, i.e., zeros and ones [see Eq. (9)].

(ii) *Compute the matrix elements of $\boldsymbol{H}_{\mathrm{matter}}$ within each subset and diagonalize each submatrix $\boldsymbol{H}_{\mathrm{matter}}^{(M_S,M_L)}$.* Most importantly, utilizing the Condon rules [61], it can be easily shown that $\boldsymbol{H}_{\mathrm{matter}}$ is block diagonal in the previously introduced subsets $\{|\Phi_\gamma^{M_S;M_L}\rangle\}$. Therefore, it is sufficient to compute only matrix elements within the subsets, i.e., $\langle\Phi_\delta^{M_S;M_L}|\hat{H}_{\mathrm{matter}}|\Phi_\gamma^{M_S;M_L}\rangle$, and to numerically diagonalize each submatrix $\boldsymbol{H}_{\mathrm{matter}}^{(M_S,M_L)}$ separately. The eigenvalues of $\boldsymbol{H}_{\mathrm{matter}}^{(M_S,M_L)}$ deliver first-order-corrected energies and its eigenstates offer a new subset of zeroth-order states having projection quantum numbers M_S and M_L. These new states are linear combinations of the Fock states $|\Phi_\gamma^{M_S;M_L}\rangle$ belonging to the subset in question. In contrast to the Fock states, the new states have the advantage of also being eigenstates of total orbital angular momentum and of total spin. Thus, from now on, we refer to the new zeroth-order states as zeroth-order LS eigenstates.

(iii) *Identify the term symbol for each pair of first-order-corrected energy and zeroth-order LS eigenstate.* To label the zeroth-order LS eigenstates, we use the set of quantum numbers (L, S, M_L, M_S) together with an additional integer index κ that runs from 1 to the number of states with (L, S, M_L, M_S). Consequently, the zeroth-order LS eigenstates read

$$|LSM_LM_S\kappa\rangle = \sum_\gamma c_{LSM_LM_S\kappa}^\gamma |\Phi_\gamma^{M_S;M_L}\rangle, \tag{11}$$

with the expansion coefficient $c_{LSM_LM_S\kappa}^\gamma$ obtained from step (ii). The values for the projection quantum numbers are directly known from the subset in question, whereas the other labels, i.e., L, S, and κ, need to be determined. The zeroth-order LS eigenstates, having the same values for L, S, and κ, form a term [62] which is characterized by a term symbol ${}^{2S+1}L(\kappa)$. Also note that all states within a term share the same energy. So let the first-order-corrected energies be denoted by $E_{LS\kappa}$. Combining this knowledge with the method of Slater diagrams, described in, e.g., Refs. [62,63], L, S, and κ can be identified for each pair of first-order-corrected energy and zeroth-order LS eigenstate.

(iv) *If terms share the same first-order-corrected energy, diagonalize $\boldsymbol{S}^2$ and/or $\boldsymbol{L}^2$ with respect to the zeroth-order LS eigenstates in question.* This step is necessary to guarantee that the zeroth-order states are all proper LS eigenstates in the end (for more details, see [61]).

The method described delivers all terms ${}^{2S+1}L(\kappa)$ together with their first-order-corrected energies $E_{LS\kappa}$ and all zeroth-order LS eigenstates $|LSM_LM_S\kappa\rangle$ for a given atom or ion in a given electronic configuration. In the following, for simplicity, the label κ is omitted, either because $\kappa = 1$ for all involved states or because it is irrelevant in the computation in question. We point out that the orbitals and their energies needed to create the submatrices $\boldsymbol{H}_{\mathrm{matter}}^{(M_S,M_L)}$ are provided by the original XATOM toolkit. Moreover, note that there exists an alternative way of constructing the LS eigenstates by employing Racah algebra [64–67]. However, here we have used the strategy that was developed by Condon and Shortley [61]. Numerical diagonalization of the relatively small matrices that arise in the approach we adopt does not determine the overall computational effort.

C. Individual state-to-state photoionization cross sections

Having at hand first-order-corrected energies and zeroth-order *LS* eigenstates [Eq. (11)] for the initial and final electronic configurations, we can compute photoionization cross sections for these individual initial and final states. Note that from now on, the index i appears when referring to the quantities of the initial state, i.e., $|L_i S_i M_{L_i} M_{S_i}\rangle$, while the index f is used for a final target state, i.e., $|L_f S_f M_{L_f} M_{S_f}\rangle$. We remark that the final target state excludes the unbound photoelectron. Thus, the total final electronic state is given by $|L_f S_f M_{L_f} M_{S_f}; \varepsilon_c l_c m_{l_c} m_{s_c}\rangle$, where the latter quantum numbers refer to those of the photoelectron. However, attributed to the use of a fully uncoupled approach for the continuum states, the total final state is no *LS* eigenstate. In order to calculate the cross section for orthogonal spin orbitals and for photons linearly polarized along the z axis [68,69], we use the first-order time-dependent perturbation theory [30] and the electric dipole approximation [31]. As long as we integrate over the photoelectron angular distribution, the latter approximation, also utilized in the original XATOM toolkit [35], works well. Then the individual state-to-state cross section for ionizing an electron in the subshell with quantum numbers n and l by absorbing a linearly polarized photon with energy ω_{in} may be written as

$$\sigma^{M_{L_i};M_{L_f}}_{^{2S_i+1}L_i;\,^{2S_f+1}L_f}(nl,\omega_{\text{in}}) = \frac{4\pi^2}{3\omega_{\text{in}}}\alpha(\varepsilon_{nl}-\varepsilon_c)^2 \sum_{l_c=|l-1|}^{l+1} l_> \left|\int_0^\infty dr u^*_{\varepsilon_c l_c}(r) r u_{nl}(r)\right|^2 \times \sum_{M_{S_f}} |C(l,l_c,1;M_{L_i}-M_{L_f},M_{L_f}-M_{L_i},0)\langle L_f S_f M_{L_f} M_{S_f}|\hat{c}_j|L_i S_i M_{L_i} S_i\rangle|^2. \tag{12}$$

In this expression, $C(\cdot)$ represents a Clebsch-Gordan coefficient [65,67], $l_> = \max(l_c, l)$, $\varepsilon_c = \omega_{\text{in}} + E_{L_i S_i} - E_{L_f S_f}$ is the energy of the photoelectron, and ε_{nl} is the orbital energy of the nl subshell [70]. Owing to the selection rules for a dipole transition [68], the first sum in Eq. (12) does not include $l_c = l$. Following the independent-particle model [71], the index j of the involved bound spin orbital (i.e., from which an electron is ejected) refers to the set of quantum numbers $(n_j, l_j, m_{l_j}, m_{s_j}) = (n, l, M_{L_i} - M_{L_f}, M_{S_i} - M_{S_f})$ with the restriction $M_{S_i} = S_i$. The interaction Hamiltonian causing one-photon absorption [30] does not affect the spin and its projection. Thereby, the cross section is independent of the initial spin projection M_{S_i} when performing a summation over the final spin projection M_{S_f}. Accordingly, Eq. (12) describes a transition between one initial zeroth-order *LS* eigenstate $|L_i S_i M_{L_i} M_{S_i}\rangle$ with arbitrary spin projection M_{S_i} and both final zeroth-order *LS* eigenstates $|L_f S_f M_{L_f} M_{S_i} + \frac{1}{2}\rangle$ and $|L_f S_f M_{L_f} M_{S_i} - \frac{1}{2}\rangle$, as long as $|M_{S_i} \pm \frac{1}{2}| \leqslant S_f$. We also remark that the matrix element $\langle L_f S_f M_{L_f} M_{S_f}|\hat{c}_j|L_i S_i M_{L_i} S_i\rangle$ can be interpreted as the overlap between the final and initial zeroth-order *LS* eigenstates. Due to the involved annihilation operator $\hat{c}_j$ (see Sec. II A), the initial state is, however, already reduced by the involved electron in the spin orbital φ_j. The larger (smaller) this overlap is, the larger (smaller) the cross section is. If the overlap is zero, the cross section is zero.

D. Individual state-to-state transition rates

The fluorescence rate for a transition of an electron from the $n_j l_j$ subshell to a hole in the lower-lying $n_h l_h$ subshell can be calculated in a similar way as the photoionization cross section [30,31,68]. Accordingly, the individual state-to-state fluorescence rate associated with a transition from the initial zeroth-order *LS* eigenstate $|L_i S_i M_{L_i} M_{S_i}\rangle$ to an accessible final target state $|L_f S_f M_{L_f} M_{S_f}\rangle$ may be written as

$$\Gamma^{M_{L_i};M_{L_f}}_{^{2S_i+1}L_i;\,^{2S_f+1}L_f}(n_j l_j, n_h l_h) = \frac{4 l_>}{3(2l_h+1)}\alpha^3 (E_{L_i S_i} - E_{L_f S_f})(\varepsilon_{n_h l_h} - \varepsilon_{n_j l_j})^2 \left|\int_0^\infty dr u^*_{n_h l_h}(r) r u_{n_j l_j}(r)\right|^2 \times \left|\sum_{h,j} C(1,l_j,l_h;M_{L_f}-M_{L_i},m_{l_j},m_{l_h})\left\langle L_f S_f M_{L_f} S_f\middle|\hat{c}^\dagger_h \hat{c}_j\middle|L_i S_i M_{L_i} S_i\right\rangle\right|^2. \tag{13}$$

Here, $l_> = \max(l_j, l_h)$. The indices j and h of the solely initially or, respectively, finally occupied bound spin orbitals (between which the electron is transferred) refer to the set of quantum numbers $(n_j, l_j, m_{l_j}, m_{s_j})$ and $(n_h, l_h, m_{l_h} = M_{L_f} - M_{L_i} + m_{l_j}, m_{s_h} = m_{s_j})$. We note that the total projections M_{L_i} and M_{L_f} determine the relation between m_{l_j} and m_{l_h} only, but not their values. Consequently, it is necessary to include in Eq. (13) a summation over all possible spin orbitals that are only occupied in the initial or the final state, respectively. Since the interaction Hamiltonian [30] does not affect the spin and its projection, and $M_{S_i} = M_{S_f}$ due to the selection rules, the transition rate is independent of the initial and final spin projection.

Another transition rate of interest is the Auger-Meitner decay rate that two electrons in the $n_j l_j$ and $n_{j'} l_{j'}$ subshells undergo transitions: one into a hole in the lower-lying $n_h l_h$ subshell and the other into the continuum. Since this process occurs via the electron-electron interaction, its transition rate

can be obtained by employing the first-order time-dependent perturbation theory with the interaction Hamiltonian given by Eq. (6) [30,69]. Accordingly, the individual state-to-state Auger-Meitner decay rate may be written as

$$\Gamma^{M_{L_i};M_{L_f}}_{^{2S_i+1}L_i;^{2S_f+1}L_f}(n_j l_j, n_{j'} l_{j'}, n_h l_h) = 2\pi \sum_{l_a}\sum_{M_{S_f}} \left| \sum_{h,j,j'} [v_{ahjj'} - v_{ahj'j}] \langle L_f S_f M_{L_f} M_{S_f} | \hat{c}^\dagger_h \hat{c}_{j'} \hat{c}_j | L_i S_i M_{L_i} S_i \rangle \right|^2, \tag{14}$$

where $v_{ahjj'}$ and $v_{ahj'j}$ are both two-electron Coulomb matrix elements given by Eq. (8). Here, the index a refers to the quantum numbers of the Auger electron, i.e., $(\varepsilon_a = E_{L_i S_i} - E_{L_f S_f}, l_a, M_{L_i} - M_{L_f}, M_{S_i} - M_{S_f})$. The sum over l_a is restricted by $|L_f - L_i| \leqslant l_a \leqslant \min(l_h + l_j + l_{j'}, L_f + L_i)$. The indices j, j', and h denote the involved spin orbitals in the corresponding $n_j l_j$, $n_{j'} l_{j'}$, and $n_h l_h$ subshells, respectively. However, it is necessary to include in Eq. (14) a summation over all possible spin orbitals that are either only occupied in the initial or the final state because the projection quantum numbers of these orbitals are not completely definite. Additionally, including a summation over the final spin projection M_{S_f} provides a transition rate that is independent of the initial spin projection.

E. Alignment parameter and ratios

We briefly introduce a few basic quantities that we employ for the investigation of orbital alignment. The alignment parameter [40–42] offers a measure of the alignment of a final ion with definite angular momentum L_f due to different projections M_{L_f}. Recall that there is no coupling to the spin for the employed interaction Hamiltonians [30] and, thus, no alignment with respect to M_{S_f}. Therefore, in what follows, we neglect the spin S_f and its projection M_{S_f}, i.e., in this section, $|L_f M_{L_f}\rangle$ refers to a final zeroth-order LS eigenstate, a sum over accessible M_{S_f} included as in Eqs. (12) and (14). Here, we briefly define the alignment parameter in our context. Further discussions and applications of the alignment and orientation parameters can be found in Refs. [40–42].

Let us start with the density matrix for the L_f under investigation [40,41],

$$\hat{\rho} = \sum_{M_{L_f}} p(M_{L_f}|L_f) |L_f M_{L_f}\rangle\langle L_f M_{L_f}|. \tag{15}$$

Here, $p(M_{L_f}|L_f)$ is the conditional population probability of the final state with projection M_{L_f} for a given L_f. For single photoionization, this probability is given by $p(M_{L_f}|L_f) = \sigma^{M_{L_i};M_{L_f}}_{^{2S_i+1}L_i;^{2S_f+1}L_f} / \sum_{M_{L_f}} \sigma^{M_{L_i};M_{L_f}}_{^{2S_i+1}L_i;^{2S_f+1}L_f}$ for an S_f and an initial state. Similarly, the population probability can be obtained for the decay processes via the transition rates in Eqs. (13) and (14). As a next step, we decompose $\hat{\rho}$ in terms of irreducible spherical tensor operators [41,72],

$$\hat{T}_{JM} = \sum_{M_{L_f}, M'_{L_f}} (-1)^{L_f - M'_{L_f}} C(L_f, L_f, J; M_{L_f}, -M'_{L_f}, M) \times |L_f M_{L_f}\rangle\langle L_f M'_{L_f}|. \tag{16}$$

Thus, we may write

$$\hat{\rho} = \sum_{J,M} \rho_{JM} \hat{T}_{JM}, \tag{17}$$

where the expansion coefficients ρ_{JM} are given by [40]

$$\rho_{JM} = \sum_{M_{L_f}} (-1)^{L_f - M_{L_f}} p(M_{L_f}|L_f) \times C(L_f, L_f, J; M_{L_f}, -M_{L_f}, M). \tag{18}$$

Note that these coefficients are only nonzero for $M = 0$. In the case of $p(-M_{L_f}|L_f) = p(M_{L_f}|L_f)$, ρ_{J0} vanishes for odd J owing to the properties of the Clebsch-Gordan coefficient [65]. Since there is no preference for $\pm M_{L_f}$ in the interaction with linearly polarized light, i.e., $p(-M_{L_f}|L_f) = p(M_{L_f}|L_f)$, ρ_{10} is always zero. Thus, the orientation parameter, defined by $\mathcal{O}_{10} = \rho_{10}/\rho_{00}$ [42], is zero and no orientation is created by the interaction with linearly polarized light.

The coefficients ρ_{J0} are also known as statistical tensors, and they define the alignment parameter as follows [42]:

$$\mathcal{A}_{20}(L_f) = \rho_{20}/\rho_{00} = \sqrt{\frac{5}{(2L_f+3)(L_f+1)L_f(2L_f-1)}} \times \sum_{M_{L_f}} \left[3M^2_{L_f} - L_f(L_f+1)\right] p(M_{L_f}|L_f). \tag{19}$$

To obtain the second line of Eq. (19), we have utilized the formula for the Clebsch-Gordan coefficients given in Ref. [65]. Note that $\mathcal{A}_{20}$ is positive (negative) when states with larger (smaller) $|M_{L_f}|$ are more likely populated than the others. For a uniform distribution, $\mathcal{A}_{20} = 0$ (no alignment), while the larger $|\mathcal{A}_{20}|$ the stronger the alignment.

In general, an ion produced by photoionization can have different L_f, but the alignment parameter can only capture one L_f. Thus, if we are interested in the distribution of all possible final states, then another quantity of interest is the ratio of individual (state-resolved) cross sections,

$$\sigma^{M_{L_i};M_{L_f}}_{^{2S_i+1}L_i;^{2S_f+1}L_f}(nl, \omega_{\rm in}) / \sigma^{M_{L_i}}_{^{2S_i+1}L_i}(nl, \omega_{\rm in}). \tag{20}$$

This provides direct information about the probability to find the ion produced in the final $^{2S_f+1}L_f$ state with projection M_{L_f}, when the atom or ion is initially in the $^{2S_i+1}L_i$ state with projection M_{L_i} and when the nl subshell is ionized. Here, $\sigma^{M_{L_i}}_{^{2S_i+1}L_i}(nl, \omega_{\rm in})$ is the subshell cross section of the nl subshell restricted to the initial state in question, summing over all possible final states. We do not distinguish between states with different spin projection as the cross sections are independent

of it. Moreover, replacing the cross sections in Eq. (20) by the corresponding transition rates [Eqs. (13) and (14)] delivers ratios of individual transition rates.

III. VALIDATION

Having discussed the basic formalism underlying our implementation in XATOM, we next proceed to explore transition energies and photoionization cross sections for explicit electronic configurations and to compare the results with experimental measurements. In particular, we employ two different theoretical strategies for describing physical processes. In the zeroth-order strategy, transition energies are computed based on zeroth-order energies for the initial and final states. The zeroth-order energies are the sum of orbital energies according to the initial or final electronic configuration [Eq. (10)]. On the other side, in the first-order strategy, transition energies are computed based on the first-order-corrected energies E_{LS} for the initial and final states (see Sec. II B). For both strategies, energies and radial integrals are calculated with orbitals and orbital energies optimized for the initial configuration only. The usage of the same set of orbitals for both the initial and final configurations avoids issues with orbital nonorthogonality [73–75]. Moreover, it should be mentioned that we still perform zeroth-order calculations using the original version of XATOM, whereas for the first-order calculations, we employ the present implementation.

Orbitals and orbital energies are numerically solved on a radial grid employed by XATOM (see Refs. [35,47] for details), based on the HFS potential [Eq. (3)] including the latter tail correction [76]. In what follows, the bound states are computed using the generalized pseudospectral method [77,78] on a nonuniform grid with 200 grid points and a maximum radius of 50 a.u. The continuum states are computed using the fourth-order Runge-Kutta method on a uniform grid [79,80] with a grid size of 0.005 a.u., employing the same potential as used in the bound-state calculation. It has been demonstrated that the cross sections and rates calculated using XATOM (zeroth-order strategy) show good agreement with the available experimental data and other calculations [35,53,54].

A. Transition energies for neon

First, the $K\alpha$ fluorescence energy and all KLL Auger-electron energies are examined for an initial Ne^+ ion with a K-shell vacancy ($1s^{-1}\ ^2S$). The results are presented in Fig. 1. It is apparent from the data that the first-order strategy is in reasonable agreement with the experimental $K\alpha$ fluorescence energy [81,82] and the KLL Auger-Meitner electron energies [83], to within less than 2%. In contrast, the energies obtained via the zeroth-order strategy differ significantly from the experimental values. These findings indicate that the first-order strategy, contained in our implementation, is the better strategy for describing the transition energy. The small difference between experiment and theory still remaining for the first-order calculation might be attributed to the use of the same set of initial and final orbitals, the neglect of higher-order terms, and relativistic effects. We remark that no value is shown for the final state of $2p^{-2}\ ^3P$ in Fig. 1 because this transition is forbidden on account of parity [30,84].

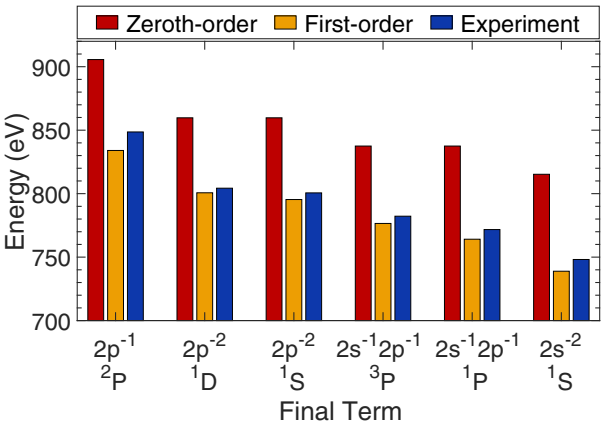

FIG. 1. Comparison of experimental $K\alpha$ fluorescence energy [81,82] and KLL Auger-electron energies [83] for neon with two theoretical strategies (see legend). The different lines are labeled by the final open subshell(s) (first line) and by the final term symbol (second line). In all cases, the Ne^+ ion is initially in the $1s^{-1}\ ^2S$ state.

B. Photoionization cross sections for argon

As a next example, we examine photoionization of a neutral argon atom ($1s^2 2s^2 2p^6 3s^2 3p^6$) in the region of the thresholds. Figure 2 shows the total photoionization cross section as a function of the photon energy in the (a) K-shell, (b) L-shell, and (c) M-shell threshold regions. The total cross sections, which are an incoherent sum over all individual

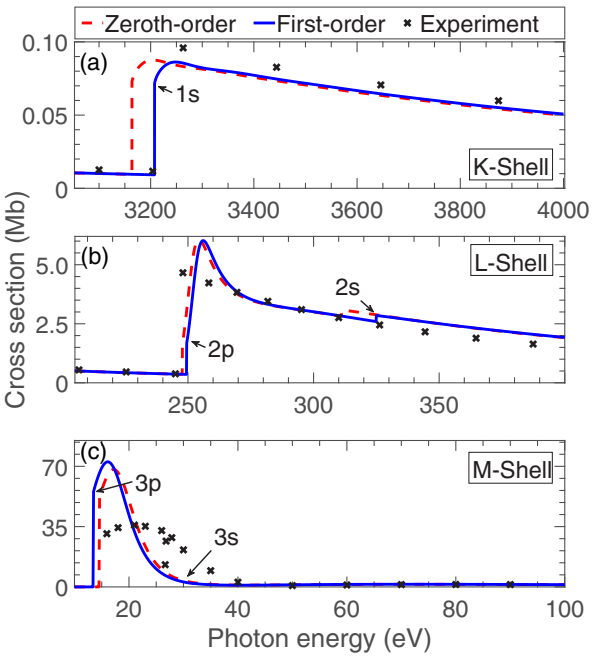

FIG. 2. Calculated total photoionization cross section, in Mb, of neutral argon as a function of the photon energy, in eV. Results for both the first-order strategy (solid blue line) and the zeroth-order strategy (dashed red line) are compared to experimental data (black crosses) reported in Ref. [85] for the K- and L-shell thresholds and Ref. [86] for the M-shell threshold.

state-to-state cross sections in Eq. (12), are depicted. Interestingly, with regard to the cross section, both the first-order and zeroth-order strategies behave very similarly, if one ignores the shift due to different threshold energies. In general, both are in acceptable agreement with the experimental values around the K- and L-shell thresholds [85] and the M-shell threshold [86], often to within less than 10%. However, especially at the L- and M-shell thresholds, the calculated cross sections are significantly higher than the experimental values (more than 50% between the $3p$ and $3s$ thresholds and ∼25% at the $2p$ and $2s$ thresholds). This observed disagreement and the lack of improvement concerning the first-order strategy mainly stem from the use of zeroth-order states in both strategies. In the present framework, first-order-corrected energies but only zeroth-order eigenstates are calculated (see Sec. II B). If the first-order states were used, it would be possible to capture a part of the interchannel coupling [87], since the first-order states are a mixture of the zeroth-order states from different electronic configurations [60]. Moreover, it should be mentioned that the experimental results in Fig. 2(c) contain resonances between the $3p$ and the $3s$ thresholds [86], but the theoretical calculations do not.

Even though our implementation only leads to an improvement on the transition energy but not on the cross section, it has the following major advantage with respect to the original version of XATOM: With the help of the zeroth-order LS eigenstates, the present implementation is capable to provide individual state-to-state cross sections and transition rates (see Secs. II C and II D), thus allowing us to study orbital alignment (see next section).

IV. RESULTS AND DISCUSSION

We employ the individual state-to-state cross sections provided by our implementation to explore orbital alignment induced by linearly polarized x rays. In particular, we consider the distribution of the states belonging to the ions produced by photoionization. As a first example, we discuss photoionization of the neutral argon atom that is initially in a closed-shell configuration. Having at hand the results for neutral argon, we then generalize them to some argon charge states in open-shell configurations. These ions can appear in the x-ray multiphoton ionization of neutral argon driven by an intense XFEL pulse.

Before starting, however, the following should be pointed out. In what follows, we focus on the photoionization of an electron in a specific subshell of $2p$ or $3p$ ($l = 1$) without any interaction between the subshells (interchannel coupling). This is because (i) ionization of the subshell with $l = 0$ always completely aligns the remaining ion since only the final state with $M_{L_f} = M_{L_i}$ is allowed and (ii) binding energies differ enough to neglect the interaction [88]. Furthermore, we focus on a specific initial zeroth-order LS eigenstate. However, for $M_{L_i} \neq 0$, we will consider a uniform distribution of initial states with $\pm M_{L_i}$, denoted in the following by $|M_{L_i}|$. This prevents an orientation of the final ion, which would be simply caused by a prior orientation of the initial ion. Therefore, the population probabilities of the final ion are identical for $\pm M_{L_f}$, i.e., $p(-M_{L_f}|L_f) = p(M_{L_f}|L_f)$. This is because Eqs. (12)–(14) are identical for a transition from M_{L_i} to $\pm M_{L_f}$ and $-M_{L_i}$ to $\mp M_{L_f}$. So there is no orientation (see Sec. II E) and we can investigate the $\pm M_{L_f}$ cases together (without summing over both signs).

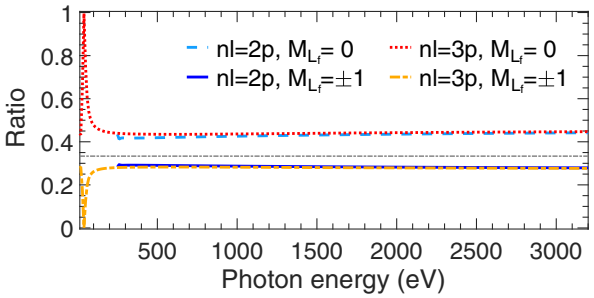

FIG. 3. Ratio of individual cross sections $\sigma^{0;M_{L_f}}_{^1S;^2P}/\sigma^0_{^1S}$ for neutral argon as a function of the photon energy from the $3p$ threshold (≈13.46 eV) to the $1s$ threshold (≈3207.51 eV). Results for different M_{L_f} for both ionizations of the $2p$ and $3p$ subshells are shown (see legend). The gray line at 1/3 indicates the case of a uniform distribution of M_{L_f}. In all cases, the atom is initially in the ^1S state with $M_{L_i} = 0$ and the final Ar^+ ion is in one of the ^2P states.

A. Orbital alignment after ionization of neutral Ar

We first investigate the orbital alignment of the Ar^+ ion following the photoionization of the $2p$ or $3p$ subshell of neutral argon ($1s^2 2s^2 2p^6 3s^2 3p^6$) by linearly polarized x rays. The calculated ratios of individual cross sections $\sigma^{0;M_{L_f}}_{^1S;^2P}/\sigma^0_{^1S}$ [Eq. (20)] are presented in Fig. 3 for all possible M_{L_f} as a function of the photon energy. Additionally, calculated alignment parameters $\mathcal{A}_{20}(P)$ [Eq. (19)] are listed in Table I for various photon energies. For initially neutral argon, $\mathcal{A}_{20}(P)$ can be directly obtained from the ratios in Fig. 3, i.e., $\mathcal{A}_{20}(P) = \sqrt{2}[\sigma^{0;1}_{^1S;^2P}/\sigma^0_{^1S} - \sigma^{0;0}_{^1S;^2P}/\sigma^0_{^1S}]$. As can be seen, in the x-ray regime, where the photon energy is greater than ∼300 eV, the resulting Ar^+ ion ($2p^{-1}$ or $3p^{-1}$) exhibits a clear orbital alignment (i.e., $\mathcal{A}_{20} < 0$), but it is not an extremely strong orbital alignment (i.e., $\mathcal{A}_{20}$ is close to zero). It increases only marginally with the photon energy and is a little stronger for the $3p$ subshell than for the $2p$ subshell. As a consequence of the alignment, almost 45% of the Ar^+ ions produced have an angular momentum projection of $M_{L_f} = 0$, while the others

TABLE I. Alignment parameter $\mathcal{A}_{20}(P)$ of the final Ar^+ ion after ionization of neutral Ar. Results for both ionizations of the $2p$ and $3p$ subshell of neutral argon are listed for various photon energies. For comparison, note that a complete alignment with respect to $M_{L_f} = 0$ would yield a value of $\mathcal{A}_{20}(P) = -\sqrt{2}$.

nl	ω_{in} (eV)	$\mathcal{A}_{20}(P)$
$3p$	40	−1.406
$2p$	300	−0.178
$3p$	300	−0.221
$2p$	1000	−0.196
$3p$	1000	−0.218
$2p$	3000	−0.228
$3p$	3000	−0.240

TABLE II. Radial integrals $|R_{\varepsilon_c 0;n1}|$ and $|R_{\varepsilon_c 2;n1}|$ as well as their ratio for various photon energies for neutral argon.

nl	$\omega_{\rm in}$ (eV)	$A = \lvert R_{\varepsilon_c 0;n1}\rvert$	$B = \lvert R_{\varepsilon_c 2;n1}\rvert$	$(A/B)^2$
$3p$	40	2.99×10^{-1}	0.71×10^{-1}	302.00
$2p$	300	0.37×10^{-1}	1.51×10^{-1}	0.06
$3p$	300	1.40×10^{-2}	3.84×10^{-2}	0.13
$2p$	1000	0.54×10^{-2}	1.81×10^{-2}	0.09
$3p$	1000	1.75×10^{-3}	4.89×10^{-3}	0.13
$2p$	3000	0.71×10^{-3}	1.85×10^{-3}	0.15
$3p$	3000	2.18×10^{-4}	5.34×10^{-4}	0.17

have $M_{L_f} = \pm 1$ with a probability of 28% for each M_{L_f} (see Fig. 3).

There are two explanations for the observed alignment. First, due to the angular momentum coupling of the photoelectron and the involved final hole for incoming radiation linearly polarized along the z axis [68,69], the ejection of an electron with $m_{l_j} = \pm 1$ is less likely than with $m_{l_j} = 0$. Hence, a transition with $M_{L_i} - M_{L_f} = m_{l_j} = \pm 1$ is less likely than one with $M_{L_i} = M_{L_f}$. In particular, ratios of individual cross sections differ by a value of 0.1. This value can be obtained from an explicit calculation of Clebsch-Gordan coefficients in Eq. (12) and is, evidently, independent of the photon energy. Second, the remaining alignment can be explained as follows. Owing to the selection rules for a dipole transition [68], the photoelectron can have two possible angular momentum quantum numbers, $l_c = l \pm 1$. In the calculation of cross sections, l_c is summed over both [see Eq. (12)]. However, for $M_{L_i} - M_{L_f} = \pm 1$ and $l = 1$, the former is forbidden as $l_c = 0 < |M_{L_i} - M_{L_f}|$, so only $l_c = 2$ contributes to the cross section. Consequently, when $M_{L_i} = 0$, the cross section for $M_{L_f} = \pm 1$ (only $l_c = 2$ contributes) is smaller than that for $M_{L_f} = 0$ (both $l_c = 0$ and $l_c = 2$ contribute). This effect becomes larger as the $l_c = 0$ contribution of the photoelectron increases. From Eq. (12), we can conclude that the amount of this reduction depends on the ratio of radial integrals $|R_{\varepsilon_c 0;n1}|^2/|R_{\varepsilon_c 2;n1}|^2$, where

$$R_{\varepsilon_c l_c;nl} = \int_0^\infty dr u^*_{\varepsilon_c l_c}(r) r u_{nl}(r). \tag{21}$$

For the initial neutral argon, the ratios of the radial integrals are shown in Table II. In the x-ray regime ($\omega_{\rm in} \gtrsim 300$ eV), the ratio of radial integrals is quite small. Therefore, cross sections for $M_{L_f} = \pm 1$ are reduced by the ratio of radial integrals only a little and, thus, the alignment is not extremely strong, as shown in Table I. Also worthy of note is that the marginal increase of the alignment with the photon energy can be attributed to the ratio of radial integrals as well. In contrast, below the x-ray regime at roughly 40 eV, an opposite situation can be discovered, as shown in Fig. 3, Table I, and Table II. Photoionization of the $3p$ subshell by a linearly polarized photon with around 40 eV predominantly produces an ion with $M_{L_f} = 0$ (i.e., $\mathcal{A}_{20} \sim -\sqrt{2}$).

B. Orbital alignment after $2p$ ionization of Ar^+ ($2p^{-1}$)

Next we proceed to investigate orbital alignment after ionization of the initially open-shell configuration of Ar^+ ($1s^2 2s^2 2p^5 3s^2 3p^6$). Here we are considering only $2p^{-1}$ for Ar^+ because (i) the partial cross section of $3p$ of neutral Ar is much smaller than that of $2p$, when the photon energy is greater than the $2p$ threshold, and (ii) fluorescence processes that can also produce a hole in the $3p$ subshell are very slow (∼2000 fs lifetime) compared to the pulse durations of XFELs (a few fs). Therefore, Ar^+ ions are barely found in the configuration $1s^2 2s^2 2p^6 3s^2 3p^5$ during interaction with XFEL pulses. Likewise, we will focus on $2p$ ionization of Ar^+ ($2p^{-1}$) in the following discussion because of the low cross section of the $3p$ subshell.

TABLE III. Alignment parameter $\mathcal{A}_{20}(P)$ and $\mathcal{A}_{20}(D)$ of the final Ar^{2+} ion ($2p^{-2}$) after $2p$ ionization of Ar^+ ($2p^{-1}\ ^2P$). Results for different $|M_{L_i}|$ are listed at a photon energy of 1000 and 3000 eV.

$\omega_{\rm in}$ (eV)	$\lvert M_{L_i}\rvert$	$\mathcal{A}_{20}(P)$	$\mathcal{A}_{20}(D)$
1000	0	0.707	−0.895
1000	1	−0.147	0.290
3000	0	0.707	−0.904
3000	1	−0.115	0.268

To explore the orbital alignment of the final Ar^{2+} ($2p^{-2}$) that is produced by the photoionization of the $2p$ subshell of Ar^+, we calculate the alignment parameters $\mathcal{A}_{20}(P)$ and $\mathcal{A}_{20}(D)$ as well as the ratios of individual cross sections $\sigma^{|M_{L_i}|;M_{L_f}}_{2P;^{2S_f+1}L_f}/\sigma^{|M_{L_i}|}_{2P}$, i.e., $\frac{1}{2}[\sigma^{+M_{L_i};M_{L_f}}_{2P;^{2S_f+1}L_f}/\sigma^{+M_{L_i}}_{2P} + \sigma^{-M_{L_i};M_{L_f}}_{2P;^{2S_f+1}L_f}/\sigma^{-M_{L_i}}_{2P}]$ for $M_{L_i} \neq 0$. As observed above for neutral argon, we expect for the orbital alignment of initial Ar^+ ions a similar, very small, and smooth change with the energy of the x-ray photons. The alignment parameters are listed at a photon energy of 1000 and 3000 eV in Table III. $A_{20}(P)$ and $A_{20}(D)$ are similar for both photon energies. For this reason, we restrict ourselves here to only the analysis of a photon energy of 1000 eV in Fig. 4, where the ratio of individual cross sections is depicted for all possible initial states. The sum of the bars for each panel in Fig. 4, after taking into account a factor of 2 for $\pm M_{L_f}$, is equal to one. Note that the alignment parameters in Table III can be obtained from the relation between the bars belonging to a final term.

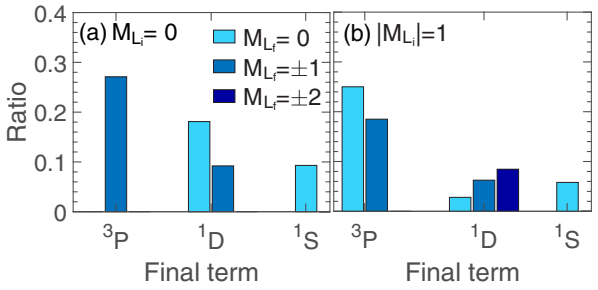

FIG. 4. Ratio of individual cross sections $\sigma^{|M_{L_i}|;M_{L_f}}_{2P;^{2S_f+1}L_f}/\sigma^{|M_{L_i}|}_{2P}$ for Ar^+ ($2p^{-1}$) at a photon energy of 1000 eV (a) for $M_{L_i} = 0$ and (b) for $|M_{L_i}| = 1$ (i.e., uniform distribution of $M_{L_i} = \pm 1$). Results for different final terms and different M_{L_f} are shown. In all cases, the atom initially is in a ^2P state and the subshell being ionized is $2p$.

Combining the findings in Fig. 4(a) and Table III, we observe for $M_{L_i} = 0$ that the majority of Ar^{2+} ions produced are in the ^3P state (∼54% uniformly distributed between $M_{L_f} = +1$ and $M_{L_f} = -1$), which is completely aligned [i.e., $\mathcal{A}_{20}(P) = 1/\sqrt{2}$]. This alignment is simply caused by the selection rules for photoionization, where a transition to $M_{L_f} = 0$ is forbidden. In particular, if $L_i + L_f + l$ is an odd number and $M_{L_i} = 0$, then only $M_{L_f} \neq 0$ is allowed. Next, most probably, is the production of ions in the ^1D state (∼37%), whereas there is only a probability of less than 10% to find the final ion in the unaligned ^1S state [always $\mathcal{A}_{20}(S) = 0$]. Note that also within the ^1D term, there is orbital alignment [i.e., $\mathcal{A}_{20}(D) < 0$]: It is twice as likely to find the state with $M_{L_f} = 0$ than those with $M_{L_f} = \pm 1$, and $M_{L_f} = \pm 2$ is forbidden by the selection rules. Thus, it is very likely to observe an alignment of the final ion, either in a ^3P or ^1D state.

Let us now discuss the outcome for $|M_{L_i}| = 1$ in Fig. 4(b) and Table III. Again the majority of Ar^{2+} ions produced are in one of the ^3P states (∼62%). However, in contrast to $M_{L_i} = 0$, here the ^3P states exhibit only a weak alignment that is comparable to that for the residual Ar^+ discussed in Sec. IV A, but a little weaker. Worthy of note is also the alignment of the final ^1D state attributed to a larger population of states with $M_{L_f} = \pm 2$ than for smaller M_{L_f} [for comparison, a complete alignment with respect to $M_{L_f} = \pm 2$ has $\mathcal{A}_{20}(D) = 2\sqrt{5/14}$].

Although most of the observations are related to angular momentum coupling, it is worthwhile to explain them explicitly with respect to the formula of the individual cross section [Eq. (12)]. A detailed understanding might be useful in a future study of alignment during multiphoton ionization, which cannot be simply explained analytically by angular momentum coupling. The observations can be explained by a combination of the subsequent aspects.

First, in the computation of individual cross sections [Eq. (12)], we sum over all accessible final spin projections, i.e., M_{S_f}. Owing to the selection rules, i.e., $|M_{S_i} - M_{S_f}| \stackrel{!}{=} \frac{1}{2}$, for the final terms with $S_f = S_i + \frac{1}{2}$, two final states ($M_{S_f} = S_i \pm \frac{1}{2}$) are involved in the transition. In contrast, for the final terms with $S_f = S_i - \frac{1}{2}$, only one final state ($M_{S_f} = S_i - \frac{1}{2}$) is allowed. As a consequence, the states for the former terms tend to have higher cross sections. It is because the cross section is independent of the initial spin projection that this argument is true for general initial states. Therefore, we conclude that final states with $S_f = S_i + \frac{1}{2}$ are generally more probable than those with $S_f = S_i - \frac{1}{2}$. This explains why transitions to the final ^3P states of Ar^{2+} are so dominant.

Second, if not forbidden, transitions preserving the angular momentum projection, i.e., $M_{L_f} = M_{L_i}$, are generally preferred, while those changing it by one are suppressed. This is attributed to the fact that the incoming x rays are linearly polarized (see Sec. IV A). It explains, for instance, why final ^1S states are a little more likely for $M_{L_i} = 0$ than for $M_{L_i} = \pm 1$. It also explains the alignment of the ^3P states for $|M_{L_i}| = 1$ and that of the ^1D states for $M_{L_i} = 0$.

However, it does not explain the alignment of the ^1D states for $|M_{L_i}| = 1$ or, more precisely, why the states with $M_{L_f} = \pm 2$ are more probable than the other ^1D states. This can be explained by the square of the overlap matrix element, $\langle L_f S_f M_{L_f} M_{S_f} | \hat{c}_j | L_i S_i M_{L_i} S_i \rangle$, also contained in the formula for the individual cross section in Eq. (12). Thus, the third point is that this overlap matrix element additionally affects the orbital alignment. Obviously, a transition with a higher overlap matrix element is more likely than that with a smaller overlap matrix element. Hence, the ratio of individual cross sections corresponding to the transition, being more probable, is enhanced. Therefore, transitions that do not preserve the angular momentum projection can be preferred when they exhibit very high overlap matrix elements. Regarding the final term ^1D, the final states with $M_{L_f} = \pm 2$ are pure Fock states and so is the initial ^2P state. When the transition is not forbidden, for pure Fock states, the matrix element $\langle L_f S_f M_{L_f} M_{S_f} | \hat{c}_j | L_i S_i M_{L_i} S_i \rangle$ is evidently unity (maximal possible value). Thus, this transition is quite dominant. On the other hand, the alignment related to the previously mentioned point can be enhanced, when overlap matrix elements are higher for transitions with $M_{L_f} = M_{L_i}$ than for the others. Note that this is the case for a transition from the initial state with $M_{L_i} = 0$ to the final ^1D states. In this context, it is worth mentioning that for neutral argon (Sec. IV A), the overlap matrix element is always unity because all involved states are pure Fock states.

Finally, some transitions are directly forbidden by the selection rules for photoionization (given in the middle of this section). This is another important, but trivial reason for the orbital alignment.

TABLE IV. Alignment parameter $\mathcal{A}_{20}(P)$ and $\mathcal{A}_{20}(D)$ of the final Ar^{3+} ion ($2p^{-3}$) after $2p$ ionization of Ar^{2+} ($2p^{-2}$). Results for different initial states are listed at a photon energy of 1000 and 3000 eV.

ω_{in} (eV)	$^{2S_i+1}L_i$	$\lvert M_{L_i}\rvert$	$\mathcal{A}_{20}(P)$	$\mathcal{A}_{20}(D)$
1000	^3P	0	0.707	−0.895
1000	^3P	1	−0.148	0.290
1000	^1D	0	−0.879	−0.598
1000	^1D	1	−0.148	−0.321
1000	^1D	2	0.707	0.743
1000	^1S	0	−0.196	
3000	^3P	0	0.707	−0.904
3000	^3P	1	−0.114	0.267
3000	^1D	0	−0.905	−0.598
3000	^1D	1	−0.114	−0.325
3000	^1D	2	0.707	0.765
3000	^1S	0	−0.230	

C. Orbital alignment after $2p$ ionization of Ar^{2+} ($2p^{-2}$)

In order to complete our understanding of orbital alignment, we finally investigate photoionization of Ar^{2+} ($1s^2 2s^2 2p^4 3s^2 3p^6$) as another example of an initial open-shell configuration. For the reasons explained in Sec. IV B, the focus is again on the photoionization of the $2p$ subshell. To characterize the orbital alignment of the final Ar^{3+} ($2p^{-3}$), we show calculated alignment parameters $\mathcal{A}_{20}(P)$ and $\mathcal{A}_{20}(D)$ in Table IV (at photon energies of 1000 and 3000 eV) and ratios of individual cross sections $\sigma^{|M_{L_i}|;M_{L_f}}_{^{2S_i+1}L_i;^{2S_f+1}L_f} / \sigma^{|M_{L_i}|}_{^{2S_i+1}L_i}$ in Fig. 5 (at 1000 eV only). It becomes evident that the degree of

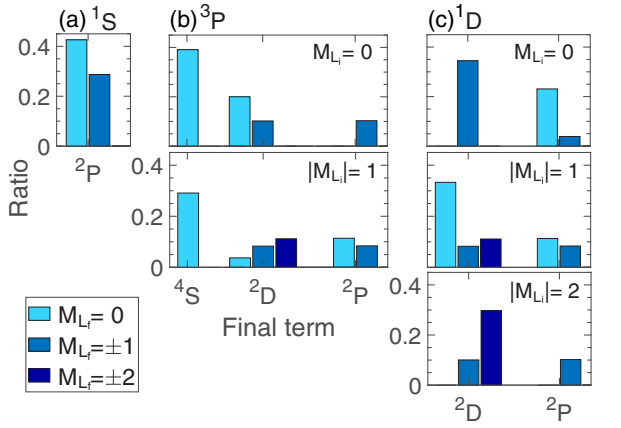

FIG. 5. Ratio of individual cross sections $\sigma^{|M_{L_i}|;M_{L_f}}_{2S_i+1L_i;^{2S_f+1}L_f}/\sigma^{|M_{L_i}|}_{2S_i+1L_i}$ for Ar^{2+} $(2p^{-2})$ at a photon energy of 1000 eV. The atom is initially in (a) the ^1S state with $M_{L_i} = 0$, (b) one of the ^3P states, or (c) one of the ^1D states. Results for different $|M_{L_i}|$ (i.e., uniform distribution of $\pm M_{L_i}$), different final terms, and different M_{L_f} are shown. In all cases, the subshell being ionized is $2p$.

alignment for the produced Ar^{3+} ions is comparable with that observed in the previous cases. Above all, the observations for the final Ar^{3+} ions can be explained by the same arguments as provided for the final Ar^{2+} ions in Sec. IV B.

Nonetheless, three things should be pointed out. First, for the initial ^3P states of Ar^{2+}, the most probable final state of Ar^{3+} is the unaligned ^4S state (∼40% for $M_{L_i} = 0$ and ∼30% for $|M_{L_i}| = 1$), as shown in Fig. 5(b). As argued in the first point in Sec. IV B, it is because of the spin quantum number being the highest for the final ^4S state that this state becomes dominant here. Second, for the initial ^1D state with $|M_{L_i}| = 2$, more than half of the resulting Ar^{3+} ions retain the angular momentum quantum number and its projection, i.e., $L_f = 2$ and $M_{L_f} = \pm 2$, as depicted in Fig. 5(c). This leads to a comparably strong alignment of the ^2D states [see Table IV and compare with $\mathcal{A}_{20}(D) = 2\sqrt{5/14}$ for a complete alignment with respect to $M_{L_f} = \pm 2$]. This alignment stems from the facts that $M_{L_f} = M_{L_i}$ transitions are preferred (Sec. IV A) and the overlap matrix element takes on the highest possible value for pure Fock states (see the third point in Sec. IV B). Third, also note the comparably high alignment of the ^2P state for initial ^1D states with $M_{L_i} = 0$ [compare with $\mathcal{A}_{20}(P) = -\sqrt{2}$ for a complete alignment with respect to $M_{L_f} = 0$]. This can be explained by the same arguments as provided for the ^2D states. In particular, here the overlap matrix element for $M_{L_f} = 0$ is two times that for $M_{L_f} = \pm 1$. Another important remark here is that for initial states with equal L_i and M_{L_i}, the alignment of the final states is almost independent of the charge state of argon and of the spin multiplicity of the initial and final states. This can be seen by comparing the alignment parameters given in Tables I, III, and IV. All this is closely related to the fact that alignment mainly depends on angular momentum coupling and that ratios of radial integrals, which additionally affect the alignment, are very similar for all charge states of argon (not shown here for brevity).

TABLE V. Alignment parameter $\mathcal{A}_{20}(P)$ and $\mathcal{A}_{20}(D)$ of the final Ar^{2+} ion $(3p^{-2})$ after $L_{23}M_{23}M_{23}$ Auger-Meitner decay of Ar^+ $(2p^{-1}\ ^2P)$. Results for different $|M_{L_i}|$ are listed.

$\lvert M_{L_i}\rvert$	$\mathcal{A}_{20}(P)$	$\mathcal{A}_{20}(D)$
0	0.707	−0.770
1	−0.354	0.385

D. Orbital alignment after Auger-Meitner decay of Ar^+ $(2p^{-1})$

We would like to point out that the lifetime of the $2p$ hole in Ar^+ $(2p^{-1})$ is about 3.9 fs, that of the $2p^2$ hole in Ar^{2+} $(2p^{-2})$ is about 1.6 fs, and that of the $2p^3$ hole in Ar^{3+} $(2p^{-3})$ is only about 0.9 fs (calculated with the first-order strategy). Therefore, it is likely that the transient hole states produced by photoionization undergo an Auger-Meitner decay before further photoionization can occur, unless the x-ray intensity is extremely high. Note that decay also happens via fluorescence, but fluorescence rates are much smaller than Auger-Meitner decay rates for the argon ions. As a consequence, it is indispensable to involve Auger-Meitner decay processes in the studies of orbital alignment. This becomes especially important when investigating the orbital alignment dynamics of ions produced by x-ray multiphoton ionization.

Here we consider as an example the $L_{23}M_{23}M_{23}$ Auger-Meitner decay of Ar^+ $(2p^{-1})$, so the final configuration is Ar^{2+} $(3p^{-2})$. To explore the orbital alignment of the final Ar^{2+} $(3p^{-2})$, we calculate alignment parameters $\mathcal{A}_{20}(P)$ and $\mathcal{A}_{20}(D)$ via Eq. (19) in Table V and ratios of individual transition rates via Eq. (14) in Figs. 6(a) and 6(b). As can be seen, for a fixed initial state, i.e., only one $|M_{L_i}|$, Auger-Meitner decay leads to a clear alignment of the final Ar^{2+} ion. However, if the initial state has no alignment, i.e., a uniform distribution of M_{L_i}, then the weighted means of the ratios of individual transition rates are equal for all M_{L_f} belonging to a final term [see Fig. 6(c)]. Here, the weighted mean is the sum over the ratios of individual transition rates for all possible M_{L_i}, weighted by the population probability $p(M_{L_i}|L_i)$ of the initial state. Note that in the uniform case, $p(M_{L_i}|L_i)$ equals $1/(2L_i + 1)$. Consequently, the final Ar^{2+} ion produced by Auger-Meitner decay of an unaligned Ar^+ ion does not possess any alignment. We have $\mathcal{A}_{20}(P) = 0$ and $\mathcal{A}_{20}(D) = 0$ when taking the weighted mean of the alignment parameters given in Table V, a factor of 2 for $|M_{L_i}| = 1$ included. The reason for the zero alignment is the following. According to the Wigner-Eckhart theorem [66,67], the transition rate is independent of the angular momentum projection of the total initial and final electronic state, the Auger electron included. Thus, a sum over the individual transition rates in Eq. (14) is independent of the final projection M_{L_f} when it is uniformly summed over the initial projection M_{L_i}. Therefore, in general, the Auger-Meitner decay processes will not create any alignment of the final ion if it initially starts with zero alignment, i.e., a uniform distribution.

However, if the initial ion is already aligned, then the final ion produced by Auger-Meitner decay will show an alignment as demonstrated in the next section.

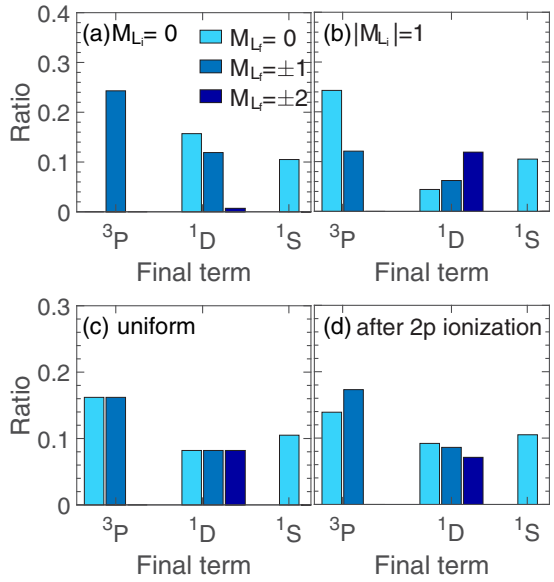

FIG. 6. Ratio of individual Auger-Meitner transition rates $\Gamma^{|M_{L_i}|;M_{L_f}}_{2_P;^{2S_f+1}L_f}/\Gamma^{|M_{L_i}|}_{2_P}$ for Ar^+ $(2p^{-1})$ (a) for $M_{L_i}=0$ and (b) for $|M_{L_i}|=1$ (i.e., uniform distribution of $M_{L_i}=\pm1$). The weighted mean of the ratios with respect to M_{L_i} is shown in (c) for a uniform distribution of M_{L_i} and in (d) for the distribution of M_{L_i} after $2p$ ionization of neutral argon at 1000 eV. Results for different final terms and different M_{L_f} are shown. In all cases, the atom initially is in a ^2P state and decays via $L_{23}M_{23}M_{23}$ Auger-Meitner decay.

E. Orbital alignment evolution in x-ray-induced ionization process

Let us finally discuss how the alignment evolves in a sequence comprising a photoionization event and an Auger-Meitner decay. We start with neutral argon $(1s^22s^22p^63s^23p^6)$ and ionize the $2p$ subshell as investigated in Sec. IV A. Then the produced Ar^+ ion $(2p^{-1})$ undergoes one $L_{23}M_{23}M_{23}$ Auger-Meitner decay. For a fixed initial state, i.e., $|M_{L_i}|$, and a uniform distribution, the corresponding alignment has been investigated in the previous section. Here, the population probability $p(M_{L_i}|L_i)$ of Ar^+ $(2p^{-1})$ before the Auger-Meitner decay is given by the ratios of individual cross sections for neutral argon in Fig. 3. To examine the alignment of the final Ar^{2+} ion $(3p^{-2})$ after the sequence of $2p$ photoionization and $L_{23}M_{23}M_{23}$ Auger-Meitner decay, the means of the ratios of individual transition rates are shown in Fig. 6(d) (at a photon energy of 1000 eV) and alignment parameters are shown in Table VI (for 300, 1000, and 3000 eV). Most importantly, we observe that the Ar^{2+} ion exhibits a slight alignment, which is much smaller than that for $M_{L_i}=0$ (see Table V). The reason for this is that the transiently Ar^+ ions produced by $2p$ photoionization also possess only a weak alignment (see Fig. 3 and Table I). Thus, they are close to the uniform distribution with zero alignment (see Sec. IV D). For increasing photon energies, this alignment after $2p$ photoionization of neutral argon becomes a little stronger (see Fig. 3 and Table I) and, with this, also the alignment of Ar^{2+} after the sequence of photoionization and Auger-Meitner decay (see Table VI).

TABLE VI. Alignment parameter $\mathcal{A}_{20}(P)$ and $\mathcal{A}_{20}(D)$ of the final Ar^{2+}ion $(3p^{-2})$ after a sequence of $2p$ ionization and $L_{23}M_{23}M_{23}$ Auger-Meitner decay of initial neutral argon. Results for different photon energies are listed.

ω_{in} (eV)	$\mathcal{A}_{20}(P)$	$\mathcal{A}_{20}(D)$
300	0.089	−0.097
1000	0.098	−0.107
3000	0.114	−0.124

V. CONCLUSION

In this paper, we have presented an implementation of improved electronic-structure calculations in the XATOM toolkit that provide individual zeroth-order LS eigenstates by employing first-order many-body perturbation theory. Based on this implementation, we have calculated individual state-to-state photoionization cross sections and transition rates. We have investigated orbital alignment after either single photoionization or one Auger-Meitner relaxation process, and then the evolution of orbital alignment in a sequence of photoionization and relaxation.

To set the stage, we have first presented a brief outline of the underlying method to calculate first-order-corrected energies and zeroth-order LS eigenstates for arbitrary electronic configurations. We have also shown an analytical expression for the individual state-to-state cross section and transition rates. Comparing $K\alpha$ fluorescence energies and KLL Auger-Meitner electron energies of Ne^+ $(1s^{-1})$ with experimental data, we have confirmed that the extended XATOM toolkit can describe transition energies significantly better than the original version. On the other hand, we have observed almost no improvement on the total photoionization cross sections for neutral argon, which can be attributed to the use of zeroth-order states.

Having the capability to calculate individual state-to-state cross sections by using the extended XATOM toolkit, we have investigated orbital alignment induced by linearly polarized x rays for initial neutral argon and two exotic open-shell configurations of argon. Some degrees of alignment has been found for a wide range of x-ray photon energies. For initial neutral argon, the ions produced by photoionization exhibit a clear preference for conservation of the angular momentum projection. For the initial open-shell ions, however, the distribution of final states is affected not only by the conservation of the angular momentum projection, but also by the final total spin quantum number, the selection rules, and, most importantly, the overlap matrix element. Finally, we have showcased how the orbital alignment is affected by Auger-Meitner decay and how it evolves during one sequence of photoionization and Auger-Meitner decay.

There are several promising perspectives for further developments. Above all, the individual state-to-state cross sections and transition rates calculated with our implementation could be embedded in the rate-equation model employed in the XATOM toolkit [31,35,54]. Solving rate equations would enable investigations of orbital alignment dynamics of ions produced by x-ray multiphoton ionization. In this way, it

could be explored whether the orbital alignment observed here for ions produced by single photoionization is enhanced or reduced by successive photoionization events and accompanying decay processes. Another interesting perspective is the improvement of the cross section by calculating and utilizing not only first-order-corrected energies but also first-order states and by taking interchannel coupling [87] into account. Lastly, relativistic effects and resonance effects are incorporated in the XATOM toolkit [53], but remain to be addressed in combination with the present implementation. Such methodological developments are not only important for many practical applications of focused XFEL beams, but are also useful for a quantitative characterization of XFEL beam properties.

[1] P. Emma *et al.*, First lasing and operation of an ångstrom-wavelength free-electron laser, Nat. Photon. **4**, 641 (2010).

[2] T. Ishikawa *et al.*, A compact x-ray free-electron laser emitting in the sub-ångström region, Nat. Photon. **6**, 540 (2012).

[3] H.-S. Kang *et al.*, Hard x-ray free-electron laser with femtosecond-scale timing jitter, Nat. Photon. **11**, 708 (2017).

[4] W. Decking *et al.*, A MHz-repetition-rate hard x-ray free-electron laser driven by a superconducting linear accelerator, Nat. Photon. **14**, 391 (2020).

[5] E. Prat *et al.*, A compact and cost-effective hard x-ray free-electron laser driven by a high-brightness and low-energy electron beam, Nat. Photon. **14**, 748 (2020).

[6] J. C. H. Spence, XFELs for structure and dynamics in biology, IUCrJ **4**, 322 (2017).

[7] I. Schlichting and J. Miao, Emerging opportunities in structural biology with x-ray free-electron lasers, Curr. Opin. Struct. Biol. **22**, 613 (2012).

[8] J. Coe and P. Fromme, Serial femtosecond crystallography opens new avenues for structural biology, Protein Pept. Lett. **23**, 255 (2016).

[9] K. Gaffney and H. N. Chapman, Imaging atomic structure and dynamics with ultrafast x-ray scattering, Science **316**, 1444 (2007).

[10] L. Young, K. Ueda, M. Gühr, P. H. Bucksbaum, M. Simon, S. Mukamel, N. Rohringer, K. C. Prince, C. Masciovecchio, M. Meyer, A. Rudenko, D. Rolles, C. Bostedt, M. Fuchs, D. A. Reis, R. Santra, H. Kapteyn, M. Murnane, H. Ibrahim, F. Légaré *et al.*, Roadmap of ultrafast x-ray atomic and molecular physics, J. Phys. B: At. Mol. Opt. Phys. **51**, 032003 (2018).

[11] C. Bostedt, J. D. Bozek, P. H. Bucksbaum, R. N. Coffee, J. B. Hastings, Z. Huang, R. W. Lee, S. Schorb, J. N. Corlett, P. Denes, P. Emma, R. W. Falcone, R. W. Schoenlein, G. Doumy, E. P. Kanter, B. Kraessig, S. Southworth, L. Young, L. Fang, M. Hoener *et al.*, Ultra-fast and ultra-intense x-ray sciences: First results from the Linac Coherent Light Source free-electron laser, J. Phys. B: At. Mol. Opt. Phys. **46**, 164003 (2013).

[12] L. Fang, T. Osipov, B. F. Murphy, A. Rudenko, D. Rolles, V. S. Petrovic, C. Bostedt, J. D. Bozek, P. H. Bucksbaum, and N. Berrah, Probing ultrafast electronic and molecular dynamics with free-electron lasers, J. Phys. B: At. Mol. Opt. Phys. **47**, 124006 (2014).

[13] J. Ullrich, A. Rudenko, and R. Moshammer, Free-electron lasers: New avenues in molecular physics and photochemistry, Annu. Rev. Phys. Chem. **63**, 635 (2012).

[14] S. H. Glenzer, L. B. Fletcher, E. Galtier, B. Nagler, R. Alonso-Mori, B. Barbrel, S. B. Brown, D. A. Chapman, Z. Chen, C. B. Curry, F. Fiuza, E. Gamboa, M. Gauthier, D. O. Gericke, A. Gleason, S. Goede, E. Granados, P. Heimann, J. Kim, D. Kraus *et al.*, Matter under extreme conditions experiments at the Linac Coherent Light Source, J. Phys. B: At. Mol. Opt. Phys. **49**, 092001 (2016).

[15] C. Pellegrini, A. Marinelli, and S. Reiche, The physics of x-ray free-electron lasers, Rev. Mod. Phys. **88**, 015006 (2016).

[16] H. N. Chapman, P. Fromme, A. Barty, T. A. White, R. A. Kirian, A. Aquila, M. S. Hunter, J. Schulz, D. P. DePonte, U. Weierstall, R. B. Doak, F. R. N. C. Maia, A. V. Martin, I. Schlichting, L. Lomb, N. Coppola, R. L. Shoeman, S. W. Epp, R. Hartmann, D. Rolles *et al.*, Femtosecond x-ray protein nanocrystallography, Nature (London) **470**, 73 (2011).

[17] E. Sobolev, S. Zolotarev, K. Giewekemeyer, J. Bielecki, K. Okamoto, H. K. N. Reddy, J. Andreasson, K. Ayyer, I. Barak, S. Bari, A. Barty, R. Bean, S. Bobkov, H. N. Chapman, G. Chojnowski, B. J. Daurer, K. Dörner, T. Ekeberg, L. Flückiger, O. Galzitskaya *et al.*, Megahertz single-particle imaging at the European XFEL, Commun. Phys. **3**, 97 (2020).

[18] M. M. Seibert, T. Ekeberg, F. R. N. C. Maia, M. Svenda, J. Andreasson, O. Jönsson, D. Odić, B. Iwan, A. Rocker, D. Westphal, M. Hantke, D. P. DePonte, A. Barty, J. Schulz, L. Gumprecht, N. Coppola, A. Aquila, M. Liang, T. A. White, A. Martin *et al.*, Single mimivirus particles intercepted and imaged with an X-ray laser, Nature (London) **470**, 78 (2011).

[19] G. Brändén, G. Hammarin, R. Harimoorthy, A. Johansson, D. Arnlund, E. Malmerberg, A. Barty, S. Tångefjord, P. Berntsen, D. P. DePonte, C. Seuring, T. A. White, F. Stellato, R. Bean, K. R. Beyerlein, L. M. Chavas, H. Fleckenstein, C. Gati, U. Ghoshdastider, L. Gumprecht *et al.*, Coherent diffractive imaging of microtubules using an X-ray laser, Nat. Commun. **10**, 2589 (2019).

[20] A. Hosseinizadeh, G. Mashayekhi, J. Copperman, P. Schwander, A. Dashti, R. Sepehr, R. Fung, M. Schmidt, C. H. Yoon, B. Hogue, G. J. Williams, A. Aquila, and A. Ourmazd, Conformational landscape of a virus by single-particle X-ray scattering, Nat. Methods **14**, 877 (2017).

[21] D. Assalauova, Y. Y. Kim, S. Bobkov, R. Khubbutdinov, M. Rose, R. Alvarez, J. Andreasson, E. Balaur, A. Contreras, H. DeMirci, L. Gelisio, J. Hajdu, M. S. Hunter, R. P. Kurta, H. Li, M. McFadden, R. Nazari, P. Schwander, A. Teslyuk, P. Walter *et al.*, An advanced workflow for single-particle imaging with the limited data at an X-ray free-electron laser, IUCrJ **7**, 1102 (2020).

[22] A. Aquila, A. Barty, C. Bostedt, S. Boutet, G. Carini, D. DePonte, P. Drell, S. Doniach, K. H. Downing, T. Earnest, H. Elmlund, V. Elser, M. Gühr, J. Hajdu, J. Hastings, S. P. Hau-Riege, Z. Huang, E. E. Lattman, F. R. N. C. Maia, S. Marchesini *et al.*, The linac coherent light source single particle imaging road map, Struct. Dyn. **2**, 041701 (2015).

[23] B. Ziaja, H. N. Chapman, R. Faustlin, S. Hau-Riege, Z. Jurek, A. V. Martin, S. Toleikis, F. Wang, E. Weckert, and R. Santra,

Limitations of coherent diffractive imaging of single objects due to their damage by intense x-ray radiation, New J. Phys. **14**, 115015 (2012).

[24] H. Fukuzawa, S.-K. Son, K. Motomura, S. Mondal, K. Nagaya, S. Wada, X.-J. Liu, R. Feifel, T. Tachibana, Y. Ito, M. Kimura, T. Sakai, K. Matsunami, H. Hayashita, J. Kajikawa, P. Johnsson, M. Siano, E. Kukk, B. Rudek, B. Erk *et al.*, Deep Inner-Shell Multiphoton Ionization by Intense X-Ray Free-Electron Laser Pulses, Phys. Rev. Lett. **110**, 173005 (2013).

[25] B. Rudek, K. Toyota, L. Foucar, B. Erk, R. Boll, C. Bomme, J. Correa, S. Carron, S. Boutet, G. J. Williams, K. R. Ferguson, R. Alonso-Mori, J. Koglin, T. Gorkhover, M. Bucher, C. Lehmann, B. Krässig, S. Southworth, L. Young, C. Bostedt *et al.*, Relativistic and resonant effects in the ionization of heavy atoms by ultra-intense hard X-rays, Nat. Commun. **9**, 4200 (2018).

[26] B. Rudek, S.-K. Son, L. Foucar, S. W. Epp, B. Erk, R. Hartmann, M. Adolph, R. Andritschke, A. Aquila, N. Berrah, C. Bostedt, J. Bozek, N. Coppola, F. Filsinger, H. Gorke, T. Gorkhover, H. Graafsma, L. Gumprecht, A. Hartmann, G. Hauser *et al.*, Ultra-efficient ionization of heavy atoms by intense X-ray free-electron laser pulses, Nat. Photon. **6**, 858 (2012).

[27] L. Young, E. P. Kanter, B. Krässig, Y. Li, A. M. March, S. T. Pratt, R. Santra, S. H. Southworth, N. Rohringer, L. F. DiMauro, G. Doumy, C. A. Roedig, N. Berrah, L. Fang, M. Hoener, P. H. Bucksbaum, J. P. Cryan, S. Ghimire, J. M. Glownia, D. A. Reis *et al.*, Femtosecond electronic response of atoms to ultra-intense X-rays, Nature (London) **466**, 56 (2010).

[28] G. Doumy, C. Roedig, S.-K. Son, C. I. Blaga, A. D. DiChiara, R. Santra, N. Berrah, C. Bostedt, J. D. Bozek, P. H. Bucksbaum, J. P. Cryan, L. Fang, S. Ghimire, J. M. Glownia, M. Hoener, E. P. Kanter, B. Krässig, M. Kuebel, M. Messerschmidt, G. G. Paulus *et al.*, Nonlinear Atomic Response to Intense Ultrashort X Rays, Phys. Rev. Lett. **106**, 083002 (2011).

[29] A. Rudenko, L. Inhester, K. Hanasaki, X. Li, S. J. Robatjazi, B. Erk, R. Boll, K. Toyota, Y. Hao, O. Vendrell, C. Bomme, E. Savelyev, B. Rudek, L. Foucar, S. H. Southworth, C. S. Lehmann, B. Krässig, T. Marchenko, M. Simon, K. Ueda *et al.*, Femtosecond response of polyatomic molecules to ultra-intense hard X-rays, Nature (London) **546**, 129 (2017).

[30] R. Santra, Concepts in x-ray physics, J. Phys. B: At. Mol. Opt. Phys. **42**, 023001 (2009).

[31] R. Santra and L. Young, Interaction of intense x-ray beams with atoms, in *Synchrotron Light Sources and Free-Electron Lasers*, edited by E. J. Jaeschke, S. Khan, J. R. Schneider, and J. B. Hastings (Springer International, Switzerland, 2016), pp. 1233–1260.

[32] K. Nass, Radiation damage in protein crystallography at X-ray free-electron lasers, Acta Crystallogr. D **75**, 211 (2019).

[33] H. M. Quiney and K. A. Nugent, Biomolecular imaging and electronic damage using X-ray free-electron lasers, Nat. Phys. **7**, 142 (2011).

[34] U. Lorenz, N. M. Kabachnik, E. Weckert, and I. A. Vartanyants, Impact of ultrafast electronic damage in single-particle x-ray imaging experiments, Phys. Rev. E **86**, 051911 (2012).

[35] S.-K. Son, L. Young, and R. Santra, Impact of hollow-atom formation on coherent x-ray scattering at high intensity, Phys. Rev. A **83**, 033402 (2011).

[36] S. Flügge, W. Mehlhorn, and V. Schmidt, Angular Distribution of Auger Electrons Following Photoionization, Phys. Rev. Lett. **29**, 7 (1972).

[37] V. L. Jacobs, Theory of atomic photoionization measurements, J. Phys. B: At. Mol. Phys. **5**, 2257 (1972).

[38] C. D. Caldwell and R. N. Zare, Alignment of Cd atoms by photoionization, Phys. Rev. A **16**, 255 (1977).

[39] C. H. Greene and R. N. Zare, Photonization-produced alignment of Cd, Phys. Rev. A **25**, 2031 (1982).

[40] K. Blum, *Density Matrix Theory and Applications* (Springer, New York, 1996).

[41] C. H. Greene and R. N. Zare, Photofragment alignment and orientation, Annu. Rev. Phys. Chem. **33**, 119 (1982).

[42] V. Schmidt, Photoionization of atoms using synchrotron radiation, Rep. Prog. Phys. **55**, 1483 (1992).

[43] U. Kleiman and U. Becker, Photoionization of closed-shell atoms: Hartree-Fock calculations of orientation and alignment, J. Electron Spectrosc. Relat. Phenom. **131-132**, 29 (2003).

[44] U. Kleiman and U. Becker, Orientation and alignment generated from photoionization of closed-shell cations, J. Electron Spectrosc. Relat. Phenom. **142**, 45 (2005).

[45] L. Young, D. A. Arms, E. M. Dufresne, R. W. Dunford, D. L. Ederer, C. Höhr, E. P. Kanter, B. Krässig, E. C. Landahl, E. R. Peterson, J. Rudati, R. Santra, and S. H. Southworth, X-Ray Microprobe of Orbital Alignment in Strong-Field Ionized Atoms, Phys. Rev. Lett. **97**, 083601 (2006).

[46] R. Santra, R. W. Dunford, E. P. Kanter, B. Krässig, S. H. Southworth, and L. Young, Strong-field control of x-ray processes, in *Advances in Atomic, Molecular, and Optical Physics*, Vol. 56, edited by E. Arimondo, P. R. Berman, and C. C. Lin (Academic Press, Amsterdam, 2008), pp. 219–257.

[47] Z. Jurek, S.-K. Son, B. Ziaja, and R. Santra, XMDYN and XATOM: Versatile simulation tools for quantitative modeling of X-ray free-electron laser induced dynamics of matter, J. Appl. Crystallogr. **49**, 1048 (2016).

[48] R. Thiele, S.-K. Son, B. Ziaja, and R. Santra, Effect of screening by external charges on the atomic orbitals and photoinduced processes within the Hartree-Fock-Slater atom, Phys. Rev. A **86**, 033411 (2012).

[49] S.-K. Son, R. Thiele, Z. Jurek, B. Ziaja, and R. Santra, Quantum-Mechanical Calculation of Ionization-Potential Lowering in Dense Plasmas, Phys. Rev. X **4**, 031004 (2014).

[50] J. J. Bekx, S.-K. Son, R. Santra, and B. Ziaja, *Ab initio* calculation of electron-impact-ionization cross sections for ions in exotic electron configurations, Phys. Rev. A **98**, 022701 (2018).

[51] J. M. Slowik, S.-K. Son, G. Dixit, Z. Jurek, and R. Santra, Incoherent x-ray scattering in single molecule imaging, New J. Phys. **16**, 073042 (2014).

[52] S.-K. Son, O. Geffert, and R. Santra, Compton spectra of atoms at high x-ray intensity, J. Phys. B: At. Mol. Opt. Phys. **50**, 064003 (2017).

[53] K. Toyota, S.-K. Son, and R. Santra, Interplay between relativistic energy corrections and resonant excitations in x-ray multiphoton ionization dynamics of Xe atoms, Phys. Rev. A **95**, 043412 (2017).

[54] S.-K. Son and R. Santra, Monte Carlo calculation of ion, electron, and photon spectra of xenon atoms in x-ray free-electron laser pulses, Phys. Rev. A **85**, 063415 (2012).

[55] C. Froese Fischer, The MCHF atomic-structure package, Comput. Phys. Commun. **64**, 369 (1991).

[56] S.-K. Son, K. Toyota, O. Geffert, J. M. Slowik, and R. Santra, XATOM—an integrated toolkit for x-ray and atomic physics, CFEL, DESY, Hamburg, Germany, 2016, Rev. 3544.
[57] J. C. Slater, A simplification of the Hartree-Fock method, Phys. Rev. **81**, 385 (1951).
[58] K. Gottfried and T. Yan, *Quantum Mechanics: Fundamentals* (Springer, New York, 2003).
[59] D. J. Griffiths, *Introduction to Quantum Mechanics*, 2nd ed. (Cambridge University Press, Cambridge, 2017).
[60] J. J. Sakurai and J. J. Napolitano, *Modern Quantum Mechanics: Pearson New International Edition* (Pearson Education, Harlow, 2014).
[61] E. U. Condon and G. H. Shortley, *The Theory of Atomic Spectra* (Cambridge University Press, Cambridge, 1970).
[62] M. Alonso and E. J. Finn, *Quantenphysik und Statistische Physik* (Oldenbourg Verlag, München, 2012).
[63] W. S. Struve, *Fundamentals of Molecular Spectroscopy* (Wiley-Interscience, New York, 1989).
[64] G. Racah, Theory of complex spectra. I, Phys. Rev. **61**, 186 (1942).
[65] G. Racah, Theory of complex spectra. II, Phys. Rev. **62**, 438 (1942).
[66] G. Racah, Theory of complex spectra. III, Phys. Rev. **63**, 367 (1943).
[67] B. R. Judd, *Operator Techniques in Atomic Spectroscopy* (McGraw-Hill, New York, 1963).
[68] I. V. Hertel and K. P. Schulz, *Atoms, Molecules and Optical Physics 1* (Springer, Berlin, 2015).
[69] R. Karazija, *Introduction to the Theory of X-Ray and Electronic Spectra of Free Atoms* (Springer, New York, 1996).
[70] Due to the inclusion of first-order correction in the energy, $E_{L_iS_i} - E_{L_fS_f}$ differs from ε_{nl}. Consequently, the cross section contains a prefactor $(\varepsilon_{nl} - \varepsilon_c)^2/\omega_{\rm in}$ rather than the usual prefactor $\omega_{\rm in}$.
[71] B. Crasemann, *Atomic Inner-Shell Processes* (Academic Press, New York, 1975).
[72] U. Fano, Description of states in quantum mechanics by density matrix and operator techniques, Rev. Mod. Phys. **29**, 74 (1957).
[73] J. Olsen, M. R. Godefroid, P. Jönsson, P. A. Malmqvist, and C. F. Fischer, Transition probability calculations for atoms using nonorthogonal orbitals, Phys. Rev. E **52**, 4499 (1995).
[74] J. Verbeek and J. H. Van Lenthe, On the evaluation of non-orthogonal matrix elements, J. Molec. Struct. Theochem **229**, 115 (1991).
[75] I. C. Hayes and A. J. Stone, Matrix elements between determinantal wave functions of non-orthogonal orbitals, Molec. Phys. **53**, 69 (1984).
[76] R. Latter, Atomic energy levels for the Thomas-Fermi and Thomas-Fermi-Dirac potential, Phys. Rev. **99**, 510 (1955).
[77] G. H. Yao and S. I. Chu, Generalized pseudospectral methods with mappings for bound and resonance state problems, Chem. Phys. Lett. **204**, 381 (1993).
[78] X. M. Tong and S. I. Chu, Theoretical study of multiple high-order harmonic generation by intense ultrashort pulsed laser fields: A new generalized pseudospectral time-dependent method, Chem. Phys. **217**, 119 (1997).
[79] J. W. Cooper, Photoionization from outer atomic subshells. A model study, Phys. Rev. **128**, 681 (1962).
[80] J. W. Manson and S. T. Cooper, Photo-ionization in the soft x-ray range: $1z$ dependence in a central-potential model, Phys. Rev. **165**, 126 (1968).
[81] A. Thomson, D. Attwood, E. Gullikson, M. Howells, K.-J. Kim, J. Kirz, J. Kortright, I. Lindau, Y. Liu, P. Pianetta, A. Robinson, J. Scofield, J. Underwood, and G. Williams, *X-Ray Data Booklet* (Center for X-Ray Optics and Advanced Light Source, Lawrence Berkeley National Laboratory, Berkeley, CA, 2009).
[82] J. A. Bearden, X-ray wavelengths, Rev. Mod. Phys. **39**, 78 (1967).
[83] A. Albiez, M. Thoma, W. Weber, and W. Mehlhorn, $KL_{2,3}$ ionization in neon by electron impact in the range 1.5-50 keV: Cross sections and alignment, Z. Phys. D **16**, 97 (1990).
[84] H. Körber and W. Mehlhorn, Das K-Auger-spectrum von neon, Z. Phys. **191**, 217 (1966).
[85] G. V. Marr and J. B. West, Absolute photoionization cross-section tables for helium, neon, argon, and krypton in the VUV spectral regions, At. Data Nucl. Data Tables **18**, 497 (1976).
[86] J. A. R. Samson and W. C. Stolte, Precision measurements of the total photoionization cross-sections of He, Ne, Ar, Kr, and Xe, J. Electron Spectrosc. Relat. Phenom. **123**, 265 (2002).
[87] A. F. Starace, Trends in the theory of atomic photoionization, Appl. Opt. **19**, 4051 (1980).
[88] G. W. F. Drake, *Springer Handbook of Atomic, Molecular, and Optical Physics* (Springer, New York, 2006).

3.2 State-resolved ionization dynamics of a neon atom induced by X-ray free-electron-laser pulses

The second publication presents a state-resolved Monte Carlo rate-equation implementation for describing state-resolved X-ray multiphoton ionization dynamics of atoms. The state-resolved approach provides more precise information about resonant excitations and electron and photon spectra than the common configuration-based approach.

The underlying project was performed by myself under the supervision of Dr. S.-K. Son and Professor Dr. R. Santra. In particular, I combined the quantum-state-resolved electronic-structure framework (Sec. 3.1) with XATOM's configuration-based Monte Carlo on-the-fly rate-equation method [26, 29]. I carried out all X-ray multiphoton ionization dynamics calculations, interpreted the outcomes, and wrote the manuscript with inputs from all authors.

State-resolved ionization dynamics of a neon atom induced by x-ray free-electron-laser pulses

Laura Budewig,[1,2] Sang-Kil Son,[1] and Robin Santra[1,2]
[1]*Center for Free-Electron Laser Science CFEL, Deutsches Elektronen-Synchrotron DESY, Notkestrasse 85, 22607 Hamburg, Germany*
[2]*Department of Physics, Universität Hamburg, Notkestrasse 9-11, 22607 Hamburg, Germany*

(Received 1 November 2022; accepted 14 December 2022; published 5 January 2023)

We present a theoretical framework to describe state-resolved ionization dynamics of neon atoms driven by ultraintense x-ray free-electron-laser pulses. In general, x-ray multiphoton ionization dynamics of atoms have been described by time-dependent populations of the electronic configurations visited during the ionization dynamics, neglecting individual state-to-state transition rates and energies. Combining a state-resolved electronic-structure calculation, based on first-order many-body perturbation theory, with a Monte Carlo rate-equation method enables us to study state-resolved dynamics based on time-dependent state populations. Our results demonstrate that configuration-based and state-resolved calculations provide similar charge-state distributions, but the differences are visible when resonant excitations are involved, which are also reflected in calculated time-integrated electron and photon spectra. In addition, time-resolved spectra of ions, electrons, and photons are analyzed for different pulse durations to explore how frustrated absorption manifests itself during the ionization dynamics of neon atoms.

DOI: 10.1103/PhysRevA.107.013102

I. INTRODUCTION

X-ray free-electron lasers (XFELs) [1–5] provide x-ray radiation with extremely high intensity and ultrashort pulse durations ranging from a few to a hundred femtoseconds [6]. Interaction with these ultraintense XFEL pulses can induce x-ray multiphoton ionization dynamics in matter [7]. Enabled by the high intensity and, thus, the extremely large number of x-ray photons in a single pulse, multiple sequences of one-photon ionization accompanied by decay processes (Auger-Meitner decay and fluorescence), refilling inner-shell vacancies, can take place. Consequently, atoms or molecules may become highly ionized during interaction with XFEL pulses [8–12]. Such x-ray multiphoton ionization dynamics can be simulated by a rate-equation approach [8,13,14] and were first investigated both experimentally and theoretically in neon atoms [8]. Further studies for neon have revealed the relevance of direct nonsequential two-photon ionization in excited neon ions [15] and resonant excitations at a specific photon energy [16]. Moreover, x-ray multiphoton ionization dynamics in heavier atoms [9–11,17,18] and molecules [12,19–21] have been examined in various ways, including resonant effects [22–25]. Typically, the ionization dynamics of atoms and molecules have been examined with measurement of ions generated after interacting with an intense XFEL pulse, but electron spectra [26–28] and photon spectra [11,27–29] are complementary to ion spectroscopy. Deepening our understanding of multiphoton ionization dynamics and the accompanying electronic damage [30–32] is relevant for applications of XFELs, like serial femtosecond crystallography [33,34] and single particle experiments [35,36], which are limited by electronic damage and structural disintegration of the sample [37].

Most of the theoretical treatments of x-ray multiphoton ionization dynamics are limited in the way that the states visited during the ionization dynamics are described only by electronic configurations in the rate-equation approach. In this way, transition energies and rates are averaged over individual electronic states for a given electron configuration. As will be discussed in detail in Sec. II C, this configuration-based approach already demands to solve a large set of coupled rate equations, and the number of rate equations explodes when resonant excitations are included [11,22,24,25]. The configuration-based rate-equation approach has been widely used and successfully applied for interpreting and designing many XFEL experiments [8–25,27–30,38–40]. However, it can treat neither individual state-to-state transitions nor detailed state-resolved ionization dynamics.

In this work, we investigate x-ray multiphoton ionization dynamics of neon atoms based on individual electronic states by extending the *ab initio* electronic-structure and ionization-dynamics toolkit XATOM [32,41,42]. Recently, a state-resolved electronic-structure framework, based on first-order many-body perturbation theory, has been introduced in XATOM [43]. As a follow-up study, we here embed these improved electronic-structure calculations into the Monte Carlo on-the-fly rate-equation method for describing ionization dynamics [9,27]. This implementation permits us to perform huge-size rate-equation calculations that are inevitable for state-resolved ionization dynamics calculations. We compare both configuration-based and state-resolved approaches for x-ray multiphoton ionization of Ne. It can be expected that resonant excitations and spectra should in general profit from our state-resolved implementation for two reasons. First, as shown in Ref. [43], the first-order-corrected energies, delivered by the improved electronic-structure calculations, often

provide better transition energies. Second, individual states associated with a configuration generally do not behave the same during ionization dynamics. Based on the state-resolved approach, we will also investigate the time evolution of charge-state distributions (CSDs) and photoelectron, Auger-Meitner electron, and fluorescence spectra during an XFEL pulse.

The paper is organized as follows. In Sec. II, we present our state-resolved Monte Carlo on-the-fly implementation in XATOM. Additionally, individual state-to-state resonant photoabsorption cross sections, which are missing in Ref. [43], are addressed. A comparison with a configuration-based Monte Carlo calculation is the topic of Sec. III, while in Sec. IV we study the time evolution of ion, electron, and photon spectra for neon for different pulse durations. We summarize our findings and discuss future perspectives in Sec. V.

II. THEORETICAL DETAILS

A. Improved electronic-structure calculations

Here, we briefly summarize the formalism underlying the improved electronic-structure calculations, implemented in XATOM. For more details, the reader is referred to Ref. [43]. XATOM is based on the Hartree-Fock-Slater (HFS) approach [32,44], in order to keep the calculations feasible and efficient for heavy atoms also and the inclusion of resonant excitations (see Sec. II C). The HFS calculations can be improved through first-order many-body perturbation theory [45,46] for the full N-electronic Hamiltonian [45]

$$\hat{H}_{\text{matter}} = \sum_{i=1}^{N}\left\{-\frac{1}{2}\nabla_i^2 - \frac{Z}{|\vec{x}_i|}\right\} + \frac{1}{2}\sum_{i\neq j}^{N}\frac{1}{|\vec{x}_i-\vec{x}_j|}. \tag{1}$$

Here, $\vec{x}_i$ is the position of an electron in the atom of nuclear charge Z, and atomic units are used. In this approach, for an electronic configuration of interest, the matrix representation of $\hat{H}_{\text{matter}}$ is created in the set of electronic Fock states. The Fock states are antisymmetrized products of spin orbitals that are eigenstates of the HFS Hamiltonian $\hat{H}^{\text{HFS}}$ [47]. The eigenstates of this matrix provide zeroth-order LS eigenstates $|LSM_LM_S\kappa\rangle$ with first-order-corrected energies $E_{LS\kappa}$, given by the eigenvalues. An important feature of the new states is that they are also eigenstates of the total orbital angular momentum and of total spin. Therefore, they can be labeled by the L and S quantum numbers and their projections M_L and M_S, respectively. Since the set of (L, S, M_L, M_S) does not always uniquely define the state, we need an additional integer index κ. Note that the states within a term ${}^{2S+1}L(\kappa)$ share the same first-order-corrected energy $E_{LS\kappa}$.

B. Individual state-to-state resonant photoabsorption cross sections

Having at hand first-order-corrected energies and zeroth-order LS eigenstates, we can perform further state-resolved calculations, e.g., cross sections and transition rates. A detailed description of state-to-state photoionization cross sections, Auger-Meitner decay rates, and fluorescence rates can be found in Ref. [43].

Previous studies of x-ray multiphoton ionization dynamics have demonstrated the importance of resonant excitations at certain photon energies for neon [8,16], krypton [17,24,25], and xenon [10,11,24,25]. Therefore, we present a calculation of individual state-to-state resonant photoabsorption cross sections, based on our improved electronic-structure framework. It can be performed in a similar way as the calculation of individual state-to-state photoionization cross sections (see Ref. [43]).

Let us consider a bound-to-bound resonant transition of an electron in the subshell with quantum numbers (n_h, l_h) to a higher-lying (n_j, l_j)-subshell by absorbing a linearly polarized photon with a photon energy ω. The associated initial zeroth-order LS eigenstate is $|L_iS_iM_{L_i}M_{S_i}\rangle$ with first-order-corrected energy $E_{L_iS_i}$, and the accessible final target state is $|L_fS_fM_{L_f}M_{S_f}\rangle$ with $E_{L_fS_f}$ (here, κ_i and κ_f are omitted for simplicity). Then, the state-to-state resonant photoabsorption cross section can be written as

$$\sigma^{M_{L_i};M_{L_f}}_{2S_i+1L_i;{}^{2S_f+1}L_f}(n_hl_h, n_jl_j, \omega) = \frac{4\pi^2}{3\omega}\alpha\delta\left(E_{L_fS_f} - E_{L_iS_i} - \omega\right)\left(\varepsilon_{n_hl_h} - \varepsilon_{n_jl_j}\right)^2 l_> \times \left|\int_0^\infty dr u^*_{n_jl_j}(r) r u_{n_hl_h}(r)\right|^2 \left|\sum_{j,h} C(l_h, l_j, 1; m_{l,_h} - m_{l_j}, 0)\langle L_fS_fM_{L_f}S_f|\hat{c}_j^\dagger\hat{c}_h|L_iS_iM_{L_i}S_i\rangle\right|^2. \tag{2}$$

In this expression, $C(\cdot)$ represents a Clebsch-Gordan coefficient [48,49] and $l_> = \max(l_h, l_j)$. The indices h and j denote the involved spin orbitals in the (n_hl_h) and (n_jl_j) subshells, respectively, between which the electron is transferred. They have orbital energies $\varepsilon_{n_hl_h}$ and $\varepsilon_{n_jl_j}$, and quantum numbers $(n_h, l_h, m_{l_h}, m_{s_h})$ and $(n_j, l_j = l_h \pm 1, m_{l_j} = m_{l_h}, m_{s_j} = m_{s_h})$, respectively. The relation between their quantum numbers can be attributed to the selection rules for a dipole transition with linearly polarized photons [50]. Creation and annihilation operators $\hat{c}_j^\dagger$ and $\hat{c}_h$ can be associated with the spin orbitals [51]. Since the interaction Hamiltonian corresponding to one-photon absorption [51] does not affect the spin and its projection, the cross section is independent of the initial and final spin projections.

According to the energy conservation law, the transition energy, $E_{L_fS_f} - E_{L_iS_i}$, equals the photon energy ω,

$$\omega = E_{L_fS_f} - E_{L_iS_i}. \tag{3}$$

Therefore, it is critical to take into account that the pulse has some energy distribution around a given peak photon energy $\omega_{\rm in}$. Let us assume a Gaussian pulse profile [22],

$$G(\omega;\omega_{\rm in},\Delta_{\omega_{\rm in}})=\frac{1}{\Delta_{\omega_{\rm in}}}\sqrt{\frac{4\ln 2}{\pi}}e^{-4\ln 2(\frac{\omega_{\rm in}-\omega}{\Delta_{\omega_{\rm in}}})^2}, \tag{4}$$

where $\Delta_{\omega_{\rm in}}$ is the full width at half maximum (FWHM) of the bandwidth of the photon energy distribution. After employing convolution with the pulse profile, the individual state-to-state resonant photoabsorption cross section for a peak photon energy $\omega_{\rm in}$ is

$$\begin{aligned}&\sigma^{M_{L_i};M_{L_f}}_{2S_i+1L_i;^{2S_f+1}L_f}(n_hl_h,n_jl_j,\omega_{\rm in})\\&\quad=\sigma^{M_{L_i};M_{L_f}}_{2S_i+1L_i;^{2S_f+1}L_f}(n_hl_h,n_jl_j,E_{L_fS_f}-E_{L_iS_i})\\&\qquad\times G(E_{L_fS_f}-E_{L_iS_i};\omega_{\rm in},\Delta_{\omega_{\rm in}}).\end{aligned} \tag{5}$$

Here, $\sigma^{M_{L_i};M_{L_f}}_{2S_i+1L_i;^{2S_f+1}L_f}(n_hl_h,n_jl_j,\omega=E_{L_fS_f}-E_{L_iS_i})$ is given by Eq. (2), but without the delta distribution that vanishes due to integration over ω.

It is also worthwhile to mention that calculating resonant photoexcitation cross sections requires additional computational parameters. First, in order to keep the calculation feasible, the number of allowed (n,l) subshells that can be resonantly excited has to be restricted and checked for computational convergence. In Sec. III, we have used a maximal n quantum number of $n_{\rm max}=7$ and a maximal l quantum number of $l_{\rm max}=2$ for Ne calculation at a photon energy of 1050 eV. Second, in order to guarantee an accurate description of higher-n states the maximum radius employed in the numerical calculation of orbital and orbital energies [32,41] has to be sufficiently large for both bound and continuum states. We used $r_{\rm max}=100$ a.u. for both in the following resonance-related calculations. Third, due to the convolution procedure, it is necessary to scan the transition energy to search for all accessible resonant bound-to-bound transitions. However, the state-resolved calculation of first-order-corrected transition energies costs a considerable amount of computational time when a lot of open subshells are included. For instance, calculating all cross sections for initial Ne^{3+} $(1s^02s^22p^44p^1)$ costs roughly 2 min in CPU time, due to the scanning of all resonant excitations with $n_{\rm max}\leqslant 7$ and $l_{\rm max}\leqslant 2$ (for comparison, the nonresonant calculation of photoionization cross sections takes less than 3 s). Therefore, when we search for accessible resonant states, we employ an energy scan criterion based on the zeroth-order transition energies, instead of the first-order-corrected values. In our calculation for Ne at 1050 eV, a bandwidth of 1% of the photon energy was considered. Then, we scan ± 157.5 eV ($\pm 15\%$ of the photon energy) to pick up resonant transitions based on the zeroth-order transition energy. Only for these resonant transitions we consider whether the first-order transition energy lies within the photon energy bandwidth. This reduces the computational time for the upper example to 30 s. Note that the differences between zeroth- and first-order transition energies are less than 50 eV in our calculations (see Table IV).

C. State-resolved ionization dynamics calculations

X-ray multiphoton ionization dynamics can be described by a rate equation approach [8,13,14]. In this approach, the time evolution of the population $P_I(t)$ of a state I is given by a set of coupled rate equations,

$$\frac{dP_I(t)}{dt}=\sum_{I'\neq I}[\Gamma_{I'\to I}P_{I'}(t)-\Gamma_{I\to I'}P_I(t)], \tag{6}$$

for all possible states $\{I\}$. In this expression, $\Gamma_{I\to I'}$ is the rate for a transition from the state I to the state I' via either photoionization, photoexcitation, or relaxation (i.e., Auger-Meitner decay or fluorescence). In a configuration-based approach $\{I\}$ are defined by all possible electronic configurations, whereas in our state-resolved approach $\{I\}$ are defined by the electronic configurations together with additional quantum numbers needed for specifying zeroth-order LS eigenstates (L,S,M_L,M_S,κ).

There are two ways for solving the set of coupled rate equations of Eq. (6): either directly with precalculated rates and cross sections [32] or via a Monte Carlo method [27]. The latter has been extended to a more efficient on-the-fly approach [9], i.e., quantities are only calculated when needed, which will be further explained in the following subsection. The Monte Carlo on-the-fly method is especially crucial for heavy atoms, for which the number of coupled rate equations to be solved becomes extremely large. The number of coupled rate equations is equivalent to the number of all possible states or all possible configurations, depending on the definition of $\{I\}$.

For the configuration-based approach, an estimate of this number can be found in Ref. [22] (also see Ref. [24] for the case of resonant excitations). Let us consider an initial electronic configuration, $1s^{N_1}2s^{N_2}2p^{N_3}3s^{N_4}3p^{N_5},\ldots$, where the number of electrons is given by $N_{\rm elec}=\sum_j^{\rm all}N_j$. During x-ray multiphoton ionization dynamics, different electronic configurations can be constructed by adding zero, one, or up to N_j electrons for each jth subshell. Here, the index j labels all subshells that can be ionized by the given photon energy via one-photon ionization and no resonant excitation is assumed. The number of all possible configurations is then evaluated by

$$N_{\rm config}=\prod_j\left(N_j+1\right). \tag{7}$$

For example, Ne has $1s^22s^22p^6$ and $N_{\rm config}=3\times 3\times 7=63$ if all subshells are accessible for one-photon ionization.

For the state-resolved approach, the number of possible zeroth-order LS eigenstates (equal to the number of electronic Fock states) can be estimated as follows. For each jth subshell with (n,l), there are $N_j^{\rm max}(=4l+2)$ spin orbitals with different $m_l(\in\{-l,-l+1,\ldots,l-1,l\})$ and $m_s(=\pm\frac{1}{2})$, which equals the maximum occupancy. By adding zero, one, or up to N_j electrons in the jth subshell, the number of possible states is given by the sum of the numbers of possibilities to distribute added electrons into $N_j^{\rm max}$ spin orbitals (each spin orbital has a maximal occupation number of one),

$$N^j_{\rm state}=\sum_{k=0}^{N_j}\binom{N_j^{\rm max}}{k}, \tag{8}$$

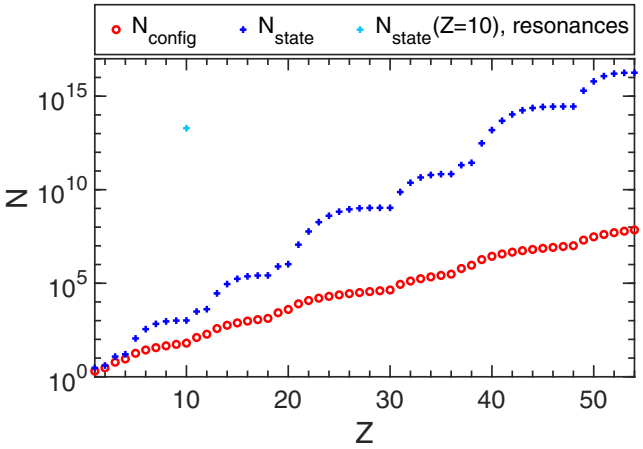

FIG. 1. Number of configurations N_{config} (red dots) and number of states N_{state} (blue crosses) as a function of the nuclear charge Z, assuming that all electrons are actively involved in the ionization dynamics. Only the nonresonant case is shown and the ground-state configurations are given by the Aufbau principle. For the resonant case, solely the point of N_{state} for neon ($Z = 10$) with $n_{\max} = 7$ and $l_{\max} = 2$ is marked (light blue).

where $\binom{a}{b}$ is a binomial coefficient. Then, the number of all possible states is given by multiplying the N^j_{state} for all j (no resonant excitation is considered),

$$N_{\text{state}} = \prod_j \sum_{k=0}^{N_j} \binom{N_j^{\max}}{k}. \tag{9}$$

If we consider the ground-state configuration, all subshells are fully occupied ($N_j = N_j^{\max}$), except for the outermost shell (index j' in what follows), which may be partially occupied. For a closed subshell ($N_j = N_j^{\max}$), $N^j_{\text{state}} = 2^{N_j}$. Thus, the number of all possible states is written as

$$N_{\text{state}} = \left[\prod_{j\neq j'} 2^{N_j}\right] \times \left[\sum_{k=0}^{N_{j'}} \binom{N_{j'}^{\max}}{k}\right]. \tag{10}$$

If the system has no partially occupied subshells initially and all the subshells are accessible for one-photon ionization, then it is further simplified to $N_{\text{state}} = 2^{N_{\text{elec}}}$. For example, Ne has 10 electrons and $N_{\text{state}} = 2^{10} = 1024$.

If resonant excitations are taken into account, a similar expression to Eq. (8) can be directly used. Let N_{so} be the number of available spin orbitals given by computational parameters $n_{\max}$ and $l_{\max}$, and N_{elec} be the number of accessible electrons for one-photon ionization or resonant excitation. Then, the number of states is given by

$$N^{\text{res}}_{\text{state}} = \sum_{k=0}^{N_{\text{elec}}} \binom{N_{\text{so}}}{k}. \tag{11}$$

Figure 1 shows the number of configurations and states as a function of the nuclear charge Z for the nonresonant cases. The ground-state electronic configurations are constructed by the Aufbau principle. For all Z the photon energy is assumed to be large enough to ionize all subshells, including the $1s$ subshell. Both N_{config} and N_{state} grow exponentially, but N_{state} is much larger than N_{config} for a given Z. For the resonant case, this number explodes even for a low-Z system like Ne with limited computational parameters ($n_{\max} = 7$ and $l_{\max} = 2$; $N_{\text{so}} = 100$). With them, $N_{\text{state}} \simeq 1.9 \times 10^{13}$, which is marked in Fig. 1. Therefore, even for low Z it is inevitable to employ a Monte Carlo on-the-fly scheme for state-resolved ionization dynamics when including resonant excitations.

D. State-resolved Monte Carlo implementation

In the state-resolved approach, the number of coupled rate equations [Eq. (6)] that have to be solved is equal to the number of states [Eq. (10)], as depicted in Fig. 1. We implement a state-resolved Monte Carlo on-the-fly algorithm within XATOM [42]. This allows us to apply our state-resolved ionization dynamics framework to heavier atoms, like argon ($Z = 18$) or xenon ($Z = 54$), and to the resonant case.

In general, in a Monte Carlo approach for ionization dynamics, we stochastically consider many trajectories for possible ionization pathways, i.e., sequences of repeated one-photon ionization and inner-shell relaxation events. The populations of entities, such as charge state, electronic configuration, or electronic state, are then obtained by averaging over an ensemble of trajectories. A detailed description of the configuration-based Monte Carlo method can be found in Ref. [27]. Extending it to a state-resolved Monte Carlo algorithm basically requires to replace a configuration index with a combination of configuration and state indexes through the whole algorithm, i.e., $I = I_{\text{config}} \to I = (I_{\text{config}}, I_{LS})$. Here, I_{config} indicates an electronic configuration and I_{LS} indicates the additional quantum numbers needed for specifying a zeroth-order LS eigenstate. Note that we do not include in I_{LS} the spin projection M_S and, hence, do not distinguish between states with different spin projection. Because of a lack of spin coupling for all involved interaction Hamiltonians, states with different spin projections always have the same transition probabilities and, consequently, behave exactly the same during the ionization dynamics. Thus, M_S can be neglected in the description of the individual states. Moreover, cross sections and rates based on configurations need to be replaced by individual state-to-state cross sections and rates [43].

For the sake of completeness, we sketch our state-resolved Monte Carlo on-the-fly implementation:

(a) Start with the initial electronic configuration I_{config}, i.e., that for the neutral atom, and calculate all zeroth-order LS eigenstates for the initial configuration via the improved electronic-structure implementation (see Sec. II A and Ref. [43]). If there is more than one LS eigenstate, the state with the minimal first-order-corrected energy $E_{LS\kappa}$ is selected. If $L \neq 0$, the M_L projection quantum number is randomly chosen as an initial condition for each trajectory. If $S \neq 0$, then the maximal spin projection is chosen for convenience (it does not influence the ionization dynamics). In this way we set up the initial state $I = (I_{\text{config}}, I_{LS})$. In order to reduce the computational effort, store the information about the electronic structure, so that it can be directly reused for further trajectories.

(b) Set up an initial value for the time t and the time step Δ_t.

(c) Calculate all individual state-to-state cross sections σ_k and transition rates Γ_k for all transitions from the current state $I = (I_{\text{config}}, I_{LS})$ to the accessible final state $I^k = (I^k_{\text{config}}, I^k_{LS})$. Transition energies are also calculated based on the first-order-corrected energies for the current state, i.e., $E_{LS\kappa}$, and the final state, i.e., $E_{L_k S_k \kappa_k}$. Note that we employ the same orbital set optimized for the current (initial) state to evaluate the final state energy [43]. Here, k is used as a label for one of the processes, running from 1 to the number of all possible individual state-resolved transitions. The index k in L_k, S_k, etc. indicates that the new state is reached via the kth process. Also, the information about the possible processes is stored for later use.

(d) Cross sections and rates determine the transition probability p_k at time t for the kth process via

$$p_k = \begin{cases} \Gamma_k \Delta_t & \text{for decay process,} \\ \sigma_k J(t) \Delta_t & \text{for photoionization/absorption,} \end{cases} \tag{12}$$

with $J(t)$ being the time-dependent photon flux.

(e) Select a process k randomly, taking into consideration the different transition probabilities p_k of all possible processes (for more details, see Ref. [27]).

(f) Counters for the time-dependent charge-state distribution (CSD) and time-resolved spectra are considered as follows. The time- and energy-bin counter for the photoelectron, the Auger-Meitner electron, or the fluorescence photon is increased by one, according to the electron kinetic energy or emitted photon energy of the selected kth process at a given time t. This counter will be used for generating time-resolved spectra in Sec. IV B. Integrating this counter over time corresponds to the spectra after time evolution shown in Sec. III B. Regarding time-dependent CSDs in Sec. IV A, the charge state of the given I is examined at every time step of time bins and the corresponding counter is increased by one.

(g) Continue by proceeding to the kth process. Set up the new electronic configuration, i.e, $I_{\text{config}} = I^k_{\text{config}}$, and the new zeroth-order LS eigenstate $|L_k S_k M_{L_k} \kappa_k\rangle$, i.e., $I_{LS} = I^k_{LS}$. To get proper first-order-corrected energies, a new electronic-structure calculation has to be performed and stored.

(h) Set up a new Δ_t based on the total transition probability, i.e., the sum over all p_k's. The new Δ_t is smaller than or equal to the initial Δ_t chosen in (b). The updated Δ_t should guarantee that the total transition probability stays significantly smaller than unity when the updated Δ_t is used. Then go to the next time step $t \to t + \Delta_t$.

(i) Repeat the time evolution [(c)–(h)], until the total transition probability is zero. When no process is available any longer, the Monte Carlo trajectory ends. The counter for the final charge is increased by one, which will produce asymptotic CSDs in Sec. III A.

(j) Run many more trajectories [(a)–(i)] and at every 100 trajectories, or in principle any other step size, check whether the final CSD is converged. If this is the case, stop the Monte Carlo iteration.

(k) Results for ensemble-averaged CSDs and spectra are obtained by dividing the corresponding counters by the total number of trajectories.

In what follows, we employ a maximal number of Monte Carlo trajectories of 100 000 and a minimal CSD convergence of 10^{-4} for asymptotic results in Sec. III and 5×10^{-5} for time-resolved results in Sec. IV, respectively. The actual numbers of Monte Carlo trajectories, being necessary to achieve the demanded convergence, range from 12 500 to 50 300. For time-independent spectra, 1-eV bins are used, whereas 2-eV bins are used for the time-resolved spectra. For the time-resolved CSD and spectra, fixed temporal bins are chosen according to the pulse duration.

III. ASYMPTOTIC RESULTS

We first contrast the configuration-based and state-resolved Monte Carlo methods regarding temporally asymptotic results for neon, i.e., CSDs (Sec. III A), and electron and photon spectra (Sec. III B) at the end of time evolution when the pulse is over and all decay processes are completed. The state-resolved calculation is performed with the present implementation, whereas for the configuration-based calculation, we employ the original version of XATOM. We do not include direct nonsequential two-photon absorption [15,52] because its contribution is much smaller than one-photon absorption if the latter is available (for example, inner-shell nonsequential two-photon absorption versus valence one-photon absorption). Above-threshold ionization in the x-ray regime [53] is also negligible in the range of intensities that current XFEL facilities can produce. For simplicity, we also do not include higher-order many-body processes such as double photoionization [54] and double Auger-Meitner decay [55] via shake-off and knockout mechanisms. Note that the branching ratio of double photoionization after Ne K-shell photoabsorption is about 23% and that of double Auger-Meitner decay is about 6% [56]. Including shake-off processes in the rate-equation approach markedly improves comparison with experimental CSDs [15,29], especially regarding the odd-even charge-state relation. Finally, the rate-equation approach employed here does not capture coherent effects such as Rabi flopping [57–62]. For a stochastic ensemble of XFEL pulses based on the self-amplified spontaneous emission principle, these are minor effects [57–59].

For x-ray beam parameters, we use a temporal Gaussian pulse envelope with 10 fs FWHM and a fluence of 10^{12} photons/μm^2. Note that these are typical x-ray parameters at current XFEL facilities [1–3]. The volume integration [63], which is necessary for quantitative comparison with experimental data, is not considered here. Following Ref. [8], three different photon energies are examined: (i) 800 eV is below the 1s threshold of neutral Ne and all Ne ions, (ii) 1050 eV lies in the middle of the 1s threshold region of a series of Ne ions, and (iii) 2000 eV is above the 1s threshold of all Ne ions. Note that in case (ii) resonant excitations for some transiently formed ions play a relevant role [16]. Thus, we include resonant bound-to-bound excitations in this case.

The computational time was about 6 min for 800 eV (21 000 Monte Carlo trajectories), about 13 min for 2000 eV (50 000 trajectories), and about 7 h for 1050 eV (18 400 trajectories) on an Intel Xenon E5-2609 CPU (single core).

A. Comparison of charge-state distributions

Figure 2 presents Ne CSDs at the three different photon energies. The population probability P_q of the charge state q

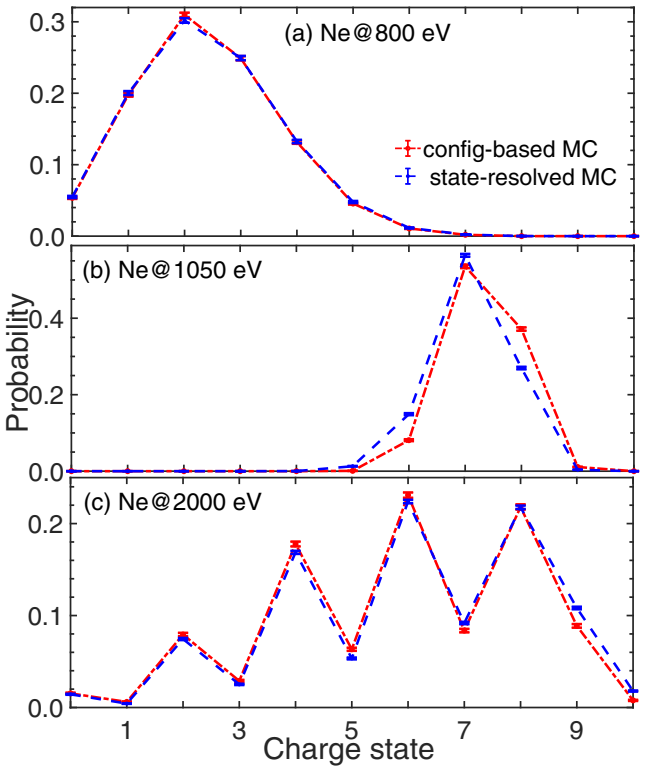

FIG. 2. Comparison of Ne CSDs obtained with the configuration-based (red) and the state-resolved (blue) Monte Carlo calculations: (a) 800 eV, (b) 1050 eV, and (c) 2000 eV. In all cases, the Gaussian-shaped pulse has a duration of 10 fs FWHM and a fixed fluence of $F = 10^{12}$ photons/μm^2 is used. For (b), resonant excitations up to $n_{max} = 7$ and $l_{max} = 2$ are considered and an energy bandwidth of 1% is assumed. The error bar indicates the statistical error.

is given by the sum of all P_I's (configurational population or state population) belonging to q. The error bars represent the statistical error estimate [64] for each charge state q, given by $\epsilon_q = \sqrt{P_q(1-P_q)/(N_{traj}-1)}$, where N_{traj} is the number of Monte Carlo trajectories. Comparison in Fig. 2 shows that the state-resolved calculation is in overall good agreement with the configuration-based calculation, in particular, when the photon energy is off resonance [Figs. 2(a) and 2(c)]. At 2000 eV, population probabilities differ beyond the error bars only for high charge states. This can be explained by slightly higher transition probabilities in the state-resolved approach caused by the use of first-order-corrected energies and the appearance of a generally nonuniform distribution of individual states for the intermediate configurations.

On the other hand, the differences between the two approaches are noticeable when resonant excitations play a role [Fig. 2(b)]. Resonant photoexcitation cross sections are sensitive to the differences between calculated transition energies and the given photon energy. As a consequence, different resonant excitations can be encountered in the state-resolved and configuration-based ionization dynamics calculations (see Table IV in the Appendix). For example, the production of Ne^{8+} is enhanced in the configuration-based calculation at the expense of suppression of Ne^{6+}. More detailed analyses regarding relevant resonances are provided later when electron and photon spectra are discussed in Sec. III B.

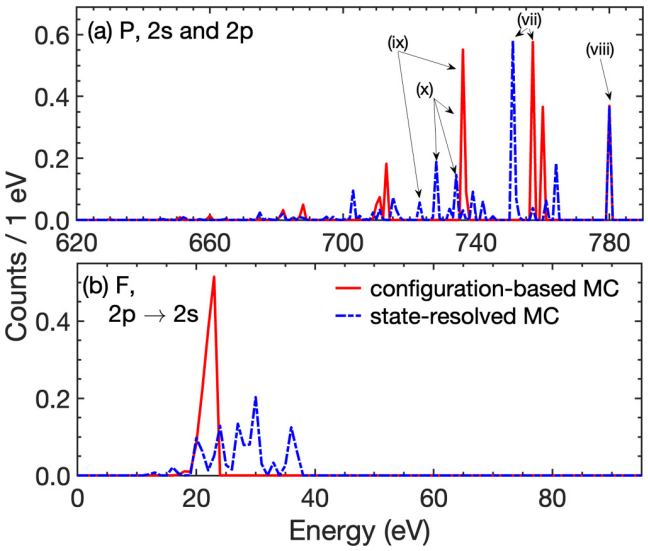

FIG. 3. (a) Photoelectron (P) and (b) fluorescence (F) spectra of Ne at a photon energy of 800 eV. Other x-ray parameters are the same as used in Fig. 2. The peak labels in (a) are explained in Table I in the Appendix.

B. Comparison of electron and photon spectra

Figure 3 shows (a) photoelectron and (b) fluorescence spectra at an incoming photon energy of 800 eV and compares the state-resolved (blue dashed line) and configuration-based (red solid line) calculations. At this photon energy, 1*s* ionization is not available, so there is no Auger-Meitner spectrum. In the photoelectron spectrum in Fig. 3(a), some of the dominant peaks are labeled with roman numbers; the corresponding physical processes are specified in Table I in the Appendix. The configuration-based approach employs transition energies computed from zeroth-order energies, i.e., the sum of orbital energies according to the involved configurations. On the other hand, in the state-resolved approach, transition energies are computed based on the first-order-corrected energies for the initial and final states. The energy levels that are degenerate in zeroth-order energies split up in first-order many-body perturbation theory. Consequently, peaks in the state-resolved spectra are not only shifted, but spectra are also broadened with more peaks. The energy shifts are clearly visible in Fig. 3(a), except for (viii) $2p$ ionization where two peaks coincide. Splittings also clearly manifest in the photoelectron lines [e.g., peaks (x) in Fig. 3(a)] and in the fluorescence spectra of Fig. 3(b), where in the configuration-based spectra many peaks coincide around 22 eV. Note that this behavior of energy shifts and splittings in the state-resolved spectra is a general feature, so it can be found at other photon energies as will be shown below.

Figure 4 shows (a) photoelectron, (b) Auger-Meitner electron, and (c) fluorescence spectra at 2000 eV with the same x-ray beam parameters as used for Fig. 2(c). The energy shifts and splittings with the state-resolved approach are clearly exhibited in the Auger-Meitner spectrum. Since the

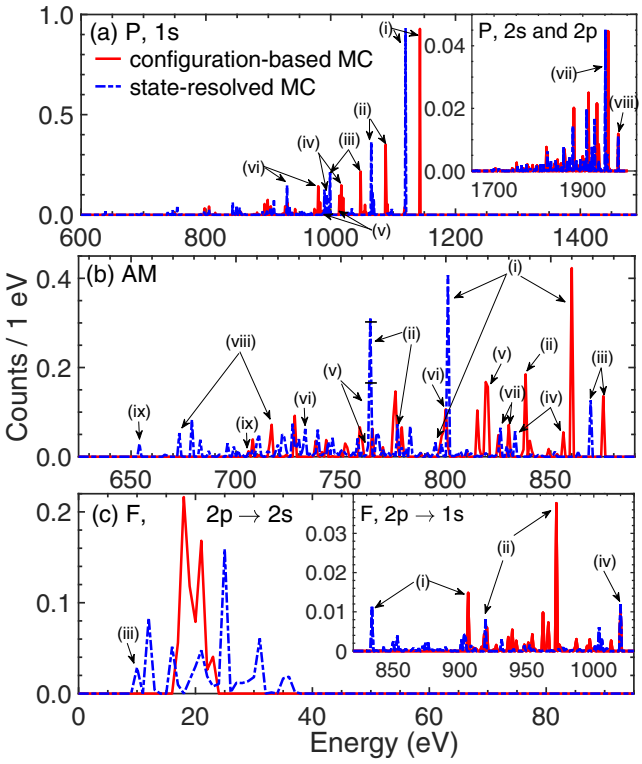

FIG. 4. (a) Photoelectron (P), (b) Auger-Meitner electron (AM), and (c) fluorescence (F) spectra of Ne at a photon energy of 2000 eV. Other x-ray parameters are the same as used in Fig. 2. The peak labels are explained in Tables I–III in the Appendix.

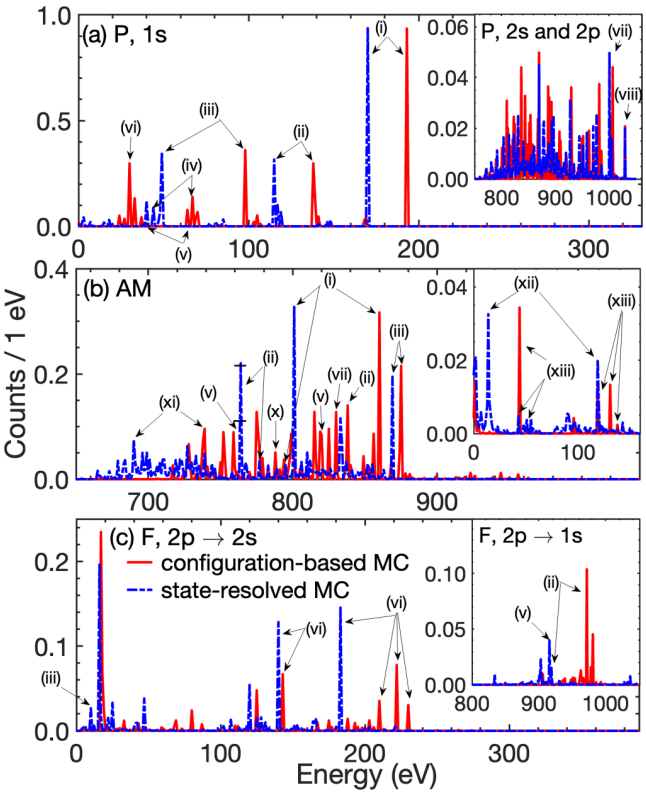

FIG. 5. (a) Photoelectron (P), (b) Auger-Meitner electron (AM), and (c) fluorescence (F) spectra of Ne at a photon energy of 1050 eV. Other parameters are the same as used in Fig. 2. The peak labels are explained in Tables I–III in the Appendix.

Auger-Meitner peaks in Fig. 4(b) are not well separated and they merge within a narrow energy window, resulting in a complex spectrum, it is critical to apply improved transition energy calculations to interpret individual peaks. For the single-core-hole Auger-Meitner line (i), the state-resolved result shows considerable improvement towards experimental data as demonstrated in Ref. [43]. The energy shift from the configuration-based result to the state-resolved result is −59 eV. For the double-core-hole Auger-Meitner line (iii), which is also called *KK–KLL* hypersatellite [65], the energy shift is somewhat smaller (−6 eV). Even in this case, the state-resolved value (868.84 eV) is closer to the experimental values (870.50 eV [65] and 870 eV [66]) than the configuration-based value (875.27 eV). Note that the prominent peak of the state-resolved approach at 764 eV in Fig. 4(b) is the sum of Auger-Meitner lines (ii) and (v) and other minor contributions that are not assigned here. Regarding the fluorescence spectra, peak (ii) in Fig. 4(c) is considerably reduced in the state-resolved approach. This is because the initial configuration of (ii) has two states, ^1P and ^3P (see Table III in the Appendix), and the latter cannot relax via $2p \rightarrow 1s$ fluorescence (final state: ^1S) since a triplet to singlet transition is forbidden in a nonrelativistic calculation. Once the triplet initial state (Ne^{8+} $1s^1 2p^1$ ^3P) is formed during the state-resolved dynamics, it has to relax via $2p \rightarrow 2s$ fluorescence, giving rise to peak (iii) in Fig. 4(c). Thus, the changes of the peak heights provide more details about underlying physical processes between state-resolved and configurations-based ionization dynamics. The fluorescence peak positions of (iv) in Fig. 4(c) coincide for both approaches.

In Fig. 5, we investigate the effects of resonant excitations on the electron and photon spectra at 1050 eV. The x-ray beam and computational parameters are the same as used in Fig. 2(b). In the state-resolved and configuration-based approaches, different resonant excitations are predominantly involved in the ionization dynamics at 1050 eV owing to different transition energy calculations (see Table IV in the Appendix). The different resonant excitations are all reflected in the spectra in Fig. 5. For example, photoelectron peak (vi) in Fig. 5(a), which is prominent in the configuration-based approach, is absent in the state-resolved approach. This is because (vi) refers to the $1s$ ionization of Ne^{3+} $1s^1 2l^6$ ($l = s, p$) and its threshold is higher than the photon energy in the state-resolved approach. Instead, resonant excitation of single-core-excited Ne^{3+} predominantly via a $1s \rightarrow 4p$ resonant transition is the alternative process (see Table IV in the Appendix). The same transition can also occur at Ne^{6+} $1s^2 2l^2$ within the state-resolved approach. These $1s \rightarrow 4p$ transitions at Ne^{3+} and Ne^{6+} are responsible for the Auger-Meitner decay involving $4p$, which explains the emergence of (xii) in Fig. 5(b), only in the state-resolved approach. On the other hand, in the configuration-based approach, the $1s \rightarrow 3p$ transition is dominant at Ne^{5+} $1s^1 2l^4$ and the resulting double-core-hole-excited state of Ne^{5+} $1s^0 2l^4 3p^1$ relaxes via

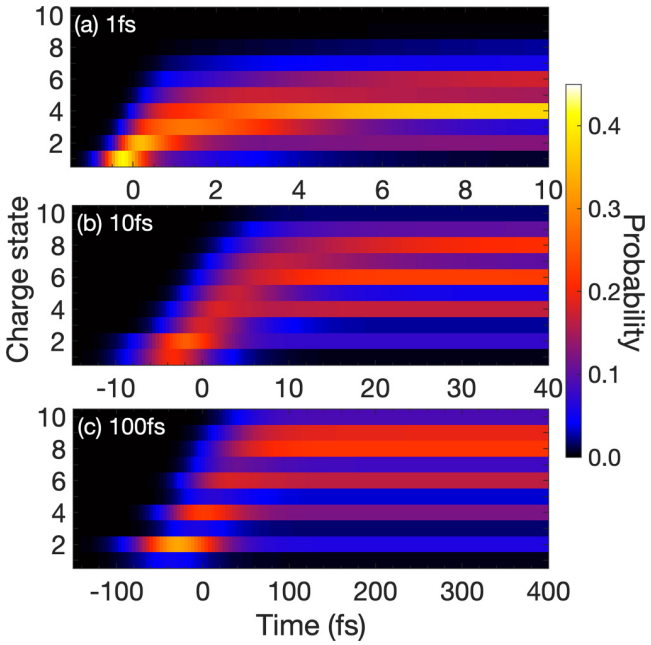

FIG. 6. Time evolution of Ne CSDs at 2000 eV for pulses duration (FWHM) of (a) 1 fs, (b) 10 fs, and (c) 100 fs. For all cases, the state-resolved Monte Carlo implementation is employed and a fixed fluence of 10^{12} photons/μm^2 is used.

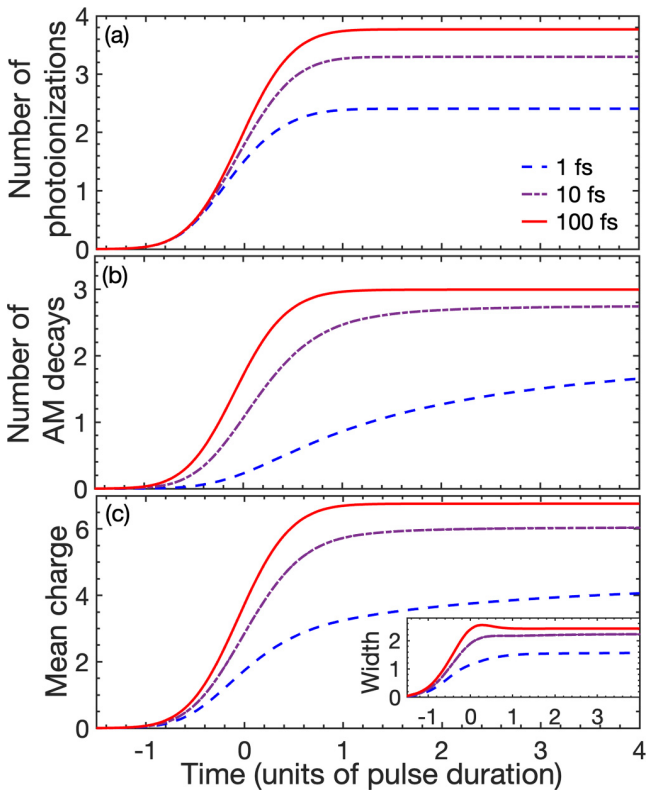

FIG. 7. Mean number of events for (a) photoionization and (b) Auger-Meitner decay in Ne at 2000 eV as a function of time. (c) Mean charge and width (inset) of the time-dependent CSDs of Ne shown in Fig. 6. For a better comparability, the time relative to the pulse duration (FWHM) is considered on the x axis.

Auger-Meitner decay, which corresponds to (x) in Fig. 5(b). Note that there is no (x) peak in the state-resolved approach in Fig. 5(b). At Ne^{7+}, further resonant excitation can happen for both approaches (see Table IV in the Appendix). The resulting single-core-hole-excited Ne^{7+} is either $1s^12p^13p^1$ for the state-resolved approach or $1s^13p^1np^1$ ($n = 3, 4, 5$) for the configuration-based approach. The latter can relax via Auger-Meitner decay [peak (xiii) in Table II], which contributes to the higher yield of Ne^{8+} in the configuration-based approach in Fig. 2(b). However, for the former case, it is most likely that $1s^12p^13p^1$ has a ^2P state, in which the Auger-Meitner decay is forbidden. Thus, in the state-resolved ionization dynamics, the state of $Ne^{7+}1s^12p^13p^1\ ^2P$ has to relax via fluorescence, giving rise to peak (v) in Fig. 5(c), which also explains why the yield of Ne^{8+} is suppressed in the state-resolved approach in Fig. 2(b). Note that regarding resonances, the state-resolved approach is in better accordance with the findings in Ref. [16].

For a short summary, photoelectron, Auger-Meitner electron, and fluorescence spectra provide a plethora of detailed information on x-ray multiphoton ionization dynamics. We demonstrate that resonant excitations and spectral information are described more accurately by the state-resolved implementation due to a general improvement of transition energies and the capture of individual state-resolved features, i.e., transition probabilities. In the next section, we explore time-resolved spectra based on the state-resolved Monte Carlo implementation.

IV. TIME EVOLUTION

We employ the state-resolved Monte Carlo implementation to examine the time evolution of CSDs and spectra for different pulse durations. We choose pulse durations of 1 fs, 10 fs, and 100 fs FWHM, covering the range of typical pulse durations for current XFEL facilities [1–6]. We consider Ne at a photon energy of 2000 eV and a fluence of $F = 10^{12}$ photons/μm^2, so that in principle all electrons can be ionized via x-ray sequential multiphoton ionization, i.e., a repeated sequence of one-photon ionization and inner-shell relaxation events. In this case, no resonant excitation is involved in the ionization dynamics.

A. Time evolution of charge-state distribution

Figure 6 presents the Ne CSDs as a function of time for pulse durations of (a) 1 fs, (b) 10 fs, and (c) 100 fs FWHM. The temporal peak is located at $t = 0$ fs. For clarity, the population of neutral Ne is not included. Note that the sum of charge populations, including the neutral atom, is unity at every time step. The charge distribution building up looks discrete, which indicates that the populations of odd charges are much smaller than those of even charges. This is a consequence of the fact that Auger-Meitner decay follows inner-shell photoionization, when the pulse duration is sufficiently longer than the Auger-Meitner lifetime. One can see that the time-dependent CSD is shifted to lower charges for a shorter pulse duration. For a short pulse duration (1 fs), the CSD peaks around +4 and highly charged ions are barely found, as shown in Fig. 6(a). It can be clearly seen that the charged ions are formed sequentially as time goes by, espe-

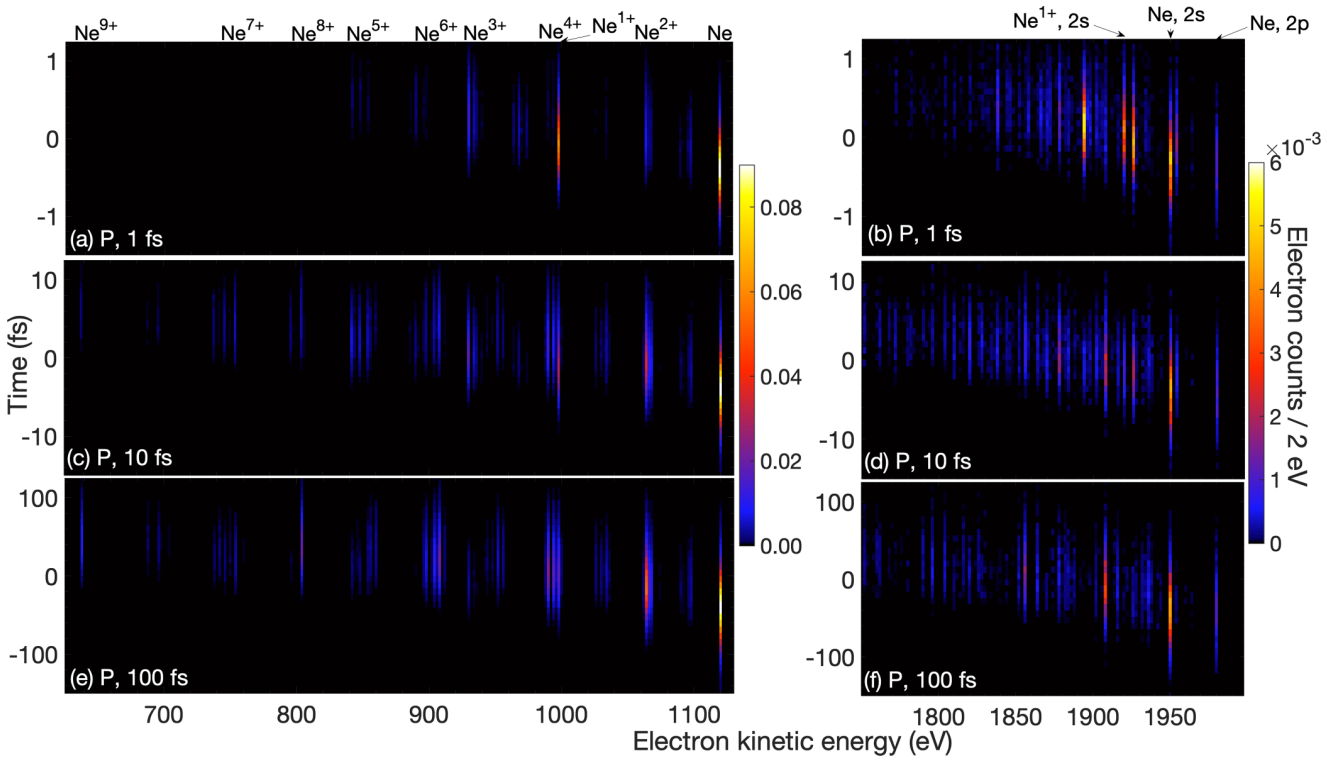

FIG. 8. Time-resolved photoelectron spectra (P) of Ne at a photon energy of 2000 eV for pulse durations (FWHM) of (a and b) 1 fs, (c and d) 10 fs, and (e and f) 100 fs. In (a), (c), and (e), the peaks belong to $1s$ ionization, while those in (b), (d), and (f) belong to $2s$ and $2p$ ionization. The peaks are labeled by the involved initial ion, i.e., Ne^{q+}: electronic configuration $1s^2 2l^{8-q}$ for even charges or $1s^1 2l^{9-q}$ for odd charges. A fluence of 10^{12} photons/μm^2 is used.

cially near the peak of the pulse. For a long pulse duration (100 fs), however, the distribution becomes broader with a less pronounced peak at +8, as shown in Fig. 6(c). These observations are all indicative of frustrated absorption [21] or intensity-induced x-ray transparency [8]. The degree of ionization is reduced for shorter pulse duration (i.e., higher intensity) because $1s$ photoionization defeats Auger-Meitner decay as the intensity increases. This has two consequences. First, a double-core-hole state is formed and, thus, the $1s$ photoionization cross section is reduced (it is zero for $1s^0$). In Fig. 7(a), the mean number of photoionization events is depicted as a function of time for the three pulse durations. It may be seen that the photoionization number decreases as the pulse duration becomes shorter. At the same time, the suppression of ionization is also caused by the reduction of the number of Auger-Meitner decays, depicted in Fig. 7(b). These two mechanisms are responsible for the decreased mean charge [Fig. 7(c)] as the pulse is decreased.

Another interesting observation here is that most changes in the time-dependent CSD take place within a time interval of $\pm 1 \times$ FWHM. However, the shorter the pulse, the more extended the time interval needed to reach the final charge, because the Auger-Meitner lifetime is often tens of femtoseconds (see more details in Sec. IV B). In Figs. 7(b) and 7(c), the 1-fs curve is not converged to the temporally asymptotic mean value even at $4 \times$ FWHM, in contrast to the longer pulse durations. Therefore, in Fig. 6(a), a longer time interval is considered for the 1-fs result.

B. Time-resolved electron and photon spectra

In order to complete our understanding of the x-ray multiphoton ionization dynamics, we calculate time-resolved photoelectron (Fig. 8), Auger-Meitner electron (Fig. 9), and fluorescence spectra (Fig. 10) for all three pulse durations. For all figures, the vertical axis is the time, using $0.08 \times$ FWHM bins, while the horizontal axis is the electron kinetic energy (Figs. 8 and 9) or the photon energy (Fig. 10), using 2-eV bins. Note that all the spectra showcase the number of emitted electrons or photons in a time interval relative to the pulse duration since the time binning is adapted for each pulse duration.

Let us start with the time-resolved photoelectron spectra in Fig. 8. The $1s$ photoelectron spectra can be grouped according to the peaks belonging to the ionization of Ne^{q+} in a possible configuration $1s^2 2l^{8-q}$ dominantly for even charges or $1s^1 2l^{9-q}$ dominantly for odd charges (with $l = s, p$). Note that the former leads to the formation of single-core-hole states, while double-core-hole states are produced via the latter. It is apparent from the spectra that lines corresponding to low odd charges (Ne^{1+} and Ne^{3+}) emerge more with shorter pulse duration in Fig. 8(a). The increased number of outer-shell ionizations of lowly charged ions can be observed in Fig. 8(b). On the other hand, the lines corresponding to the photoionization of highly charged ions appear more for longer pulse durations as shown in Figs. 8(c) and 8(e), which is consistent with the observation in Fig. 6.

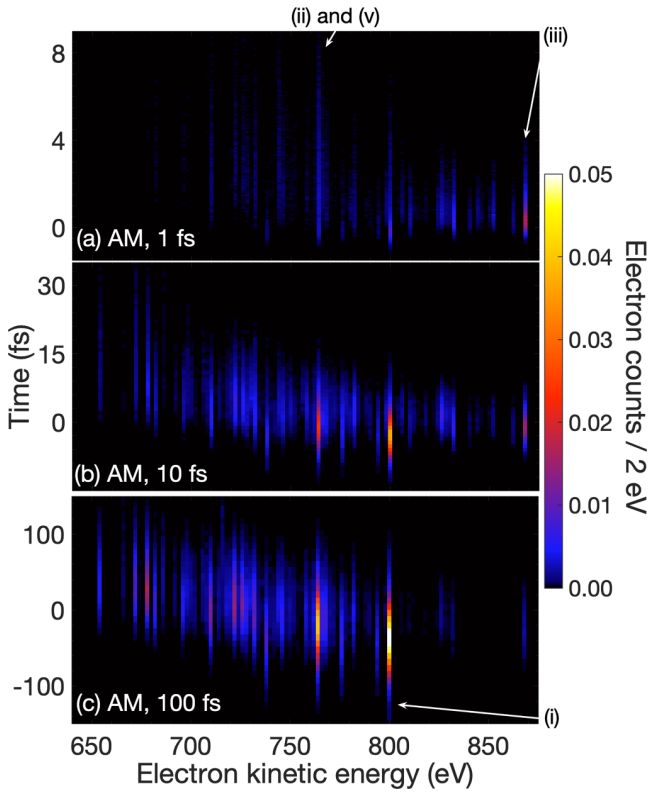

FIG. 9. Time-resolved Auger-Meitner electron spectra (AM) of Ne at a photon energy of 2000 eV for pulse durations (FWHM) of (a) 1 fs, (b) 10 fs, and (c) 100 fs. Some peaks are labeled by the transitions listed in Table II in the Appendix. A fluence of 10^{12} photons/μm^2 is used.

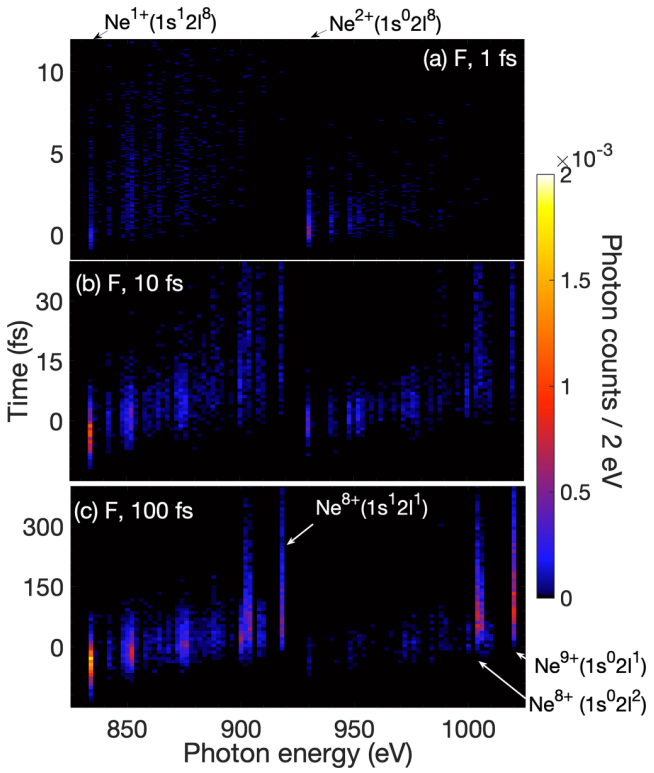

FIG. 10. Time-resolved $2p \rightarrow 1s$ fluorescence spectra (F) of Ne at a photon energy of 2000 eV for pulse durations (FWHM) of (a) 1 fs, (b) 10 fs, and (c) 100 fs. Some peaks are labeled by the involved initial configurations. A fluence of 10^{12} photons/μm^2 is used.

Figure 9 shows the time-resolved Auger-Meitner spectra. For long pulse durations, Auger-Meitner decay immediately follows inner-shell ionization and many lines appear in the spectrum, as shown in Fig. 9(c). Here, *immediately* is meant relative to the pulse duration, i.e., when the Auger-Meitner lifetime is sufficiently short in comparison to both the pulse duration and the inverse of the resulting inner-shell photoionization rate, so that Auger-Meitner decay can beat further photoionization. When several Auger-Meitner decays are possible for an initial ion state, lines for more probable processes appear a bit earlier in time. When the pulse duration is decreased, however, Auger-Meitner decay that takes place on longer time scales than the short pulse duration barely occurs during the pulse. Consequently, the number of processes per time bin is reduced, resulting in weaker lines, covering a longer time range, in Figs. 9(a) and 9(b). This reduction of Auger-Meitner decays suppresses refilling of the $1s$ shell and, thus, further inner-shell photoabsorption, which is one of the mechanisms underlying frustrated absorption as discussed in the previous section. Note that in our state-resolved calculation the time scales for Auger-Meitner decay for Ne ions are in the range from 818 as (Ne^{2+} $1s^02s^22p^6$) to 46 fs (Ne^{7+} $1s^12s^12p^1$). Thus, most Auger-Meitner decays still take place within 10 fs, as shown in Fig. 9(b). Yet another interesting point is that the decay of the double-core-hole state of Ne^{2+}, i.e., peak (iii), is clearly visible for 1 fs and 10 fs, but is almost absent for 100 fs. This hypersatellite line is located at the highest energy and is well separated from other lines, which provided direct evidence of double-core-hole formation [8,65,66]. Decays of other double-core-hole states, with lower energies than peak (iii), can also be observed mainly for short pulse durations.

Finally, we turn to the fluorescence spectra for inner-shell relaxation via $2p \rightarrow 1s$ transition as shown in Fig. 10. We do not show the $2p \rightarrow 2s$ fluorescence spectra that are mainly generated long after the pulse on time scales up to $\sim$10 ns. For the $2p \rightarrow 1s$ fluorescence, we can make very similar observations as for the Auger-Meitner spectra, even though Auger-Meitner decay is much more dominant. However, due to lower fluorescence rates in comparison with Auger-Meitner rates, relaxation of highly charged ions via fluorescence takes place on relatively longer time scales even beyond that shown in Fig. 10. Interestingly, single-core-hole and double-core-hole spectra for Ne ions are well separated and ordered by charge, i.e., the higher the charge state, the higher the photon energy for a fixed number of core electrons. (An analogous effect was observed in XFEL experiments on warm dense aluminum [67].) The $1s$–$2p$ fluorescence energy is given by $\omega_{\text{fluo}} = E_I - E_F$, where the initial state I has one or two $1s$ holes and the final state F has one $1s$ hole less than I. When I has a double $1s$ vacancy, E_I contains a strong Coulomb repulsion penalty because the two $1s$ holes are spatially close

TABLE I. Ionization potentials of selected processes calculated with the state-resolved approach, $E_{\mathrm{IP}}^{(1)}$, and the configuration-based approach, $E_{\mathrm{IP}}^{(0)}$. Photoemission lines in Figs. 3(a), 4(a), and 5(a) are assigned by $E = \omega_{\mathrm{in}} - E_{\mathrm{IP}}$ and their labels are listed below.

Label	Process	$E_{\mathrm{IP}}^{(1)}$(eV)	$E_{\mathrm{IP}}^{(0)}$ (eV)
(i)	Ne, $1s^22s^22p^6 \rightarrow 1s^12s^22p^6$	880 ($^1S \rightarrow {}^2S$)	857
(ii)	Ne^{2+}, $1s^22s^22p^4 \rightarrow 1s^12s^22p^4$	935 ($^1D \rightarrow {}^2D$)	912
(iii)	Ne^{1+}, $1s^12s^22p^6 \rightarrow 1s^02s^22p^6$	1001 ($^2S \rightarrow {}^1S$)	952
(iv)	Ne^{4+}, $1s^22s^12p^3 \rightarrow 1s^12s^12p^3$	1006 ($^1D \rightarrow {}^2D$)	983
(v)	Ne^{4+}, $1s^22s^22p^2 \rightarrow 1s^12s^22p^2$	1010 ($^1D \rightarrow {}^2D$)	986
(vi)	Ne^{3+}, $1s^12s^22p^4 \rightarrow 1s^02s^22p^4$	1070 ($^2D \rightarrow {}^1D$)	1020
(vii)	Ne, $1s^22s^22p^6 \rightarrow 1s^22s^12p^6$	49 ($^1S \rightarrow {}^2S$)	43
(viii)	Ne, $1s^22s^22p^6 \rightarrow 1s^22s^22p^5$	20 ($^1S \rightarrow {}^2P$)	20
(ix)	Ne^{1+}, $1s^22s^12p^6 \rightarrow 1s^22s^02p^6$	72 ($^2S \rightarrow {}^1S$)	64
(x)	Ne^{1+}, $1s^22s^22p^5 \rightarrow 1s^22s^12p^5$	66 ($^2P \rightarrow {}^3P$)	64
		77 ($^2P \rightarrow {}^1P$)	–

to each other. Thus, the fluorescence lines from double-core-hole states are higher than those from single-core-hole states corresponding to the same charge state. As the charge state increases, both E_I and E_F increase, but the increase is less for E_F than E_I because in state F there is more screening by $1s$ electrons than in state I. Consequently, the fluorescence energy gets larger for higher charge states, which are generated at later times. All these features are demonstrated in the time-dependent fluorescence spectra: In each panel of Fig. 10, there are two groups of transition lines—associated with single- and double-core-hole states, respectively—that move toward higher energies with increasing time.

V. CONCLUSION

In this paper, we have presented an implementation of state-resolved Monte Carlo calculations for describing x-ray multiphoton ionization dynamics. Our implementation in the XATOM toolkit employs an improved electronic-structure calculation that is based on first-order many-body perturbation theory. We have compared the new state-resolved and the original configuration-based Monte Carlo calculations for neon at three different photon energies, including a resonant case. The differences in the CSD are negligible when resonances do not matter. Therefore, in these cases the original configuration-

TABLE II. Peak assignment in the Auger-Meitner electron spectra [Figs. 4(b) and 5(b)]. Transition energies for the state-resolved approach, $E_{\mathrm{tr}}^{(1)}$, and the configuration-based approach, $E_{\mathrm{tr}}^{(0)}$, are listed for the underlying process.

Label	Process	$E_{\mathrm{tr}}^{(1)}$ (eV)	$E_{\mathrm{tr}}^{(0)}$ (eV)
(i)	Ne^{1+}, $1s^12s^22p^6 \rightarrow 1s^22s^22p^4$	801($^2S \rightarrow {}^1D$)	860
		795 ($^2S \rightarrow {}^1S$)	–
(ii)	Ne^{1+}, $1s^12s^22p^6 \rightarrow 1s^22s^12p^5$	764 ($^2S \rightarrow {}^1P$)	838
	$\rightarrow 1s^22s^12p^5$	777 ($^2S \rightarrow {}^3P$)	–
(iii)	Ne^{2+}, $1s^02s^22p^6 \rightarrow 1s^12s^22p^4$	869 ($^1S \rightarrow {}^2D$)	875
		863 ($^1S \rightarrow {}^2S$)	–
(iv)	Ne^{2+}, $1s^02s^22p^6 \rightarrow 1s^12s^12p^5$	833 ($^1S \rightarrow {}^2P$)	856
(v)	Ne^{3+}, $1s^12s^22p^4 \rightarrow 1s^22s^22p^2$	764 ($^2D \rightarrow {}^1D$)	820
		758 ($^2D \rightarrow {}^1S$)	–
(vi)	Ne^{3+}, $1s^12s^22p^4 \rightarrow 1s^22s^12p^3$	733 ($^2D \rightarrow {}^1D$)	800
		729 ($^2D \rightarrow {}^1P$)	–
(vii)	Ne^{4+}, $1s^02s^22p^4 \rightarrow 1s^12s^22p^2$	826 ($^1D \rightarrow {}^2D$)	830
(viii)	Ne^{7+}, $1s^12s^12p^1 \rightarrow 1s^22s^02p^0$	673 ($^2P \rightarrow {}^1S$)	717
(ix)	Ne^{7+}, $1s^12s^22p^0 \rightarrow 1s^22s^02p^0$	654 ($^2S \rightarrow {}^1S$)	706
(x)	Ne^{5+}, $1s^02s^22p^23p^1 \rightarrow 1s^12s^12p^13p^1$	–	788
(xi)	Ne^{6+}, $1s^12p^2np^1 \rightarrow 1s^22p^0np^1$	690 ($n = 4$; $^1F \rightarrow {}^2P$)	741 ($n = 5$)
		690 ($n = 4$; $^1D \rightarrow {}^2P$)	739 ($n = 6$)
		–	737 ($n = 7$)
(xii)	Ne^{6+}, $1s^24p^2 \rightarrow 1s^22p^1$	119 ($^3P \rightarrow {}^2P$)	125
		14 ($^3D \rightarrow {}^2P$)	13
(xiii)	Ne^{7+}, $1s^13p^1np^1 \rightarrow 1s^12p^1$	43 ($n = 3$; $^2P \rightarrow {}^1P$)	44 ($n = 3$)
	$1s^13p^1np^1 \rightarrow 1s^12p^1$	51 ($n = 3$; $^2D \rightarrow {}^3P$)	119 ($n = 5$)
		–	131 ($n = 6$)
		–	138 ($n = 7$)

TABLE III. Peak assignment in the fluorescence spectra [Figs. 4(c) and 5(c)]. Transition energies for the state-resolved approach, $E_{\mathrm{tr}}^{(1)}$, and the configuration-based approach, $E_{\mathrm{tr}}^{(0)}$, are listed for the underlying process.

Label	Process	$E_{\mathrm{tr}}^{(1)}$ (eV)	$E_{\mathrm{tr}}^{(0)}$ (eV)
(i)	Ne^{1+}, $1s^1 2s^2 2p^6 \rightarrow 1s^2 2s^2 2p^5$	834 ($^2S \rightarrow {}^2P$)	906
(ii)	Ne^{8+}, $1s^1 2s^0 2p^1 \rightarrow 1s^2 2s^0 2p^0$	919 ($^1P \rightarrow {}^1S$)	972
(iii)	Ne^{8+}, $1s^1 2s^0 2p^1 \rightarrow 1s^1 2s^1 2p^0$	10 ($^3P \rightarrow {}^3S$)	11
		7 ($^1P \rightarrow {}^1S$)	–
(iv)	Ne^{9+}, $1s^0 2s^0 2p^1 \rightarrow 1s^1 2s^0 2p^0$	1020 ($^2P \rightarrow {}^2S$)	1020
(v)	Ne^{7+}, $1s^1 2p^1 3p^1 \rightarrow 1s^2 2p^0 3p^1$	916 ($^2P \rightarrow {}^2P$)	–
(vi)	Ne^{7+}, $1s^2 np^1 \rightarrow 1s^2 2s^1$	140 ($n = 3$; $^2P \rightarrow {}^2S$)	143 ($n = 3$)
		183 ($n = 4$; $^2P \rightarrow {}^2S$)	188 ($n = 4$)
		203 ($n = 5$; $^2P \rightarrow {}^2S$)	210 ($n = 5$)
		214 ($n = 6$; $^2P \rightarrow {}^2S$)	222 ($n = 6$)
		220 ($n = 7$; $^2P \rightarrow {}^2S$)	230 ($n = 7$)

based version of XATOM already produces quite good results, as demonstrated in former studies [9–11,15,17,18]. However, resonant excitations and spectral information profit from the improved first-order-corrected transition energies in the new implementation. Our results have demonstrated that CSD for the resonance case and calculated electron and photon spectra are improved by using state-resolved ionization dynamics calculations. Employing the state-resolved Monte Carlo implementation, we have investigated CSDs and spectra of neon atoms at a photon energy of 2000 eV for three different XFEL pulse durations. In addition to asymptotic quantities, we have computed time-resolved CSDs and spectra, which highlight the mechanisms through which different pulse durations affect the asymptotic observables. In our example, frustrated absorption clearly manifests itself in the time-resolved spectra as the pulse duration gets shorter. Particularly, it is the dynamical interplay between the suppression of Auger-Meitner decay and the suppression of inner-shell photoabsorption that lies at the heart of *frustrated absorption*—not the suppression of photoabsorption alone.

We conclude with an outlook. An important next step could be to employ our state-resolved Monte Carlo implementation to explore the orbital alignment of the ions [43,68] produced during the x-ray multiphoton ionization dynamics. Another promising perspective for further development is to compare our results on time-dependent quantities with experimental measurements. Experimental methods that may allow such measurements could be attosecond transient absorption spectroscopy [69,70] and attosecond streaking measurements [71–73]. These methods have already been employed to investigate ionization dynamics under conditions in which only a few processes were involved [74,75]. Probing dynamics during x-ray multiphoton ionization may be experimentally challenging due to a wide variety of involved charge states and emitted photo- and Auger-Meitner electrons that are not always well separated, either in time or in energy.

TABLE IV. Dominant resonant excitations at a photon energy of 1050 eV (1% bandwidth). Transition energies and cross sections for the state-resolved approach, $E_{\mathrm{tr}}^{(1)}$ and $\sigma^{(1)}$, and the configuration-based approach, $E_{\mathrm{tr}}^{(0)}$ and $\sigma^{(0)}$, are listed for the underlying process. For brevity, only a range of transition energies in the state-resolved approach are given instead of individual state-to-state transition energies. For the same reason, only subshell cross sections, i.e., averages over initial states and sums over all final states, are shown. For Ne^{3+} ($1s^1 2l^6$), Ne^{5+} ($1s^1 2l^4$), Ne^{5+} ($1s^2 2l^2 4p^1$), Ne^{6+} ($1s^2 2l^2$), and Ne^{7+} ($1s^2 2l^1$) with $l = s, p$, similar resonant excitations are also possible for other electronic configurations than given here, but are not listed for brevity.

Process	n	$E_{\mathrm{tr}}^{(1)}$ (eV)	$\sigma^{(1)}$ (Mb)	$E_{\mathrm{tr}}^{(0)}$ (eV)	$\sigma^{(0)}$ (Mb)
Ne^{3+}, $1s^1 2s^2 2p^4 \rightarrow 1s^0 2s^2 2p^4 np^1$	4	1043–1059	6.98×10^{-2}	–	–
	5	1050–1065	7.74×10^{-3}	–	–
Ne^{5+}, $1s^1 2s^2 2p^2 \rightarrow 1s^0 2s^2 2p^2 np^1$	3	–	–	1043	1.28×10^{-1}
Ne^{5+}, $1s^2 2s^2 4p^1 \rightarrow 1s^1 2s^2 4p^1 np^1$	4	1052–1054	2.73×10^{-1}	1031	2.62×10^{-5}
Ne^{6+}, $1s^2 2s^0 2p^2 \rightarrow 1s^1 2s^0 2p^2 np^1$	4	1040–1053	2.85×10^{-1}	–	–
	5	1056–1070	7.60×10^{-3}	1041	2.97×10^{-2}
	6	1065–1069	6.19×10^{-3}	1050	1.23×10^{-1}
	7	–	–	1055	4.32×10^{-2}
Ne^{7+}, $1s^2 2s^0 2p^1 \rightarrow 1s^1 2s^0 2p^1 np^1$	3	1036–1046	1.73×10^{-1}	–	–
	4	–	–	1063	6.26×10^{-3}
Ne^{7+}, $1s^2 np^1 \rightarrow 1s^1 3p^1 np^1$	3	1064–1067	9.51×10^{-3}	1047	8.67×10^{-1}
	4	1067–1070	1.34×10^{-4}	1056	4.84×10^{-1}
	5	1070	2.44×10^{-6}	1061	7.07×10^{-2}
	6	1070	3.14×10^{-7}	1063	1.77×10^{-2}
	7	1070	7.67×10^{-8}	1064	6.85×10^{-3}

ACKNOWLEDGMENTS

We acknowledge support from DASHH (Data Science in Hamburg - HELMHOLTZ Graduate School for the Structure of Matter) with Grant No. HIDSS-0002.

APPENDIX: PHYSICAL PROCESSES AND TRANSITION ENERGIES

For dominant physical processes, calculated ionization potentials and transition energies are listed in Tables I–IV.

[1] P. Emma, R. Akre, J. Arthur, R. Bionta, C. Bostedt, J. Bozek, A. Brachmann, P. Bucksbaum, R. Coffee, F.-J. Decker *et al.*, First lasing and operation of an ångstrom-wavelength free-electron laser, Nat. Photonics **4**, 641 (2010).

[2] T. Ishikawa, H. Aoyagi, T. Asaka, Y. Asano, N. Azumi, T. Bizen, H. Ego, K. Fukami, T. Fukui, Y. Furukawa *et al.*, A compact x-ray free-electron laser emitting in the sub-ångström region, Nat. Photonics **6**, 540 (2012).

[3] W. Decking, S. Abeghyan, P. Abramian, A. Abramsky, A. Aguirre, C. Albrecht, P. Alou, M. Altarelli, P. Altmann, K. Amyan *et al.*, A MHz-repetition-rate hard x-ray free-electron laser driven by a superconducting linear accelerator, Nat. Photonics **14**, 391 (2020).

[4] H.-S. Kang, C.-K. Min, H. Heo, C. Kim, H. Yang, G. Kim, I. Nam, S. Y. Baek, H.-J. Choi, G. Mun *et al.*, Hard x-ray free-electron laser with femtosecond-scale timing jitter, Nat. Photonics **11**, 708 (2017).

[5] E. Prat, R. Abela, M. Aiba, A. Alarcon, J. Alex, Y. Arbelo, C. Arrell, V. Arsov, C. Bacellar, C. Beard *et al.*, A compact and cost-effective hard x-ray free-electron laser driven by a high-brightness and low-energy electron beam, Nat. Photonics **14**, 748 (2020).

[6] C. Pellegrini, A. Marinelli, and S. Reiche, The physics of x-ray free-electron lasers, Rev. Mod. Phys. **88**, 015006 (2016).

[7] R. Santra and L. Young, in *Synchrotron Light Sources and Free-Electron Lasers*, edited by E. J. Jaeschke, S. Khan, J. R. Schneider, and J. B. Hastings (Springer International Publishing, Switzerland, 2016), pp. 1233–1260.

[8] L. Young, E. P. Kanter, B. Krässig, Y. Li, A. M. March, S. T. Pratt, R. Santra, S. H. Southworth, N. Rohringer, L. F. DiMauro *et al.*, Femtosecond electronic response of atoms to ultra-intense x-rays, Nature (London) **466**, 56 (2010).

[9] H. Fukuzawa, S.-K. Son, K. Motomura, S. Mondal, K. Nagaya, S. Wada, X.-J. Liu, R. Feifel, T. Tachibana, Y. Ito *et al.*, Deep Inner-Shell Multiphoton Ionization by Intense X-Ray Free-Electron Laser Pulses, Phys. Rev. Lett. **110**, 173005 (2013).

[10] B. Rudek, S.-K. Son, L. Foucar, S. W. Epp, B. Erk, R. Hartmann, M. Adolph, R. Andritschke, A. Aquila, N. Berrah *et al.*, Ultra-efficient ionization of heavy atoms by intense x-ray free-electron laser pulses, Nat. Photonics **6**, 858 (2012).

[11] B. Rudek, K. Toyota, L. Foucar, B. Erk, R. Boll, C. Bomme, J. Correa, S. Carron, S. Boutet, G. J. Williams *et al.*, Relativistic and resonant effects in the ionization of heavy atoms by ultra-intense hard x-rays, Nat. Commun. **9**, 4200 (2018).

[12] A. Rudenko, L. Inhester, K. Hanasaki, X. Li, S. J. Robatjazi, B. Erk, R. Boll, K. Toyota, Y. Hao, O. Vendrell *et al.*, Femtosecond response of polyatomic molecules to ultra-intense hard x-rays, Nature (London) **546**, 129 (2017).

[13] N. Rohringer and R. Santra, X-ray nonlinear optical processes using a self-amplified spontaneous emission free-electron laser, Phys. Rev. A **76**, 033416 (2007).

[14] M. G. Makris, P. Lambropoulos, and A. Mihelič, Theory of Multiphoton Multielectron Ionization of Xenon under Strong 93-eV Radiation, Phys. Rev. Lett. **102**, 033002 (2009).

[15] G. Doumy, C. Roedig, S.-K. Son, C. I. Blaga, A. D. DiChiara, R. Santra, N. Berrah, C. Bostedt, J. D. Bozek, P. H. Bucksbaum *et al.*, Nonlinear Atomic Response to Intense Ultrashort X Rays, Phys. Rev. Lett. **106**, 083002 (2011).

[16] W. Xiang, C. Gao, Y. Fu, J. Zeng, and J. Yuan, Inner-shell resonant absorption effects on evolution dynamics of the charge state distribution in a neon atom interacting with ultraintense x-ray pulses, Phys. Rev. A **86**, 061401(R) (2012).

[17] B. Rudek, D. Rolles, S.-K. Son, L. Foucar, B. Erk, S. Epp, R. Boll, D. Anielski, C. Bostedt, S. Schorb *et al.*, Resonance-enhanced multiple ionization of krypton at an x-ray free-electron laser, Phys. Rev. A **87**, 023413 (2013).

[18] K. Motomura, H. Fukuzawa, S.-K. Son, S. Mondal, T. Tachibana, Y. Ito, M. Kimura, K. Nagaya, T. Sakai, K. Matsunami *et al.*, Sequential multiphoton multiple ionization of atomic argon and xenon irradiated by x-ray free-electron laser pulses from SACLA, J. Phys. B: At. Mol. Opt. Phys. **46**, 164024 (2013).

[19] N. Berrah, A. Sanchez-Gonzalez, Z. Jurek, R. Obaid, H. Xiong, R. J. Squibb, T. Osipov, A. Lutman, L. Fang, T. Barillot *et al.*, Femtosecond-resolved observation of the fragmentation of buckminsterfullerene following x-ray multiphoton ionization, Nat. Phys. **15**, 1279 (2019).

[20] B. F. Murphy, T. Osipov, Z. Jurek, L. Fang, S.-K. Son, M. Mucke, J. H. D. Eland, V. Zhaunerchyk, R. Feifel, L. Avaldi *et al.*, Femtosecond x-ray-induced explosion of C_{60} at extreme intensity, Nat. Commun. **5**, 4281 (2014).

[21] M. Hoener, L. Fang, O. Kornilov, O. Gessner, S. T. Pratt, M. Gühr, E. P. Kanter, C. Blaga, C. Bostedt, J. D. Bozek *et al.*, Ultraintense X-Ray Induced Ionization, Dissociation, and Frustrated Absorption in Molecular Nitrogen, Phys. Rev. Lett. **104**, 253002 (2010).

[22] K. Toyota, S.-K. Son, and R. Santra, Interplay between relativistic energy corrections and resonant excitations in x-ray multiphoton ionization dynamics of Xe atoms, Phys. Rev. A **95**, 043412 (2017).

[23] S.-K. Son, R. Boll, and R. Santra, Breakdown of frustrated absorption in x-ray sequential multiphoton ionization, Phys. Rev. Res. **2**, 023053 (2020).

[24] P. J. Ho, E. P. Kanter, and L. Young, Resonance-mediated atomic ionization dynamics induced by ultraintense x-ray pulses, Phys. Rev. A **92**, 063430 (2015).

[25] P. J. Ho, C. Bostedt, S. Schorb, and L. Young, Theoretical Tracking of Resonance-Enhanced Multiple Ionization Pathways in X-ray Free-Electron Laser Pulses, Phys. Rev. Lett. **113**, 253001 (2014).

[26] T. Mazza, M. Ilchen, M. D. Kiselev, E. V. Gryzlova, T. M. Baumann, R. Boll, A. De Fanis, P. Grychtol, J. Montaño,

V. Music *et al.*, Mapping Resonance Structures in Transient Core-Ionized Atoms, Phys. Rev. X **10**, 041056 (2020).
[27] S.-K. Son and R. Santra, Monte Carlo calculation of ion, electron, and photon spectra of xenon atoms in x-ray free-electron laser pulses, Phys. Rev. A **85**, 063415 (2012).
[28] J. M. Schäfer, L. Inhester, S.-K. Son, R. F. Fink, and R. Santra, Electron and fluorescence spectra of a water molecule irradiated by an x-ray free-electron laser pulse, Phys. Rev. A **97**, 053415 (2018).
[29] C. Buth, R. Beerwerth, R. Obaid, N. Berrah, L. S. Cederbaum, and S. Fritzsche, Neon in ultrashort and intense x-rays from free electron lasers, J. Phys. B: At. Mol. Opt. Phys. **51**, 055602 (2018).
[30] U. Lorenz, N. M. Kabachnik, E. Weckert, and I. A. Vartanyants, Impact of ultrafast electronic damage in single-particle x-ray imaging experiments, Phys. Rev. E **86**, 051911 (2012).
[31] H. M. Quiney and K. A. Nugent, Biomolecular imaging and electronic damage using x-ray free-electron lasers, Nat. Phys. **7**, 142 (2011).
[32] S.-K. Son, L. Young, and R. Santra, Impact of hollow-atom formation on coherent x-ray scattering at high intensity, Phys. Rev. A **83**, 033402 (2011).
[33] H. N. Chapman, P. Fromme, A. Barty, T. A. White, R. A. Kirian, A. Aquila, M. S. Hunter, J. Schulz, D. P. DePonte, U. Weierstall *et al.*, Femtosecond x-ray protein nanocrystallography, Nature (London) **470**, 73 (2011).
[34] J. Coe and P. Fromme, Serial femtosecond crystallography opens new avenues for structural biology, Protein Pept. Lett. **23**, 255 (2016).
[35] E. Sobolev, S. Zolotarev, K. Giewekemeyer, J. Bielecki, K. Okamoto, H. Reddy, J. Andreasson, K. Ayyer, I. Barák, S. Bari *et al.*, Megahertz single-particle imaging at the European XFEL, Commun. Phys. **3**, 97 (2020).
[36] M. M. Seibert, T. Ekeberg, F. R. N. C. Maia, M. Svenda, J. Andreasson, O. Jönsson, D. Odić, B. Iwan, A. Rocker, D. Westphal *et al.*, Single mimivirus particles intercepted and imaged with an x-ray laser, Nature (London) **470**, 78 (2011).
[37] K. Nass, Radiation damage in protein crystallography at x-ray free-electron lasers, Acta Cryst. D **75**, 211 (2019).
[38] O. Ciricosta, H.-K. Chung, R. W. Lee, and J. S. Wark, Simulations of neon irradiated by intense x-ray laser radiation, High Energy Density Phys. **7**, 111 (2011).
[39] C. Buth, J.-C. Liu, M. H. Chen, J. P. Cryan, L. Fang, J. M. Glownia, M. Hoener, R. N. Coffee, and N. Berrah, Ultrafast absorption of intense x rays by nitrogen molecules, J. Chem. Phys. **136**, 214310 (2012).
[40] J.-C. Liu, N. Berrah, L. S. Cederbaum, J. P. Cryan, J. M. Glownia, K. J. Schafer, and C. Buth, Rate equations for nitrogen molecules in ultrashort and intense x-ray pulses, J. Phys. B: At. Mol. Opt. Phys. **49**, 075602 (2016).
[41] Z. Jurek, S.-K. Son, B. Ziaja, and R. Santra, XMDYN and XATOM: Versatile simulation tools for quantitative modeling of x-ray free-electron laser induced dynamics of matter, J. Appl. Cryst. **49**, 1048 (2016).
[42] S.-K. Son, K. Toyota, O. Geffert, J. M. Slowik, and R. Santra, XATOM–an integrated toolkit for x-ray and atomic physics, CFEL, DESY, Hamburg, Germany, 2016, Rev. 3544.
[43] L. Budewig, S.-K. Son, and R. Santra, Theoretical investigation of orbital alignment of x-ray-ionized atoms in exotic electronic configurations, Phys. Rev. A **105**, 033111 (2022).
[44] J. C. Slater, A simplification of the Hartree-Fock method, Phys. Rev. **81**, 385 (1951).
[45] D. J. Griffiths, *Introduction to Quantum Mechanics*; *Introduction to Quantum Mechanics* 2nd ed. (Cambridge University Press, Cambridge, 2017).
[46] J. J. Sakurai and J. J. Napolitano, *Modern Quantum Mechanics: Pearson New International Edition* (Pearson Education, Harlow, 2014).
[47] K. Gottfried and T. Yan, *Quantum Mechanics: Fundamentals* (Springer, New York, 2003).
[48] G. Racah, Theory of complex spectra. II, Phys. Rev. **62**, 438 (1942).
[49] B. R. Judd, *Operator Techniques in Atomic Spectroscopy* (McGraw-Hill Book Company, New York, 1963).
[50] I. V. Hertel and K. P. Schulz, *Atoms, Molecules and Optical Physics 1* (Springer, Berlin, 2015).
[51] R. Santra, Concepts in x-ray physics, J. Phys. B: At. Mol. Opt. Phys. **42**, 023001 (2009).
[52] A. Sytcheva, S. Pabst, S.-K. Son, and R. Santra, Enhanced nonlinear response of Ne^{8+} to intense ultrafast x-rays, Phys. Rev. A **85**, 023414 (2012).
[53] M. Tilley, A. Karamatskou, and R. Santra, Wave-packet propagation based calculation of above-threshold ionization in the x-ray regime, J. Phys. B: At. Mol. Opt. Phys. **48**, 124001 (2015).
[54] T. Schneider, P. L. Chocian, and J.-M. Rost, Separation and Identification of Dominant Mechanisms in Double Photoionization, Phys. Rev. Lett. **89**, 073002 (2002).
[55] P. Kolorenč, V. Averbukh, R. Feifel, and J. Eland, Collective relaxation processes in atoms, molecules and clusters, J. Phys. B: At. Mol. Opt. Phys. **49**, 082001 (2016).
[56] N. Saito and I. H. Suzuki, Shake-off processes in photoionization and auger transition for rare gases irradiated by soft x-rays, Phys. Scr. **49**, 80 (1994).
[57] N. Rohringer and R. Santra, Resonant Auger effect at high x-ray intensity, Phys. Rev. A **77**, 053404 (2008).
[58] N. Rohringer and R. Santra, Strongly driven resonant Auger effect treated by an open-quantum-system approach, Phys. Rev. A **86**, 043434 (2012).
[59] E. P. Kanter, B. Krässig, Y. Li, A. M. March, P. Ho, N. Rohringer, R. Santra, S. H. Southworth, L. F. DiMauro, G. Doumy *et al.*, Unveiling and Driving Hidden Resonances with High-Fluence, High-Intensity X-Ray Pulses, Phys. Rev. Lett. **107**, 233001 (2011).
[60] Y. Li, C. Gao, W. Dong, J. Zeng, Z. Zhao, and J. Yuan, Coherence and resonance effects in the ultra-intense laser-induced ultrafast response of complex atoms, Sci. Rep. **6**, 18529 (2016).
[61] S. Nandi, E. Olofsson, M. Bertolino, S. Carlström, F. Zapata, D. Busto, C. Callegari, M. D. Fraia, P. Eng-Johnsson, R. Feifel *et al.*, Observation of Rabi dynamics with a short-wavelength free-electron laser, Nature (London) **608**, 488 (2022).
[62] S. M. Cavaletto, C. Buth, Z. Harman, E. P. Kanter, S. H. Southworth, L. Young, and C. H. Keitel, Resonance fluorescence in ultrafast and intense x-ray free-electron-laser pulses, Phys. Rev. A **86**, 033402 (2012).
[63] K. Toyota, Z. Jurek, S.-K. Son, H. Fukuzawa, K. Ueda, N. Berrah, B. Rudek, D. Rolles, A. Rudenko, and R. Santra, xcalib: A focal spot calibrator for intense x-ray free-electron laser pulses based on the charge state distributions of light atoms, J. Synchrotron Rad. **26**, 1017 (2019).

[64] B. Efron and R. J. Tibshirani, *An Introduction to the Bootstrap* (Chapman and Hall/CRC, Philadelphia, 1994).

[65] S. H. Southworth, E. P. Kanter, B. Krässig, L. Young, G. B. Armen, J. C. Levin, D. L. Ederer, and M. H. Chen, Double K-shell photoionization of neon, Phys. Rev. A **67**, 062712 (2003).

[66] G. Goldsztejn, T. Marchenko, R. Püttner, L. Journel, R. Guillemin, S. Carniato, P. Selles, O. Travnikova, D. Céolin, A. F. Lago *et al.*, Double-Core-Hole States in Neon: Lifetime, Post-Collision Interaction, and Spectral Assignment, Phys. Rev. Lett. **117**, 133001 (2016).

[67] S. M. Vinko, O. Ciricosta, B. I. Cho, K. Engelhorn, H.-K. Chung, C. R. D. Brown, T. Burian, J. Chalupský, R. W. Falcone, C. Graves *et al.*, Creation and diagnosis of a solid-density plasma with an x-ray free-electron laser, Nature (London) **482**, 59 (2012).

[68] E. V. Gryzlova, A. N. Grum-Grzhimailo, M. D. Kiselev, and M. M. Popova, Evolution of the ionic polarization in multiple sequential ionization: General equations and an illustrative example, arXiv:2207.11279.

[69] E. Goulielmakis, Z.-H. Loh, A. Wirth, R. Santra, N. Rohringer, V. S. Yakovlev, S. Zherebtsov, T. Pfeifer, A. M. Azzeer, M. F. Kling *et al.*, Real-time observation of valence electron motion, Nature **466**, 739 (2010).

[70] H. Wang, M. Chini, S. Chen, C.-H. Zhang, F. He, Y. Cheng, Y. Wu, U. Thumm, and Z. Chang, Attosecond Time-Resolved Autoionization of Argon, Phys. Rev. Lett. **105**, 143002 (2010).

[71] J. Itatani, F. Quere, G. L. Yudin, M. Y. Ivanov, F. Krausz, and P. B. Corkum, Attosecond Streak Camera, Phys. Rev. Lett. **88**, 173903 (2002).

[72] M. Hentschel, R. Kienberger, C. Spielmann, G. A. Reider, N. Milosevic, T. Brabec, P. Corkum, U. Heinzmann, M. Drescher, and F. Krausz, Attosecond metrology, Nature (London) **414**, 509 (2001).

[73] F. Krausz and M. Ivanov, Attosecond physics, Rev. Mod. Phys. **81**, 163 (2009).

[74] M. Drescher, M. Hentschel, R. Kienberger, M. Uliberacker, V. Yakovlev, A. Scrinzi, T. Westerwalbesloh, U. Kleineberg, U. Heinzmann, and F. Krausz, Time-resolved atomic inner-shell spectroscopy, Nature (London) **419**, 803 (2002).

[75] M. Schultze, M. Fiess, N. Karpowicz, J. Ggnon, M. Korbman, M. Hofstetter, S. Neppl, A. L. Cavalieri, Y. Komninos, T. Mercouris *et al.*, Delay in photoemission, Science **328**, 1658 (2010).

3.3 X-ray-induced atomic transitions via machine learning: A computational investigation

The third publication presents a machine-learning-based state-resolved Monte Carlo implementation. This implementation combines state-resolved X-ray multiphoton ionization dynamics calculations with machine-learning models for predicting atomic transition parameters. The purpose of machine learning is to reduce the high computational effort of huge-sized state-resolved calculations.

The underlying project was performed by myself under the supervision of Professor Dr. R. Santra and Professor Dr.-Ing. M. Tropmann-Frick. In particular, I trained, evaluated, and optimized the machine-learning models and embedded them into the state-resolved Monte Carlo implementation (Sec. 3.2). I also evaluated the overall performance of the machine-learning-based implementation, discussed its limitations, and wrote the manuscript with inputs from all authors.

X-ray-induced atomic transitions via machine learning: A computational investigation

Laura Budewig,[1,2] Sang-Kil Son,[1] Zoltan Jurek,[1] Malik Muhammad Abdullah,[1]
Marina Tropmann-Frick,[3] and Robin Santra[1,2]
[1]*Center for Free-Electron Laser Science CFEL, Deutsches Elektronen-Synchrotron DESY, Notkestr. 85, 22607 Hamburg, Germany*
[2]*Department of Physics, Universität Hamburg, Notkestr. 9-11, 22607 Hamburg, Germany*
[3]*Department of Computer Science, University of Applied Sciences Hamburg, Berliner Tor 7, 20099 Hamburg, Germany*

(Received 17 November 2023; accepted 13 February 2024; published 11 March 2024)

Intense x-ray free-electron laser pulses can induce multiple sequences of one-photon ionization and accompanying decay processes in atoms, producing highly charged atomic ions. Considering individual quantum states during these processes provides more precise information about the x-ray multiphoton ionization dynamics than the common configuration-based approach. However, in such a state-resolved approach, extremely huge-sized rate-equation calculations are inevitable. Here we present a strategy that embeds machine-learning models into a framework for atomic state-resolved ionization dynamics calculations. Machine learning is employed for the required atomic transition parameters, whose calculations possess the computationally most expensive steps. We find for argon that both feedforward neural networks and random forest regressors can predict these parameters with acceptable, but limited accuracy. State-resolved ionization dynamics of argon, in terms of charge-state distributions and electron and photon spectra, are also presented. Comparing fully calculated and machine-learning-based results, we demonstrate that the proposed machine-learning strategy works in principle and that the performance, in terms of charge-state distributions and electron and photon spectra, is good. Our work establishes a first step toward accelerating the calculation of atomic state-resolved ionization dynamics induced by high-intensity x rays.

DOI: 10.1103/PhysRevResearch.6.013265

I. INTRODUCTION

The enormous peak brightness of x-ray free-electron lasers (XFELs) [1–5], such as the European XFEL [6], offers exciting new opportunities for the structure determination of biomolecules with almost atomic resolution [7–13]. However, due to the high-intensity x rays the electronic structure of the investigated sample is unavoidably damaged [14–17]. As a consequence, the sample undergoes structural disintegration [18], which limits such applications.

A critical process, underlying these damages, is x-ray multiphoton ionization dynamics in atoms and molecules [19]. High-intensity x rays induce multiple sequences of one-photon ionization accompanied by Auger-Meitner decay or x-ray fluorescence. As a result, atoms or molecules often become very highly ionized during the interaction with intense XFEL pulses [20–24]. A validated approach to simulate the x-ray multiphoton ionization dynamics is by solving a coupled set of rate equations [20,25,26] describing the time-dependent populations of the electronic configurations visited during the ionization dynamics. Such a configuration-based rate-equation approach has been widely used and successfully applied for interpreting and designing many XFEL experiments [20–43].

However, the configuration-based approach does not include individual quantum states and individual state-to-state transitions and, thereby, cannot capture state-resolved ionization dynamics. A state-resolved approach delivers more detailed information about the x-ray multiphoton ionization dynamics, especially regarding resonant excitations and spectra. This has recently been demonstrated for neon atoms [44]. To explore state-resolved ionization dynamics based on time-dependent quantum state populations, it is necessary to include all possible electronic quantum states that may be formed by removing zero, one, or more electrons from the ground state of the neutral atom. The corresponding number of involved states is dramatically larger than the number of electronic configurations. For example, even for an isolated argon atom without considering resonant or relativistic effects the number of involved states is 262144 [44], whereas only 1323 electronic configurations are involved [34]. Thus, apart from very light atoms like neon, solving rate equations in an extremely large space of states is unavoidable. Therefore, the huge-sized rate equation calculations are performed via a more efficient Monte Carlo on-the-fly rate-equation method [21,38]. However, even with such a Monte Carlo method, the computational effort for the state-resolved ionization dynamics calculations is inevitably large (as will be demonstrated in Sec. III C). The main bottleneck in the state-resolved ionization dynamics calculations is the first-principle calculation of all required atomic transition parameters, i.e., transition energies, cross sections, and rates, which has to be performed on the fly.

With machine learning nowadays being a thriving and actively investigated field, it is natural to ask whether this critical

challenge of high computational effort might be addressed by applying a suitable machine learning strategy. Machine learning, deep learning included, has already successfully supported natural science in various ways [45–47]. A prototype example is the application to protein structure predictions with atomic accuracy [48]. Other important applications of machine learning include the prediction of x-ray absorption spectra [49–52], the identification of phase transitions in condensed matter [53], the characterization and calibration of laser pulses [54–57], as well as its use in electronic-structure theory [58–63], just to name a few (for more see, e.g., Refs. [45,46] and references therein). One high-impact role that machine learning has been playing in electronic-structure theory so far is in speeding up the construction of potential-energy surfaces [64–67]. A recent review about the progress of machine learning in the context of potential-energy surfaces can be found in Ref. [68]. Furthermore, another interesting approach is to reduce the high computational effort in configuration-interaction calculations by preselecting only the most important configurations via machine-learning models [69,70].

In this work, we present a strategy that embeds machine-learning models for predicting atomic transition parameters into a Monte Carlo on-the-fly rate-equation method for describing atomic state-resolved ionization dynamics. Recently, a state-resolved Monte Carlo implementation [44], based on a framework for performing quantum-state-resolved first-principle calculations of atomic transition parameters [71], was introduced in the *ab initio* electronic-structure and ionization dynamics toolkit XATOM [16,72,73]. We here combine the state-resolved Monte Carlo implementation with machine-learning models for predicting atomic transition parameters. This machine-learning-based implementation can reproduce the results for neon published in Ref. [44]. However, for neon, the computational effort is too small to gain much with it. Therefore, here, we choose to focus on the much more challenging problem of state-resolved ionization dynamics of argon. Our work establishes a first step towards accelerating huge-sized rate-equation calculations for easily examining x-ray-induced ionization dynamics for a variety of atoms and x-ray parameters.

The paper is organized as follows: In Sec. II, a description of the methods used to obtain the results presented in Sec. III can be found. In Sec. III A, we demonstrate how to collect data of x-ray-induced atomic transitions via a Monte Carlo approach, before analyzing the performance of the machine-learning models (i.e., neural networks and random forest regressors) in Sec. III B. The performance, in terms of charge-state distributions (CSDs) and spectra, is the topic of Sec. III C. The paper finishes with a conclusion and future perspectives in Sec. IV.

II. THEORETICAL DETAILS

A. State-resolved Monte Carlo calculations

We perform state-resolved x-ray multiphoton ionization dynamics calculations using the state-resolved Monte Carlo implementation [44] in the XATOM toolkit [16,72,73]. This implementation is based on a nonrelativistic quantum-state-resolved electronic-structure framework [71], also embedded in XATOM. It performs first-principle calculations of atomic first-order-corrected transition energies as well as state-to-state cross sections and transition rates.

To provide an overview of the accuracy of the quantum-state-resolved electronic-structure framework employed, we list selected K and L fluorescence and KLL Auger-Meitner transition energies for Ar^{1+} and Ar^{2+} (hypersatellites) in Table I. Transition energies are calculated with two different orbital optimization strategies within this framework: based on first-order-corrected energies calculated with orbitals and orbital energies optimized (i) for the initial electronic configuration only and (ii) for the initial and final electronic configurations individually. Both strategies are compared with relativistic calculations [74,75,77,79] and experimental measurements [74,76,78,79], which are in almost perfect agreement with one another (see Table I). Relativistic, quantum-electrodynamic, and finite-nuclear-size effects [74] are not included in the quantum-state-resolved electronic-structure framework employed. As a consequence, transition energies calculated with both strategies are less accurate and exhibit no spin-orbit splitting. Nonetheless, the selected transitions in Table I demonstrate an accuracy of more than 90% (initial optimization) or 97% (individual optimization), respectively. The individual optimization delivers more accurate results, however, at the expense of computational efficiency. Therefore, in what follows, we optimize for the initial electronic configuration only (as done in Refs. [44,71]). The main focus in this work is on the usage of machine learning for atomic transition parameters, whose accuracy does not affect the general machine-learning approach.

Furthermore, a Monte Carlo on-the-fly rate-equation method [21,38] is employed for describing the time evolution of the atomic quantum state populations. The number of coupled rate equations (= the number of individual states involved in the x-ray multiphoton ionization dynamics) is extremely large. For instance, for argon atoms, this number is 2^{18} when all subshells are accessible for one-photon ionization, but relativistic and resonant effects are not included [44]. Therefore, the Monte Carlo method is critical since it permits us to efficiently perform huge-sized rate-equation calculations by stochastically sampling possible ionization pathways.

In the present work, we restrict the time propagation of the x-ray multiphoton ionization dynamics to a time interval of 1 ps. This implies that decay processes that occur on timescales much longer than 1 ps are assumed not to be of interest. Therefore, the rates are set to zero when they are smaller than $\Gamma_{\text{thres}} = 10^{-7}$ a.u. (corresponding to the timescale of 240 ps). In what follows, these comparatively slow processes are referred to as quasiforbidden transitions. This is reasonable since processes occurring later are actually modified by plasma processes. Thus, the model of an isolated atom assumed in our calculations breaks down after some time. Note that, at this point, the few-femtosecond ionizing pulse is long over.

Let us briefly explain what we mean by an individual quantum state and an individual state-to-state transition in the following. In our state-resolved approach, a state I is defined by the electronic configuration, $1s^{N_{1s}}2s^{N_{2s}}2p^{N_{2p}}\cdots$, together

TABLE I. Accuracy of the underlying quantum-state-resolved electronic-structure framework in XATOM. Selected fluorescence and Auger-Meitner (hypersatellite) transition energies for argon are calculated with this framework [71] based on orbitals and orbital energies optimized (i) for the initial electronic configuration only and (ii) for the initial and final electronic configurations individually. Results are compared with (iii) more accurate relativistic calculations and (iv) experimental data (references are given next to values in the table), which contain energy splittings due to spin-orbit coupling.

	Transition energy $E_{I^i \to I^f}$ (eV)				Difference (%)	
Process	(i) XATOM	(ii) XATOM–ind.	(iii) Relativistic	(iv) Experiment	(iv) − (i)	(iv) − (ii)
Ar^{1+}, $1s^1 2s^2 2p^6 3s^2 3p^6$ (^2S)	2931.5	2946.4	2957.9 [74]	2957.7 [74]	0.9	0.4
$\to$ $1s^2 2s^2 2p^5 3s^2 3p^6$ (^2P)			2955.9 [74]	2955.6 [74]	0.8	0.3
Ar^{1+}, $1s^1 2s^2 2p^6 3s^2 3p^6$ (^2S)	3140.3	3180.4	3191.5 [74]	3190.5 [74]	1.6	0.3
$\to$ $1s^2 2s^2 2p^6 3s^2 3p^5$ (^2P)			3191.3 [74]	3190.5 [74]	1.6	0.3
Ar^{1+}, $1s^2 2s^2 2p^5 3s^2 3p^6$ (^2P)	202.4	215.3	219.5 [74]	220.2 [74]	8.8	2.3
$\to$ $1s^2 2s^2 2p^6 3s^1 3p^6$ (^2S)			221.5 [74]	221.8 [74]	9.6	3.0
Ar^{2+}, $1s^0 2s^2 2p^6 3s^2 3p^6$ (^2S)	3105.9	3118.0	3131.5 [75]	3133.0 [76]	0.9	0.5
$\to$ $1s^1 2s^2 2p^5 3s^2 3p^6$ (^1P)						
Ar^{1+}, $1s^1 2s^2 2p^6 3s^2 3p^6$ (^2S)	2646.9	2650.6	2661.8 [77]	2660.6 [78]	0.5	0.4
$\to$ $1s^2 2s^2 2p^4 3s^2 3p^6$ (^1D)						
Ar^{1+}, $1s^1 2s^2 2p^6 3s^2 3p^6$ (^2S)	2634.8	2638.6	2649.9 [77]	2650.6 [78]	0.6	0.5
$\to$ $1s^2 2s^2 2p^4 3s^2 3p^6$ (^1S)						
Ar^{2+}, $1s^0 2s^2 2p^6 3s^2 3p^6$ (^1S)	2765.4	2766.4	2779.2 [79]	2779.6 [79]	0.5	0.5
$\to$ $1s^1 2s^2 2p^4 3s^2 3p^6$ (^2D)						
Ar^{2+}, $1s^0 2s^2 2p^6 3s^2 3p^6$ (^1S)	2752.5	2762.6	2769.6 [79]	2768.9 [79]	0.6	0.2
$\to$ $1s^1 2s^2 2p^4 3s^2 3p^6$ (^2S)						

with additional quantum numbers (L, S, M_L, κ) (that specify a so-called zeroth-order LS eigenstate [71]). For each state, there is a corresponding (term-specific) first-order-corrected energy $E_{LS\kappa}$ that is the same for all states within a term $^{2S+1}L(\kappa)$. Note that the spin projection quantum number M_S is missing in the description of an individual quantum state. Since in our approach none of the interaction Hamiltonians couples to the spin [44,71], transition probabilities are independent of M_S and, thus, we are not interested in spin projection quantum numbers. From now on the index i refers to the initial state (before a certain process is happening), while for the final target state we use the index f. Then, an individual state-to-state transition is a transition from an individual quantum state I^i to I^f with first-order-corrected transition energy $E^{(1)}_{I^i \to I^f}$, cross section $\sigma_{I^i \to I^f}$ for photoabsorption or transition rate $\Gamma_{I^i \to I^f}$ for Auger-Meitner decay or fluorescence, respectively. (The corresponding equations are given in Ref. [71].)

B. The machine-learning models

The tasks of the machine-learning models are to predict for a given transition from an individual quantum state I^i to I^f the first-order-corrected transition energy $E^{(1)}_{I^i \to I^f}$ (E model) and the cross section $\sigma_{I^i \to I^f}$ for photoabsorption (P model) or the transition rate $\Gamma_{I^i \to I^f}$ for Auger-Meitner decay (AM model) and fluorescence (F model). These four tasks are solved by separate machine-learning models. All are regression problems [80] with the following inputs (i.e., features) and outputs (i.e., labels).

The features are given by the following quantities based on our definition of an individual quantum state in Sec. II A:

(i) occupation numbers n^i_{occ} of the initial electronic configuration, i.e., $(N^i_{1s}, N^i_{2s}, N^i_{2p}, \dots)$;

(ii) quantum numbers qn_i of the initial state, i.e., $(L_i, S_i, M_{L_i}, \kappa_i)$;

(iii) type of process p being considered, i.e., (involved hole, first involved electron, second involved electron {for AM, otherwise zero}, kind of process {1:P, 2:AM, 3:F});

(iv) quantum numbers qn_f of the final state, i.e., $(L_f, S_f, M_{L_f}, \kappa_f)$.

The first case gives N_{orb} features, where N_{orb} is the number of subshells involved in the initial electronic configuration, and the rest provides four features per each case. Thus, the total number of features N_{features} in a feature vector is given by

$$N_{\text{features}} = N_{\text{orb}} + 12. \tag{1}$$

Note that the type of process being considered can be interchanged with the occupation numbers n^f_{occ} of the final electronic configuration. Here, the former is employed in the feature vector to reduce the number of features, which is especially important for heavy atoms and/or the inclusion of resonant effects.

It is also worthwhile to mention that (as can be seen from Ref. [71]) cross sections and decay rates are invariant under a change of the angular-momentum projection quantum numbers $M_{L_i} \to -M_{L_i}$ and simultaneously $M_{L_f} \to -M_{L_f}$—a relation the machine-learning models fail to learn. Therefore, we force the machine-learning models to preserve this symmetry by using $M_{L_i} \geqslant 0$ as a feature only. More precisely,

$$\text{if } M_{L_i} \begin{cases} > 0 : M_{L_i} \text{ and } M_{L_f} \\ = 0 : M_{L_i} = 0 \text{ and } |M_{L_f}| \\ < 0 : |M_{L_i}| \text{ and } -M_{L_f} \end{cases} \tag{2}$$

are taken as features for the projection quantum numbers.

Another important point is that the individual models are not given all features as inputs, only those that are relevant.

Transition energies are independent of M_{L_i} and M_{L_f}—another relation the machine-learning model fails to learn. Hence, for the energy model, they are not used and, therefore, $N^{\mathrm{E}}_{\mathrm{features}} = N_{\mathrm{features}} - 2$. Similarly, for the other three models the kind of process (P, AM, or F) is an unnecessary feature as it is fixed *a priori* by the model used. Additionally, features for involved holes and electrons are only important if they exist for the process in question. Consequently, we have $N^{\mathrm{P}}_{\mathrm{features}} = N_{\mathrm{features}} - 3$, $N^{\mathrm{AM}}_{\mathrm{features}} = N_{\mathrm{features}} - 1$, and $N^{\mathrm{F}}_{\mathrm{features}} = N_{\mathrm{features}} - 2$.

The label is always only one number since each task has its own machine-learning model:

$$y^{\mathrm{pred}} = \begin{cases} E^{(1)}_{I^i \to I^f} \text{ in eV for E model} \\ \sigma_{I^i \to I^f} \text{ in a.u. for P model} \\ \Gamma_{I^i \to I^f} \text{ in a.u. for AM model} \\ \Gamma_{I^i \to I^f} \text{ in a.u. for F model.} \end{cases} \tag{3}$$

Data preparation depends on the type of machine-learning model used. For the neural networks, the widely recommended Z-score normalization is applied to each feature x_k [81], i.e.,

$$x'_k = \frac{x_k - \mu_k}{\sigma_k}, \tag{4}$$

with mean μ_k and standard deviation σ_k of the kth feature with respect to all training data. Consequently, the prepared input data form a distribution with zero mean and unit standard deviation. For the random forest regressors, however, no feature normalization is required since it is not distance-based.

The energy values cover a wide range from 0 eV to the energy of the incoming x rays, typically a few thousand electronvolts. For the neural network, they are also normalized by Z-score normalization [see Eq. (4)] in order to keep their values in a smaller range. For the random forest regressor, the pure energy values are used.

Cross sections and rates cover several orders of magnitude. Thus, logarithmic scaling might be useful and is, in fact, applied for the random forest regressors. For the neural networks, however, we prefer to use pure cross section and rate values by, instead, respecting the wide range in the loss function and the output activation (see Sec. II C) without any scaling. The advantage is that this avoids back-scaling, which in combination with Z-score normalization is prone to errors, especially for very small cross sections and rates.

C. Neural network

Neural networks [80,82,83] are the central tool of deep learning. In general, they consist of a sequence of several sets of linear transformations followed by nonlinear activations. Each step in this sequence is called a layer [59]. The number of layers in the neural network determines its depth. Based on a chosen loss function and an optimizer, they are trained via back-propagation [84]. The basic idea of a (deep) neural network is that each layer is effectively learning a more complex representation of the raw input features and that this reduces the number of parameters needed to be fitted [85].

TABLE II. Neural network architecture: number of units per layer for each neural network trained in this work (see Sec. II C).

Model	In	1	2	3	4	5	Out
E	15	512	256	128	64	32	1
P	14	1024	512	256	128	64	1
AM	16	1024	512	256	128	64	1
F	15	1024	512	256	128	64	1

1. Hyperparameter tuning

Before explaining the neural network architecture and the hyperparameters employed in the present work, let us briefly explain the general way we have made these decisions. This will make some of our reasoning in the following two paragraphs clearer. The neural network architecture and hyperparameters are determined by "trial and error." Due to high training efforts and fluctuations in loss values from training to training, a more systematic and automated hyperparameter optimization, e.g., by a grid search [80], would not be well suited for our purpose. It is especially worthwhile to note that our models are system-specific. As will be explained in Sec. II E, for each machine-learning-based Monte Carlo calculation, the models need to be retrained. If we also had to re-optimize the hyperparameters for (almost) every machine-learning-based Monte Carlo calculation, this would be in clear contrast to our goal of speeding up the calculations. Moreover, for speeding up calculations, models should also be chosen such that training is not more time consuming than really necessary. Consequently, our aim is not to find the perfect hyperparameters and the best possible model performance for a given training set. Note that differences between different models are often anyhow only very small. Instead, it is more critical to build models, hyperparameters included, that allow us to train them for different training sets and training set sizes with a good (but not necessarily perfect) performance within an acceptable amount of time.

2. Network architecture

For our neural networks, we employ the popular deep learning library Keras [86] of the TensorFlow machine-learning platform [87]. Our neural networks are standard feedforward neural networks with seven layers, input and output layer included, and with the number of units given in Table II. This neural network architecture has sufficient model capacity to approximately fit the data, but not enough to nearly perfectly interpolate the training data (see Sec. III B). For argon, interpolating training data as suggested by the "modern" interpolation hypothesis [88] is a tough task because it actually requires very large neural networks and, concomitantly, very long training times (see Sec. III B). Therefore, we have chosen this network architecture as a compromise between computational effort and numerical accuracy. Of course, other neural network architectures with comparable capacity would work similarly well.

For the activation function, the hyperbolic tangent (tanh) is chosen. Indeed, nowadays, in the deep learning community rectified linear units (ReLU) or variants thereof are much more recommended [80,89]. Nonetheless, in our numerical

investigations we have found that for the situations considered in this work, tanh matches or sometimes even outperforms the other available activation functions. To improve the training process with tanh activation, weights are initialized following the "GlorotUniform" initializer explained in Ref. [90]. Energy values are normalized to zero mean and are in principle unbounded. Thus, for the energy model a linear output layer is a rational choice. On the other hand, cross sections and rates are unnormalized and cover a range between zero and unity. Hence, we chose a sigmoid output layer. Of course, in the typical ranges of output values ($\approx 10^{-3}$ to 10^{-7}) sigmoid is almost constant. But for the present models, this seems not to be a very serious problem. Overfitting to the training data is reduced by regularizing the models with dropout [91] with a soft probability of 0.01 (E) or 0.05–0.1 (P, AM, and F), respectively. We do not regularize our models very strongly due to the model capacity being too low for interpolating training data.

3. Optimization

The neural networks are trained on mini batches of size 2^{11} using the Adam optimization algorithm [92] with early stopping and a maximum of 1200 epochs (i.e., forward and backward passes through the neural network). We have chosen Adam as it is known to be fairly robust to the choice of hyperparameters, like the learning rate. The learning rate for Adam is set to 0.0005 (E) and 0.001 (P, AM, and F). Most important for the learning is the loss function on which the optimization is performed. For the energy model, the mean squared error (MSE) on the training set is employed. MSE on a general dataset D with size N_D in one dimension is given by

$$L_D^{\mathrm{MSE}} = \frac{1}{N_D} \sum_{j=1}^{N_D} \left(y_j^{\mathrm{calc}} - y_j^{\mathrm{pred}}\right)^2, \tag{5}$$

where y_j^{calc} is the label value of the jth example in D and y_j^{pred} is the prediction, respectively. However, MSE only works well if labels cover a similar range. Otherwise, errors in small label values will be overlooked. Therefore, for the other three models, we define a mean squared logarithmic error (MSLE) as

$$L_D^{\mathrm{MSLE}} = \frac{1}{N_D} \sum_{j=1}^{N_D} \left(\log_{10}\left[y_j^{\mathrm{calc}} + \epsilon\right] - \log_{10}\left[y_j^{\mathrm{pred}} + \epsilon\right]\right)^2, \tag{6}$$

on which they are trained. In this expression, $\epsilon = 10^{-10}$ is used for numerical stability. Values smaller than ϵ are practically treated as zero. The value of 10^{-10} makes sense since smaller photoionization cross sections are negligible. Due to the choice of sigmoid output activation, it is guaranteed that all $y_j^{\mathrm{pred}} > 0$. (They are set to zero later if they are found to be very small). Note that MSLE basically measures by how many orders of magnitude y_j^{calc} and y_j^{pred} differ.

4. Performance measure

Finally, we need to evaluate how well the trained model behaves on a test set not seen during training. A way of measuring the performance of the model is to compute the MSE (for E) or MSLE (for P, AM, and F) on the test set. In addition to this, for each example in the test set the absolute error $y_j^{\mathrm{calc}} - y_j^{\mathrm{pred}}$ or the logarithmic error $\log_{10}[y_j^{\mathrm{calc}} + \epsilon] - \log_{10}[y_j^{\mathrm{pred}} + \epsilon]$ can be calculated and represented in a histogram. For the AM or F models, however, there is one problem with the (quasi-)forbidden transitions. If $y_j^{\mathrm{calc}} = 0$ but $y_j^{\mathrm{pred}} > 0$ or vice versa, the logarithmic error mainly depends on our choice of ϵ. As a consequence, MSLE can be quite large and (at least) for a human-based interpretation loses its usefulness. Therefore, we perform the following: We measure the accuracy on the whole test set (or any other dataset we are interested in). The accuracy,

$$A_D = \frac{\#\text{ of correct predictions}}{N_D}, \tag{7}$$

here is a measure of how good the machine-learning model learns whether a transition is allowed or (quasi-)forbidden, i.e., "# of correct predictions" includes the cases in which $y_j^{\mathrm{calc}} > 0$ and $y_j^{\mathrm{pred}} > 0$ or $y_j^{\mathrm{calc}} = 0$ and $y_j^{\mathrm{pred}} = 0$. Knowing the accuracy, all wrong predictions, i.e., $y_j^{\mathrm{calc}} = 0$ but $y_j^{\mathrm{pred}} > 0$ or $y_j^{\mathrm{calc}} > 0$ but $y_j^{\mathrm{pred}} = 0$, can, then, be excluded from the computation of MSLE and error histograms without any loss of information. It should be stressed that during training only MSLE is evaluated, but the accuracy is not. Embedding accuracy into training by, e.g., using a preceding classification model may be pursued in a future investigation.

D. Random forest regressor

A powerful alternative to neural networks is the random forest regressor technique [93,94]. They are known to be much faster and much easier to tune with respect to hyperparameters than neural networks. But they have a limited capacity due to a lack of the depth that deep neural networks can have [95].

Random forest regressors are a decision-tree-based ensemble method. Briefly explained, the algorithm hierarchically separates the input space into subsets with respect to a specific feature and relation operators, i.e., it creates a decision tree. For each node (i.e., subset), the most important feature and the best split are controlled by a loss function; here we use MSE (for all models). To improve generalization, several of these trees are built and the final prediction is obtained as an average over all trees.

For our random forest regressors, we made use of the scikit-learn implementation [96] with 100 trees in the forest. In accordance with the "modern" interpolation hypothesis [88], we barely regularize our models (i.e., the whole training dataset is used for building each tree and nodes are expanded in an unrestricted manner). This enables us to perfectly fit the training data and does not bound the test performance by a poor training performance. The only regularization performed here is that only $N_{\mathrm{features}}^{\mathrm{Model}} - 6$ features are randomly chosen at each node. As for the neural networks, these regularizations are determined by "trial and error" with respect to the model performance, the time efficiency, and the robustness to different training sets. Performance is measured in the same manner as for the neural networks (using MSE for the E model and MSLE for the P, AM, and F models).

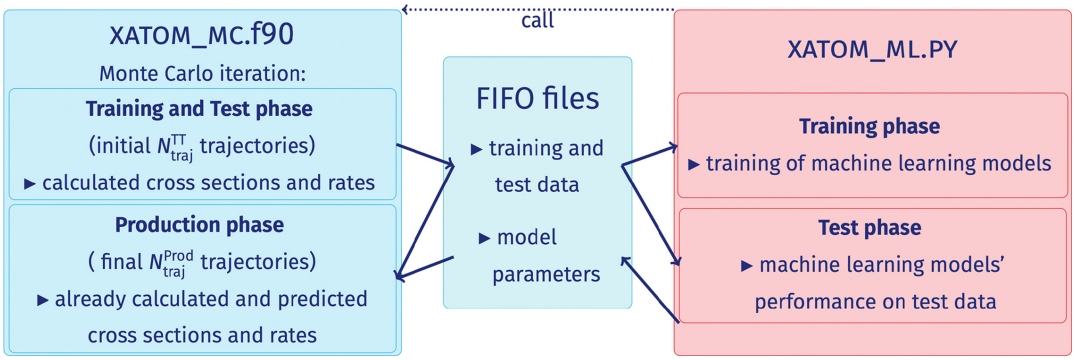

FIG. 1. Structure of the machine-learning-based state-resolved Monte Carlo implementation. The state-resolved Monte Carlo part in Fortran is called XATOM_MC, while XATOM_ML is the machine-learning part in Python. The arrows indicate that data are streamed into (→) or are obtained from (←) the FIFO files.

E. Machine-learning-based state-resolved Monte Carlo implementation

The state-resolved Monte Carlo calculations, described in Sec. II A, are computationally very expensive for situations in which a large number of orbitals is involved (i.e., for heavier atoms or when resonant excitations are included), caused by an exponentially large number of states involved in the x-ray multiphoton ionization dynamics (see Ref. [44]). We approach this challenge by employing a machine-learning strategy to support the high-level Monte Carlo calculations. For this, we implement a machine-learning-based version of the state-resolved Monte Carlo implementation within XATOM [73], which closely couples the Monte Carlo calculation (Sec. II A) with a machine-learning algorithm (Secs. II C or II D). It is sketched in Fig. 1. The state-resolved Monte Carlo implementation written in Fortran is coupled to the machine-learning part written in Python via FIFO (first-in-first-out) special files. This enables a hand-in-hand exchange of the most important information or data without storing them physically on the disk.

We separate the Monte Carlo part into two iterative phases: (i) an initial training and test phase and (ii) a final production phase. During the first N_{traj}^{TT} Monte Carlo trajectories (training and test phase, where TT indicates training and test phase), the electronic structure as well as the atomic transition parameters, i.e., transition energies, cross sections and rates, are explicitly calculated via quantum-state-resolved first-principle calculations. The calculated atomic transition parameters are collected and redirected to a FIFO file as a combined set of training and test data. The data are split up randomly into training data (85% of the data calculated) and test data (15% of the data calculated). Based on these data, the machine-learning models are trained and their performance is evaluated. The trained model parameters are redirected into another FIFO file. Based on them the machine-learning algorithms are reconstructed in Fortran. This does not include any complicated training procedures. It just means evaluating the sequence of linear functions and activation functions, whose parameters are determined by the read-in parameters. Using reconstructed machine-learning models eliminates the need for further calls of the machine-learning part in Python. Hence, no further communication between Fortran and Python, requiring further data sharing, is necessary in the final production phase. In the production phase a lot of further Monte Carlo trajectories (N_{traj}^{Prod}) are run until either the maximum number of trajectories is reached or CSDs are converged. During these Monte Carlo trajectories no further quantum-state-resolved first-principle calculations are performed. On the one hand, atomic transition parameters stored in memory are employed. This is the case when the transition at hand, for which we want to know the atomic transition parameters, has already been visited during the training and test phase and atomic transition parameters are stored. On the other hand, atomic transition parameters for transitions newly visited and, thus, not stored yet are predicted on the fly via the reconstructed machine-learning models.

Results of x-ray multiphoton ionization dynamics calculations in Sec. III C are obtained in a way that all Monte Carlo trajectories add up to a total number of 80 000 ($=N_{traj}^{TT} + N_{traj}^{Prod}$).

III. RESULTS AND DISCUSSION

We examine the performance of the machine-learning-based state-resolved Monte Carlo implementation for atomic argon at a photon energy of 5 keV. For such a photon energy, in principle all electrons can be ionized via x-ray sequential multiphoton ionization, i.e., a repeated sequence of one-photon ionization and inner-shell relaxation events. Therefore, no resonant excitation is involved in the x-ray multiphoton ionization dynamics. Following Ref. [44], we use a temporal Gaussian pulse envelope with 10 fs (full width at half maximum) and a fluence of 10^{12} photons/μm^2. Neither relativistic effects [34], nor nonsequential two-photon absorption, higher-order many-body processes such as shake-off, nor volume integration are included in the calculations (see Ref. [44] and references therein). Due to the lack of volume integration, a quantitative comparison with experimental results is not directly possible.

A. Data collection

Before exploring the machine-learning-based results, we start by considering how to choose the number of Monte Carlo trajectories for the training and test phase and the production phase. For the machine-learning-based state-resolved Monte Carlo implementation, the quantity that can easily be tuned in order to determine the size of the training and test datasets

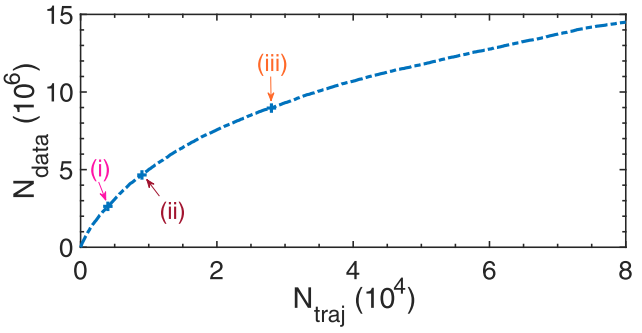

FIG. 2. Number of atomic transition parameters N_{data} collected as a function of the number of Monte Carlo trajectories N_{traj} for argon at 5 keV. The arrows indicate the three different cases considered in this work (see Table III).

is the number of Monte Carlo trajectories during the training and test phase ($N_{\text{traj}}^{\text{TT}}$). Figure 2 shows the number of atomic transition parameters (N_{data}) collected as a function of the number of Monte Carlo trajectories (N_{traj}). Of course, this relation slightly varies from one Monte Carlo calculation to another, but, nonetheless, Fig. 2 gives a very good orientation on N_{data}. As can be seen, for argon at 5 keV, N_{data} is very high ($\approx 10^7$). This is related to the huge number of individual states involved in the calculations (Sec. II A). Moreover, N_{data} seems not to be saturated as N_{traj} increases, within the range of N_{traj} we used (up to $N_{\text{traj}} = 80\,000$). This makes successfully training the machine-learning models a tough task, as we are going to demonstrate in Sec. III B. On the other hand, this presents a situation in which a successful implementation of machine learning can be really helpful, in contrast with light atoms like neon. For our studies in Secs. III B and III C, we have chosen three different $N_{\text{traj}}^{\text{TT}}$ such that they cover a wide range of the curve in Fig. 2, i.e., $N_{\text{traj}}^{\text{TT}} = 4000$, 9000, and 28 000, as listed in Table III.

To gain an overview of the remaining number of Monte Carlo trajectories in the production phase, in Fig. 3 we show argon CSDs obtained using the state-resolved Monte Carlo implementation (no machine learning) [44] with different numbers of Monte Carlo trajectories N_{traj}. The error bars represent the statistical error estimate of the Monte Carlo calculation for each charge state q, given by $\epsilon_q = \sqrt{P_q(1-P_q)/(N_{\text{traj}}-1)}$, where P_q is the population probability of the charge state q. Note the proportionality of the Monte Carlo error to $1/\sqrt{N_{\text{traj}}-1}$, causing comparably large errors for small N_{traj}. Figure 3 demonstrates that for 10 000 Monte Carlo trajectories the CSD is almost converged. It should be mentioned that more Monte Carlo trajectories are necessary

TABLE III. Number of training and test Monte Carlo trajectories $N_{\text{traj}}^{\text{TT}}$ as well as the corresponding training and test dataset size ($N_{\text{data}}^{\text{TT}}$) for the three different cases considered in this work for argon at 5 keV.

Label	$N_{\text{traj}}^{\text{TT}}$	$N_{\text{data}}^{\text{TT}}$
(i)	4000	2 686 711
(ii)	9000	4 680 860
(iii)	28 000	8 965 379

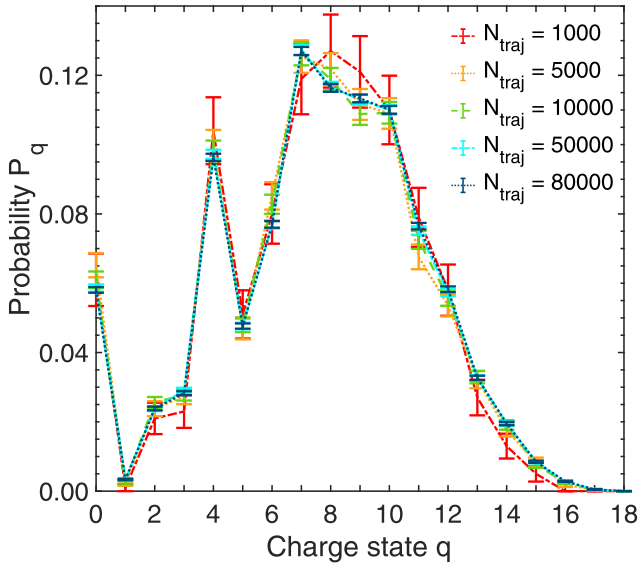

FIG. 3. Convergence behavior of argon CSDs as a function of the number of Monte Carlo trajectories N_{traj}. Results are obtained with the state-resolved Monte Carlo implementation of Ref. [44] (no machine learning). The error bars indicate the statistical error.

for convergence of state-resolved quantities such as spectra. Due to this and in order to be safely sure that Monte Carlo errors are sufficiently small for our purpose, we utilize here 80 000 Monte Carlo trajectories in total (i.e., training and test plus residual production trajectories). Note further that CSDs in Fig. 3 are converged when N_{data} is still far from a saturation point (Fig. 2). This demonstrates that only a small fraction of frequently visited transitions is critical for the ionization dynamics calculations. This is also the reason why the Monte Carlo method is so powerful [38] and why the machine-learning-based state-resolved Monte Carlo implementation works (see Sec. III C).

B. Performance of machine-learning models

Let us next discuss machine-learning results for argon, employing both neural networks (Sec. II C) and random forest regressors (Sec. II D). We examine also how the machine-learning performance depends on the training set size. In particular, the three different dataset sizes (i.e., combined set of training and test data) listed in Table III are considered. According to the feature for the kind of process ($p = 1$, 2, or 3; see Sec. II B), each dataset is separated into the individual subdatasets for the P model (25%–28% of $N_{\text{data}}^{\text{TT}}$), the AM model (57%–59% of $N_{\text{data}}^{\text{TT}}$), and the F model (15%–16% of $N_{\text{data}}^{\text{TT}}$). For the E model, duplications with respect to the energy label are removed. (Thus, 29%–35% of $N_{\text{data}}^{\text{TT}}$ are left over for the subdatasets for the E model.) Moreover, 85% of randomly selected data are employed as data for training a model, while the remaining 15% serve as test data.

To inspect the model's performance on the unseen test dataset, we show three-dimensional scatter plots of predicted data in Figs. 4(a)–4(d) and 5(a)–5(d) and the distribution of absolute or logarithmic errors in Figs. 4(e)–4(h) and 5(e)–5(h). For Figs. 4(a)–4(d) and 5(a)–5(d), the vertical axis

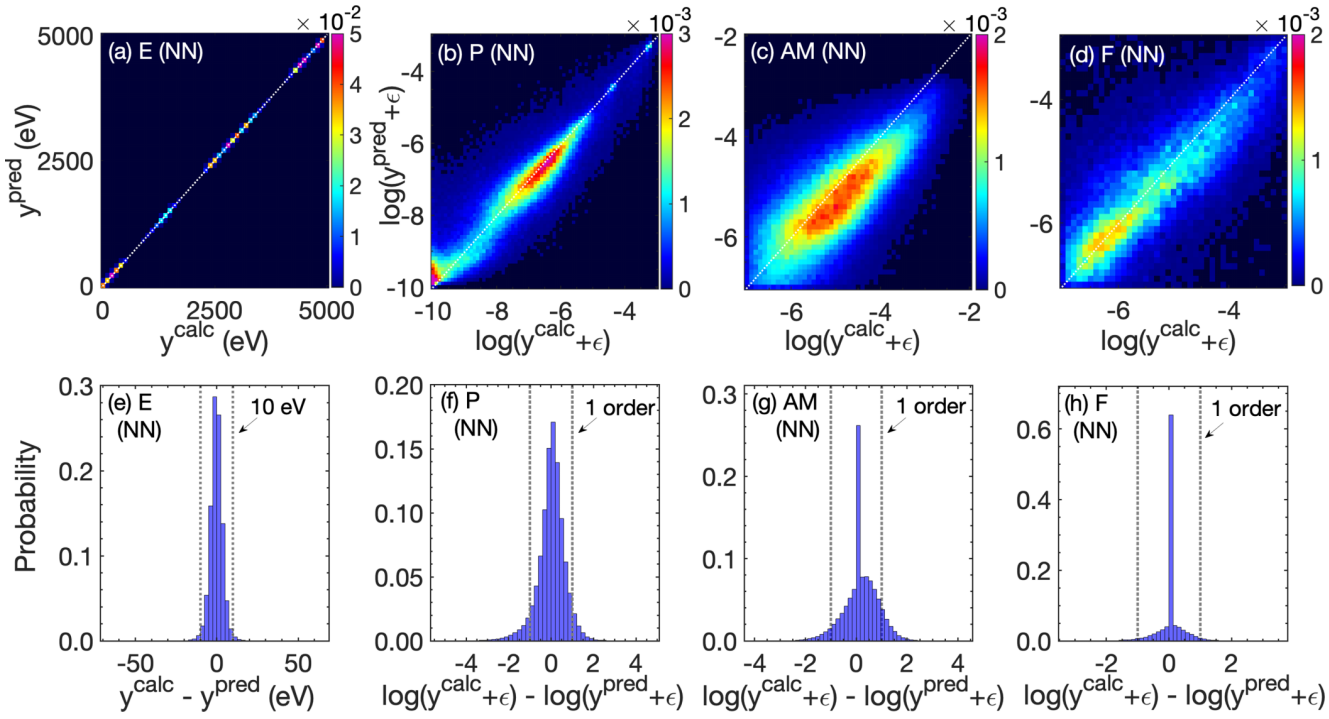

FIG. 4. Performance of the neural networks (NN) in terms of (a)–(d) scatter plots and of (e)–(h) error histograms: (a), (e) the transition energy E in eV; (b), (f) the photoionization cross section (P) in logarithmic scaling; (c), (g) the Auger-Meitner decay rate (AM) in logarithmic scaling; and (d), (h) the fluorescence rate (F) in logarithmic scaling. The color bars in panels (a)–(d) show the relative number of pairs $(y^{\text{calc}}, y^{\text{pred}})$, scaled by (a) 10^{-2} or (b)–(d) 10^{-3}. The dotted white line indicates the identity mapping. We consider the test dataset of case (ii).

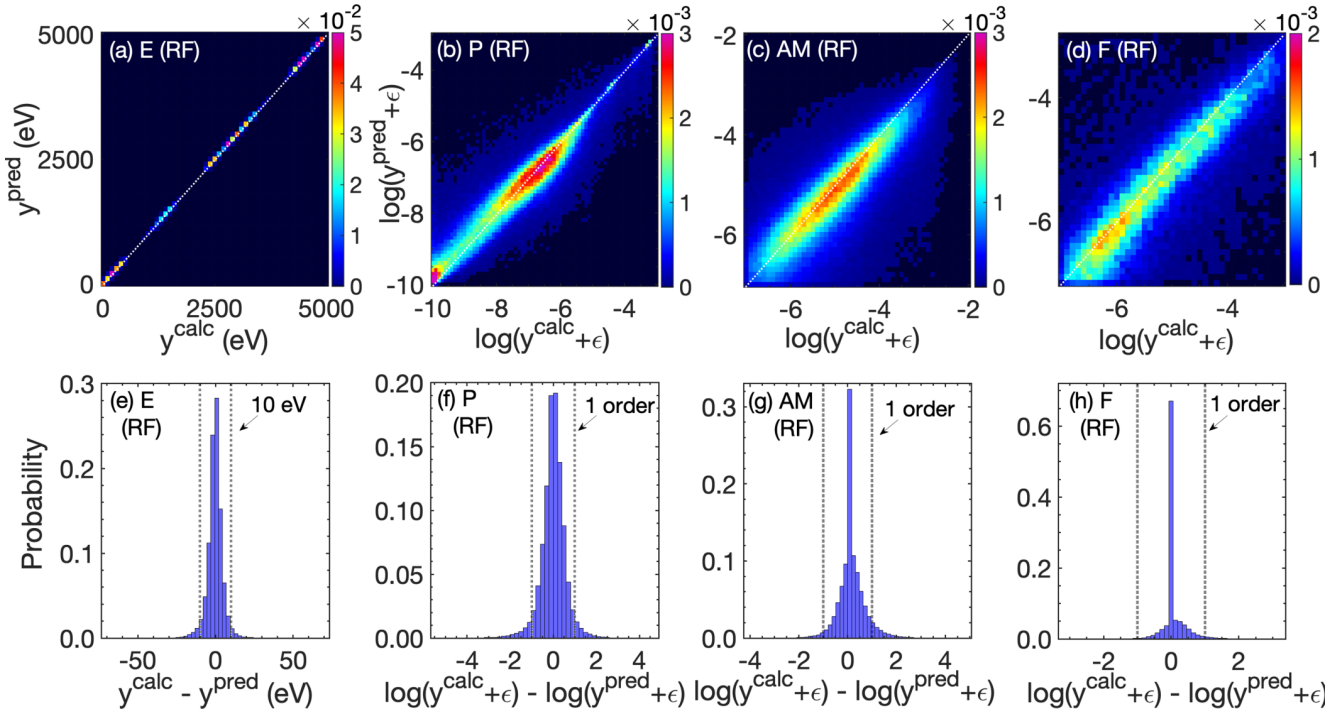

FIG. 5. Performance of the random forest regressors (RF) in terms of (a)–(d) scatter plots and of (e)–(h) error histograms: the panels show the same quantities as in Fig. 4.

TABLE IV. Test error statistics for the neural networks (NN) and random forest regressors (RF): MSE loss (L^{MSE}) [Eq. (5)] in eV^2 for the energy model (E) and MSLE loss (L^{MSLE}) [Eq. (6)] for the photoionization cross section (P), Auger-Meitner decay rate (AM), and fluorescence rate (F) models, evaluated on the test datasets of all three cases (Table III). For the AM and F models, additionally the accuracy (A) [Eq. (7)] is given, in %.

		NN			RF		
Model	L or A	(i)	(ii)	(iii)	(i)	(ii)	(iii)
E	L_{Test}	13.1	12.2	9.4	30.4	27.0	24.8
P	L_{Test}	0.42	0.41	0.43	0.36	0.32	0.26
AM	L_{Test}	0.44	0.46	0.49	0.32	0.32	0.29
	A_{Test}	87.7	86.6	84.3	87.7	87.6	87.9
F	L_{Test}	0.13	0.14	0.15	0.11	0.10	0.09
	A_{Test}	90.9	91.0	89.5	89.0	89.3	89.6

is the predicted energy in eV [Figs. 4(a) and 5(a)] or the predicted cross section [Figs. 4(b) and 5(b)] or rate [Figs. 4(c), 5(c) and 4(d), 5(d)] in logarithmic scaling, while the horizontal axis is the underlying calculated value. For both, 100-eV bins [Figs. 4(a) and 5(a)] or 0.1 bins [Figs. 4(b), 5(b), 4(c), 5(c), and 4(d), 5(d)], respectively, are used. The color bars show the relative number of scatter points, scaled by 10^{-2} [Figs. 4(a) and 5(a)] or 10^{-3} [Figs. 4(b), 5(b), 4(c), 5(c), and 4(d), 5(d)], i.e., the number of pairs of calculation and prediction within a bin divided by the total number of test data for the model in question. The three-dimensional plots supplement the common two-dimensional scatter plots by further information about the distribution of scatter points, which is sensible when the number of data is large, i.e., here, on the order of 10^5. Moreover, for brevity, only results for the case (ii) are given in the figures (for the other cases see below in the context of Table IV).

It becomes evident from Figs. 4(e) and 5(e) that transition energies are mostly predicted with better than 10-eV accuracy [i.e., the sum of error bars within the 10-eV window yields 99% (NN) or 94% (RF) for case (ii)] and with at most around 50 eV difference. The good performance of the energy model is underlined by Figs. 4(a) and 5(a), looking very similar to the identity mapping of $y^{\mathrm{pred}} = y^{\mathrm{calc}}$. In contrast with the energy model, cross section and rate models perform less accurately for argon. Most predictions [85%–98% for case (ii)] deviate from the calculation by less than an order of magnitude [see first-order windows in Figs. 4(f)–4(h) and 5(f)–5(h)]. However, deviations up to four orders of magnitude are possible. Comparably poor predictions can occur for all cross sections or rates, even though higher calculated values seem to be a little bit less inaccurate [see Figs. 4(b)–4(d) and 5(b)–5(d)]. Nonetheless, of course, a better accuracy is actually needed the higher the calculated cross section or rate. Using MSLE loss during training, the models cannot respect this in the model training and evaluation. Moreover, we observe that fluorescence rates are predicted the best, while Auger-Meitner decay rates possess the largest deviations. Interestingly, for photoionization and Auger-Meitner decay, there is a tendency that predictions are smaller than the calculated cross sections or rates [see Figs. 4(b), 4(c) and 5(b), 5(c)].

TABLE V. Training times, real and CPU, in minutes for the neural networks (NN) and the random forest regressors (RF) for all four models. We consider the training datasets of all three cases (Table III).

		Real time (min)		CPU time (min)	
Data set	Model	NN	RF	NN	RF
(i)	E	92	5	2674	5
	P	112	4	4339	4
	AM	228	9	8904	9
	F	40	2	1549	2
(ii)	E	153	9	4401	9
	P	187	8	7233	8
	AM	399	22	15733	22
	F	102	4	3965	4
(iii)	E	247	16	7526	16
	P	346	15	13833	15
	AM	691	45	28627	45
	F	211	8	8523	8

It is also worthy to note that 84%–91% of transitions for Auger-Meitner or fluorescence decay are classified as allowed or (quasi-)forbidden when also being allowed or (quasi-)forbidden, respectively. The test accuracy is listed in Table IV for both the neural network and the random forest regressor. For the other transitions that are classified incorrectly, the corresponding rates, i.e., those the transition actually has or the one the actually (quasi-)forbidden transition receives, are mostly also small ($\approx 10^{-6}$ a.u.). Some of them are, however, comparably high with up to 10^{-3} a.u. (not shown for brevity). Recall that these wrongly classified transitions are not included in any other quantity to measure the test performance, like the error distribution, to stress that this does not cause alone the deviations from a perfect performance.

Next, we examine how the performance of the machine-learning model depends on the training set size. Table IV reports test loss and accuracy for all three dataset cases in Table III and for both the neural network and the random forest regressor. (For more details on these quantities see Sec. II C.) More training data improve the energy model, which is already quite good, whereas the cross section and rate models only marginally profit for the random forest regressor or do not profit at all for the neural networks. A possible explanation for the lack of improvement, especially for the neural networks, might be a too low model capacity that slows down the gain of better generalization (see below in the context of Table VI). In this context, it is important to emphasize that using more data for training does not have an essential impact on the machine-learning model's performance, but enhances training times more than linearly. Table V compares training times for all three different dataset cases (Table III). Calculations were performed on AMD EPYC 7302 16-Core processors with a maximum number of 64 virtual cores (threads).

We now contrast the neural network and the random forest regressor. As expected, both behave generally fairly similarly (compare Figs. 4 and 5). From the results in Table IV, we conclude that neural networks are better suited for predicting

TABLE VI. Training and validation performance of the neural networks (NN): MSE loss (L^{MSE}) [Eq. (5)] in eV^2 for the energy model (E) and MSLE loss (L^{MSLE}) [Eq. (6)] for the photoionization cross section (P), Auger-Meitner decay rate (AM), and fluorescence rate (F) models, evaluated on the training (Tr) and validation (V) datasets of all three cases (Table III). For the AM and F models, additionally the accuracy (A) [Eq. (7)] is given in %.

Model	L or A	(i) NN	(ii) NN	(iii) NN
E	L_{Tr}	8.2	8.0	5.9
	L_{V}	11.6	10.7	8.1
P	L_{Tr}	0.22	0.29	0.36
	L_{V}	0.42	0.42	0.43
AM	L_{Tr}	0.39	0.42	0.48
	A_{Tr}	91.4	88.7	85.3
	L_{V}	0.44	0.46	0.50
	A_{V}	87.8	86.6	84.3
F	L_{Tr}	0.09	0.11	0.13
	A_{Tr}	96.5	95.2	91.9
	L_{V}	0.14	0.14	0.15
	A_{V}	90.9	90.6	89.6

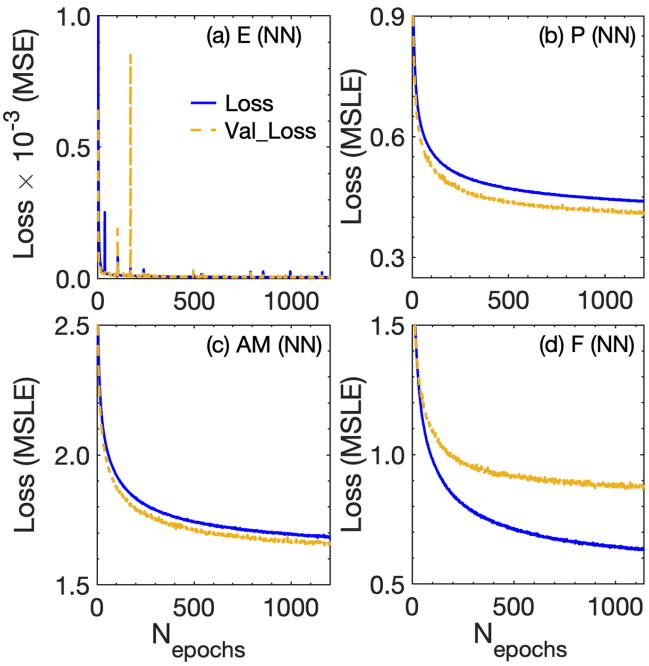

FIG. 6. Loss curves of the neural networks (NN): loss evaluated on the training data (blue) and the validation data (orange) as a function of the number of epochs trained for all four models. In panel (a) the MSE loss [Eq. (5)] in Z-score scaling and in panels (b)–(d) the unscaled MSLE loss [Eq. (6)] is shown. We consider the training dataset of case (ii).

energies. However, for cross sections and rates, the random forest regressors outperform the neural networks. Random forest regressors for cross section and rate predictions exhibit an improvement with more data, while those for neural networks decline. As a consequence, this increases the difference between neural networks and random forest regressors with increasing training set sizes. Most importantly, neural networks have a critical disadvantage. Training is very expensive (see Table V). It can cost several hours for a single neural network, although multiple cores are utilized (real time $\ll$ CPU time). Unlike neural networks, random forest regressors are trained in less than an hour even for the largest training sets on a single core (real time = CPU time).

To complete our understanding of the neural networks' performance, we finally briefly examine the training and validation losses in Table VI. (For the random forest regressors, those investigations are not possible since training data are interpolated and, thus, always have near zero loss.) Note that per default in TensorFlow some of the data are separated from the training data and are used as validation data. Here, we use 10% of the training data for validation. The results in Table VI demonstrate that the capacities of the cross section and rate models are too low to nearly perfectly fit the training data. The task of predicting cross sections and rates is too complex. This can be seen by the large training losses, increasing with more training data. As a consequence, validation and test data cannot be predicted very accurately either. Whether a network architecture with a higher model capacity can significantly overcome this limitation remains an open question at the moment (that might be answered in the future). However, it is most likely that a higher model capacity will lead to a substantial increase in training time. Therefore, the chosen network architecture is a compromise between computational effort and numerical accuracy. In contrast, for the energy model, the capacity seems to be sufficient since predicting transition energies is an easier task. In addition, Fig. 6 shows the evolution of training and validation losses with the number of epochs trained for the case (ii) only. We remark that using dropout during training increases the training loss and, hence, it is normal that validation losses can be smaller than training losses. For the final loss, dropout is not included. Thus, the training losses in Table VI are smaller than in Fig. 6. Moreover, we note that the losses for the Auger-Meitner decay and fluorescence rate models are clearly larger in Fig. 6 than in Table VI due to wrongly classified transitions. As can be seen, loss curves are quite smooth and almost converged. Even early stopping before the maximal number of 1200 epochs due to increasing validation loss is possible [see Fig. 6(d)]. Especially for the cross section and rate models, the losses decrease only by a few percent (<10%) during the last 600 epochs. As a consequence, training longer would not have a notable effect on training, validation, and test performances. Since training times are approximately linear in the number of epochs trained, we may, on the contrary, save some training time by using fewer epochs without a noticeable reduction in performance.

C. Results for machine-learning-based state-resolved Monte Carlo calculations

Having investigated the performance of different machine-learning models in the previous section, we now study the performance of x-ray multiphoton ionization-dynamics calculations carried out with the machine-learning-based state-resolved Monte Carlo implementation introduced in Sec. II E. For simplicity, we only employ the neural networks of Sec. III B as machine-learning models in the production

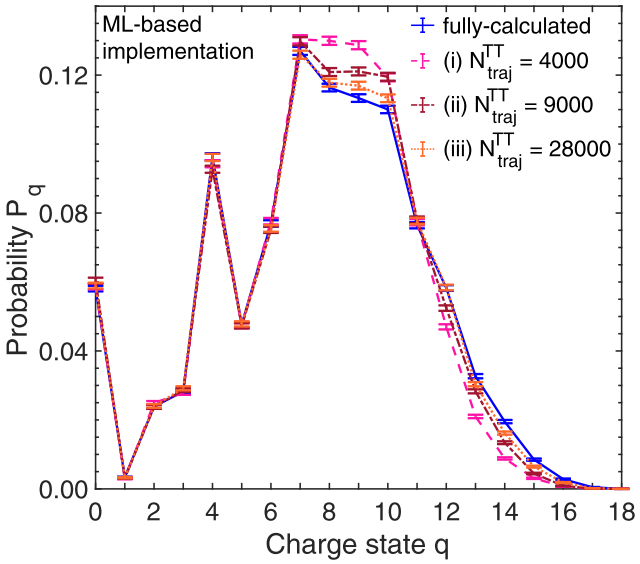

FIG. 7. Comparison of machine-learning-based CSDs with the fully calculated CSD. Results are obtained with the state-resolved Monte Carlo implementation without machine learning [44] (fully calculated) and with the machine-learning-based (ML-based) state-resolved Monte Carlo implementation [Sec. II E] for different numbers of training and test Monte Carlo trajectories $N_{\text{traj}}^{\text{TT}}$ (Table III). The error bars indicate the statistical error of the Monte Carlo calculation.

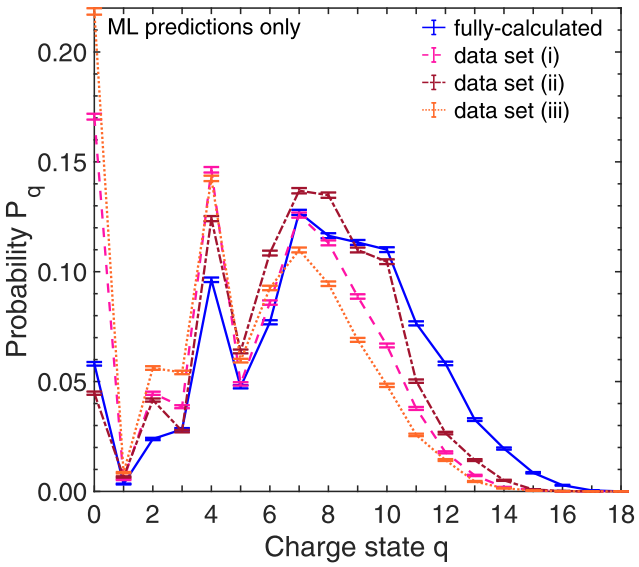

FIG. 8. Similar to Fig. 7, but all atomic transition parameters are predicted by the previously trained neural networks for the different datasets (Table III).

phase. Random forest regressors perform comparably to neural networks, as shown in Sec. III B. However, they are a bit harder to embed in the state-resolved Monte Carlo implementation due to the large number of individual trees, which all need to be redirected to the FIFO file and reconstructed in Fortran (see Sec. II E). We compare machine-learning-based state-resolved Monte Carlo calculations for argon with state-resolved Monte Carlo calculations using the implementation introduced in Ref. [44] (in which no machine learning is employed).

Figure 7 compares argon CSDs for all three previously considered dataset cases, which correspond to different numbers of training and test Monte Carlo trajectories (Table III). All machine-learning-based CSDs match the overall behavior of the fully calculated CSD (i.e., in which no machine learning is employed). Especially for low charge states (i.e., $q \leqslant 7$), the agreement is good for all three machine-learning cases. For larger charge states, however, deviations beyond the Monte Carlo errors can be observed, which are enhanced the smaller the number of training and test Monte Carlo trajectories [cases (i) and (ii)]. This is because of the machine-learning predictions of atomic transition parameters for the transitions newly visited in the production phase. As seen in Sec. III B, the predictions for cross sections and rates made by the neural networks are not very accurate. Since the transitions newly visited in the production phase are not directly sampled from the same distribution as the training and test data used in Sec. III B, they are generally expected to be predicted even less accurately (not shown for brevity) [49,80]. The fact that the machine-learning-based CSDs are, nonetheless, quite good relies on the use of atomic transition parameters already calculated. For ≈14% [case (i)], ≈24% [case (ii)], or ≈40% [case (iii)] of individual initial states all possible atomic transition parameters are calculated in the training and test phase, and are used in the production phase (see Sec. II E). It also explains the improvement with more training and test Monte Carlo trajectories attributed to more calculated atomic transition parameters.

To illustrate this point, in Fig. 8, we show comparisons of CSDs where the machine-learning-based CSDs are obtained by using only machine-learning predictions for atomic transition parameters. In particular, we do not use the machine-learning-based implementation as described in Sec. II E, combining both calculated and predicted atomic transition parameters. Instead, for Fig. 8, only the production phase is run with all atomic transition parameters being predicted by the previously trained neural networks. As can be seen, when only predicted atomic transition parameters are used the overall behavior of the machine-learning-based CSDs still roughly matches that of the fully calculated CSD. But the agreement is no longer close to being quantitative.

In this context, let us briefly come back to the random forest regressors (Sec. III B), which perfectly interpolate the training data. Thus, employing random forest regressors, it would barely make a difference whether atomic transition parameters already calculated are used or whether all atomic transition parameters are predicted by the random forest regressors. In particular, Figs. 7 and 8 would look very similar to each other and this would make the above investigation impossible. Moreover, having at hand the atomic transition parameters already calculated in the training and test phase (see Sec. II E), we do not consider this as an advantage of the random forest regressors.

Figures 9(a) and 9(b) show the photoelectron spectra, Figs. 9(c) and 9(d) show the Auger-Meitner electron spectra, and Figs. 9(e) and 9(f) show the fluorescence spectra with an energy resolution of 1 eV. At this energy resolution, the

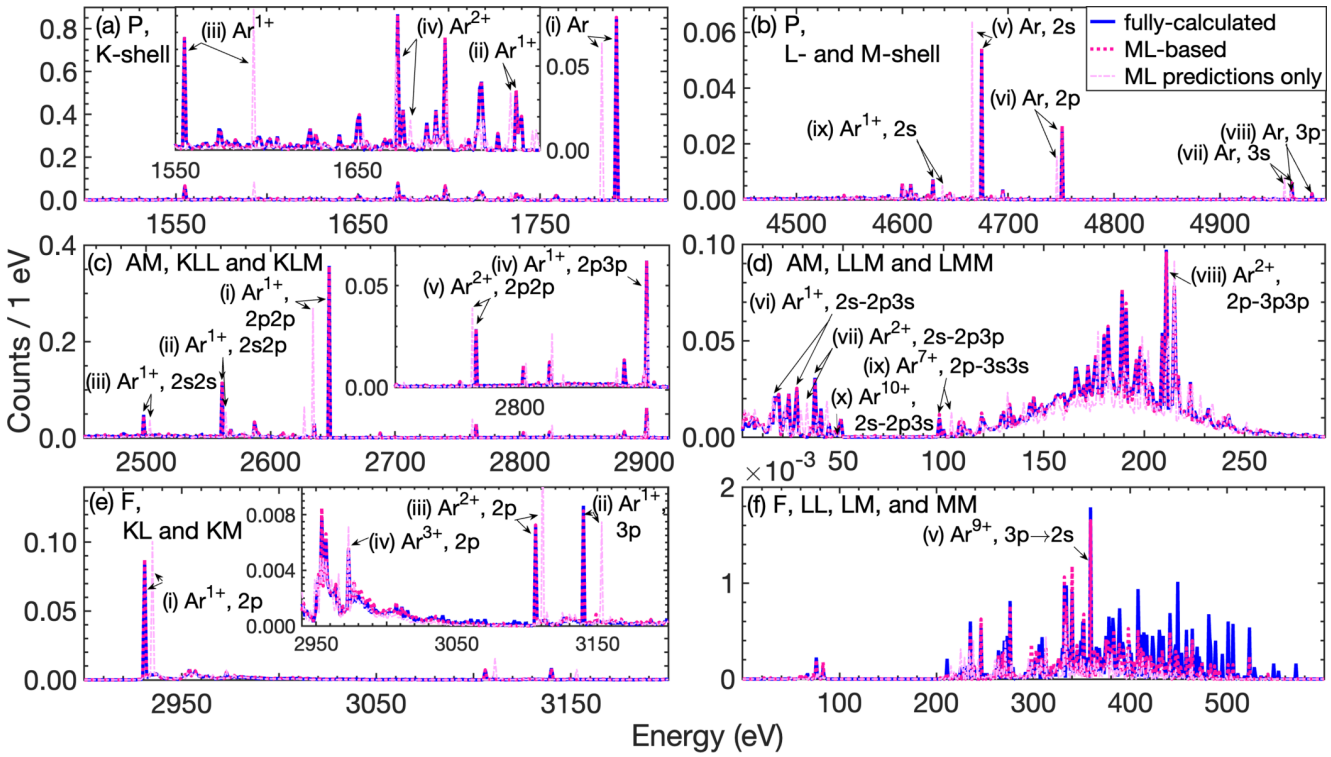

FIG. 9. Comparison of machine-learning-based (ML-based) and fully calculated spectra for (a), (b) photoelectron (P); (c), (d) Auger-Meitner electron (AM); and (e), (f) fluorescence (F). Calculations obtained with the state-resolved Monte Carlo implementation without machine learning [44] (blue) are compared with those obtained with the machine-learning-based state-resolved Monte Carlo implementation (Sec. II E) for case (i) in Table III (magenta). Additionally, results with all atomic transition parameters being predicted by the previously trained neural networks (pink) are given. The peak labels are explained in Tables VII–IX.

Auger-Meitner electron and the x-ray fluorescence spectra form a quasicontinuum over most parts of the energy ranges shown. Like the CSD, fully calculated results obtained with the implementation of Ref. [44] are compared with machine-learning-based results obtained with the implementation of Sec. II E, as well as those that are based only on machine-learning predictions. [For brevity, only case (i) of Table III is shown.] Some of the dominant peaks that can be assigned to at most two dominant processes are labeled with roman numbers; the corresponding transitions are specified in Table VII [for Figs. 9(a) and 9(b)], Table VIII [for Figs. 9(c) and 9(d)], and Table IX [for Figs. 9(e) and 9(f)].

Most importantly, we observe in Fig. 9 that the machine-learning-based spectra obtained with the implementation of Sec. II E (magenta lines) are in overall very good agreement with the fully calculated ones, apart from small details. This is due to the fact that spectral features are dominated by peaks belonging to very low charge states (see Tables VII–IX). But for low charge states, the corresponding atomic transition parameters are mostly all already calculated in the training and

TABLE VII. Peak assignment in the photoelectron spectra [Figs. 9(a) and 9(b)]. Calculated transition energies, $E^{\mathrm{calc}}_{I^i\to I^f}$, and transition energies predicted by the neural network [case (i)], $E^{\mathrm{pred}}_{I^i\to I^f}$, are listed for the underlying process.

Label	Process	$E^{\mathrm{calc}}_{I^i\to I^f}$ (eV)	$E^{\mathrm{pred}}_{I^i\to I^f}$ (eV)
(i)	Ar, $1s^22s^22p^63s^23p^6$ (^1S) → $1s^12s^22p^63s^23p^6$ (^2S)	1792	1784
(ii)	Ar^{1+}, $1s^22s^22p^53s^23p^6$ (^2P) → $1s^12s^22p^53s^23p^6$ (^3P)	1737	1734
	Ar^{3+}, $1s^22s^22p^63s^13p^4$ (^2D) → $1s^12s^22p^63s^13p^4$ (^1D)		1731
(iii)	Ar^{1+}, $1s^12s^22p^63s^23p^6$ (^2S) → $1s^02s^22p^63s^23p^6$ (^1S)	1555	1593
(iv)	Ar^{2+}, $1s^22s^22p^43s^23p^6$ (^1D) → $1s^12s^22p^43s^23p^6$ (^2D)	1672	1671
	Ar^{2+}, $1s^22s^22p^43s^23p^6$ (^1S) → $1s^12s^22p^43s^23p^6$ (^2S)		1679
(v)	Ar, $1s^22s^22p^63s^23p^6$ (^1S) → $1s^22s^12p^63s^23p^6$ (^2S)	4675	4666
(vi)	Ar, $1s^22s^22p^63s^23p^6$ (^1S) → $1s^22s^22p^53s^23p^6$ (^2P)	4751	4746
(vii)	Ar, $1s^22s^22p^63s^23p^6$ (^1S) → $1s^22s^22p^63s^13p^6$ (^2S)	4968	4961
(viii)	Ar, $1s^22s^22p^63s^23p^6$ (^1S) → $1s^22s^22p^63s^23p^5$ (^2P)	4987	4967
(ix)	Ar^{1+}, $1s^12s^22p^63s^23p^6$ (^2S) → $1s^12s^12p^63s^23p^6$ (^1S)	4629	4638

TABLE VIII. Peak assignment in the Auger-Meitner electron spectra [Figs. 9(c) and 9(d)]. Calculated transition energies, $E^{\text{calc}}_{I^i\to I^f}$, and transition energies predicted by the neural network [case (i)], $E^{\text{pred}}_{I^i\to I^f}$, are listed for the underlying process.

Label	Process	$E^{\text{calc}}_{I^i\to I^f}$ (eV)	$E^{\text{pred}}_{I^i\to I^f}$ (eV)
(i)	Ar^{1+}, $1s^12s^22p^63s^23p^6$ $(^2S)\rightarrow$ $1s^22s^22p^43s^23p^6$ (^1D)	2647	2634
(ii)	Ar^{1+}, $1s^12s^22p^63s^23p^6$ $(^2S)\rightarrow$ $1s^22s^12p^53s^23p^6$ (^1P)	2561	2564
(iii)	Ar^{1+}, $1s^12s^22p^63s^23p^6$ $(^2S)\rightarrow$ $1s^22s^02p^63s^23p^6$ (^1S)	2498	2503
(iv)	Ar^{1+}, $1s^12s^22p^63s^23p^6$ $(^2S)\rightarrow$ $1s^22s^22p^53s^23p^5$ (^1D)	2902	2903
(v)	Ar^{2+}, $1s^02s^22p^63s^23p^6$ $(^1S)\rightarrow$ $1s^12s^22p^43s^23p^6$ (^2D)	2765	2762
(vi)	Ar^{1+}, $1s^22s^12p^63s^23p^6$ $(^2S)\rightarrow$ $1s^22s^22p^53s^13p^6$ (^1P)	27	16
(vii)	Ar^{2+}, $1s^22s^12p^53s^23p^6$ $(^1P)\rightarrow$ $1s^22s^22p^43s^23p^5$ (^2P)	36	32
(viii)	Ar^{2+}, $1s^22s^22p^43s^23p^6$ $(^1D)\rightarrow$ $1s^22s^22p^53s^23p^4$ (^2D)	211	212
(ix)	Ar^{7+}, $1s^22s^22p^53s^23p^0$ $(^2P)\rightarrow$ $1s^22s^22p^63s^03p^0$ (^1S)	98	104
(x)	Ar^{10+}, $1s^22s^12p^43s^13p^0$ $(^3D)\rightarrow$ $1s^22s^22p^33s^03p^0$ (^2D)	<0	47

test phase. Thus, they are unaltered by machine learning and the good agreement mainly relies on atomic transition parameters already calculated. The small deviations in the spectra are caused by the influence of the error between predictions and calculations on the x-ray multiphoton ionization dynamics; here mostly indirectly via the impact on the population of the underlying initial states, so that there is no energy shift [e.g., peak (ix) in Fig. 9(d) or peak (v) in Fig. 9(f)]. Shifts in energy affect peaks that are too small to be visible.

Let us also examine the machine-learning-based spectra obtained by using predicted atomic transition parameters only (pink lines in Fig. 9). Interestingly, even in this situation the spectra roughly capture the overall behavior of the fully calculated spectra. Indeed, peak positions are shifted in energy, however, mostly within less than 10 eV (see Tables VII–IX and Sec. III B). Also the peak heights do not match very well. Nonetheless, the neural networks are good enough to recognize general tendencies in the x-ray multiphoton ionization dynamics, e.g., more Auger-Meitner decay than fluorescence decay [compare peak (i) in Fig. 9(c) to peak (i) in Fig. 9(e)]. Furthermore, it is worth mentioning that for high charge states *LLM* Auger-Meitner decay [i.e., $2s$–$2p3l$ ($l = s, p$)] is often actually forbidden due to calculated transition energies being smaller than zero. However, the neural network is unable to learn this. Consequently, actually forbidden transitions can take place in the machine-learning-based calculations [see, e.g., peak (x) in Fig. 9(d)]. In the present situation, this has only a minor impact.

Next, we investigate the time effort of the production phase in the machine-learning-based state-resolved Monte Carlo implementation (Sec. II E). Table X lists the computational times for a production phase consisting of 5000 Monte Carlo trajectories based on the three cases in Table III. For comparison, a fully calculated state-resolved Monte Carlo calculation (i.e., using the implementation in Ref. [44]) is also included with the same number of 5000 Monte Carlo trajectories. All calculations are performed on Intel Xeon E5-2630L with a single core. A significant reduction in the computational times can be found for the production phases. Using atomic transition parameters already calculated and machine-learning predictions for those not already calculated is on average six to ten times faster than the full calculation. The more atomic transition parameters are already calculated, the faster is the production phase [compare cases (i)–(iii) in Table X] since fewer predictions made by the machine-learning models are required. [But note that this gain is at the expense of a more expensive training and test phase and machine-learning model training (see Table V).] Although machine-learning models are employed in the production phase, there is still a non-negligible time effort of about 2 hours for just 5000 Monte Carlo trajectories. Predicting a single transition via the reconstructed deep neural networks is indeed fast (<5 ms). However, predicting a huge number of transitions (order of 10^6) is notably expensive.

To evaluate the overall saving in computational times for the machine-learning-based state-resolved Monte Carlo implementation, timings for the training and test phase, for the training of the machine-learning models, and for the production phase must be compared with the full state-resolved Monte Carlo calculation. However, such timings mainly depend on the available computer architecture (i.e., parallelization of the calculations, cluster usage, number of available cores). Therefore, we do not further discuss this point here. Having at hand Tables V and X enables us to

TABLE IX. Peak assignment in the fluorescence spectra [Figs. 9(e) and 9(f)]. Calculated transition energies, $E^{\text{calc}}_{I^i\to I^f}$, and transition energies predicted by the neural network [case (i)], $E^{\text{pred}}_{I^i\to I^f}$, are listed for the underlying process.

Label	Process	$E^{\text{calc}}_{I^i\to I^f}$ (eV)	$E^{\text{pred}}_{I^i\to I^f}$ (eV)
(i)	Ar^{1+}, $1s^12s^22p^63s^23p^6$ $(^2S)\rightarrow$ $1s^22s^22p^53s^23p^6$ (^2P)	2931	2935
(ii)	Ar^{1+}, $1s^12s^22p^63s^23p^6$ $(^2S)\rightarrow$ $1s^22s^22p^63s^23p^5$ (^2P)	3140	3153
(iii)	Ar^{2+}, $1s^02s^22p^63s^23p^6$ $(^1S)\rightarrow$ $1s^12s^22p^53s^23p^6$ (^1P)	3106	3111
(iv)	Ar^{3+}, $1s^12s^22p^43s^23p^6$ $(^2D)\rightarrow$ $1s^22s^22p^33s^23p^6$ (^2D)	2973	2973
(v)	Ar^{9+}, $1s^22s^12p^53s^03p^1$ $(^1D)\rightarrow$ $1s^22s^22p^53s^03p^0$ (^2P)	359	357

TABLE X. Timings for the production phase of the machine-learning-based state-resolved Monte Carlo implementation based on the cases in Table III and for $N_{\text{traj}}^{\text{Prod}} = 5000$. Average real times are compared with the full calculation with $N_{\text{traj}} = 5000$ using the implementation in Ref. [44] [no machine learning (ML)].

	No ML	ML (i)	ML (ii)	ML (iii)
Average real time	15 h 27 min	2 h 28 min	2 h 6 min	1 h 30 min

estimate for a given computer architecture whether the embedding of machine learning is more time efficient than the full calculation.

Finally, another advantage of the machine-learning-based state-resolved Monte Carlo implementation should be stressed. In the production phase it is not necessary to perform electronic-structure calculations [71], which are the fundamental basis for the calculation of individual state-to-state cross sections and transition rates. To reduce the computational time, electronic-structure information is stored in memory. However, storing electronic-structure information for argon uses more than 100 times more memory than for storing just atomic transition parameters. In particular, the amount of memory used for storing the relevant information, i.e., electronic-structure information and atomic transition parameters, during 5000 Monte Carlo trajectories is on the order of 10^4 megabytes. As a consequence, with the machine-learning-based state-resolved Monte Carlo implementation the memory usage can be dramatically reduced. In particular, the amount of memory used for storing the relevant information, i.e., only atomic transition parameters, in the production phase is on the order of 10^2 megabytes.

IV. CONCLUSION

In this paper, we have presented a machine-learning-based state-resolved Monte Carlo implementation for computing x-ray multiphoton ionization dynamics using the XATOM toolkit. The objective of machine learning is here to accelerate the extremely time-consuming state-resolved calculations of atomic transition parameters. In particular, in an initial training and test phase of the Monte Carlo calculation, quantum-state-resolved first-principles calculations of atomic transition parameters are carried out and these data serve for training and testing of the machine-learning models. The trained and tested machine-learning models are then employed in a final production phase for predicting atomic transition parameters for transitions newly visited in this phase.

We have compared the performance of neural networks and random forest regressors as possible machine-learning models. Both types of machine-learning models exhibit a similar accuracy for the prediction of atomic transition parameters, although neural networks have the critical disadvantage of very expensive training. Subsequently, we have discussed state-resolved CSDs as well as electron and photon spectra for argon, which have not been presented before. We compare results obtained by the machine-learning-based state-resolved Monte Carlo implementation embedding the neural networks to fully calculated results obtained with the implementation in Ref. [44]. Our work demonstrates that the proposed machine-learning-based state-resolved Monte Carlo implementation works in principle and that the performance, in terms of CSDs and spectra, is good. The achieved level of accuracy in CSDs and spectra is satisfactory in view of the fact that, for instance, higher-order many-body processes are neglected [44] and that calculated cross sections and rates are not perfect either [71]. Once the machine-learning models are trained, the final production phase can be performed faster than the full calculation. However, two main shortcomings have become evident: (i) the accuracy of the machine-learning predictions is limited, especially for less likely transitions, and (ii) training the neural networks is also quite time consuming.

In summary, let us briefly answer the question whether state-resolved ionization dynamics calculations can be accelerated by the presented machine-learning-based state-resolved Monte Carlo implementation. When a computer cluster is available, running several fully calculated Monte Carlo calculations—each with only a small number of trajectories—in parallel on several cluster nodes is indeed the more powerful method. This is attributed to large training times of the machine-learning models, limited prediction accuracy, and the need for fully calculated training and test Monte Carlo trajectories anyhow in the machine-learning-based calculations. But, if the computational resources are restricted, i.e., only a single or few computers and/or rather limited memory are available, then the machine-learning-based state-resolved Monte Carlo implementation is a promising option. After an expensive training and test phase, state-resolved ionization dynamics calculations can be performed more easily for a sufficiently large number of Monte Carlo trajectories. Another optional application of the machine-learning-based state-resolved Monte Carlo implementation would be its use in an x-ray parameter scan, i.e., performing a lot of x-ray multiphoton ionization dynamics calculations with different fluence and/or pulse duration values. In this case, the advantage is that machine-learning models need to be trained only a single time and can then be reused in all other calculations. Note that for a scan of the photon energy, this would not be possible because cross sections are photon-energy specific.

There are several promising perspectives for future developments of the machine-learning-based state-resolved Monte Carlo implementation. First, an important point is further feature engineering by adding more features and then sending the resulting feature vectors through, for instance, autoencoders [97] or using principal component analyses [80]. A better suited feature representation might help the machine-learning models to learn and, thus, can improve the performance. Other interesting directions for improving the machine-learning models would be ensemble methods, like gradient boosted trees [98], batch normalization [80], advanced random forest methods [95], inclusion of feedback, like in recurrent neural networks [80], or combining the power of neural networks and random forest regressors [94,99]. Training times for neural networks are often reduced by using GPUs instead of CPUs [80]. A further point is that for a new Monte Carlo calculation using a different atomic species and/or a different photon energy in principle the machine-learning models have to be reoptimized on the newly collected atomic transition parameters. A question here is whether information

gained from previous Monte Carlo calculations can be transferred to a new Monte Carlo calculation and whether this can accelerate training and/or improve the machine-learning models' performance. Lastly, another interesting aspect is that the main computational effort of the state-resolved Monte Carlo calculations is due to the extremely huge number of atomic transition parameters that need to be calculated or predicted. But are atomic transition parameters for all transitions really required? Or could a machine-learning model maybe select the most dominant transitions for a visited initial state, so that predictions (or calculations) could be restricted to this subset of dominant transitions (in spirit of proposals made in Refs. [69,70,100] for configuration-interaction calculations)? Such developments are crucial before many practical applications can really profit from the presented machine-learning-based state-resolved Monte Carlo implementation.

An attractive application of great scientific interest is the extension of the machine-learning-based state-resolved Monte Carlo implementation to atoms as heavy as xenon. Especially for heavy atoms, relativistic, quantum-electrodynamic, and finite-nuclear-size effects play an important role [34]. It is, therefore, desirable to embed them into the quantum-state-resolved electronic-structure calculations [44,71], although this further expands substantially the number of atomic transition parameters required and the computational effort. Consequently, accelerating huge-sized ionization dynamics calculations will be a promising perspective for the realization of more accurate calculations. It is also an important step toward the quantitative exploration of a wide variety of different atomic systems and toward the optimization of x-ray beam parameters for applications of x-ray free-electron lasers.

ACKNOWLEDGMENTS

L.B., M.T.-F., and R.S. acknowledge support by DASHH (Data Science in Hamburg - HELMHOLTZ Graduate School for the Structure of Matter) with Grant No. HIDSS-0002. L.B., S.-K.S., Z.J., M.M.A., and R.S. acknowledge support from DESY (Hamburg, Germany), a member of the Helmholtz Association HGF.

[1] P. Emma, R. Akre, J. Arthur, R. Bionta, C. Bostedt, J. Bozek, A. Brachmann, P. Bucksbaum, R. Coffee, F.-J. Decker *et al.*, First lasing and operation of an ångstrom-wavelength free-electron laser, Nat. Photon. **4**, 641 (2010).

[2] T. Ishikawa, H. Aoyagi, T. Asaka, Y. Asano, N. Azumi, T. Bizen, H. Ego, K. Fukami, T. Fukui, Y. Furukawa *et al.*, A compact x-ray free-electron laser emitting in the sub-ångström region, Nat. Photon. **6**, 540 (2012).

[3] H.-S. Kang, C.-K. Min, H. Heo, C. Kim, H. Yang, G. Kim, I. Nam, S. Y. Baek, H.-J. Choi, G. Mun *et al.*, Hard x-ray free-electron laser with femtosecond-scale timing jitter, Nat. Photon. **11**, 708 (2017).

[4] E. Prat, R. Abela, M. Aiba *et al.*, A compact and cost-effective hard x-ray free-electron laser driven by a high-brightness and low-energy electron beam, Nat. Photon. **14**, 748 (2020).

[5] C. Pellegrini, A. Marinelli, and S. Reiche, The physics of x-ray free-electron lasers, Rev. Mod. Phys. **88**, 015006 (2016).

[6] W. Decking, S. Abeghyan, P. Abramian, A. Abramsky, A. Aguirre, C. Albrecht, P. Alou, M. Altarelli, P. Altmann, K. Amyan *et al.*, A MHz-repetition-rate hard x-ray free-electron laser driven by a superconducting linear accelerator, Nat. Photon. **14**, 391 (2020).

[7] J. C. H. Spence, XFELs for structure and dynamics in biology, IUCrJ **4**, 322 (2017).

[8] I. Schlichting and J. Miao, Emerging opportunities in structural biology with x-ray free-electron lasers, Curr. Opin. Struct. Biol. **22**, 613 (2012).

[9] E. Sobolev, S. Zolotarev, K. Giewekemeyer, J. Bielecki, K. Okamoto, H. Reddy, J. Andreasson, K. Ayyer, I. Barák, S. Bari *et al.*, Megahertz single-particle imaging at the European XFEL, Commun. Phys. **3**, 97 (2020).

[10] M. M. Seibert, T. Ekeberg, F. R. N. C. Maia, M. Svenda, J. Andreasson, O. Jönsson, D. Odić, B. Iwan, A. Rocker, D. Westphal *et al.*, Single mimivirus particles intercepted and imaged with an x-ray laser, Nature (London) **470**, 78 (2011).

[11] H. N. Chapman, P. Fromme, A. Barty, T. A. White, R. A. Kirian, A. Aquila, M. S. Hunter, J. Schulz, D. P. DePonte, U. Weierstall *et al.*, Femtosecond x-ray protein nanocrystallography, Nature (London) **470**, 73 (2011).

[12] J. Coe and P. Fromme, Serial femtosecond crystallography opens new avenues for structural biology, Protein Pept. Lett. **23**, 255 (2016).

[13] D. Assalauova, Y. Y. Kim, S. Bobkov, R. Khubbutdinov, M. Rose, R. Alvarez, J. Andreasson, E. Balaur, A. Contreras, H. DeMirci *et al.*, An advanced workflow for single-particle imaging with the limited data at an x-ray free-electron laser, IUCrJ **7**, 1102 (2020).

[14] U. Lorenz, N. M. Kabachnik, E. Weckert, and I. A. Vartanyants, Impact of ultrafast electronic damage in single-particle x-ray imaging experiments, Phys. Rev. E **86**, 051911 (2012).

[15] H. M. Quiney and K. A. Nugent, Biomolecular imaging and electronic damage using x-ray free-electron lasers, Nat. Phys. **7**, 142 (2011).

[16] S.-K. Son, L. Young, and R. Santra, Impact of hollow-atom formation on coherent x-ray scattering at high intensity, Phys. Rev. A **83**, 033402 (2011).

[17] K. Nass, Radiation damage in protein crystallography at x-ray free-electron lasers, Acta Crystallogr., Sect. D: Struct. Biol. **75**, 211 (2019).

[18] R. Neutze, R. Wouts, D. van der Spoel, E. Weckert, and J. Hajdu, Potential for biomolecular imaging with femtosecond x-ray pulses, Nature (London) **406**, 752 (2000).

[19] R. Santra and L. Young, in *Synchrotron Light Sources and Free-Electron Lasers*, edited by E. J. Jaeschke, S. Khan, J. R. Schneider, and J. B. Hastings (Springer International Publishing, Switzerland, 2016), pp. 1233–1260.

[20] L. Young, E. P. Kanter, B. Krässig, Y. Li, A. M. March, S. T. Pratt, R. Santra, S. H. Southworth, N. Rohringer, L. F. DiMauro *et al.*, Femtosecond electronic response of atoms to ultra-intense x-rays, Nature (London) **466**, 56 (2010).

[21] H. Fukuzawa, S.-K. Son, K. Motomura, S. Mondal, K. Nagaya, S. Wada, X.-J. Liu, R. Feifel, T. Tachibana, Y. Ito *et al.*, Deep inner-shell multiphoton ionization by intense x-ray free-electron laser pulses, Phys. Rev. Lett. **110**, 173005 (2013).

[22] B. Rudek, K. Toyota, L. Foucar, B. Erk, R. Boll, C. Bomme, J. Correa, S. Carron, S. Boutet, G. J. Williams *et al.*, Relativistic and resonant effects in the ionization of heavy atoms by ultra-intense hard x-rays, Nat. Commun. **9**, 4200 (2018).

[23] B. Rudek, S.-K. Son, L. Foucar, S. W. Epp, B. Erk, R. Hartmann, M. Adolph, R. Andritschke, A. Aquila, N. Berrah *et al.*, Ultra-efficient ionization of heavy atoms by intense x-ray free-electron laser pulses, Nat. Photon. **6**, 858 (2012).

[24] A. Rudenko, L. Inhester, K. Hanasaki, X. Li, S. J. Robatjazi, B. Erk, R. Boll, K. Toyota, Y. Hao, O. Vendrell *et al.*, Femtosecond response of polyatomic molecules to ultra-intense hard x-rays, Nature (London) **546**, 129 (2017).

[25] N. Rohringer and R. Santra, X-ray nonlinear optical processes using a self-amplified spontaneous emission free-electron laser, Phys. Rev. A **76**, 033416 (2007).

[26] M. G. Makris, P. Lambropoulos, and A. Mihelič, Theory of multiphoton multielectron ionization of xenon under strong 93-eV radiation, Phys. Rev. Lett. **102**, 033002 (2009).

[27] G. Doumy, C. Roedig, S.-K. Son, C. I. Blaga, A. D. DiChiara, R. Santra, N. Berrah, C. Bostedt, J. D. Bozek, P. H. Bucksbaum *et al.*, Nonlinear atomic response to intense ultrashort x rays, Phys. Rev. Lett. **106**, 083002 (2011).

[28] W. Xiang, C. Gao, Y. Fu, J. Zeng, and J. Yuan, Inner-shell resonant absorption effects on evolution dynamics of the charge state distribution in a neon atom interacting with ultraintense x-ray pulses, Phys. Rev. A **86**, 061401(R) (2012).

[29] B. Rudek, D. Rolles, S.-K. Son, L. Foucar, B. Erk, S. Epp, R. Boll, D. Anielski, C. Bostedt, S. Schorb *et al.*, Resonance-enhanced multiple ionization of krypton at an x-ray free-electron laser, Phys. Rev. A **87**, 023413 (2013).

[30] K. Motomura, H. Fukuzawa, S.-K. Son, S. Mondal, T. Tachibana, Y. Ito, M. Kimura, K. Nagaya, T. Sakai, K. Matsunami *et al.*, Sequential multiphoton multiple ionization of atomic argon and xenon irradiated by x-ray free-electron laser pulses from SACLA, J. Phys. B: At., Mol. Opt. Phys. **46**, 164024 (2013).

[31] N. Berrah, A. Sanchez-Gonzalez, Z. Jurek, R. Obaid, H. Xiong, R. J. Squibb, T. Osipov, A. Lutman, L. Fang, T. Barillot *et al.*, Femtosecond-resolved observation of the fragmentation of buckminsterfullerene following x-ray multiphoton ionization, Nat. Phys. **15**, 1279 (2019).

[32] B. F. Murphy, T. Osipov, Z. Jurek, L. Fang, S.-K. Son, M. Mucke, J. H. D. Eland, V. Zhaunerchyk, R. Feifel, L. Avaldi *et al.*, Femtosecond x-ray-induced explosion of C_{60} at extreme intensity, Nat. Commun. **5**, 4281 (2014).

[33] M. Hoener, L. Fang, O. Kornilov, O. Gessner, S. T. Pratt, M. Gühr, E. P. Kanter, C. Blaga, C. Bostedt, J. D. Bozek *et al.*, Ultraintense x-ray induced ionization, dissociation, and frustrated absorption in molecular nitrogen, Phys. Rev. Lett. **104**, 253002 (2010).

[34] K. Toyota, S.-K. Son, and R. Santra, Interplay between relativistic energy corrections and resonant excitations in x-ray multiphoton ionization dynamics of Xe atoms, Phys. Rev. A **95**, 043412 (2017).

[35] S.-K. Son, R. Boll, and R. Santra, Breakdown of frustrated absorption in x-ray sequential multiphoton ionization, Phys. Rev. Res. **2**, 023053 (2020).

[36] P. J. Ho, E. P. Kanter, and L. Young, Resonance-mediated atomic ionization dynamics induced by ultraintense x-ray pulses, Phys. Rev. A **92**, 063430 (2015).

[37] P. J. Ho, C. Bostedt, S. Schorb, and L. Young, Theoretical tracking of resonance-enhanced multiple ionization pathways in x-ray free-electron laser pulses, Phys. Rev. Lett. **113**, 253001 (2014).

[38] S.-K. Son and R. Santra, Monte Carlo calculation of ion, electron, and photon spectra of xenon atoms in x-ray free-electron laser pulses, Phys. Rev. A **85**, 063415 (2012).

[39] J. M. Schäfer, L. Inhester, S.-K. Son, R. F. Fink, and R. Santra, Electron and fluorescence spectra of a water molecule irradiated by an x-ray free-electron laser pulse, Phys. Rev. A **97**, 053415 (2018).

[40] C. Buth, R. Beerwerth, R. Obaid, N. Berrah, L. S. Cederbaum, and S. Fritzsche, Neon in ultrashort and intense x-rays from free electron lasers, J. Phys. B: At., Mol. Opt. Phys. **51**, 055602 (2018).

[41] O. Ciricosta, H.-K. Chung, R. W. Lee, and J. S. Wark, Simulations of neon irradiated by intense x-ray laser radiation, High Energy Density Phys. **7**, 111 (2011).

[42] C. Buth, J.-C. Liu, M. H. Chen, J. P. Cryan, L. Fang, J. M. Glownia, M. Hoener, R. N. Coffee, and N. Berrah, Ultrafast absorption of intense x rays by nitrogen molecules, J. Chem. Phys. **136**, 214310 (2012).

[43] J.-C. Liu, N. Berrah, L. S. Cederbaum, J. P. Cryan, J. M. Glownia, K. J. Schafer, and C. Buth, Rate equations for nitrogen molecules in ultrashort and intense x-ray pulses, J. Phys. B: At., Mol. Opt. Phys. **49**, 075602 (2016).

[44] L. Budewig, S.-K. Son, and R. Santra, State-resolved ionization dynamics of a neon atom induced by x-ray free-electron-laser pulses, Phys. Rev. A **107**, 013102 (2023).

[45] G. Carleo, I. Cirac, K. Cranmer, L. Daudet, M. Schuld, N. Tishby, L. Vogt-Maranto, and L. Zdeborová, Machine learning and the physical sciences, Rev. Mod. Phys. **91**, 045002 (2019).

[46] A. Karthikeyan and U. D. Priyakumar, Artificial intelligence: Machine learning for chemical sciences, J. Chem. Sci. **134**, 2 (2022).

[47] O. A. von Lilienfeld and K. Burke, Retrospective on a decade of machine learning for chemical discovery, Nat. Commun. **11**, 4895 (2020).

[48] J. Jumper, R. Evans, A. Pritzel, T. Green, M. Figurnov, O. Ronneberger, K. Tunyasuvunakool, R. Bates, A. Žídek, A. Potapenko *et al.*, Highly accurate protein structure prediction with alphafold, Nature (London) **596**, 583 (2021).

[49] C. D. Rankine, M. M. M. Madkhali, and T. J. Penfold, A deep neural network for the rapid prediction of x-ray absorption spectra, J. Phys. Chem. A **124**, 4263 (2020).

[50] M. R. Carbone, M. Topsakal, D. Lu, and S. Yoo, Machine-learning x-ray absorption spectra to quantitative accuracy, Phys. Rev. Lett. **124**, 156401 (2020).

[51] D. Golze, M. Hirvensalo, P. Hernández-León, A. Aarva, J. Etula, T. Susi, P. Rinke, T. Laurila, and M. A. Caro, Accurate

computational prediction of core-electron binding energies in carbon-based materials: A machine-learning model combining density-functional theory and *GW*, Chem. Mater. **34**, 6240 (2022).

[52] K. Ghosh, A. Stuke, M. Todorović, P. B. Jørgensen, M. N. Schmidt, A. Vehtari, and P. Rinke, Deep learning spectroscopy: Neural networks for molecular excitation spectra, Adv. Sci. (Weinheim, Ger.) **6**, 1801367 (2019).

[53] J. Carrasquilla and R. G. Melko, Machine learning phases of matter, Nat. Phys. **13**, 431 (2017).

[54] A. Sanchez-Gonzalez, P. Micaelli, C. Olivier, T. R. Barillot, M. Ilchen, A. A. Lutman, A. Marinelli, T. Maxwell, A. Achner, M. Agåker *et al.*, Accurate prediction of x-ray pulse properties from a free-electron laser using machine learning, Nat. Commun. **8**, 15461 (2017).

[55] O. Geffert, D. Kolbasova, A. Trabattoni, F. Calegari, and R. Santra, In situ characterization of few-femtosecond laser pulses by learning from first-principles calculations, Opt. Lett. **47**, 3992 (2022).

[56] D. Kolbasova and R. Santra, Laser-pulse characterization using strong-field autocorrelation patterns and random-forest-based machine learning, Phys. Rev. A **107**, 013520 (2023).

[57] N. Breckwoldt, S.-K. Son, T. Mazza, A. Rörig, R. Boll, M. Meyer, A. C. LaForge, D. Mishra, N. Berrah, and R. Santra, Machine-learning calibration of intense x-ray free-electron-laser pulses using Bayesian optimization, Phys. Rev. Res. **5**, 023114 (2023).

[58] G. Montavon, M. Rupp, V. Gobre, A. Vazquez-Mayagoitia, K. Hansen, A. Tkatchenko, K.-R. Müller, and O. A. von Lilienfeld, Machine learning of molecular electronic properties in chemical compound space, New J. Phys. **15**, 095003 (2013).

[59] J. Westermayr, M. Gastegger, K. T. Schütt, and R. J. Maurer, Perspective on integrating machine learning into computational chemistry and materials science, J. Chem. Phys. **154**, 230903 (2021).

[60] O. A. von Lilienfeld, K.-R. Müller, and A. Tkatchenko, Exploring chemical compound space with quantum-based machine learning, Nat. Rev. Chem. **4**, 347 (2020).

[61] L. Fiedler, N. A. Modine, S. Schmerler, D. J. Vogel, G. A. Popoola, A. P. Thompson, S. Rajamanickam, and A. Cangi, Predicting electronic structures at any length scale with machine learning, npj Comput. Mater. **9**, 115 (2023).

[62] L. Fiedler, K. Shah, M. Bussmann, and A. Cangi, Deep dive into machine learning density functional theory for materials science and chemistry, Phys. Rev. Mater. **6**, 040301 (2022).

[63] A. Stuke, M. Todorović, M. Rupp, C. Kunkel, K. Ghosh, L. Himanen, and P. Rinke, Chemical diversity in molecular orbital energy predictions with kernel ridge regression, J. Chem. Phys. **150**, 204121 (2019).

[64] T. B. Blank, S. D. Brown, A. W. Calhoun, and D. J. Doren, Neural network models of potential energy surfaces, J. Chem. Phys. **103**, 4129 (1995).

[65] J. Behler and M. Parrinello, Generalized neural-network representation of high-dimensional potential-energy surfaces, Phys. Rev. Lett. **98**, 146401 (2007).

[66] O. T. Unke, D. Koner, S. Patra, S. Käser, and M. Meuwly, High-dimensional potential energy surfaces for molecular simulations: From empiricism to machine learning, Mach. Learn.: Sci. Technol. **1**, 013001 (2020).

[67] G. Schmitz, I. H. Godtliebsen, and O. Christiansen, Machine learning for potential energy surfaces: An extensive database and assessment of methods, J. Chem. Phys. **150**, 244113 (2019).

[68] A. M. Tokita and J. Behler, How to train a neural network potential, J. Chem. Phys. **159**, 121501 (2023).

[69] J. P. Coe, Machine learning configuration interaction, J. Chem. Theory Comput. **14**, 5739 (2018).

[70] P. Bilous, A. Pálffy, and F. Marquardt, Deep-learning approach for the atomic configuration interaction problem on large basis sets, Phys. Rev. Lett. **131**, 133002 (2023).

[71] L. Budewig, S.-K. Son, and R. Santra, Theoretical investigation of orbital alignment of x-ray-ionized atoms in exotic electronic configurations, Phys. Rev. A **105**, 033111 (2022).

[72] Z. Jurek, S.-K. Son, B. Ziaja, and R. Santra, XMDYN and XATOM: Versatile simulation tools for quantitative modeling of x-ray free-electron laser induced dynamics of matter, J. Appl. Crystallogr. **49**, 1048 (2016).

[73] S.-K. Son, K. Toyota, O. Geffert, J. M. Slowik, and R. Santra, *XATOM-An Integrated Toolkit for X-Ray and Atomic Physics* (CFEL, DESY, Hamburg, 2016), Rev. 3544.

[74] R. D. Deslattes, E. G. Kessler, P. Indelicato, L. de Billy, E. Lindroth, and J. Anton, X-ray transition energies: New approach to a comprehensive evaluation, Rev. Mod. Phys. **75**, 35 (2003).

[75] M. C. Martins, A. M. Costa, J. P. Santos, F. Parente, and P. Indelicato, Relativistic calculation of two-electron one-photon and hypersatellite transition energies, J. Phys. B: At., Mol. Opt. Phys. **37**, 3785 (2004).

[76] E. Mikkola and J. Ahopelto, $K\alpha^h$ hypersatellite spectrum and K shell double photoionization cross-section for Ar, Phys. Scr. **27**, 297 (1983).

[77] C. Briançon and J. P. Desclaux, Relativistic Dirac-Fock calculations of KLL Auger transition energies in intermediate coupling, Phys. Rev. A **13**, 2157 (1976).

[78] M. O. Krause, Argon KLL auger spectrum: A test of theory, Phys. Rev. Lett. **34**, 633 (1975).

[79] R. Püttner, Y. Li, J. Zeng, D. Koulentianos, T. Marchenko, R. Guillemin, L. Journel, O. Travnikova, M. Zmerli, D. Céolin *et al.*, Argon $1s^{-2}$ Auger hypersatellites, J. Phys. B: At., Mol. Opt. Phys. **54**, 024001 (2020).

[80] I. Goodfellow, Y. Bengio, and A. Courville, *Deep Learning* (MIT Press, Cambridge, England, 2016).

[81] Y. LeCun, L. Bottou, G. Orr, and K. Muller, Efficient backprop, in *Neural Networks: Tricks of the Trade*, edited by G. Orr and G. B. Müller (Springer, Berlin, Heidelberg, 1998).

[82] C. M. Bishop, *Neural Networks for Pattern Recognition* (Oxford University Press, New York, 1995).

[83] L. Long and X. Zeng, *Beginning Deep Learning with TensorFlow* (Apress, Berkeley, 2022).

[84] D. E. Rumelhart, G. E. Hinton, and R. J. Williams, Learning representations by back-propagating errors, Nature (London) **323**, 533 (1986).

[85] S. Liang and R. Srikant, Why deep neural networks for function approximation? in *5th International Conference on Learning Representations ICLR*, edited by Y. Bengio and Y. LeCun (OpenReview.net, Toulon, 2017).

[86] F. Chollet *et al.*, *Keras*, https://keras.io (2015).

[87] M. Abadi, P. Barham, J. Chen, Z. Chen, A. Davis, J. Dean, M. Devin, S. Ghemawat, G. Irving, M. Isard *et al.*, Tensorflow: A system for large-scale machine learning, in *Proceedings of the 12th USENIX Conference on Operating Systems Design and Implementation* (USENIX Association, USA, 2016), pp. 265–283.

[88] M. Belkin, D. Hsu, S. Ma, and S. Mandal, Reconciling modern machine-learning practice and the classical bias–variance trade-off, Proc. Natl. Acad. Sci. USA **116**, 15849 (2019).

[89] S. Sharma, S. Sharma, and A. Athaiya, Activation functions in neural networks, Int. J. Eng. Appl. Sci. Technol. **4**, 310 (2020).

[90] X. Glorot and Y. Bengio, Understanding the difficulty of training deep feedforward neural networks, in *Proceedings of the Thirteenth International Conference on Artificial Intelligence and Statistics*, edited by Y. W. Teh and M. Titterington (PMLR, Italy, 2010), pp. 249–256.

[91] N. Srivastava, G. Hinton, A. Krizhevsky, I. Sutskever, and R. Salakhutdinov, Dropout: A simple way to prevent neural networks from overfitting, J. Mach. Learn. Res. **15**, 1929 (2014).

[92] D. P. Kingma and J. Ba, Adam: A method for stochastic optimization, in *Proceedings of the 3rd International Conference on Learning Representations*, edited by Y. Bengio and Y. LeCun (ICLR, San Diego, USA, 2015).

[93] L. Breiman, Random forests, Mach. Learn. **45**, 5 (2001).

[94] P. Roßbach, *Neural Networks vs. Random Forests—Does it always have to be Deep Learning?* (Frankfurt School of Finance and Management, Germany, 2018).

[95] Z.-H. Zhou and J. Feng, Deep forest: Towards an alternative to deep neural networks, in *Proceedings of the Twenty-Sixth International Joint Conference on Artificial Intelligence*, edited by C. Sierra (IJCAI, Melbourne, 2017).

[96] F. Pedregosa, G. Varoquaux, A. Gramfort, V. Michel, B. Thirion, O. Grisel, M. Blondel, P. Prettenhofer, R. Weiss, V. Dubourg *et al.*, Scikit-learn: Machine learning in python, J. Mach. Learn. Res. **12**, 2825 (2011).

[97] A. A. Patel, *Hands-On Unsupervised Learning Using Python* (O'Reilly Media, Inc., Sebastopol, 2019).

[98] J. H. Friedman, Greedy function approximation: A gradient boosting machine, Ann. Stat. **29**, 1189 (2001).

[99] G. Biau, E. Scornet, and J. Welbl, Neural random forests, Sankhya A **81**, 347 (2019).

[100] C. Qu, P. L. Houston, Q. Yu, R. Conte, P. Pandey, A. Nandi, and J. M. Bowman, Machine learning classification can significantly reduce the cost of calculating the Hamiltonian matrix in CI calculations, J. Chem. Phys. **159**, 071101 (2023).

3.4 Electron-cloud alignment dynamics induced by an intense X-ray free-electron laser pulse

The fourth publication presents an application of the state-resolved Monte Carlo implementation (Sec. 3.2) for a complete description of X-ray multiphoton ionization dynamics. This offers insight into the alignment of the electron cloud of atoms, being initially perfectly spherically symmetric, through intense X-ray pulses generated by X-ray free-electron lasers.

The underlying project was performed by myself under the supervision of Dr. S.-K. Son and Professor Dr. R. Santra. In particular, I carried out the X-ray multiphoton ionization dynamics calculations with the state-resolved Monte Carlo implementation (Sec. 3.2). I also analyzed the results regarding orbital- and spin-angular momentum and, most importantly, electron-cloud alignment and wrote the manuscript with inputs from all authors.

communications physics

Article

https://doi.org/10.1038/s42005-024-01852-x

Electron-cloud alignment dynamics induced by an intense X-ray free-electron laser pulse: a case study on atomic argon

Check for updates

Laura Budewig[1,2], Sang-Kil Son[1] & Robin Santra[1,2]

In an intense X-ray free-electron laser (XFEL) pulse, atoms are sequentially ionised by multiple X-ray photons. Photoionisation generally induces an alignment of the electron cloud of the produced atomic ion regarding its orbital-angular-momentum projections. However, how the alignment evolves during sequential X-ray multi-photon ionisation accompanied by decay processes has been unexplored. Here we present a theoretical prediction of the time evolution of the electron-cloud alignment of argon ions induced by XFEL pulses. To this end, we calculate state-resolved ionisation dynamics of atomic argon interacting with an intense linearly polarised X-ray pulse, which generates ions in a wide range of charge states with non-zero orbital- and spin-angular momenta. Employing time-resolved alignment parameters, we predict the existence of non-trivial alignment dynamics during intense XFEL pulses. This implies that even if initially the atomic electron cloud is perfectly spherically symmetric, X-ray multi-photon ionisation can lead to noticeable reshaping of the electron cloud.

Sequential multi-photon processes have attracted attention with the recent advent of X-ray free-electron lasers (XFELs)[1–5]. XFELs provide ultraintense and ultrashort X-ray pulses[6] with high degrees of typically linear polarisation[7,8]. Exposed to such an intense X-ray pulse, an atom absorbs more than one photon predominantly via sequences of one-photon ionisation events[9,10] accompanied by Auger-Meitner decay or X-ray fluorescence[11,12]. As a consequence of these so-called X-ray multi-photon ionisation dynamics[9], high atomic charge states are formed within a single X-ray pulse[10–15]. Because this unavoidably damages the electronic structure of the irradiated sample[16–20], applications of XFELs such as biomolecular imaging[21–29] are affected. Therefore, understanding X-ray multi-photon ionisation dynamics is critical. For atoms, they have been widely explored theoretically and/or experimentally based on ion[10–15,30–36], electron[12,35–37], and photon[12,14,33,36] spectra. Complementary information can be obtained by studying the electron cloud alignment of atomic ions, but this requires computationally expensive quantum state-resolved descriptions of atomic ions and X-ray-induced transitions[36,38,39].

An alignment of the electron cloud of atomic ions (hereinafter: ion alignment) with nonzero orbital-angular momentum is induced by photoionisation with different ionisation probabilities for different orbital-angular-momentum projection states[40–46]. As a consequence of this ion alignment, subsequently emitted Auger-Meitner electrons and fluorescence photons are anisotropically distributed[46–51] and fluorescence photons are also polarised[47,52,53]. Angular distributions of photoelectrons emitted from the aligned ions are likewise affected[54] supplementary to their fundamental anisotropy[55–57]. On the one hand, all these make ion alignment experimentally accessible[42–44,51,53]. On the other hand, angle-resolved spectroscopy experiments[58–61] may profit from its theoretical study. However, how ion alignment is affected by X-ray multi-photon ionisation dynamics driven by an intense X-ray pulse is so far unknown.

Comparably strong alignments have been encountered in strong-field ionised[62,63] and resonantly-excited[64] atoms. Further, sequential double and triple ionisations driven by extreme ultraviolet (XUV) pulses have been investigated via photoelectron angular distributions[54,60,61,65,66]. Recently, alignment in XUV-ionised[39] and X-ray-ionised[38] atoms up to Kr^{3+}[39] and Ar^{3+}[38], respectively, has been theoretically explored with a focus on a single ionisation step. In all these studies, multiple competing sequences of photoionisation and accompanying decay processes were not systematically involved, either because they are absent or to simplify computations. But, they matter for the interaction with intense X-ray pulses.

Extending a former study[38], we here investigate the time evolution of ion alignment during an intense linearly polarised X-ray pulse. To this end, we performed state-resolved X-ray multi-photon ionisation dynamics calculations[36,38] for atomic argon (Ar), which simulate the time evolution of individual quantum-state populations. An individual quantum state is defined by an electronic configuration together with quantum numbers (L, S, M_L, κ). Here, L is the total orbital-angular momentum with projection M_L, S is the total spin-angular momentum (whose projection is irrelevant),

[1]Center for Free-Electron Laser Science CFEL, Deutsches Elektronen-Synchrotron DESY, Notkestr. 85, 22607 Hamburg, Germany. [2]Department of Physics, University of Hamburg, Notkestr. 9-11, 22607 Hamburg, Germany. e-mail: robin.santra@cfel.de

and κ guarantees uniqueness. Individual quantum states differing only in M_L form an energy level, defined by an electronic configuration together with a term $^{2S+1}L(\kappa)$. Enabled by these calculations, not only time-resolved charge-state distributions and electron and photon spectra but also ion orbital- and spin-angular momentum and alignment are explored. We demonstrate that ion alignment (averaged over all individual quantum states populated at a given time) shows a highly non-linear behaviour and is suppressed by X-ray multi-photon ionisation dynamics. However, we find that the degree of alignment reached is not negligible for the individual atomic charge states populated.

Results

State-resolved X-ray multi-photon ionisation dynamics for Ar are calculated for an X-ray pulse having a temporal Gaussian pulse envelope of 10 fs FWHM (full width at half maximum) and a fluence (not volume-integrated) of 10^{12} photons per μm^2 (unless noted otherwise). These are typical XFEL pulse parameters[1,2,4], in particular for atomic, molecular, and optical physics instrumentations[67–70]. Such a high fluence has been realised not only in a series of gas-phase XFEL experiments on atoms, molecules, and clusters[10,13,31,37,71,72], but also in many serial crystallography experiments[27–29]. Even higher fluences are required for single-particle imaging at XFELs[16,19,20,29]. We consider X-rays being linearly polarised along the z axis (quantisation axis) and intentionally chose Ar at a photon energy of 1.5 keV to increase the possibility of ion alignment induced by non-trivial ionisation dynamics. At this photon energy, there is no K-shell ($1s$) ionisation, which cannot create ion alignment without electron correlation effects[39]. Instead, L-shell ($2s$ and $2p$) photoionisation in Ar initiates non-trivial X-ray multi-photon multiple ionisation, including M-shell ($3s$ and $3p$) electrons. The target system can be any atomic species, including open-shell systems, when the above conditions are fulfilled. We chose neutral Ar atoms because corresponding gas-phase samples are straightforward to produce for experiments, and it is beneficial to have zero alignment at the beginning.

Ion, electron, and photon spectra

In order to examine the X-ray multi-photon ionisation dynamics of Ar driven by an intense linearly polarised X-ray pulse, we present in Fig. 1 calculated electron and photon spectra and charge-state distribution.

During the intense X-ray pulse, several photons per atom are absorbed sequentially. Consequently, a wealth of spectral lines characterises the time-resolved photoelectron spectrum in Fig. 1a. Here, the vertical and horizontal axes are the time and energy, using 0.4-fs and 1-eV bins, respectively. The photoelectron spectrum is grouped into large L-shell and minor M-shell spectra. Each subspectrum is dominated by lines for the ionisation of neutral Ar, occurring early in time. These lines are followed in time by a flat quasi-

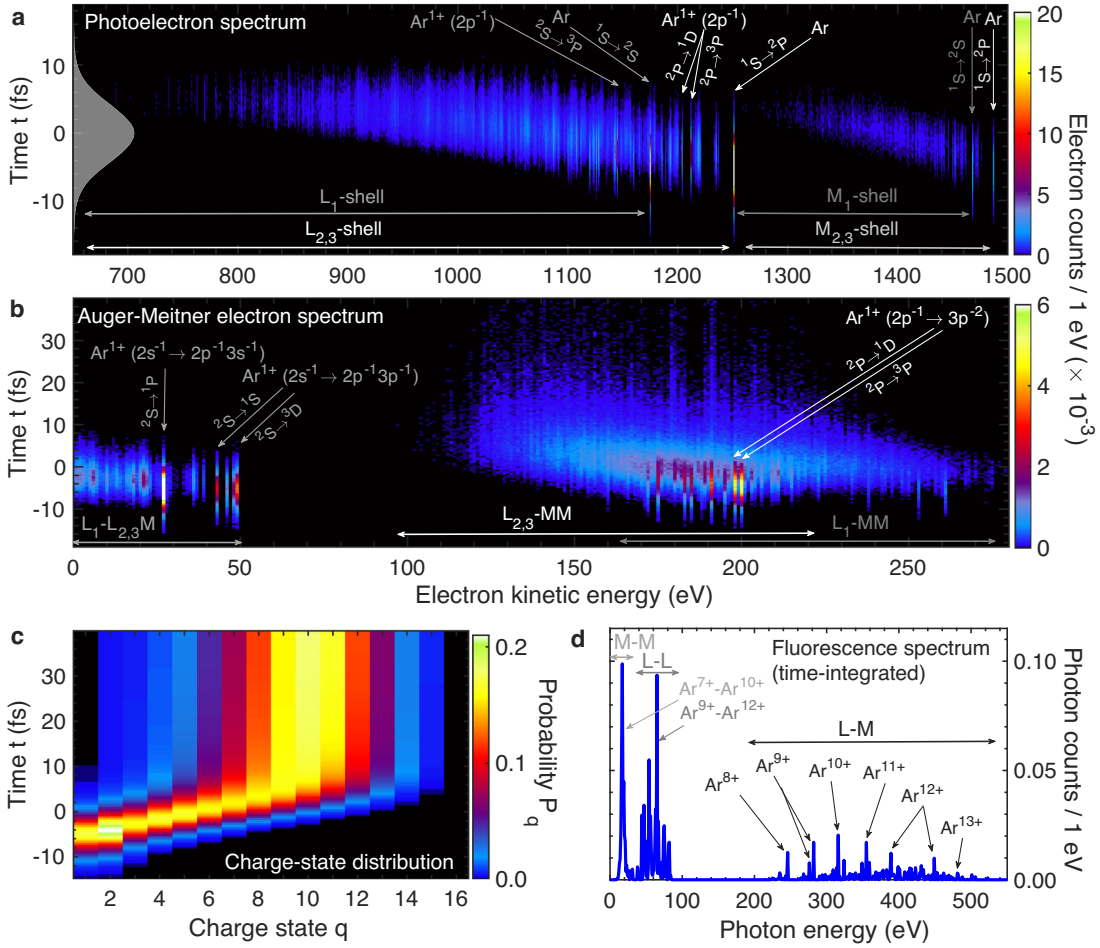

Fig. 1 | Overview of X-ray multi-photon ionisation dynamics of Ar at a photon energy of 1.5 keV, a fixed fluence of 10^{12} photons per μm^2, and a pulse duration of 10 fs FWHM. a Time-resolved photoelectron spectrum. The temporal shape of the X-ray pulse is depicted with a grey-shaded area. **b** Time-resolved Auger-Meitner electron spectrum. **c** Time evolution of the charge-state distribution. **d** Time-integrated fluorescence spectrum. In panels **a**, **b**, and **d**, double arrows indicate the subspectra, defined by the involved subshells, i.e., L_1 ($2s$), $L_{2,3}$ ($2p$), M_1 ($3s$), and/or $M_{2,3}$ ($3p$). In **b** and **d**, the first subshell index refers to the initial vacancy, whereas the latter refer to the subshells from which the electrons are removed. Single arrows indicate ions involved in the transition via initial charge state, involved electronic configuration(s) (holes indicated), and/or terms (^{2S+1}L). For all panels, the statistical errors obtained via bootstrap estimate are too small to be shown.

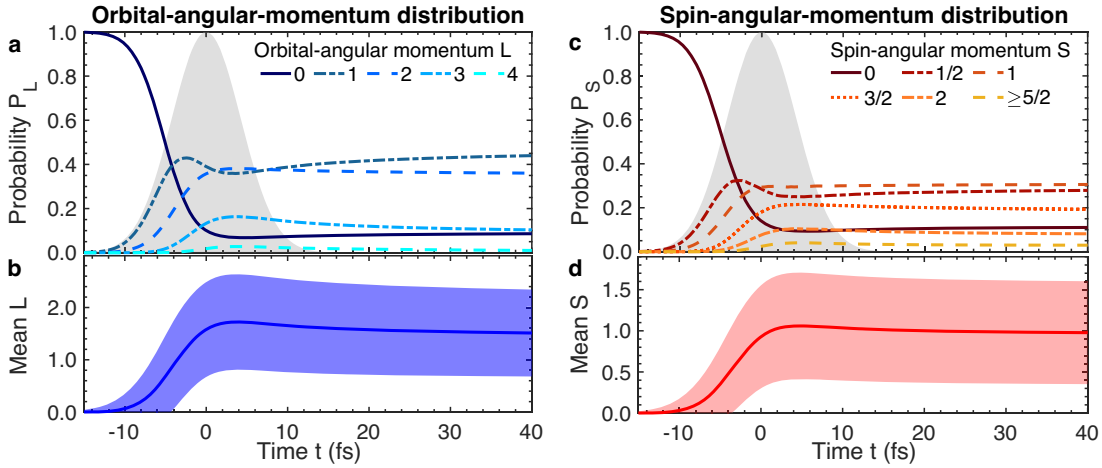

Fig. 2 | Time evolution of ion orbital-angular momentum *L* and spin-angular momentum *S* of Ar induced by an intense XFEL pulse with a fixed fluence of 10^{12} photons per μm². **a** Probability P_L of individual *L*. **b** Mean of the orbital-angular-momentum distribution together with its width (area around mean). **c**, **d** The spin-angular-momentum distribution is presented likewise (with $S = 5/2, \ldots, 4$ collected in one line). The temporal pulse shape is depicted by the grey-shaded areas in **a** and **c**. For all panels, the statistical errors obtained via bootstrap estimate are too small to be shown.

continuum, moving toward lower energy and weaker lines with time. The quasi-continua are generated by photoionisation of ions produced by preceding ionisation and/or decay processes. These intermediate ions, generally, exhibit a manifold of relatively weak state-to-state transitions between different energy levels.

L-shell ionisation is mostly immediately accompanied by Auger-Meitner decay as demonstrated by the time-resolved Auger-Meitner electron spectrum in Fig. 1b. Similar to the photoelectron spectrum, the Auger-Meitner electron spectrum exhibits two energetically-separated quasi-continua, the *L–LM* and *L–MM* spectra. Here, an Auger-Meitner channel *L–MM* means that an initial *L*-shell vacancy is filled by an electron from the *M*-shell, accompanied by the ejection of another electron from the *M*-shell. In the *L–LM* channel the initial *L*-shell vacancy decays such that in the final state, one electron has been removed from a higher-lying *L*-shell orbital and the other electron has been removed from the *M*-shell. The *L–LM* and *L–MM* spectra are generated by a plethora of energy levels involved in the given channels. The *L–LM* spectrum dominates at early times up to around 5 fs, but is energetically forbidden later. In contrast to the *L–LM* spectrum, the *L–MM* spectrum extends to times beyond the X-ray pulse due to the long lifetimes of some intermediate ion states. Nonetheless, most Auger-Meitner decays (≈ 95%) take place within 40 fs after the peak of the X-ray pulse.

As a result of sequences of one-photon ionisation accompanied by Auger-Meitner decay, charged ions are formed as shown by the time-resolved charge-state distribution in Fig. 1c. Here, the sum of probabilities P_q of all charge states q ($q = 0, +1, \cdots, +16$) is unity at each time. As can be seen, charged ions are formed sequentially as time goes by, with most changes before and around the peak of the X-ray pulse. When the X-ray pulse is over, most ions (≈ 78% at 40 fs) have reached a charge of +8 to +12.

The highly-charged ions relax via fluorescence into stable states when the X-ray pulse is over and Auger-Meitner decay is suppressed by a lack of *M*-shell electrons. This is depicted in Fig. 1d by the time-integrated fluorescence spectrum, generated by Ar^{7+} to Ar^{13+}. Fluorescence is a very weak process, especially without *K*-shell holes. The associated lifetimes range from 674 fs (Ar^{15+} $1s^2 2s^0 2p^0 3s^0 3p^1$) to 8×10^5 fs (Ar^{15+} $1s^2 2s^0 2p^1 3s^0 3p^0$) (state-resolved fluorescence rate calculations[38]). Therefore, fluorescence predominantly occurs for highly-charged ions after the end of the X-ray multi-photon ionisation dynamics. Only about 1% of fluorescence decays take place within 40 fs after the peak of the X-ray pulse.

Orbital- and spin-angular-momentum distributions

The time-resolved orbital-angular-momentum distribution is of interest because alignment parameters consider ions with definite orbital-angular momentum *L*. In Fig. 2a, we plot the time-resolved probability P_L of ions with definite *L* ($L = 0, \ldots, 4$), which is given by all individual quantum states with quantum number *L* populated at a given time. Initially, neutral Ar is in an *S*-state ($L = 0$) and is included in $P_{L=0}$. Induced by the X-ray pulse, neutral Ar turns into ions in *P*-states ($L = 1$; up to ≈ 43%). In subsequent sequences of one-photon ionisation accompanied by Auger-Meitner decay, also *D*-states ($L = 2$; up to 38%), a few *F*-states ($L = 3$; < 16%), and little *G*-states ($L = 4$; < 3%) are formed at the expense of *S*- and *P*-states. *F*- and *G*-states are rare because unstable electronic configurations with several holes simultaneously in the 2*p*- and 3*p*-shells are required. As a consequence of their instability, they (stepwise) decay into stable *S*- and *P*-states. Note that these decays occur on time scales much longer than the time window in Fig. 2a. In the end (when all decay processes are completed) many *P*-states, some *S*- and *D*-states, but neither *F*- nor *G*-states are left over (Table 1). In Fig. 2b, the mean of the orbital-angular-momentum distribution $\bar{L} = \sum_L L P_L$ and its width $\Delta_L = \sqrt{\sum_L L^2 P_L - \bar{L}^2}$ are shown. The maximum mean and width are reached shortly after the peak of the X-ray pulse (at about 4 fs), which stresses that at this time the maximum number of ions with $L > 1$ is achieved.

Table 1 | Orbital- and spin-angular-momentum distributions when the pulse is over and all decay processes are completed

L	**0**	**1**	**2**	**3**	**4**	
$P_L(t \to \infty)$	0.23	0.60	0.17	0.00	0.00	
S	**0**	**1/2**	**1**	**3/2**	**2**	**≥5/2**
$P_S(t \to \infty)$	0.12	0.30	0.30	0.17	0.07	0.04

The corresponding time evolution is shown in Fig. 2.

The time-resolved spin-angular-momentum distribution, shown in Fig. 2c, d, scrutinises the spin *S* ($S = 0, 1/2, \ldots, 4$) instead of *L*. Similar to the orbital-angular-momentum distribution, the majority of ions is found in low non-zero spin states ($S = 1/2, 1, 3/2$) during and after the X-ray pulse. The maximum mean spin is also reached shortly after the peak of the X-ray pulse. The difference is that the spin-angular-momentum distribution barely evolves after the X-ray pulse is over (compare Fig. 2c and Table 1). This is because Auger-Meitner and fluorescence decays change *S* only by 1/2 or not at all, respectively (non-relativistic selection rules). Consequently, decays from some very high spin states, generally having low *L*, are spin-forbidden.

Ion alignment dynamics

Before defining the time-dependent alignment parameter, let us explore in Fig. 3a–d the time-resolved distribution of orbital-angular-momentum

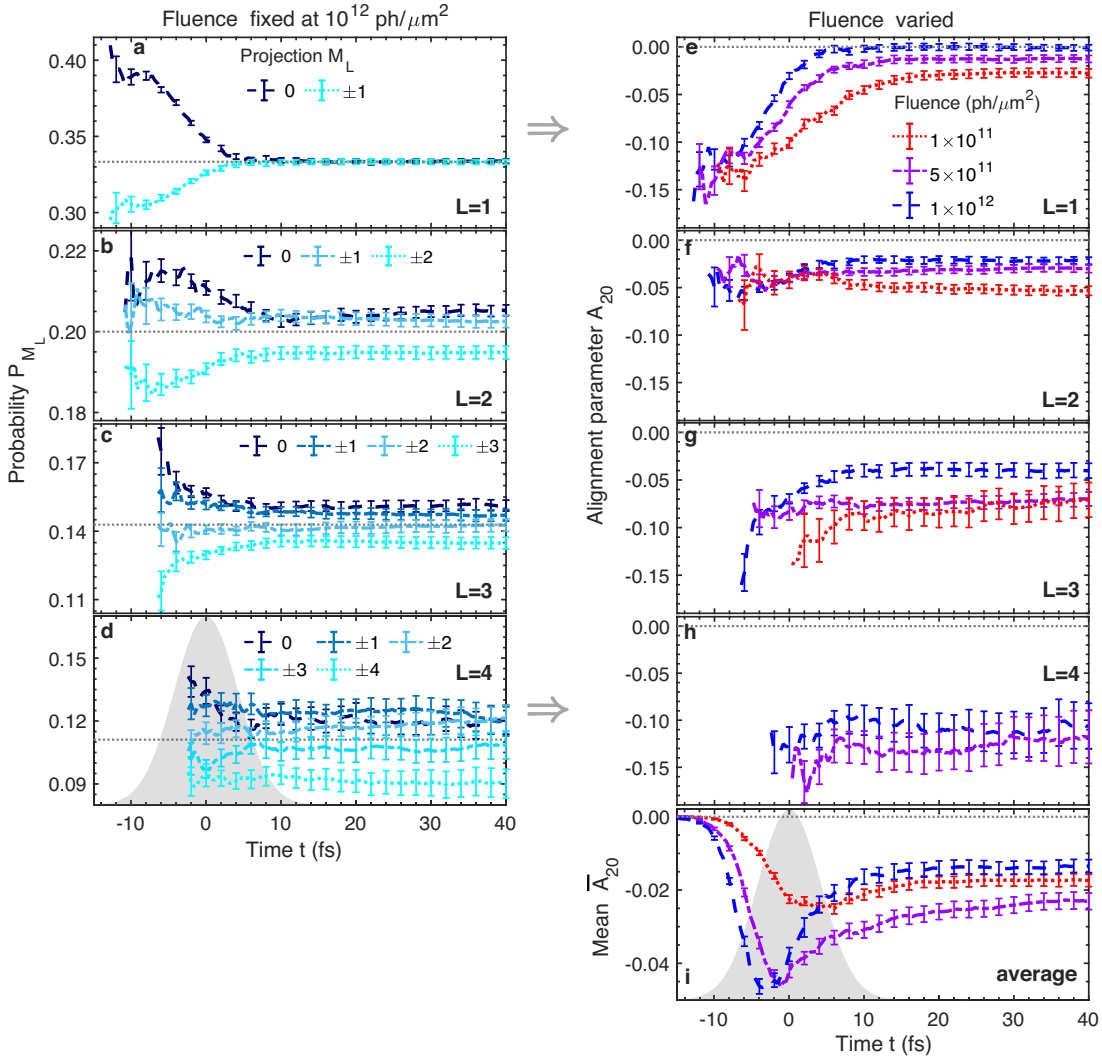

Fig. 3 | Alignment dynamics of Ar ions induced by an intense XFEL pulse. **a–d** The distribution of orbital-angular-momentum projections M_L of ions with definite orbital-angular momentum L is shown by their probabilities P_{M_L} as a function of time at a fixed fluence of 10^{12} photons per μm^2. The dotted grey lines at $1/(2L+1)$ indicate a uniform distribution. **e–h** From the probabilities P_{M_L} the alignment parameter A_{20} for a definite L is calculated and compared for three different fluences. **i** The mean alignment parameter $\bar{A}_{20}$, averaged over all L, is shown for the same fluences. In all panels, the error bars every 2 fs indicate the statistical error obtained via bootstrap estimate. Insufficient statistics are avoided by the restriction $P_L \geq 0.005$ at each time step (**a–h**). The temporal pulse shape is sketched by grey shading in **d** and **i**.

projections M_L for the given L. For ions with definite L, the probabilities P_{M_L} of $M_L = -L, \ldots, +L$ are obtained by summing up probabilities of all individual quantum states with M_L for the given L and at a given time. Note that $P_{M_L} = P_{-M_L}$ because no orientation[38,45] is created by linearly polarised X-rays. For the dominating P-state ($L = 1$), we observe in Fig. 3a that at the beginning of the X-ray pulse and the X-ray multi-photon ionisation dynamics, P-states are aligned along the X-ray polarisation direction ($P_{M_L=0} > P_{M_L=\pm1}$). In the course of X-ray multi-photon ionisation dynamics, their alignment is reduced ($P_{M_L=0}$ decreases, whereas $P_{M_L=\pm1}$ increases), until an almost uniform distribution ($P_{M_L=0} = P_{M_L=\pm1} = 1/3$) is reached shortly after the peak of the X-ray pulse (at about 3 fs). For higher L (Fig. 3b–d), no uniform distribution (the dashed line) is reached after the X-ray pulse and, consequently, their alignment is less reduced (which is further discussed later). The statistical errors are larger than those for $L = 1$ due to smaller numbers of realisations.

The degree and direction of alignment is described by the alignment parameter A_{20}, which is also applicable to ion ensembles. Based on the probabilities P_{M_L}, A_{20} for ions with definite L is defined as[38,45,73,74]

$$A_{20}(L) = \sqrt{\frac{5}{f_L}} \times \sum_{M_L} \left[3M_L^2 - L(L+1)\right] P_{M_L}, \qquad (1)$$

where $f_L = (2L+3)(L+1)L(2L-1)$. The alignment parameter is negative ($A_{20} < 0$), when ions with smaller $|M_L|$ are more populated than others, and positive ($A_{20} > 0$), when ions with larger $|M_L|$ are more populated. $A_{20} = 0$ indicates a uniform distribution. The meaning of A_{20} is further elaborated on in the next section, and extreme values of A_{20} are listed in Table 2. The A_{20} calculated with the time-resolved probabilities P_{M_L} in Fig. 3a–d is shown for the given L in Fig. 3e–h (blue line for a fixed fluence of 10^{12} photons per μm^2). For P-states, A_{20} is initially about -0.16, which is already not an extremely strong alignment compared to the perfect alignment of $A_{20} = -\sqrt{2}$ (Table 2). With time $|A_{20}|$ decreases almost to zero. For higher L, A_{20} is also negative, but with only a weakly declining trend in time.

Table 2 | Perfect alignment ($A_{20}<0$) and anti-alignment ($A_{20}>0$) where all ions have either $M_L = 0$ or $M_L = |L|$, respectively

	Alignment parameter A_{20}	
L	$M_L = 0$	$M_L = \|L\|$
1	$-\sqrt{2}$	$\sqrt{1/2}$
2	$-\sqrt{10/7}$	$\sqrt{10/7}$
3	$-\sqrt{4/3}$	$\sqrt{25/12}$
4	$-\sqrt{100/77}$	$\sqrt{28/11}$

This gives the minimum or the maximum alignment parameter A_{20}.

Figures 3 e–h also show how the alignment of each L depends on the X-ray fluence applied (number of incoming X-rays per unit area[9]). Fluence-dependencies are important in volume integration[75], necessary for quantitative comparisons with experiments. The fluence of 10^{12} photons per μm^2, considered so far, is compared with two lower fluences: 5×10^{11} photons per μm^2 and 10^{11} photons per μm^2. No strong fluence-dependence of A_{20} is observed because ionisation dynamics are mainly only reduced and delayed with lower fluence. For lower fluences, therefore, the evolution of A_{20} is delayed, so that the alignment is less reduced with time. Thus, the saturation value reached after the X-ray pulse is sensitive to the X-ray fluence applied, and its absolute magnitude decreases as the fluence increases. We observe that the absolute magnitude of this saturation value is enhanced with increasing L, which is to be further analysed later. As a result, for $L > 1$, alignment is not negligible for all fluences, in contrast to P-states.

Figure 3i demonstrates what happens to the ion alignment when averaging over L. It shows the mean alignment parameter $\bar{A}_{20} = \sum_L P_L \times A_{20}(L)$ (unaligned neutral Ar included). As can be seen, $\bar{A}_{20}$ exhibits a highly non-linear behaviour. Before the X-ray pulse, neutral Ar is unaligned ($\bar{A}_{20}$=0). At the beginning of the X-ray pulse, p-shell ionisation of neutral Ar creates a negative ion alignment ($\bar{A}_{20}$<0) and $|\bar{A}_{20}|$ increases as more ions are produced. Around the peak of the X-ray pulse, $|\bar{A}_{20}|$ is maximised ($\bar{A}_{20} \approx -0.047$ for 10^{12} photons per μm^2). At this time, most neutral Ar is already ionised (see $P_{q=1}$ in Fig. 1c). If there were only single photoionisation, $|\bar{A}_{20}|$ would continue increasing up to $\bar{A}_{20} \approx -0.12$ (ensemble of Ar^{1+} produced in 59% by p-shell ionisation). However, due to progressing photoionisation accompanied by Auger-Meitner decay involving mainly P- and D-states, $|\bar{A}_{20}|$ noticeably decreases. A saturation value is reached at the end of the X-ray pulse, which is clearly sensitive to the X-ray fluence applied. On the one hand, the higher the fluence, the more $|\bar{A}_{20}|$ is reduced compared to its maximum because of enhanced X-ray multi-photon ionisation dynamics. On the other hand, for low fluence (10^{11} photons per μm^2), only around 50% of the atoms are ionised at all and, thus, the maximum of $|\bar{A}_{20}|$ is very small. As a consequence, to see a maximum alignment, the fluence should be large enough to ionise most atoms ($> 10^{11}$ photons per μm^2), but should not induce too much X-ray multi-photon ionisation dynamics ($< 10^{12}$ photons per μm^2).

To analyse the ion alignment further, we present in Fig. 4a–d charge-resolved alignment parameters A_{20}^q for different L. Note that $A_{20}(L) = \sum_{q=1}^{16} P_q^L A_{20}^q(L)$ with the charge-state probabilities P_q^L for definite L ($\sum_{q=1}^{16} P_q^L = 1$). P_q^L evolves sequentially in time and charge similar to P_q (Fig. 1c) though lack of initially neutral Ar causes much larger P_q^L for low q at early times. A_{20}^q is clearly non-zero and exhibits very different values and signs for different q and L. For P-states, intermediately-charged ions are weakly aligned ($A_{20}^q < 0$) or weakly anti-aligned ($A_{20}^q > 0$) along the X-ray polarisation (Fig. 4a). But Ar^{1+} produced early by single $2p$ or $3p$ ionisation[38] is clearly aligned along the X-ray polarisation ($A_{20}^{q=1} \approx -0.21$) and Ar^{14+} and Ar^{15+} produced less and later are clearly anti-aligned ($A_{20}^{q=14} \approx +0.05$). For P-states, only $P_{M_L=0}$ and $P_{M_L=\pm1}$ determined the A_{20} value. $P_{M_L=0} > P_{M_L=\pm1}$ results in a negative A_{20}, while $P_{M_L=0} < P_{M_L=\pm1}$ gives a positive A_{20}. Typically, p-shell ionisation preferentially increases $P_{M_L=0}$[38].

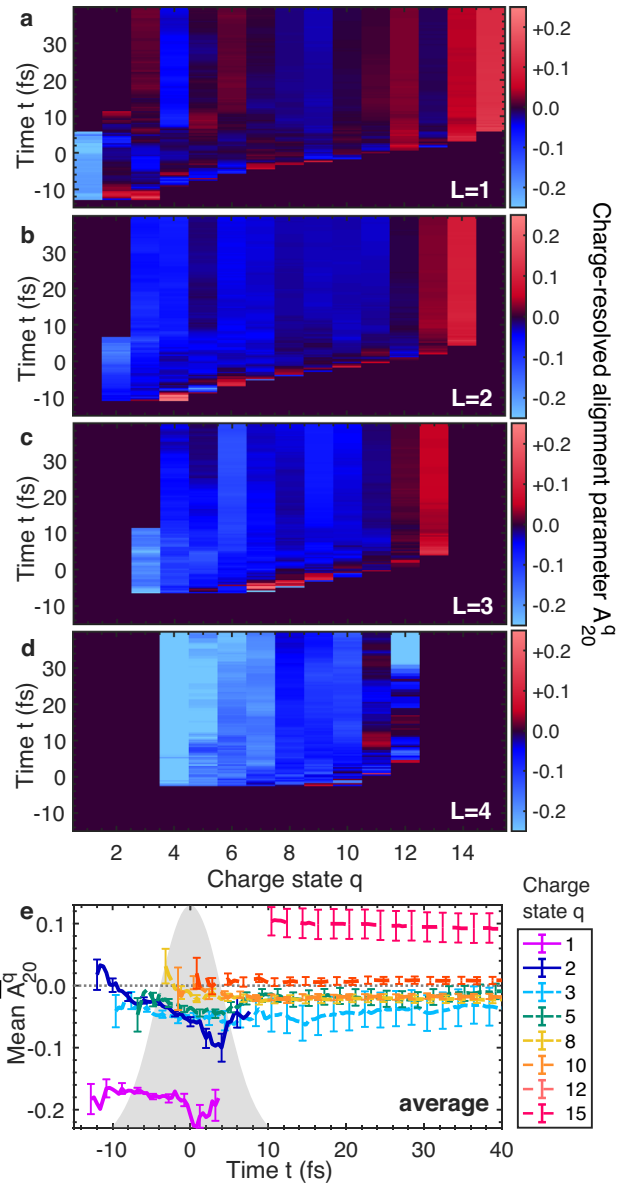

Fig. 4 | Differently charged Ar ions demonstrate different degrees and directions of alignment. a–d The charge-resolved alignment parameter A_{20}^q for different orbital-angular momenta L. Red and blue indicate A_{20}^q>0 and A_{20}^q<0, respectively. **e** The average over all L for selected charge states q. Grey shading indicates the temporal pulse shape. Error bars obtained via bootstrap estimate are shown only in **e**. In **a–d**, they are not shown, but are slightly larger than those in **e**. Insufficient statistics are avoided by the restriction $P_q^L \geq 0.005$ at each time step. A fluence of 10^{12} photons per μm^2 is used.

On the other hand, the $M_L = 0 \rightarrow M_L = 0$ transition is prohibited when the sum of ion and involved bound electron angular momenta is odd, which effectively increases $P_{M_L=\pm1}$. The interplay of these two tendencies combined with the manifold of parallel and competing state-to-state transitions reduces the degree of alignment and changes its direction, already for Ar^{2+}. For comparison, a single (unaveraged) sequence of $2p$ ionisation and Auger-Meitner decay leads to $A_{20}^{q=2} \approx 0.1$[38]. In contrast to P-states, $|A_{20}^q|$ for $L > 1$ is larger and becomes clearly positive only for very highly charged ions ($q \geq 12$). This is attributed to a reduced effect of prohibited transitions on the alignment when the ions involved in a transition have higher L. It also explains why in Fig. 3 a non-vanishing alignment is observed for $L > 1$ at

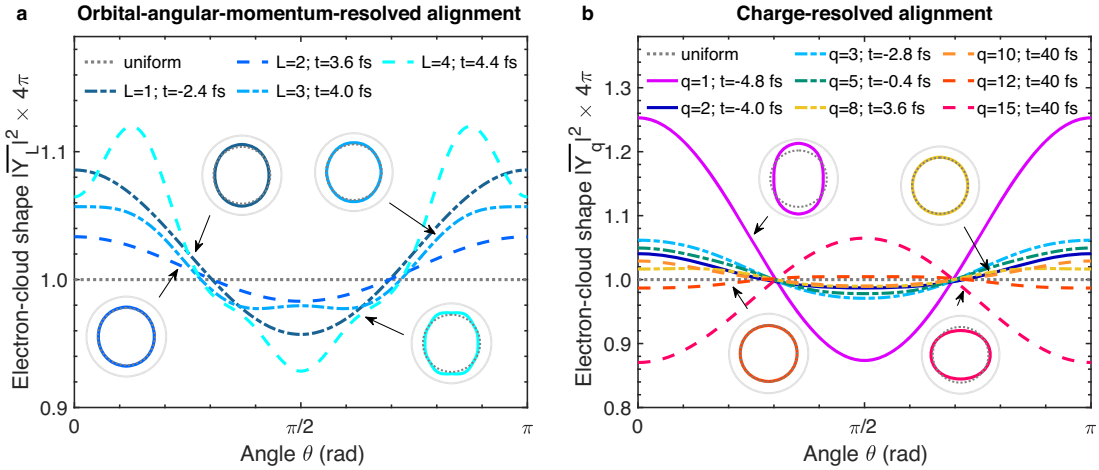

Fig. 5 | Spatial shape of the electron cloud of Ar ions produced by an intense XFEL pulse at specific points *t* in time. a Electron-cloud shape $|\bar{Y}_L|^2$ for ions with definite orbital-angular momentum L (charge-averaged) at time t with maximum P_L (Fig. 2a). **b** Electron-cloud shape $|\bar{Y}_q|^2$ for ions in a few selected charge states q (L-averaged) at time t with maximum P_q (Fig. 1c). The insets in both panels show polar plots of a few selected electron-cloud shapes. The vertical axis ($\theta = 0$ rad and $\theta = \pi$ rad) corresponds to the X-ray polarisation axis. A fluence of 10^{12} photons per μm^2 is used.

long times in contrast to $L = 1$. In Fig. 4e, the charge-resolved alignment parameter $\bar{A}_{20}^{q}$ averaged over all L is presented for selected q. From Figs. 3i and 4e, we conclude that the reduction of ion alignment is mostly the result of averaging over all L and q. Our results suggest that L-resolved or q-resolved quantities are beneficial for detecting ion alignment dynamics.

Spatial shapes of aligned electron clouds

To develop some intuition about ion alignment, we show in Fig. 5 spatial shapes of electron clouds for selected ions produced at some exemplary times t. At the times selected, the corresponding ion yield becomes the largest during the time evolution; the corresponding alignment parameters as a function of time are given in Figs. 3 and 4. In Fig. 5a, we consider ions with different L, but average over all q. The spatial shape of the electron cloud, averaged over all projections M_L, is determined by using the quantity

$$|\bar{Y}_L(\theta)|^2 = \sum_{M_L=-L}^{L} P_{M_L} |Y_L^{M_L}(\theta,\phi)|^2. \qquad (2)$$

Here, $Y_L^{M_L}$ is a spherical harmonic (squaring eliminates the ϕ-dependence) and P_{M_L} is the time-resolved probability for definite L at time t (Fig. 3a–d). In Fig. 5b, we consider ions in a few selected charge states q, but average over all L. In this case, the spatial shape of the electron cloud, $|\bar{Y}_q(\theta)|^2$, is the L-average over all $|\bar{Y}_L(\theta)|^2$ [Eq. (2)] after replacing the P_{M_L} with the $P_{M_L}^{q}$ underlying A_{20}^{q} (Fig. 4). Taking the vertical axis as the X-ray polarisation (z) axis, we observe for most selected electron clouds an oval, prolate shape (corresponding to $A_{20} < 0$). Only highly-charged ions ($q \geq 12$) exhibit an oblate shape ($A_{20} > 0$). For a few selected electron clouds ($L = 4$ in Fig. 5a and $q = 1, 15$ in Fig. 5b) the deviations from a uniform distribution (circle; dotted grey lines in Fig. 5) are quite pronounced and clearly visible in the polar plots.

Discussion

The present paper presents a complete state-resolved description of X-ray multi-photon ionisation dynamics, including electron-cloud alignment in an XFEL pulse. The calculated alignment parameter for Ar^{1+} ($A_{20}^{q=1} \approx -0.21$) acceptably agrees with previous works[38,44,54], taking into account the photon-energy dependence. Due to X-ray multi-photon ionisation, the magnitude of the alignment parameter after averaging over L and q becomes relatively small (< 0.05) as depicted in Fig. 3i. However, when we analyse the alignment parameter for individual L and q (Fig. 4a–d), individual L (Fig. 3e–h), and individual q (Fig. 4e), its magnitude is larger than the averaged value. Non-trivial ion alignment dynamics for individual quantum states are predicted. We expect that this result can be generalised to other atomic species (ionised under suitable conditions), photon energies (below the respective K-shell threshold), and (femtosecond) pulse durations. Observing electron-cloud alignment dynamics induced by XFEL pulses requires few-femtosecond- or even attosecond-resolved measurements sensitive to M_L quantum-state distributions.

Desirable are time-resolved measurements of Auger-Meitner electron angular distributions[42,44,48,49,76] generated in XFEL experiments. Best suited for this propose are transitions involving only a single continuum wave for the Auger-Meitner electron[48,49], e.g., final ions with zero L. Then, the anisotropy parameter[47,50,77–80] is directly proportional to the alignment parameter for the initial ion. Future developments in this direction will enable deeper insights into electron-cloud alignment in an XFEL pulse, including the impact of effects so far neglected, such as non-dipole effects[54,66,81] or spin-orbit coupling[62–64,82]. A further possibility is to apply circularly polarised X-ray pulses[8,83–86]. Even though the direction of alignment changes[40], based on the present results, we expect similar electron-cloud alignment dynamics during a circularly polarised X-ray pulse. However, how the orientation induced by the circularly polarised X-ray pulse behaves is an open question.

Lastly, we would like to comment on electric alignment (orientation) in molecular targets induced by XFEL pulses. Here, we demonstrate that the polarisation of the X-ray beam is imprinted on the atomic electron-cloud dynamics on ultrafast time scales. We anticipate a similar impact on the electron-cloud dynamics in molecules. However, this depends in detail on the strength of interatomic interactions and remains to be investigated in a future study.

Methods

For X-ray multi-photon ionisation dynamics calculations, we employ XATOM[20,87,88], which has been successfully applied for interpreting XFEL experiments[11–15,31,32,34,35,89]. XATOM has recently been extended to state-resolved ionisation dynamics with a Monte Carlo implementation[36], based on a non-relativistic quantum-state-resolved electronic-structure framework[38] for isolated atoms. For any given electronic configuration, it provides zeroth-order states with quantum numbers (L, S, M_L, κ) and term-specific first-order-corrected energies $E_{LS\kappa}$. On this basis, state-to-state transition parameters for photoionisation, Auger-Meitner decay, and fluorescence are calculated from first principles. Since they are independent of the spin projection M_S, M_S is neglected in this work.

A Monte Carlo on-the-fly rate-equation method[11,12] is employed for describing the time evolution of individual quantum-state populations. The number of individual quantum states involved is already very large for argon[36], i.e., 2^{16}, which would be challenging without a Monte Carlo on-the-fly approach. Next to the Monte Carlo method a couple of simplifications are critical to efficiently perform calculations. We made several approximations: non-sequential two-photon absorption[34,90], higher-order many-body processes such as double photoionisation[91] and double Auger-Meitner decay[92], coherent effects[93–96], inter-channel coupling[97,98], relativistic effects[32,99], finite-nuclear-size effects[99], and non-dipole effects[100,101] are not included in this work.

Due to the Monte Carlo method all presented results contain statistical errors. Statistical errors are obtained via bootstrap estimate[102] using 50 bootstrap samples of 200,000 Monte Carlo trajectories. For the results in Figs. 1 and 2, errors are two orders of magnitude smaller than the dominant quantities themselves and are, consequently, omitted. The calculated errors become quite large, particularly for propagation at early times and for large L in Fig. 3, because the number of ions of interest is too small. To avoid such insufficient statistics, results in Figs. 3 and 4 are only plotted when the underlying ion probability is ≥0.005. We expect that the overall trend shown in Figs. 3 and 4 will remain unchanged when more Monte Carlo trajectories are used.

Data availability

The raw data and the underlying data for the figures can be obtained from the authors upon request.

Code availability

The state-resolved Monte Carlo implementation in the XATOM toolkit is available from the authors upon request.

Received: 10 June 2024; Accepted: 25 October 2024;
Published online: 07 November 2024

References

1. Emma, P. et al. First lasing and operation of an ångstrom-wavelength free-electron laser. *Nat. Photon.* **4**, 641–647 (2010).
2. Decking, W. et al. A MHz-repetition-rate hard x-ray free-electron laser driven by a superconducting linear accelerator. *Nat. Photon.* **14**, 391–397 (2020).
3. Kang, H.-S. et al. Hard x-ray free-electron laser with femtosecond-scale timing jitter. *Nat. Photon.* **11**, 708–713 (2017).
4. Ishikawa, T. et al. A compact x-ray free-electron laser emitting in the sub-ångström region. *Nat. Photon.* **6**, 540–544 (2012).
5. Prat, E. et al. A compact and cost-effective hard x-ray free-electron laser driven by a high-brightness and low-energy electron beam. *Nat. Photon.* **14**, 748–756 (2020).
6. Pellegrini, C., Marinelli, A. & Reiche, S. The physics of x-ray free-electron lasers. *Rev. Mod. Phys.* **88**, 015006 (2016).
7. Schulze, K. S. et al. Towards perfectly linearly polarized x-rays. *Phys. Rev. Res.* **4**, 013220 (2022).
8. Allaria, E. et al. Control of the polarization of a vacuum-ultraviolet, high-gain, free-electron laser. *Phys. Rev. X* **4**, 041040 (2014).
9. Santra, R. and Young, L. Interaction of intense x-ray beams with atoms, in *Synchrotron Light Sources and Free-Electron Lasers*, edited by Jaeschke, E. J., Khan, S., Schneider, J. R., and Hastings, J. B. (Springer International Publishing, Switzerland, 2016), pp. 1233–1260. https://doi.org/10.1007/978-3-319-14394-1_25.
10. Young, L. et al. Femtosecond electronic response of atoms to ultra-intense x-rays. *Nature* **466**, 56–61 (2010).
11. Fukuzawa, H. et al. Deep inner-shell multiphoton ionization by intense x-ray free-electron laser pulses. *Phys. Rev. Lett.* **110**, 173005 (2013).
12. Son, S.-K. & Santra, R. Monte Carlo calculation of ion, electron, and photon spectra of xenon atoms in x-ray free-electron laser pulses. *Phys. Rev. A* **85**, 063415 (2012).
13. Rudek, B. et al. Relativistic and resonant effects in the ionization of heavy atoms by ultra-intense hard x-rays. *Nat. Commun.* **9**, 4200 (2018).
14. Rudek, B. et al. Ultra-efficient ionization of heavy atoms by intense x-ray free-electron laser pulses. *Nat. Photon.* **6**, 858–865 (2012).
15. Motomura, K. et al. Sequential multiphoton multiple ionization of atomic argon and xenon irradiated by x-ray free-electron laser pulses from SACLA. *J. Phys. B: Mol. Opt. Phys.* **46**, 164024 (2013).
16. Lorenz, U., Kabachnik, N. M., Weckert, E. & Vartanyants, I. A. Impact of ultrafast electronic damage in single-particle x-ray imaging experiments. *Phys. Rev. E* **86**, 051911 (2012).
17. Quiney, H. M. & Nugent, K. A. Biomolecular imaging and electronic damage using x-ray free-electron lasers. *Nat. Phys.* **7**, 142–146 (2011).
18. Nass, K. Radiation damage in protein crystallography at x-ray free-electron lasers. *Acta Cryst. D.* **75**, 211–218 (2019).
19. Neutze, R., Wouts, R., van der Spoel, D., Weckert, E. & Hajdu, J. Potential for biomolecular imaging with femtosecond x-ray pulses. *Nature* **406**, 752–757 (2000).
20. Son, S.-K., Young, L. & Santra, R. Impact of hollow-atom formation on coherent x-ray scattering at high intensity. *Phys. Rev. A* **83**, 033402 (2011).
21. Spence, J. C. H. XFELs for structure and dynamics in biology. *IUCrJ* **4**, 322–339 (2017).
22. Schlichting, I. & Miao, J. Emerging opportunities in structural biology with x-ray free-electron lasers. *Curr. Opin. Struct. Biol.* **22**, 613–626 (2012).
23. Sobolev, E. et al. Megahertz single-particle imaging at the European XFEL. *Commun. Phys.* **3**, 97 (2020).
24. Seibert, M. M. et al. Single mimivirus particles intercepted and imaged with an x-ray laser. *Nature* **470**, 78–81 (2011).
25. Chapman, H. N. et al. Femtosecond x-ray protein nanocrystallography. *Nature* **470**, 73–77 (2011).
26. Coe, J. & Fromme, P. Serial femtosecond crystallography opens new avenues for structural biology. *Protein Pept. Lett.* **23**, 255–272 (2016).
27. Galli, L. et al. Towards phasing using high x-ray intensity. *IUCrJ* **2**, 627–634 (2015).
28. Nass, K. et al. Structural dynamics in proteins induced by and probed with x-ray free-electron laser pulses. *Nat. Commun.* **11**, 1814 (2020).
29. Chapman, H. N. X-ray free-electron lasers for the structure and dynamics of macromolecules. *Annu. Rev. Biochem.* **88**, 35–58 (2019).
30. Xiang, W., Gao, C., Fu, Y., Zeng, J. & Yuan, J. Inner-shell resonant absorption effects on evolution dynamics of the charge state distribution in a neon atom interacting with ultraintense x-ray pulses. *Phys. Rev. A* **86**, 061401(R) (2012).
31. Rörig, A. et al. Multiple-core-hole resonance spectroscopy with ultraintense x-ray pulses. *Nat. Commun.* **14**, 5738 (2023).
32. Toyota, K., Son, S.-K. & Santra, R. Interplay between relativistic energy corrections and resonant excitations in x-ray multiphoton ionization dynamics of Xe atoms. *Phys. Rev. A* **95**, 043412 (2017).
33. Buth, C. et al. Neon in ultrashort and intense x-rays from free electron lasers. *J. Phys. B: Mol. Opt. Phys.* **51**, 055602 (2018).
34. Doumy, G. et al. Nonlinear atomic response to intense ultrashort x rays. *Phys. Rev. Lett.* **106**, 083002 (2011).
35. Son, S.-K., Boll, R. & Santra, R. Breakdown of frustrated absorption in x-ray sequential multiphoton ionization. *Phys. Rev. Res.* **2**, 023053 (2020).

36. Budewig, L., Son, S.-K. & Santra, R. State-resolved ionization dynamics of a neon atom induced by x-ray free-electron-laser pulses. *Phys. Rev. A* **107**, 013102 (2023).
37. Mazza, T. et al. Mapping resonance structures in transient core-ionized atoms. *Phys. Rev. X* **10**, 041056 (2020).
38. Budewig, L., Son, S.-K. & Santra, R. Theoretical investigation of orbital alignment of x-ray-ionized atoms in exotic electronic configurations. *Phys. Rev. A* **105**, 033111 (2022).
39. Gryzlova, E. V., Grum-Grzhimailo, A. N., Kiselev, M. D. & Popova, M. M. Evolution of the ionic polarization in multiple sequential ionization: general equations and an illustrative example. *Phys. Rev. A* **107**, 013111 (2023).
40. Kleiman, U. & Lohmann, B. Photoionization of closed-shell atoms: Hartree–fock calculations of orientation and alignment. *J. Electron Spectrosc. Relat. Phenom.* **131-132**, 29–50 (2003).
41. Caldwell, C. D. & Zare, R. N. Alignment of Cd atoms by photoionization. *Phys. Rev. A* **16**, 255–262 (1977).
42. Southworth, S. H. et al. Photoelectron and Auger electron asymmetries: Alignment of $Xe^{+2}D_{\frac{5}{2}}$ by photoionization. *Phys. Rev. A* **24**, 2257–2260 (1981).
43. Küst, H., Kleiman, U. & Mehlhorn, W. Alignment after Xe L_3 photoionization by synchrotron radiation. *J. Phys. B: Mol. Opt. Phys.* **36**, 2073–2082 (2003).
44. Becker, U. Complete photoionisation experiments. *J. Electron Spectrosc. Relat. Phenom.* **96**, 105–115 (1998).
45. Schmidt, V. Photoionization of atoms using synchrotron radiation. *Rep. Prog. Phys.* **55**, 1483–1659 (1992).
46. Flügge, S., Mehlhorn, W. & Schmidt, V. Angular distribution of Auger electrons following photoionization. *Phys. Rev. Lett.* **29**, 7–9 (1972).
47. Berezhko, E. G., Kabachnik, N. M. & Rostovsky, V. S. Potential-barrier effects in inner-shell photoionisation and their influence on the anisotropy of x-rays and Auger electrons. *J. Phys. B: Mol. Opt. Phys.* **11**, 1749 (1978).
48. Cleff, B. & Mehlhorn, W. On the angular distribution of Auger electrons. *Phys. Lett. A* **37**, 3–4 (1971).
49. Cleff, B. & Mehlhorn, W. Angular distribution of $L_3M_{2,3}M_{2,3}$ ($^1S_0$) Auger electrons of argon. *J. Phys. B: Mol. Opt. Phys.* **7**, 605–611 (1974).
50. Berezhko, E. G. & Kabachnik, N. M. Theoretical study of inner-shell alignment of atoms in electron impact ionisation: angular distribution and polarisation of x-rays and Auger electrons. *J. Phys. B: Mol. Opt. Phys.* **10**, 2467–2477 (1977).
51. Schmoranzer, H. et al. Angular distribution of the fluorescence radiation of Kr II satellite states. *J. Phys. B: Mol. Opt. Phys.* **30**, 4463–4480 (1997).
52. Hrdý, J., Henins, A. & Bearden, J. A. Polarization of the L_{α_1} x rays of mercury. *Phys. Rev. A* **2**, 1708–1711 (1970).
53. Kronast, W., Huster, R. & Mehlhorn, W. Alignment of atoms following photoionisation. *Z. Phys. D.* **2**, 285–296 (1986).
54. Alexei, S. F., Grum-Grzhimailo, N., Gryzlova, E. V. & Kabachnik, N. M. Photoelectron angular distributions and correlations in sequential double and triple atomic ionization by free electron lasers. *J. Mod. Opt.* **63**, 334–357 (2016).
55. Cooper, J. & Zare, R. N. Angular distribution of photoelectrons. *J. Chem. Phys.* **48**, 942–943 (1968).
56. Manson, S. T. & Cooper, J. W. Angular distribution of photoelectrons: Outer shells of noble gases. *Phys. Rev. A* **2**, 2170–2171 (1970).
57. Davis, V. T. *Introduction to Photoelectron Angular Distributions* (Springer, Switzerland, 2022).
58. Al Moussalami, S. et al. First angle-resolved photoelectron measurements following inner-shell resonant excitation in a singly charged ion. *Phys. Rev. Lett.* **76**, 4496–4499 (1996).
59. Rouvellou, B. et al. Photoelectron spectroscopy experiments on singly charged positive-ions using synchrotron radiation. *Nucl. Instrum. Methods Phys. Res., B* **134**, 287–303 (1998).
60. Rouzée, A. et al. Angle-resolved photoelectron spectroscopy of sequential three-photon triple ionization of neon at 90.5 eV photon energy. *Phys. Rev. A* **83**, 031401 (2011).
61. Braune, M. et al. Electron angular distributions of noble gases in sequential two-photon double ionization. *J. Mod. Opt.* **63**, 324–333 (2016).
62. Young, L. et al. X-ray microprobe of orbital alignment in strong-field ionized atoms. *Phys. Rev. Lett.* **97**, 083601 (2006).
63. Santra, R. et al. Strong-field control of x-ray processes, in *Advances in Atomic, Molecular, and Optical Physics*, edited by Arimondo, E., Berman, P. R., and Lin, C. C. (Academic Press, Amsterdam, 2008), vol. 56, pp. 219–257. https://doi.org/10.1016/S1049-250X(08)00014-1.
64. Heinrich-Josties, E., Pabst, S. & Santra, R. Controlling the 2*p* hole alignment in neon via the 2*s*-3*p* fano resonance. *Phys. Rev. A* **89**, 043415 (2014).
65. Mondal, S. et al. Photoelectron angular distributions for the two-photon sequential double ionization of xenon by ultrashort extreme ultraviolet free electron laser pulses. *J. Phys. B: Mol. Opt. Phys.* **46**, 164022 (2013).
66. Ilchen, M. et al. Symmetry breakdown of electron emission in extreme ultraviolet photoionization of argon. *Nat. Commun.* **9**, 4659 (2018).
67. Khubbutdinov, R. et al. High spatial coherence and short pulse duration revealed by the Hanbury Brown and twiss interferometry at the European XFEL. *Struc. Dyn.* **8**, 044305 (2021).
68. Ferguson, K. R. et al. The atomic, molecular and optical science instrument at the linac coherent light source. *J. Synchrotron Rad.* **22**, 492–497 (2015).
69. Tschentscher, T. et al. Photon beam transport and scientific instruments at the European XFEL. *Appl. Sci.* **7**, 592 (2017).
70. Mazza, T. et al. The beam transport system for the small quantum systems instrument at the European XFEL: optical layout and first commissioning results. *J. Synchrotron Rad.* **30**, 457–467 (2023).
71. Rudenko, A. et al. Femtosecond response of polyatomic molecules to ultra-intense hard x-rays. *Nature* **546**, 129–132 (2017).
72. Murphy, B. F. et al. Femtosecond x-ray-induced explosion of C_{60} at extreme intensity. *Nat. Commun.* **5**, 4281 (2014).
73. Blum, K. *Density Matrix Theory and Applications* (Springer, New York, 1996).
74. Greene, C. H. & Zare, R. N. Photofragment Alignment and Orientation. *Ann. Rev. Phys. Chem.* **33**, 119–150 (1982).
75. Toyota, K. et al. xcalib: a focal spot calibrator for intense x-ray free-electron laser pulses based on the charge state distributions of light atoms. *J. Synchrotron Rad.* **26**, 1017–1030 (2019).
76. Ueda, K. et al. Angular distribution of Auger electrons in resonantly enhanced transitions from 3p photoexcited Ca^+ ions. *J. Phys. B: Mol. Opt. Phys.* **31**, 4331–4348 (1998).
77. Lohmann, B. *Angle and Spin Resolved Auger Emission* (Springer, Berlin Heidelberg, 1994).
78. Lohmann, B. Analyses and model calculations on the angular distribution and spin polarization of Auger electrons. *J. Phys. B: Mol. Opt. Phys.* **23**, 3147–3166 (1990).
79. Blum, K., Lohmann, B. & Taute, E. Angular distribution and polarisation of Auger electrons. *J. Phys. B: Mol. Opt. Phys.* **19**, 3815–3826 (1986).
80. Albiez, A., Thoma, M., Weber, W. & Mehlhorn, W. $KL_{2,3}$ ionization in neon by electron impact in the range 1.5-50 keV: cross sections and alignment. *Z. Phys. D.* **16**, 97–106 (1990).
81. Krässig, B. et al. Nondipolar asymmetries of photoelectron angular distributions. *Phys. Rev. Lett.* **75**, 4736–4739 (1995).

82. Chen, M. H. Effect of intermediate coupling on angular distribution of Auger electrons. *Phys. Rev. A* **45**, 1684–1689 (1992).
83. Mazza, T. et al. Determining the polarization state of an extreme ultraviolet free-electron laser beam using atomic circular dichroism. *Nat. Commun.* **5**, 3648 (2014).
84. Lutman, A. A. et al. Polarization control in an x-ray free-electron laser. *Nat. Photon.* **10**, 468–472 (2016).
85. Prat, E. et al. An x-ray free-electron laser with a highly configurable undulator and integrated chicanes for tailored pulse properties. *Nat. Commun.* **14**, 5069 (2023).
86. Perosa, G. et al. Femtosecond polarization shaping of free-electron laser pulses. *Phys. Rev. Lett.* **131**, 045001 (2023).
87. Jurek, Z., Son, S.-K., Ziaja, B. & Santra, R. XMDYN and XATOM: versatile simulation tools for quantitative modeling of x-ray free-electron laser induced dynamics of matter. *J. Appl. Cryst.* **49**, 1048–1056 (2016).
88. Son, S.-K. et al. XATOM—an integrated toolkit for x-ray and atomic physics, in XRAYPAC, v2.0.0 (2024), GitLab https://gitlab.desy.de/CDT/xraypac.
89. Rudek, B. et al. Resonance-enhanced multiple ionization of krypton at an x-ray free-electron laser. *Phys. Rev. A* **87**, 023413 (2013).
90. Sytcheva, A., Pabst, S., Son, S.-K. & Santra, R. Enhanced nonlinear response of Ne^{8+} to intense ultrafast x rays. *Phys. Rev. A* **85**, 023414 (2012).
91. Schneider, T., Chocian, P. L. & Rost, J.-M. Separation and identification of dominant mechanisms in double photoionization. *Phys. Rev. Lett.* **89**, 073002 (2002).
92. Kolorenč, P., Averbukh, V., Feifel, R. & Eland, J. Collective relaxation processes in atoms, molecules and clusters. *J. Phys. B: Mol. Opt. Phys.* **49**, 082001 (2016).
93. Rohringer, N. & Santra, R. X-ray nonlinear optical processes using a self-amplified spontaneous emission free-electron laser. *Phys. Rev. A* **76**, 033416 (2007).
94. Rohringer, N. & Santra, R. Resonant Auger effect at high x-ray intensity. *Phys. Rev. A* **77**, 053404 (2008).
95. Kanter, E. P. et al. Unveiling and driving hidden resonances with high-fluence, high-intensity x-ray pulses. *Phys. Rev. Lett.* **107**, 233001 (2011).
96. Li, Y. et al. Coherence and resonance effects in the ultra-intense laser-induced ultrafast response of complex atoms. *Sci. Rep.* **6**, 18529 (2016).
97. Drake, G. W. F. *Springer Handbook of Atomic, Molecular, and Optical Physics* (Springer, New York, 2006).
98. Starace, A. F. Trends in the theory of atomic photoionization. *Appl. Opt.* **19**, 4051–4062 (1980).
99. Deslattes, R. D. et al. X-ray transition energies: new approach to a comprehensive evaluation. *Rev. Mod. Phys.* **75**, 35–99 (2003).
100. Demekhin, P. V. On the breakdown of the electric dipole approximation for hard x-ray photoionization cross sections. *J. Phys. B: Mol. Opt. Phys.* **47**, 025602 (2014).
101. Hemmers, O., Guillemin, R. & Lindle, D. W. Nondipole effects in soft X-ray photoemission. *Radiat. Phys. Chem.* **70**, 123–147 (2004).
102. Efron, B. & Tibshirani, R. J. *An introduction to the bootstrap* (Chapman and Hall/CRC, Philadelphia, PA, 1994).

Acknowledgements

L. B. and R. S. acknowledge support by DASHH (Data Science in Hamburg - HELMHOLTZ Graduate School for the Structure of Matter) with Grant-No. HIDSS-0002. L. B., S.-K. S., and R. S. acknowledge support from DESY (Hamburg, Germany), a member of the Helmholtz Association HGF. This work was supported in part by Deutsche Forschungsgemeinschaft (DFG, German Research Foundation) - 491245950.

Author contributions

L.B. carried out the calculations using the XATOM toolkit, interpreted the results and wrote the manuscript with input from all authors. S.-K.S. and R.S. jointly supervised this work.

Funding

Open Access funding enabled and organized by Projekt DEAL.

Competing interests

The authors declare no competing interests.

Additional information

Correspondence and requests for materials should be addressed to Robin Santra.

Peer review information *Communications Physics* thanks the anonymous reviewers for their contribution to the peer review of this work.

Chapter 4

Conclusion and Outlook

In this cumulative dissertation, I have presented a state-resolved Monte Carlo rate-equation implementation for simulating state-resolved X-ray multiphoton ionization dynamics of atoms and have discussed a machine-learning strategy to reduce its computational cost. The state-resolved Monte Carlo rate-equation implementation is capable of describing electron-cloud alignment dynamics of ions produced by interaction of atoms with an intense X-ray free-electron laser (XFEL) pulse. The main conclusions of this dissertation are:

- For charge-state distributions, the common configuration-based rate-equation calculations are sufficient. But the state-resolved rate-equation calculations provide more precise information about resonant excitations as well as electron and photon spectra than the common configuration-based rate-equation calculations.

- A machine-learning strategy to reduce the computational cost of the state-resolved rate-equation calculations works in principle. Its performance, in terms of charge-state distributions and electron and photon spectra, is good when combining calculated atomic transition parameters with atomic transition parameters being predicted by machine-learning models.

- Even if initially the atomic electron cloud is perfectly spherically symmetric, it is notably reshaped by an intense linearly polarized XFEL pulse for individual atomic charge and/or orbital-angular-momentum states.

In the following, more detailed outlines of the key findings for all different scientific contributions are individually provided along with an outlook. Because the first scientific contribution (Sec. 3.1) has already been part of my master thesis [136], it is discussed together with the second scientific contribution (Sec. 3.2), for which it delivers the fundamental basis.

Quantum-state-resolved electronic-structure and X-ray multiphoton ionization dynamics calculations

As a first critical step regarding state-resolved X-ray multiphoton ionization dynamics calculations, I have developed a nonrelativistic quantum-state-resolved electronic-structure framework for isolated atoms and atomic ions (Sec. 3.1). This framework employs first-order many-body perturbation theory to improve the Hartree-Fock-Slater calculations in the XATOM toolkit. A comparison of transition energies of neon has demonstrated that the use of first-order-corrected energies provides more accurate transition energies than the original Hartree-Fock-Slater calculations. Focusing on a single X-ray-induced atomic transition, I have also studied the electron-cloud alignment of argon ions up to Ar^{3+} and have found a nonneglegible degree of alignment.

As a follow-up study (Sec. 3.2), the quantum-state-resolved electronic-structure framework has been combined with the Monte Carlo on-the-fly rate-equation method to describe state-resolved X-ray multiphoton ionization dynamics. The resulting state-resolved Monte Carlo rate-equation implementation has been applied to perform state-resolved calculations for neon, which have been compared to configuration-based calculations. This comparison has shown that charge-state distributions only differ little for X-ray photon energies that do not induce resonant photoabsorption transitions. In these cases, the configuration-based calculations produce already quite good charge-state distributions [27–30, 33, 34]. However, resonant photoabsorption transitions and electron and photon spectra clearly profit from the improved first-order-corrected transition energies used in the state-resolved calculations. Moreover, I have analyzed time-resolved spectra of ions, electrons, and photons at different pulse durations. This enables detailed insight into ultrafast dynamics of state-resolved X-ray multiphoton ionization, including the phenomenon of frustrated absorption.

As motivated in the introduction, the most attractive application of the state-resolved Monte Carlo rate-equation implementation is the study of electron-cloud alignment dynamics in an intense XFEL pulse. This application has been performed in Sec. 3.4. Apart from that, a very promising perspective is to use the state-resolved Monte Carlo rate-equation implementation to support the interpretation of XFEL experiments by providing detailed state-resolved information. Recently, high-resolution fluorescence spectra of neon have been measured in experiments at the European XFEL[1]. The state-resolved Monte Carlo rate-equation implementation has not only been employed to help assign individual term-resolved fluores-

[1] Two corresponding manuscripts are in preparation.

cence peaks, but also to elucidate multi-resonant mechanisms of transient ionization and excitation dynamics. Additionally, it may be interesting to compare not only temporally asymptotic but also time-resolved spectra with experiments. Potential experimental methods that may allow a comparison of time-resolved quantities are attosecond transient absorption spectroscopy [216, 217] and attosecond streaking measurements [218–220].

Also of great scientific interest is to perform state-resolved X-ray multiphoton ionization dynamics calculations for atoms as heavy as xenon. For xenon, resonant excitations have recently been studied at the European XFEL in combination with configuration-based calculations [42]. But especially for heavy atoms, relativistic, quantum-electrodynamic, and finite-nuclear-size effects play an important role [40, 135]. Therefore, improving the accuracy of the underlying quantum-state-resolved electronic-structure framework is desirable. It can not only be improved by including the above mentioned crucial effects but also by utilizing advanced first-order states, by including interchannel coupling [221, 222], or by an individual optimization of orbitals and orbital energies when calculating cross sections and transition rates. Next to this, the accuracy of X-ray multiphoton ionization dynamics calculations can clearly be improved by including higher-order many-body processes via shake-off and knockout mechanisms [34, 49]. However, all these potential improvements will substantially expand the number of individual quantum states and/or X-ray-induced atomic transitions involved in the state-resolved Monte Carlo rate-equation calculation. Thus, the computational effort, being already extremely large for heavy atoms, will further increase dramatically. As a consequence, accelerating state-resolved Monte Carlo rate-equation calculations is a first crucial step for the realization of more accurate state-resolved calculations. Accelerating them via machine learning has been the topic of the next scientific contribution.

X-ray-induced atomic transitions via machine learning

In Sec. 3.3, I have discussed whether the high computational cost of huge-sized state-resolved X-ray multiphoton ionization dynamics calculations can be reduced via a machine-learning strategy. This strategy combines the state-resolved Monte Carlo rate-equation implementation with machine-learning models for predicting atomic transition parameters. Their state-resolved calculation, performed on the fly, is the main bottleneck in the Monte Carlo calculation. As potential machine-learning models, neural networks and random forest regressors have been employed and their performances have been compared for argon. This comparison has shown that both types of machine-learning models predict atomic transition parameters with similarly acceptable accuracy, although neural networks exhibit much longer

training times. Moreover, I have employed the resulting machine-learning-based state-resolved Monte Carlo implementation for calculating charge-state distributions and electron and photon spectra for argon. Comparing the machine-learning-based calculations with full calculations, I have demonstrated that the achieved level of accuracy in charge-state distributions and spectra is satisfactory, especially also in view of a couple of simplifications made in the calculations (see Secs. 3.1 and 3.2). The reason for this good performance, in terms of charge-state distributions and spectra, relies on the combination of calculated atomic transition parameters for the most important X-ray-induced atomic transitions with predicted atomic transition parameters for the remaining less likely ones. Atomic transition parameters are calculated and collected in an initial state-resolved Monte Carlo rate-equation calculation. Once the machine-learning models are trained on them, the final machine-learning-based state-resolved Monte Carlo rate-equation calculation is performed much faster than a full calculation. However, two main shortcomings have become evident: (i) the accuracy of the machine-learning predictions is limited, especially for less likely X-ray-induced atomic transitions, and (ii) training the neural networks is also quite time consuming. Therefore, whether we profit from the present machine-learning-based state-resolved Monte Carlo implementation depends on the available computer architecture.

As a consequence of these limitations, further developments of the machine-learning-based state-resolved Monte Carlo implementation are crucial before we can really profit from it. Promising perspectives are extended feature engineering to support the learning process [83, 177] and improving the machine-learning models by using gradient boosted trees [223], batch normalization [83], advanced random forest methods [224], recurrent neural networks [83], or neural networks combined with random forest regressors [180, 225]. Training times may be reduced by using GPUs instead of CPUs [83] or by transferring knowledge between different machine-learning-based calculations. Another interesting aspect is to preselect the most important X-ray-induced atomic transitions via machine-learning models similar to machine-learning approaches in configuration interaction calculations [130, 131, 226]. If some of these developments are successful, the machine-learning-based state-resolved Monte Carlo implementation will also be applicable to heavier atoms. For heavy atoms, the machine-learning-based implementation is crucial to make state-resolved X-ray multiphoton ionization dynamics calculations feasible in the future.

Electron-cloud alignment dynamics

Finally in Sec. 3.4, I have presented insight into the possibility to reshape the electron cloud of atoms, initially being perfectly spherically symmetric, through an

ultraintense and ultrashort linearly polarized X-ray pulse. In particular, I have simulated state-resolved X-ray multiphoton ionization dynamics for argon using the developed state-resolved Monte Carlo rate-equation implementation. The simulations have illustrated that X-ray multiphoton ionization dynamics generate ions in a wide range of charge states with nonzero orbital- and spin-angular momentum. When it is averaged over all individual quantum states populated at a given time, the electron-cloud alignment shows a highly nonlinear behavior but is suppressed with progressing X-ray multiphoton ionization dynamics. For individual orbital-angular-momentum and charge states formed during X-ray multiphoton ionization dynamics, the simulations have, however, clearly demonstrated nontrivial and non-negligible electron-cloud alignment dynamics.

This offers opportunities for detecting exciting electron-cloud alignment dynamics in XFEL experiments, using few-femtosecond- or attosecond-resolved measurements sensitive to the distribution of orbital-angular-momentum projection states. A promising way to make electron-cloud alignment experimentally accessible is via Auger-Meitner electron angular distributions [56, 58, 75, 76, 212]. Best suited for this purpose are transitions involving only a single continuum wave for the Auger-Meitner electron [75, 76], e.g., final ions with zero L. In this case, the anisotropy parameter [61, 74, 77, 201, 207, 209] is directly proportional to the alignment parameter for the initial ion as also demonstrated in Sec. 2.4.5. When such experimental measurements are available, a next interesting perspective will be to investigate whether the observed electron-cloud alignment dynamics are noticeably affected by so far neglected effects like nondipole effects [66, 70, 227], shake-off effects, or spin-orbit coupling [62–64, 214]. Lastly, it may be considered how the electron-cloud alignment behaves when applying circularly polarized X-ray pulses [228–232]. Based on the present results, similar electron-cloud alignment dynamics are expected during a circularly polarized X-ray pulse even though the direction of alignment changes [54]. However, how the orientation induced by the circularly polarized X-ray pulse behaves is an open question.

Having at hand state-resolved calculations helps deepening our understanding of X-ray multiphoton ionization dynamics in atoms and completes it by information about the alignment dynamics of the electron cloud of the produced ions. A deeper understanding of X-ray multiphoton ionization dynamics is relevant for interpreting XFEL experiments, for optimizing XFEL beam parameters, and, in the end, for supporting applications of XFELs like single-particle imaging. Computational efficiency of the state-resolved calculations is a building block to a quantitative exploration of a wide variety of different atomic species and XFEL beam parameters.

Bibliography

[1] P. Emma, R. Akre, J. Arthur, R. Bionta, C. Bostedt, J. Bozek, A. Brachmann, P. Bucksbaum, R. Coffee, F.-J. Decker, et al., First lasing and operation of an ångstrom-wavelength free-electron laser, *Nat. Photon.* **4**, 641–647 (2010). doi:10.1038/nphoton.2010.176.

[2] T. Ishikawa, H. Aoyagi, T. Asaka, Y. Asano, N. Azumi, T. Bizen, H. Ego, K. Fukami, T. Fukui, Y. Furukawa, et al., A compact x-ray free-electron laser emitting in the sub-ångström region, *Nat. Photon.* **6**, 540–544 (2012). doi:10.1038/nphoton.2012.141.

[3] H.-S. Kang, C.-K. Min, H. Heo, C. Kim, H. Yang, G. Kim, I. Nam, S. Y. Baek, H.-J. Choi, G. Mun, et al., Hard x-ray free-electron laser with femtosecond-scale timing jitter, *Nat. Photon.* **11**, 708–713 (2017). doi:10.1038/s41566-017-0029-8.

[4] W. Decking, S. Abeghyan, P. Abramian, A. Abramsky, A. Aguirre, C. Albrecht, P. Alou, M. Altarelli, P. Altmann, K. Amyan, et al., A MHz-repetition-rate hard x-ray free-electron laser driven by a superconducting linear accelerator, *Nat. Photon.* **14**, 391–397 (2020). doi:10.1038/s41566-020-0607-z.

[5] E. Prat, R. Abela, M. Aiba, et al., A compact and cost-effective hard x-ray free-electron laser driven by a high-brightness and low-energy electron beam, *Nat. Photon.* **14**, 748–756 (2020). doi:10.1038/s41566-020-00712-8.

[6] J. C. H. Spence, XFELs for structure and dynamics in biology, *IUCrJ* **4**, 322–339 (2017). doi:10.1107/S2052252517005760.

[7] I. Schlichting and J. Miao, Emerging opportunities in structural biology with x-ray free-electron lasers, *Curr. Opin. Struct. Biol.* **22**, 613–626 (2012). doi:10.1016/j.sbi.2012.07.015.

[8] L. Fang, T. Osipov, B. F. Murphy, A. Rudenko, D. Rolles, V. S. Petrovic, C. Bostedt, J. D. Bozek, P. H. Bucksbaum, and N. Berrah, Probing ultrafast

electronic and molecular dynamics with free-electron lasers, *J. Phys. B: At. Mol. Opt. Phys.* **47**, 124006 (2014). doi:10.1088/0953-4075/47/12/124006.

[9] J. Ullrich, A. Rudenko, and R. Moshammer, Free-Electron Lasers: New Avenues in Molecular Physics and Photochemistry, *Annu. Rev. Phys. Chem.* **63**, 635–660 (2012). doi:10.1146/annurev-physchem-032511-143720.

[10] S. Pandey, R. Bean, T. Sato, I. Poudyal, J. Bielecki, J. C. Villarreal, O. Yefanov, V. Mariani, T. A. White, C. Kupitz, et al., Time-resolved serial femtosecond crystallography at the European XFEL, *Nat. Methods* **17**, 73–78 (2020). doi:10.1038/s41592-019-0628-z.

[11] C. Pellegrini, A. Marinelli, and S. Reiche, The physics of x-ray free-electron lasers, *Rev. Mod. Phys.* **88**, 015006 (2016). doi:10.1103/RevModPhys.88.015006.

[12] E. Sobolev, S. Zolotarev, K. Giewekemeyer, J. Bielecki, K. Okamoto, H. Reddy, J. Andreasson, K. Ayyer, I. Barák, S. Bari, et al., Megahertz single-particle imaging at the European XFEL, *Commun. Phys.* **3**, 97 (2020). doi:10.1038/s42005-020-0362-y.

[13] M. M. Seibert, T. Ekeberg, F. R. N. C. Maia, M. Svenda, J. Andreasson, O. Jönsson, D. Odić, B. Iwan, A. Rocker, D. Westphal, et al., Single mimivirus particles intercepted and imaged with an x-ray laser, *Nature (London)* **470**, 78–81 (2011). doi:10.1038/nature09748.

[14] H. N. Chapman, P. Fromme, A. Barty, T. A. White, R. A. Kirian, A. Aquila, M. S. Hunter, J. Schulz, D. P. DePonte, U. Weierstall, et al., Femtosecond x-ray protein nanocrystallography, *Nature (London)* **470**, 73–77 (2011). doi:10.1038/nature09750.

[15] J. Coe and P. Fromme, Serial femtosecond crystallography opens new avenues for structural biology, *Protein Pept Lett.* **23**, 255–272 (2016). doi:10.2174/0929866523666160120152937.

[16] D. Assalauova, Y. Y. Kim, S. Bobkov, R. Khubbutdinov, M. Rose, R. Alvarez, J. Andreasson, E. Balaur, A. Contreras, H. DeMirci, et al., An advanced workflow for single-particle imaging with the limited data at an x-ray free-electron laser, *IUCrJ* **7**, 1102–1113 (2020). doi:10.1107/S2052252520012798.

[17] A. Hosseinizadeh, G. Mashayekhi, J. Copperman, P. Schwander, A. Dashti, R. Sepehr, R. Fung, M. Schmidt, C. H. Yoon, B. Hogue, et al., Conformational

landscape of a virus by single-particle X-ray scattering, *Nat. Methods* **14**, 877–881 (2017). doi:10.1038/nmeth.4395.

[18] U. Lorenz, N. M. Kabachnik, E. Weckert, and I. A. Vartanyants, Impact of ultrafast electronic damage in single-particle x-ray imaging experiments, *Phys. Rev. E* **86**, 051911 (2012). doi:10.1103/PhysRevE.86.051911.

[19] H. M. Quiney and K. A. Nugent, Biomolecular imaging and electronic damage using x-ray free-electron lasers, *Nat. Phys.* **7**, 142–146 (2011). doi:10.1038/nphys1859.

[20] S.-K. Son, L. Young, and R. Santra, Impact of hollow-atom formation on coherent x-ray scattering at high intensity, *Phys. Rev. A* **83**, 033402 (2011). doi:10.1103/PhysRevA.83.033402.

[21] K. Nass, Radiation damage in protein crystallography at x-ray free-electron lasers, *Acta Cryst. D* **75**, 211–218 (2019). doi:10.1107/S2059798319000317.

[22] R. Neutze, R. Wouts, D. van der Spoel, E. Weckert, and J. Hajdu, Potential for biomolecular imaging with femtosecond x-ray pulses, *Nature (London)* **406**, 752–757 (2000). doi:10.1038/35021099.

[23] B. Ziaja, H. N. Chapman, R. Faustlin, S. Hau-Riege, Z. Jurek, A. V. Martin, S. Toleikis, F. Wang, E. Weckert, and R. Santra, Limitations of coherent diffractive imaging of single objects due to their damage by intense x-ray radiation, *New J. Phys.* **14**, 115015 (2012). doi:10.1088/1367-2630/14/11/115015.

[24] R. Santra and L. Young, Interaction of intense x-ray beams with atoms, in *Synchrotron Light Sources and Free-Electron Lasers*, edited by E. J. Jaeschke, S. Khan, J. R. Schneider, and J. B. Hastings (Springer International Publishing, Switzerland, 2016), pp. 1233–1260.

[25] L. Young, E. P. Kanter, B. Krässig, Y. Li, A. M. March, S. T. Pratt, R. Santra, S. H. Southworth, N. Rohringer, L. F. DiMauro, et al., Femtosecond electronic response of atoms to ultra-intense x-rays, *Nature (London)* **466**, 56–61 (2010). doi:10.1038/nature09177.

[26] S.-K. Son and R. Santra, Monte Carlo calculation of ion, electron, and photon spectra of xenon atoms in x-ray free-electron laser pulses, *Phys. Rev. A* **85**, 063415 (2012). doi:10.1103/PhysRevA.85.063415.

[27] B. Rudek, K. Toyota, L. Foucar, B. Erk, R. Boll, C. Bomme, J. Correa, S. Carron, S. Boutet, G. J. Williams, et al., Relativistic and resonant effects in the ionization of heavy atoms by ultra-intense hard x-rays, *Nat. Commun.* **9**, 4200 (2018). doi:10.1038/s41467-018-06745-6.

[28] B. Rudek, S.-K. Son, L. Foucar, S. W. Epp, B. Erk, R. Hartmann, M. Adolph, R. Andritschke, A. Aquila, N. Berrah, et al., Ultra-efficient ionization of heavy atoms by intense x-ray free-electron laser pulses, *Nat. Photon.* **6**, 858–865 (2012). doi:10.1038/nphoton.2012.261.

[29] H. Fukuzawa, S.-K. Son, K. Motomura, S. Mondal, K. Nagaya, S. Wada, X.-J. Liu, R. Feifel, T. Tachibana, Y. Ito, et al., Deep inner-shell multiphoton ionization by intense x-ray free-electron laser pulses, *Phys. Rev. Lett.* **110**, 173005 (2013). doi:10.1103/PhysRevLett.110.173005.

[30] K. Motomura, H. Fukuzawa, S.-K. Son, S. Mondal, T. Tachibana, Y. Ito, M. Kimura, K. Nagaya, T. Sakai, K. Matsunami, et al., Sequential multiphoton multiple ionization of atomic argon and xenon irradiated by x-ray free-electron laser pulses from SACLA, *J. Phys. B: At. Mol. Opt. Phys.* **46**, 164024 (2013). doi:10.1088/0953-4075/46/16/164024.

[31] N. Rohringer and R. Santra, X-ray nonlinear optical processes using a self-amplified spontaneous emission free-electron laser, *Phys. Rev. A* **76**, 033416 (2007). doi:10.1103/PhysRevA.76.033461.

[32] M. G. Makris, P. Lambropoulos, and A. Mihelič, Theory of multiphoton multielectron ionization of xenon under strong 93-eV radiation, *Phys. Rev. Lett.* **102**, 033002 (2009). doi:10.1103/PhysRevLett.102.033002.

[33] B. Rudek, D. Rolles, S.-K. Son, L. Foucar, B. Erk, S. Epp, R. Boll, D. Anielski, C. Bostedt, S. Schorb, et al., Resonance-enhanced multiple ionization of krypton at an x-ray free-electron laser, *Phys. Rev. A* **87**, 023413 (2013). doi:10.1103/PhysRevA.87.023413.

[34] G. Doumy, C. Roedig, S.-K. Son, C. I. Blaga, A. D. DiChiara, R. Santra, N. Berrah, C. Bostedt, J. D. Bozek, P. H. Bucksbaum, et al., Nonlinear atomic response to intense ultrashort x rays, *Phys. Rev. Lett.* **106**, 083002 (2011). doi:10.1103/PhysRevLett.106.083002.

[35] W. Xiang, C. Gao, Y. Fu, J. Zeng, and J. Yuan, Inner-shell resonant absorption effects on evolution dynamics of the charge state distribution in a neon atom

interacting with ultraintense x-ray pulses, *Phys. Rev. A* **86**, 061401(R) (2012). doi:10.1103/PhysRevA.86.061401.

[36] N. Berrah, A. Sanchez-Gonzalez, Z. Jurek, R. Obaid, H. Xiong, R. J. Squibb, T. Osipov, A. Lutman, L. Fang, T. Barillot, et al., Femtosecond-resolved observation of the fragmentation of buckminsterfullerene following x-ray multiphoton ionization, *Nat. Phys.* **15**, 1279–1283 (2019). doi:10.1038/s41567-019-0665-7.

[37] A. Rudenko, L. Inhester, K. Hanasaki, X. Li, S. J. Robatjazi, B. Erk, R. Boll, K. Toyota, Y. Hao, O. Vendrell, et al., Femtosecond response of polyatomic molecules to ultra-intense hard x-rays, *Nature (London)* **546**, 129–132 (2017). doi:10.1038/nature22373.

[38] B. F. Murphy, T. Osipov, Z. Jurek, L. Fang, S.-K. Son, M. Mucke, J. H. D. Eland, V. Zhaunerchyk, R. Feifel, L. Avaldi, et al., Femtosecond x-ray-induced explosion of C_{60} at extreme intensity, *Nat. Commun.* **5**, 4281 (2014). doi:10.1038/ncomms5281.

[39] M. Hoener, L. Fang, O. Kornilov, O. Gessner, S. T. Pratt, M. Gühr, E. P. Kanter, C. Blaga, C. Bostedt, J. D. Bozek, et al., Ultraintense x-ray induced ionization, dissociation, and frustrated absorption in molecular nitrogen, *Phys. Rev. Lett.* **104**, 253002 (2010). doi:10.1103/PhysRevLett.104.253002.

[40] K. Toyota, S.-K. Son, and R. Santra, Interplay between relativistic energy corrections and resonant excitations in x-ray multiphoton ionization dynamics of Xe atoms, *Phys. Rev. A* **95**, 043412 (2017). doi:10.1103/PhysRevA.95.043412.

[41] S.-K. Son, R. Boll, and R. Santra, Breakdown of frustrated absorption in x-ray sequential multiphoton ionization, *Phys. Rev. Research* **2**, 023053 (2020). doi:10.1103/PhysRevResearch.2.023053.

[42] A. Rörig, S.-K. Son, T. Mazza, P. Schmidt, T. M. Baumann, B. Erk, M. Ilchen, J. Laksman, V. Music, S. Pathak, et al., Multiple-core-hole resonance spectroscopy with ultraintense x-ray pulses, *Nat. Commun.* **14**, 5738 (2023). doi:10.1038/s41467-023-41505-1.

[43] P. J. Ho, E. P. Kanter, and L. Young, Resonance-mediated atomic ionization dynamics induced by ultraintense x-ray pulses, *Phys. Rev. A* **92**, 063430 (2015). doi:10.1103/PhysRevA.92.063430.

[44] P. J. Ho, C. Bostedt, S. Schorb, and L. Young, Theoretical tracking of resonance-enhanced multiple ionization pathways in x-ray free-electron laser pulses, *Phys. Rev. Lett.* **113**, 253001 (2014). doi:10.1103/PhysRevLett.113.253001.

[45] O. Ciricosta, H.-K. Chung, R. W. Lee, and J. S. Wark, Simulations of neon irradiated by intense x-ray laser radiation, *High Energy Density Phys.* **7**, 111–116 (2011). doi:10.1016/j.hedp.2011.02.003.

[46] C. Buth, J.-C. Liu, M. H. Chen, J. P. Cryan, L. Fang, J. M. Glownia, M. Hoener, R. N. Coffee, and N. Berrah, Ultrafast absorption of intense x rays by nitrogen molecules, *J. Chem. Phys.* **136**, 214310 (2012). doi:10.1063/1.4722756.

[47] J.-C. Liu, N. Berrah, L. S. Cederbaum, J. P. Cryan, J. M. Glownia, K. J. Schafer, and C. Buth, Rate equations for nitrogen molecules in ultrashort and intense x-ray pulses, *J. Phys. B: At. Mol. Opt. Phys.* **49**, 075602 (2016). doi:10.1088/0953-4075/49/7/075602.

[48] C. Bostedt, J. D. Bozek, P. H. Bucksbaum, R. N. Coffee, J. B. Hastings, Z. Huang, R. W. Lee, S. Schorb, J. N. Corlett, P. Denes, et al., Ultra-fast and ultra-intense x-ray sciences: first results from the Linac Coherent Light Source free-electron laser, *J. Phys. B: At. Mol. Opt. Phys.* **46**, 164003 (2013). doi:10.1088/0953-4075/46/16/164003.

[49] C. Buth, R. Beerwerth, R. Obaid, N. Berrah, L. S. Cederbaum, and S. Fritzsche, Neon in ultrashort and intense x-rays from free electron lasers, *J. Phys. B: At. Mol. Opt. Phys.* **51**, 055602 (2018). doi:10.1088/1361-6455/aaa39a.

[50] A. Sytcheva, S. Papst, S.-K. Son, and R. Santra, Enhanced nonlinear response of Ne^{8+} to intense ultrafast x rays, *Phys. Rev. A* **85**, 023414 (2012). doi:10.1103/PhysRevA.95.023414.

[51] J. M. Schäfer, L. Inhester, S.-K. Son, R. F. Fink, and R. Santra, Electron and fluorescence spectra of a water molecule irradiated by an x-ray free-electron laser pulse, *Phys. Rev. A* **97**, 053415 (2018). doi:10.1103/PhysRevA.97.053415.

[52] T. Mazza, M. Ilchen, M. D. Kiselev, E. V. Gryzlova, T. M. Baumann, R. Boll, A. De Fanis, P. Grychtol, J. Montaño, V. Music, et al., Mapping resonance structures in transient core-ionized atoms, *Phys. Rev. X* **10**, 041056 (2020). doi:10.1103/PhysRevX.10.041056.

[53] C. H. Greene and R. N. Zare, Photofragment Alignment and Orientation, *Ann. Rev. Phys. Chem.* **33**, 119–150 (1982). doi:10.1146/annurev.pc.33.100182.001003.

[54] U. Kleiman and B. Lohmann, Photoionization of closed-shell atoms: Hartree–fock calculations of orientation and alignment, *J. Electron Spectrosc. Relat. Phenom.* **131-132**, 29–50 (2003). doi:10.1016/S0368-2048(03)00034-3.

[55] C. D. Caldwell and R. N. Zare, Alignment of cd atoms by photoionization, *Phys. Rev. A* **16**, 255–262 (1977). doi:10.1103/PhysRevA.16.255.

[56] S. H. Southworth, P. H. Kobrin, C. M. Truesdale, D. Lindle, S. Owaki, and D. A. Shirley, Photoelectron and auger electron asymmetries: Alignment of $Xe^{+2}D_{\frac{5}{2}}$ by photoionization, *Phys. Rev. A* **24**, 2257–2260 (1981). doi:10.1103/PhysRevA.24.2257.

[57] H. Küst, U. Kleiman, and W. Mehlhorn, Alignment after Xe L_3 photoionization by synchrotron radiation, *J. Phys. B: At. Mol. Opt. Phys.* **36**, 2073 (2003). doi:10.1088/0953-4075/36/10/315.

[58] U. Becker, Complete photoionisation experiments, *J. Electron Spectrosc. Relat. Phenom.* **96**, 105–115 (1998). doi:10.1016/S0368-2048(98)00226-6.

[59] V. Schmidt, Photoionization of atoms using synchrotron radiation, *Rep. Prog. Phys.* **55**, 1483–1659 (1992). doi:10.1088/0034-4885/55/9/003.

[60] S. Flügge, W. Mehlhorn, and V. Schmidt, Angular distribution of auger electrons following photoionization, *Phys. Rev. Lett.* **29**, 7–9 (1972). doi:10.1103/PhysRevLett.29.7.

[61] K. Blum, Density matrices, state multipoles, and their physical interpretation, in *Fundamental Processes in Atomic Collision Physics*, edited by H. Kleinpoppen, J. S. Briggs, and H. O. Lutz (Springer US, Boston, MA, 1985), pp. 103–132.

[62] L. Young, D. A. Arms, E. M. Dufresne, R. W. Dunford, D. L. Ederer, C. Höhr, E. P. Kanter, B. Krässig, E. C. Landahl, E. R. Peterson, et al., X-ray microprobe of orbital alignment in strong-field ionized atoms, *Phys. Rev. Lett.* **97**, 083601 (2006). doi:10.1103/PhysRevLett.97.083601.

[63] R. Santra, R. W. Dunford, E. P. Kanter, B. Krässig, S. H. Southworth, and L. Young, Strong-field control of x-ray processes, in *Advances in Atomic,*

Molecular, and Optical Physics, edited by E. Arimondo, P. R. Berman, and C. C. Lin (Academic Press, Amsterdam, 2008), pp. 219–257.

[64] E. Heinrich-Josties, S. Pabst, and R. Santra, Controlling the $2p$ hole alignment in neon via the $2s$-$3p$ fano resonance, *Phys. Rev. A* **89**, 043415 (2014). doi:10.1103/PhysRevA.89.043415.

[65] E. V. Gryzlova, A. N. Grum-Grzhimailo, M. D. Kiselev, and M. M. Popova, Evolution of the ionic polarization in multiple sequential ionization: general equations and an illustrative example, *Phys. Rev. A* **107**, 013111 (2023). doi:10.1103/PhysRevA.107.013111.

[66] A. N. Grum-Grzhimailo, E. V. Gryzlova, S. Fritzsche, and N. M. Kabachnik, Photoelectron angular distributions and correlations in sequential double and triple atomic ionization by free electron lasers, *J. Mod. Opt.* **63**, 334–357 (2016). doi:10.1080/09500340.2015.1047805.

[67] A. Rouzée, P. Johnsson, E. V. Gryzlova, H. Fukuzawa, A. Yamada, W. Siu, Y. Huismans, E. Louis, F. Bijkerk, D. M. P. Holland, et al., Angle-resolved photoelectron spectroscopy of sequential three-photon triple ionization of neon at 90.5 eV photon energy, *Phys. Rev. A* **83**, 031401 (2011). doi:10.1103/PhysRevA.83.031401.

[68] S. Mondal, R. Ma, K. Motomura, H. Fukuzawa, A. Yamada, K. Nagaya, S. Yase, Y. Mizoguchi, M. Yao, A. Rouzée, et al., Photoelectron angular distributions for the two-photon sequential double ionization of xenon by ultrashort extreme ultraviolet free electron laser pulses, *J. Phys. B: At. Mol. Opt. Phys.* **46**, 164022 (2013). doi:10.1088/0953-4075/46/16/164022.

[69] M. Braune, G. Hartmann, M. Ilchen, A. Knie, T. Lischke, A. Reinköster, A. Meissner, S. Deinert, L. Glaser, O. Al-Dossary, et al., Electron angular distributions of noble gases in sequential two-photon double ionization, *J. Mod. Opt.* **63**, 324–333 (2016). doi:10.1080/09500340.2015.1047422.

[70] M. Ilchen, G. Hartmann, E. V. Gryzlova, A. Achner, E. Allaria, A. Beckmann, M. Braune, J. Buck, C. Callegari, R. N. Coffee, et al., Symmetry breakdown of electron emission in extreme ultraviolet photoionization of argon, *Nat. Commun.* **9**, 4659 (2018). doi:10.1038/s41467-018-07152-7.

[71] J. Cooper and R. N. Zare, Angular distribution of photoelectrons, *J. Chem. Phys.* **48**, 942–943 (1968). doi:10.1063/1.1668742.

[72] S. T. Manson and J. W. Cooper, Angular distribution of photoelectrons: Outer shells of noble gases, *Phys. Rev. A* **2**, 2170–2171 (1970). doi:10.1103/PhysRevA.2.2170.

[73] V. T. Davis, *Introduction to Photoelectron Angular distributions* (Springer, Switzerland, 2022).

[74] E. G. Berezhko, N. M. Kabachnik, and V. S. Rostovsky, Potential-barrier effects in inner-shell photoionisation and their influence on the anisotropy of x-rays and auger electrons, *J. Phys. B: At. Mol. Opt. Phys.* **11**, 1749 (1978). doi:10.1088/0022-3700/11/10/012.

[75] B. Cleff and W. Mehlhorn, On the angular distribution of auger electrons, *Phys. Lett. A* **37**, 3–4 (1971). doi:10.1016/0375-9601(71)90303-3.

[76] B. Cleff and W. Mehlhorn, Angular distribution of $L_3M_{2,3}M_{2,3}(^1S_0)$ auger electrons of argon, *J. Phys. B: At. Mol. Opt. Phys.* **7**, 605 (1974). doi:10.1088/0022-3700/7/5/010.

[77] E. G. Berezhko and N. M. Kabachnik, Theoretical study of inner-shell alignment of atoms in electron impact ionisation: angular distribution and polarisation of x-rays and auger electrons, *J. Phys. B: At. Mol. Opt. Phys.* **10**, 2467 (1977). doi:10.1088/0022-3700/10/12/025.

[78] H. Schmoranzer, S. Lauer, F. Vollweiler, A. Ehresmann, V. L. Sukhorukov, B. M. Lagutin, I. D. Petrov, P. V. Demekhin, K.-H. Schartner, B. Magel, et al., Angular distribution of the fluorescence radiation of Kr II satellite states, *J. Phys. B: At. Mol. Opt. Phys.* **30**, 4463 (1997). doi:10.1088/0953-4075/30/20/010.

[79] J. Hrdý, A. Henins, and J. A. Bearden, Polarization of the L_{α_1} x rays of mercury, *Phys. Rev. A* **2**, 1708–1711 (1970). doi:10.1103/PhysRevA.2.1708.

[80] W. Kronast, R. Huster, and W. Mehlhorn, Alignment of atoms following photoionisation, *Z. Phys. D* **2**, 285–296 (1986). doi:10.1007/BF01426233.

[81] S. Al Moussalami, J. M. Bizau, B. Rouvellou, D. Cubaynes, L. Journel, F. J. Wuilleumier, J. Obert, J. C. Putaux, T. J. Morgan, and M. Richter, First angle-resolved photoelectron measurements following inner-shell resonant excitation in a singly charged ion, *Phys. Rev. Lett.* **76**, 4496–4499 (1996). doi:10.1103/PhysRevLett.76.4496.

[82] B. Rouvellou, J. M. Bizau, J. Obert, S. Al Moussalami, N. Berland, C. Blancard, E. Bouisset, D. Cubaynes, S. Diehl, L. Journel, et al., Photoelectron spectroscopy experiments on singly charged positive-ions using synchrotron radiation, *Nucl. Instrum. Methods Phys. Res. Sec. B: Beam Interactions with Materials and Atoms* **134**, 287–303 (1998). doi:10.1016/S0168-583X(98)00561-8.

[83] I. Goodfellow, Y. Bengio, and A. Courville, *Deep Learning* (MIT Press, Cambridge, England, 2016).

[84] P. P. Shinde and S. Shah, A review of machine learning and deep learning applications, in *2018 Fourth International Conference on Computing Communication Control and Automation (ICCUBEA)* (IEEE, India, 2018), pp. 1–6.

[85] S. Tufail, H. Riggs, M. Tariq, and A. I. Sarwat, Advancements and challenges in machine learning: A comprehensive review of models, libraries, applications, and algorithms, *Electronics* **12**, 1789 (2023). doi:10.3390/electronics12081789.

[86] G. N. Yannakakis, M. Maragoudakis, and J. Hallam, Preference learning for cognitive modeling: A case study on entertainment preferences, *IEEE Trans. Syst. Man. Cybern. A* **39**, 1165–1175 (2009). doi:10.1109/TSMCA.2009.2028152.

[87] T. M. Rausch, N. D. Derra, and L. Wolf, Predicting online shopping cart abandonment with machine learning approaches, *Int. J. Mark. Res.* **64**, 89–112 (2020). doi:10.1177/1470785320972526.

[88] D. Koggalahewa, Y. Xu, and E. Foo, An unsupervised method for social network spammer detection based on user information interests, *J. Big Data* **9**, 7 (2022). doi:10.1186/s40537-021-00552-5.

[89] R. Ganguli, A. Mehta, and S. Sen, A survey on machine learning methodologies in social network analysis, in *2020 8th International Conference on Reliability, Infocom Technologies and Optimization (Trends and Future Directions)* (IEEE, India, 2020), pp. 484–489.

[90] H. Wang, Z. Lei, X. Zhang, B. Zhou, and J. Peng, A review of deep learning for renewable energy forecasting, *Energy Convers. Manag.* **198**, 111799 (2019). doi:10.1016/j.enconman.2019.111799.

[91] M. Tan, S. Yuan, S. Li, Y. Su, H. Li, and F. He, Ultra-short-term industrial power demand forecasting using lstm based hybrid ensemble learning, *IEEE Trans. Power Syst.* **35**, 2937–2948 (2020). doi:10.1109/TPWRS.2019.2963109.

[92] A. Gupta, A. Anpalagan, L. Guan, and A. S. Khwaja, Deep learning for object detection and scene perception in self-driving cars: Survey, challenges, and open issues, *Array* **10**, 100057 (2021). doi:10.1016/j.array.2021.100057.

[93] M. Bertolini, D. Mezzogori, M. Neroni, and F. Zammori, Machine learning for industrial applications: A comprehensive literature review, *Expert Syst. Appl.* **175**, 114820 (2021). doi:10.1016/j.eswa.2021.114820.

[94] K. Shailaja, B. Seetharamulu, and M. A. Jabbar, Machine learning in healthcare: A review, in *2018 Second International Conference on Electronics, Communication and Aerospace Technology (ICECA)* (IEEE, India, 2018), pp. 910–914.

[95] Y. Shi, D. Reker, J. D. Byrne, A. R. Kirtane, K. Hess, Z. Wang, N. Navamajiti, C. C. Young, Z. Fralish, Z. Zhang, et al., Screening oral drugs for their interactions with the intestinal transportome via porcine tissue explants and machine learning, *Nat. Biomed. Eng.* **8**, 278–290 (2024). doi:10.1038/s41551-023-01128-9.

[96] S. Azizi, L. Culp, J. Freyberg, B. Mustafa, S. Baur, S. Kornblith, T. Chen, N. Tomasev, J. Mitrović, P. Strachan, et al., Robust and data-efficient generalization of self-supervised machine learning for diagnostic imaging, *Nat. Biomed. Eng.* **7**, 756–779 (2023). doi:10.1038/s41551-023-01049-7.

[97] A. L. Beam and I. S. Kohane, Big Data and Machine Learning in Health Care, *JAMA* **319**, 1317–1318 (2018). doi:10.1001/jama.2017.18391.

[98] M. Frid-Adar, I. Diamant, E. Klang, M. Amitai, J. Goldberger, and H. Greenspan, Gan-based synthetic medical image augmentation for increased cnn performance in liver lesion classification, *Neurocomputing* **321**, 321–331 (2018). doi:10.1016/j.neucom.2018.09.013.

[99] C. Réda, E. Kaufmann, and A. Delahaye-Duriez, Machine learning applications in drug development, *Comput. Struct. Biotechnol. J.* **18**, 241–252 (2020). doi:10.1016/j.csbj.2019.12.006.

[100] A. Krizhevsky, I. Sutskever, and G. E. Hinton, ImageNet classification with deep convolutional neural networks, in *Advances in Neural Information Pro-*

cessing Systems, edited by F. Pereira, C. Burges, L. Bottou, and K. Weinberger (Curran Associates, Inc., 2012).

[101] A. Krizhevsky and G. Hinton, Learning multiple layers of features from tiny images (Technical report, University of Toronto, Toronto, Ontario, 2009).

[102] G. Hinton, L. Deng, D. Yu, G. E. Dahl, A.-r. Mohamed, N. Jaitly, A. Senior, V. Vanhoucke, P. Nguyen, T. N. Sainath, et al., Deep neural networks for acoustic modeling in speech recognition: The shared views of four research groups, *IEEE Signal Process. Mag.* **29**, 82–97 (2012). doi:10.1109/MSP.2012.2205597.

[103] G. E. Dahl, D. Yu, L. Deng, and A. Acero, Context-dependent pre-trained deep neural networks for large-vocabulary speech recognition, *IEEE Transactions on Audio, Speech, and Language Processing* **20**, 30–42 (2012). doi:10.1109/TASL.2011.2134090.

[104] T. Schomacker and M. Tropmann-Frick, Language representation models: An overview, *Entropy* **23**, 1422 (2021). doi:10.3390/e23111422.

[105] Y. Goldberg, A primer on neural network models for natural language processing, *J. Artif. Intell. Res.* **57**, 345–420 (2016). doi:10.1613/jair.4992.

[106] G. Carleo, I. Cirac, K. Cranmer, L. Daudet, M. Schuld, N. Tishby, L. Vogt-Maranto, and L. Zdeborová, Machine learning and the physical sciences, *Rev. Mod. Phys.* **91**, 045002 (2019). doi:10.1103/RevModPhys.91.045002.

[107] A. Karthikeyan and U. D. Priyakumar, Artificial intelligence: machine learning for chemical sciences, *J. Chem. Sci.* **134**, 2 (2021). doi:10.1007/s12039-021-01995-2.

[108] O. A. von Lilienfeld and K. Burke, Retrospective on a decade of machine learning for chemical discovery, *Nat. Commun.* **11**, 4895 (2020). doi:10.1038/s41467-020-18556-9.

[109] J. Jumper, R. Evans, A. Pritzel, T. Green, M. Figurnov, O. Ronneberger, K. Tunyasuvunakool, R. Bates, A. Žídek, A. Potapenko, et al., Highly accurate protein structure prediction with AlphaFold, *Nature (London)* **596**, 583–589 (2021). doi:10.1038/s41586-021-03819-2.

[110] C. D. Rankine, M. M. M. Madkhali, and T. J. Penfold, A deep neural network for the rapid prediction of x-ray absorption spectra., *J. Phys. Chem. A* **124**, 4263–4270 (2020). doi:10.1021/acs.jpca.0c03723.

[111] M. R. Carbone, M. Topsakal, D. Lu, and S. Yoo, Machine-learning x-ray absorption spectra to quantitative accuracy, *Phys. Rev. Lett.* **124**, 156401 (2020). doi:10.1103/PhysRevLett.124.156401.

[112] D. Golze, M. Hirvensalo, P. Hernández-León, A. Aarva, J. Etula, T. Susi, P. Rinke, T. Laurila, and M. A. Caro, Accurate computational prediction of core-electron binding energies in carbon-based materials: A machine-learning model combining density-functional theory and GW, *Chem. Mater.* **34**, 6240–6254 (2022). doi:10.1021/acs.chemmater.1c04279.

[113] K. Ghosh, A. Stuke, M. Todorović, P. B. Jørgensen, M. N. Schmidt, A. Vehtari, and P. Rinke, Deep learning spectroscopy: Neural networks for molecular excitation spectra, *Adv. Sci.* **6**, 1801367 (2019). doi:10.1002/advs.201801367.

[114] J. Carrasquilla and R. G. Melko, Machine learning phases of matter, *Nat. Phys.* **13**, 431–434 (2017). doi:10.1038/nphys4035.

[115] A. Sanchez-Gonzalez, P. Micaelli, C. Olivier, T. R. Barillot, M. Ilchen, A. A. Lutman, A. Marinelli, T. Maxwell, A. Achner, M. Agåker, et al., Accurate prediction of x-ray pulse properties from a free-electron laser using machine learning, *Nat. Commun.* **8**, 15461 (2017). doi:10.1038/ncomms15461.

[116] O. Geffert, D. Kolbasova, A. Trabattoni, F. Calegari, and R. Santra, In situ characterization of few-femtosecond laser pulses by learning from first-principles calculations, *Opt. Lett.* **47**, 3992–3995 (2022). doi:10.1364/OL.460513.

[117] D. Kolbasova and R. Santra, Laser-pulse characterization using strong-field autocorrelation patterns and random-forest-based machine learning, *Phys. Rev. A* **107**, 013520 (2023). doi:10.1103/PhysRevA.107.013520.

[118] N. Breckwoldt, S.-K. Son, T. Mazza, A. Rörig, R. Boll, M. Meyer, A. C. LaForge, D. Mishra, N. Berrah, and R. Santra, Machine-learning calibration of intense x-ray free-electron-laser pulses using bayesian optimization, *Phys. Rev. Research* **5**, 023114 (2023). doi:10.1103/PhysRevResearch.5.023114.

[119] G. Montavon, M. Rupp, V. Gobre, A. Vazquez-Mayagoitia, K. Hansen, A. Tkatchenko, K.-R. Müller, and O. A. von Lilienfeld, Machine learning of molecular electronic properties in chemical compound space, *New J. Phys.* **15**, 095003 (2013). doi:10.1088/1367-2630/15/9/095003.

[120] J. Westermayr, M. Gastegger, K. T. Schütt, and R. J. Maurer, Perspective on integrating machine learning into computational chemistry and materials science, *J. Chem. Phys.* **154**, 230903 (2021). doi:10.1063/5.0047760.

[121] O. A. von Lilienfeld, K.-R. Müller, and A. Tkatchenko, Exploring chemical compound space with quantum-based machine learning, *Nat. Rev. Chem.* **4**, 347–358 (2020). doi:10.1038/s41570-020-0189-9.

[122] L. Fiedler, N. A. Modine, S. Schmerler, D. J. Vogel, G. A. Popoola, A. P. Thompson, S. Rajamanickam, and A. Cangi, Predicting electronic structures at any length scale with machine learning, *npj Comput. Mater.* **9**, 115 (2023). doi:10.1038/s41524-023-01070-z.

[123] L. Fiedler, K. Shah, M. Bussmann, and A. Cangi, Deep dive into machine learning density functional theory for materials science and chemistry, *Phys. Rev. Mater.* **6**, 040301 (2022). doi:10.1103/PhysRevMaterials.6.040301.

[124] A. Stuke, M. Todorović, M. Rupp, C. Kunkel, K. Ghosh, L. Himanen, and P. Rinke, Chemical diversity in molecular orbital energy predictions with kernel ridge regression., *J. Chem. Phys.* **150**, 204121 (2019). doi:10.1063/1.5086105.

[125] T. B. Blank, S. D. Brown, A. W. Calhoun, and D. J. Doren, Neural network models of potential energy surfaces, *J. Chem. Phys.* **103**, 4129–4137 (1995). doi:10.1063/1.469597.

[126] J. Behler and M. Parrinello, Generalized neural-network representation of high-dimensional potential-energy surfaces, *Phys. Rev. Lett.* **98**, 146401 (2007). doi:10.1103/PhysRevLett.98.146401.

[127] O. T. Unke, D. Koner, S. Patra, S. Käser, and M. Meuwly, High-dimensional potential energy surfaces for molecular simulations: from empiricism to machine learning, *Mach. learn.: sci. technol.* **1** (2019).

[128] G. Schmitz, I. H. Godtliebsen, and O. Christiansen, Machine learning for potential energy surfaces: An extensive database and assessment of methods., *J. Chem. Phys.* **150 24**, 244113 (2019). doi:10.1063/1.5100141.

[129] A. M. Tokita and J. Behler, How to train a neural network potential, *J. Chem. Phys.* **159**, 121501 (2023). doi:10.1063/5.0160326.

[130] J. P. Coe, Machine learning configuration interaction, *J. Chem. Theory Comput.* **14**, 5739–5749 (2018). doi:10.1021/acs.jctc.8b00849.

[131] P. Bilous, A. Pálffy, and F. Marquardt, Deep-learning approach for the atomic configuration interaction problem on large basis sets, *Phys. Rev. Lett.* **131**, 133002 (2023). doi:10.1103/PhysRevLett.131.133002.

[132] Z. Jurek, S.-K. Son, B. Ziaja, and R. Santra, XMDYN and XATOM: Versatile simulation tools for quantitative modeling of X-ray free-electron laser induced dynamics of matter, *J. Appl. Cryst.* **49**, 1048–1056 (2016). doi:10.1107/S1600576716006014.

[133] J. C. Slater, A Simplification of the Hartree-Fock Method, *Phys. Rev.* **81**, 385–390 (1951). doi:10.1103/PhysRev.81.385.

[134] C. Froese Fischer, The MCHF atomic-structure package, *Comput. Phys. Commun.* **64**, 369–398 (1991). doi:10.1016/0010-4655(91)90133-6.

[135] R. D. Deslattes, E. G. Kessler, P. Indelicato, L. de Billy, E. Lindroth, and J. Anton, X-ray transition energies: new approach to a comprehensive evaluation, *Rev. Mod. Phys.* **75**, 35–99 (2003). doi:10.1103/RevModPhys.75.35.

[136] L. Budewig, Master's thesis, Universität Hamburg (July 2021).

[137] R. Santra, Many-electron problem, [unpublished lecture notes].

[138] R. Santra, Concepts in x-ray physics, *J. Phys. B: At. Mol. Opt. Phys.* **42**, 023001 (2009). doi:10.1088/0953-4075/42/2/023001.

[139] M. Born and R. Oppenheimer, Zur Quantentheorie der Molekeln, *Ann. Phys.* **389**, 457–484 (1927). doi:10.1002/andp.19273892002.

[140] D. J. Griffiths, *Introduction to Quantum Mechanics; second edition* (Cambridge Univ. Press, Cambridge, 2017).

[141] K. Gottfried and T. Yan, *Quantum Mechanics: Fundamentals* (Springer, New York, 2003).

[142] J. J. Sakurai and J. J. Napolitano, *Modern Quantum Mechanics: Pearson New International Edition* (Pearson Education Limited, Harlow, 2014).

[143] A. Thomson, D. Attwood, E. Gullikson, M. Howells, K.-J. Kim, J. Kirz, J. Kortright, I. Lindau, Y. Liu, P. Pianetta, et al., *X-Ray Data Booklet* (Center for X-Ray Optics and Advanced Light Source, Lawrence Berkeley National Laboratory, Berkeley, CA, 2009), [Online; accessed June 20, 2020], https://xdb.lbl.gov/.

[144] J. Als-Nielsen and D. McMorrow, *Elements of Modern X-ray Physics* (John Wiley and Sons, Ltd, New York, 2011).

[145] A. L. Fetter and J. D. Walecka, *Quantum Theory of Many-Particle Systems* (McGraw-Hill Book Company, New York, 1971).

[146] G. Drake, *Springer Handbook of Atomic, Molecular, and Optical Physics*, Springer Handbooks (Springer, New York, 2007).

[147] D. Craig and T. Thirunamachandran, *Molecular Quantum Electrodynamics* (Dover Publications, New York, 2012).

[148] F. Bechstedt, *Many-Body Approach to Electronic Exitations* (Springer, Berlin Heidelberg, 2015).

[149] I. V. Hertel and K. P. Schulz, *Atoms, Molecules and Optical Physics 1* (Springer, Berlin Heidelberg, 2015).

[150] R. Karazija, *Introduction to the Theory of X-Ray and Electronic Spectra of Free Atoms* (Springer, New York, 1996).

[151] S.-K. Son, O. Geffert, and R. Santra, Compton spectra of atoms at high x-ray intensity, *J. Phys. B: At. Mol. Opt. Phys.* **50**, 064003 (2017). doi:10.1088/1361-6455/aa59cb.

[152] J. M. Slowik, S.-K. Son, G. Dixit, Z. Jurek, and R. Santra, Incoherent x-ray scattering in single molecule imaging, *New J. Phys.* **16**, 073042 (2014). doi:10.1088/1367-2630/16/7/073042.

[153] S.-K. Son, H. N. Chapman, and R. Santra, Multiwavelength anomalous diffraction at high x-ray intensity, *Phys. Rev. Lett.* **107**, 218102 (2011). doi:10.1103/PhysRevLett.107.218102.

[154] J. H. Hubbell, H. A. Gimm, and I. Øverbø, Pair, Triplet, and Total Atomic Cross Sections (and Mass Attenuation Coefficients) for 1 MeV-100 GeV Photons in Elements Z=1 to 100, *J. Phys. Chem. Ref. Data* **9**, 1023–1148 (1980). doi:10.1063/1.555629.

[155] N. Rohringer and R. Santra, Resonant auger effect at high x-ray intensity, *Phys. Rev. A* **77**, 053404 (2008). doi:10.1103/PhysRevA.77.053404.

[156] N. Rohringer and R. Santra, Strongly driven resonant auger effect treated by an open-quantum-system approach, *Phys. Rev. A* **86**, 043434 (2012). doi:10.1103/PhysRevA.86.043434.

[157] E. P. Kanter, B. Krässig, Y. Li, A. M. March, P. Ho, N. Rohringer, R. Santra, S. H. Southworth, L. F. DiMauro, G. Doumy, et al., Unveiling and driving hidden resonances with high-fluence, high-intensity x-ray pulses, *Phys. Rev. Lett.* **107**, 233001 (2011). doi:10.1103/PhysRevLett.107.233001.

[158] Y. Li, C. Gao, W. Dong, J. Zeng, Z. Zhao, and J. Yuan, Coherence and resonance effects in the ultra-intense laser-induced ultrafast response of complex atoms, *Sci. Rep.* **6**, 18529 (2016). doi:10.1038/srep18529.

[159] S. Nandi, E. Olofsson, M. Bertolino, S. Carlström, F. Zapata, D. Busto, C. Callegari, M. D. Fraia, P. Eng-Johnsson, R. Feifel, et al., Observation of rabi dynamics with a short-wavelength free-electron laser, *Nature* **608**, 488–493 (2022). doi:10.1038/s41586-022-04948-y.

[160] S. M. Cavaletto, C. Buth, Z. Harman, E. P. Kanter, S. H. Southworth, L. Young, and C. H. Keitel, Resonance fluorescence in ultrafast and intense x-ray free-electron-laser pulses, *Phys. Rev. A* **86**, 033402 (2012). doi:10.1103/PhysRevA.86.033402.

[161] N. Rohringer, D. Ryan, R. A. London, M. Purvis, F. Albert, J. Dunn, J. D. Bozek, C. Bostedt, A. Graf, R. Hill, et al., Atomic inner-shell x-ray laser at 1.46 nanometres pumped by an x-ray free-electron laser, *Nature* **481**, 488–491 (2012). doi:10.1038/nature10721.

[162] N. Rohringer and R. London, Atomic inner-shell x-ray laser pumped by an x-ray free-electron laser, *Phys. Rev. A* **80**, 013809 (2009). doi:10.1103/PhysRevA.80.013809.

[163] T. Schneider, P. L. Chocian, and J.-M. Rost, Separation and identification of dominant mechanisms in double photoionization, *Phys. Rev. Lett.* **89**, 073002 (2002). doi:10.1103/PhysRevLett.89.073002.

[164] P. Kolorenč, V. Averbukh, R. Feifel, and J. Eland, Collective relaxation processes in atoms, molecules and clusters, *J. Phys. B: At. Mol. Opt. Phys.* **49**, 082001 (2016). doi:10.1088/0953-4075/49/8/082001.

[165] N. Saito and I. H. Suzuki, Shake-off processes in photoionization and auger transition for rare gases irradiated by soft x-rays, *Phys. Scr.* **49**, 80–85 (1994). doi:10.1088/0031-8949/49/1/011.

[166] K. Blum, *Density Matrix Theory and Applications* (Springer, New York, 1996).

[167] B. Efron and R. J. Tibshirani, *An introduction to the bootstrap* (Chapman and Hall/CRC, Philadelphia, PA, 1994).

[168] *Einführung in maschinelles Lernen*, [Online; accessed April 4, 2024], https://developers.google.com/machine-learning/crash-course/.

[169] T. Mitchell, *Machine Learning* (McGraw-Hill, New York, 1997).

[170] B. E. Boser, I. M. Guyon, and V. N. Vapnik, A training algorithm for optimal margin classifiers, in *COLT92:Proceedings of the Fifth Annual Workshop on Computational Learning Theory*, edited by D. Haussler (Association for Computing Machinery, Pittsburgh Pennsylvania USA, 1992), pp. 144–152.

[171] C. Cortes and V. Vapnik, Support-vector networks, *Mach. Learn.* **20**, 273–297 (1995). doi:10.1007/BF00994018.

[172] C. K. I. Williams and C. E. Rasmussen, Gaussian processes for regression, in *Advances in neural information processing systems 8*, edited by D. Touretzk, M. Mozer, and M. Hasselmo (MIT Press, Cambridge, 1996), pp. 514–520.

[173] T. Hofmann, B. Schölkopf, and A. J. Smola, Kernel methods in machine learning, *Ann. Stat.* **36**, 1171–1220 (2008). doi:10.1214/009053607000000677.

[174] L. Breiman, J. Friedman, R. Olshen, and C. Stone, *Classification and Regression Trees* (Chapman and Hall/CRC., New York, 1984).

[175] L. Long and X. Zeng, *Beginning Deep Learning with TensorFlow* (Apress, Berkeley, CA, 2022).

[176] C. M. Bishop, Neural networks for pattern recognition (Oxford University Press, New York, 1995).

[177] A. A. Patel, *Hands-On Unsupervised Learning Using Python* (O'Reilly Media, Inc., Sebastopol, 2019).

[178] Y. LeCun, L. Bottou, G. Orr, and K. Muller, Efficient backprop, in *Neural Networks: Tricks of the trade*, edited by G. Orr and G. B. Müller (Springer, Berlin, Heidelberg, 1998).

[179] S. Raschka and V. Mirjalili, *Machine Learning mit Python und Keras, TensorFlow 2 und Scikit-learn: Das umfassende Praxis-Handbuch für Data Science, Deep Learning und Predictive Analytics* (MITP, Germany, 2021).

[180] P. Roßbach, Neural networks vs. random forests – does it always have to be deep learning? (Frankfurt School of Finance and Managment, Germany, 2018).

[181] S. Liang and R. Srikant, Why deep neural networks for function approximation?, in *5th International Conference on Learning Representations ICLR*, edited by Y. Bengio and Y. LeCun (OpenReview.net, Toulon, 2017).

[182] D. E. Rumelhart, G. E. Hinton, and R. J. Williams, Learning representations by back-propagating errors, *Nature (London)* **323**, 533–536 (1986). doi:10.1038/323533a0.

[183] Y. LeCun, L. Jackel, B. Boser, J. Denker, H. Graf, I. Guyon, D. Henderson, R. Howard, and W. Hubbard, Handwritten digit recognition: applications of neural network chips and automatic learning, *IEEE Commun. Mag.* **27**, 41–46 (1989). doi:10.1109/35.41400.

[184] S. Sharma, S. Sharma, and A. Athaiya, Activation functions in neural networks, *Int. J. Eng. Appl. Sci. Technol.* **4**, 310–316 (2020). doi:10.33564/IJEAST.2020.v04i12.054.

[185] E. J. Michaud, Z. Liu, and M. Tegmark, Precision machine learning, *Entropy* **25**, 175 (2022). doi:10.3390/e25010175.

[186] X. Glorot and Y. Bengio, Understanding the difficulty of training deep feedforward neural networks, in *Proceedings of the Thirteenth International Conference on Artificial Intelligence and Statistics*, edited by Y. W. Teh and M. Titterington (PMLR, Italy, 2010), pp. 249–256.

[187] K. He, X. Zhang, S. Ren, and J. Sun, Delving deep into rectifiers: Surpassing human-level performance on imagenet classification, in *2015 IEEE International Conference on Computer Vision (ICCV)* (IEEE, Chile, 2015), pp. 1026–1034.

[188] L. Bottou, On-line algorithms and stochastic approximations, in *On-Line Learning and Neural Networks*, edited by D. Saad (Cambridge University Press, Cambridge, UK, 1999), pp. 9–42.

[189] D. R. Wilson and T. R. Martinez, The general inefficiency of batch training for gradient descent learning, *Neural Networks* **16**, 1429–1451 (2003). doi:10.1016/S0893-6080(03)00138-2.

[190] B. Polyak, Some methods of speeding up the convergence of iteration methods, *USSR Comput. Math. Math. Phys.* **4**, 1–17 (1964). doi:10.1016/0041-5553(64)90137-5.

[191] T. Tieleman and G. Hinton, Lecture 6.5-rmsprop: Divide the gradient by running average of its recent magnitude, in *COURSERA: Neural networks for machine learning* (2012), pp. 26–31.

[192] D. P. Kingma and J. Ba, Adam: A method for stochastic optimization, in *Proceedings of the 3rd International Conference on Learning Representations ICLR*, edited by Y. Bengio and Y. LeCun (ICLR, San Diego, USA, 2015).

[193] *Backpropagation-Algorithmus*, [Online; accessed May 15, 2024], https://developers-dot-devsite-v2-prod.appspot.com/machine-learning/crash-course/backprop-scroll?hl=de.

[194] N. Srivastava, G. Hinton, A. Krizhevsky, I. Sutskever, and R. Salakhutdinov, Dropout: A simple way to prevent neural networks from overfitting, *J. Mach. Learn. Res.* **15**, 1929–1958 (2014).

[195] M. Belkin, D. Hsu, S. Ma, and S. Mandal, Reconciling modern machine-learning practice and the classical bias–variance trade-off, *Proc. Natl. Acad. Sci. U.S.A.* **116**, 15849–15854 (2019). doi:10.1073/pnas.1903070116.

[196] L. Breiman, Random forests, *Mach. Learn.* **45**, 5–32 (2001). doi:10.1023/A:1010933404324.

[197] *Random Forest Regressor*, [Online; accessed May 25, 2024], https://scikit-learn.org/stable/modules/generated/sklearn.ensemble.RandomForestRegressor.

[198] P. Geurts, D. Ernst, and L. Wehenkel, Extremely randomized trees, *Mach. Learn.* **63**, 3–42 (2006). doi:10.1007/s10994-006-6226-1.

[199] D. H. Wolpert, The lack of a priori distinctions between learning algorithms, *Neural Comput.* **8**, 1341–1390 (1996). doi:10.1162/neco.1996.8.7.1341.

[200] D. Wolpert and W. Macready, No free lunch theorems for optimization, *IEEE Trans. Evol. Comput.* **1**, 67–82 (1997). doi:10.1109/4235.585893.

[201] B. Lohmann, *Angle and Spin Resolved Auger Emission* (Springer, Berlin Heidelberg, 1994).

[202] U. Fano, Description of states in quantum mechanics by density matrix and operator techniques, *Rev. Mod. Phys.* **29**, 74–93 (1957). doi:10.1103/RevModPhys.29.74.

[203] G. Racah, Theory of complex spectra. II, *Phys. Rev.* **62**, 438–462 (1942). doi:10.1103/PhysRev.62.438.

[204] B. R. Judd, *Operator Techniques in Atomic Spectroscopy* (McGraw-Hill Book Company, New York, 1963).

[205] D. Brink and G. Satchler, *Angular Momentum* (Clarendon Press, Oxford, 1962).

[206] I. Lindgren and J. Morrison, *Atomic Many-Body Theory* (Springer-Verlag, Berlin Heidelberg, 1982).

[207] B. Lohmann, Analyses and model calculations on the angular distribution and spin polarization of auger electrons, *J. Phys. B: At. Mol. Opt. Phys.* **23**, 3147 (1990). doi:10.1088/0953-4075/23/18/018.

[208] A. R. Edmonds, *Angular Momentum in Quantum Mechanics* (Princeton University Press, Princeton, 1957).

[209] A. Albiez, M. Thoma, W. Weber, and W. Mehlhorn, $KL_{2,3}$ ionization in neon by electron impact in the range 1.5-50 keV: cross sections and alignment, *Z. Phys. D* **16**, 97–106 (1990). doi:10.1007/BF01679570.

[210] A. Y. Elizarov and I. I. Tupitsyn, Analysis of the angular distribution of auger electrons in a Xe atom, *J. Exp. Theor. Phys.* **97**, 658–667 (2003). doi:10.1134/1.1625056.

[211] E. G. Berezhko, N. M. Kabachnik, and V. V. Sizov, The theory of coincidence experiments on electron impact ionisation of inner atomic shells, *J. Phys. B: At. Mol. Opt. Phys.* **11**, 1819 (1978). doi:10.1088/0022-3700/11/10/017.

[212] K. Ueda, N. M. Kabachnik, J. B. West, K. J. Ross, H.-J. Beyer, H. Hamdy, and H. Kleinpoppen, Angular distribution of auger electrons in resonantly enhanced transitions from 3p photoexcited ions, *J. Phys. B: At. Mol. Opt. Phys.* **31**, 4331 (1998). doi:10.1088/0953-4075/31/19/018.

[213] A. Hausmann, B. Kämmerling, H. Kossmann, and V. Schmidt, New approach for a perfect experiment: 2p photoionization in atomic magnesium, *Phys. Rev. Lett.* **61**, 2669–2672 (1988). doi:10.1103/PhysRevLett.61.2669.

[214] M. H. Chen, Effect of intermediate coupling on angular distribution of auger electrons, *Phys. Rev. A* **45**, 1684–1689 (1992). doi:10.1103/PhysRevA.45.1684.

[215] S.-K. Son, K. Toyota, O. Geffert, J. M. Slowik, and R. Santra, *XATOM-An Integrated Toolkit for X-Ray and Atomic Physics*, (CFEL, DESY, Hamburg, 2016), Rev. 3544.

[216] E. Goulielmakis, Z.-H. Loh, A. Wirth, R. Santra, N. Rohringer, V. S. Yakovlev, S. Zherebtsov, T. Pfeifer, A. M. Azzeer, M. F. Kling, et al., Real-time observation of valence electron motion, *Nature* **466**, 739–744 (2010). doi:10.1038/nature09212.

[217] H. Wang, M. Chini, S. Chen, C.-H. Zang, F. He, Y. Cheng, Y. Wu, U. Thumm, and Z. Chang, Attosecond time-resolved autoionization of argon, *Phys. Rev. Lett.* **105**, 143002 (2010). doi:10.1103/PhysRevLett.105.143002.

[218] J. Itatani, F. Quere, G. L. Yudin, M. Y. Ivanov, F. Krausz, and P. B. Corkum, Attosecond streak camera, *Phys. Rev. Lett.* **88**, 173903 (2002). doi:10.1103/PhysRevLett.88.173903.

[219] M. Hentschel, R. Kienberger, C. Spielmann, G. A. Reider, N. Milosevic, T. Brabec, P. Corkum, U. Heinzmann, M. Drescher, and F. Krausz, Attosecond metrology, *Nature* **414**, 509–513 (2001). doi:10.1038/35107000.

[220] F. Krausz and M. Ivanov, Attosecond physics, *Rev. Mod. Phys.* **81**, 163–234 (2009). doi:10.1103/RevModPhys.81.163.

[221] A. F. Starace, Trends in the theory of atomic photoionization, *Appl. Opt.* **19**, 4051–4062 (1980). doi:10.1364/AO.19.004051.

[222] G. W. F. Drake, *Springer Handbook of Atomic, Molecular, and Optical Physics* (Springer, New York, 2006).

[223] J. H. Friedman, Greedy function approximation: A gradient boosting machine., *Ann. Stat.* **29**, 1189–1232 (2001). doi:10.1214/AOS/1013203451.

[224] Z.-H. Zhou and J. Feng, Deep forest: Towards an alternative to deep neural networks, in *Proceedings of the Twenty-Sixth International Joint Conference on Artificial Intelligence*, edited by C. Sierra (International Joint Conferences on Artificial Intelligence, Melbourne, 2017).

[225] G. Biau, E. Scornet, and J. Welbl, Neural random forests, *Sankhya A* **81**, 347–386 (2019). doi:10.1007/s13171-018-0133-y.

[226] C. Qu, P. L. Houston, Q. Yu, R. Conte, P. Pandey, A. Nandi, and J. M. Bowman, Machine learning classification can significantly reduce the cost of calculating the Hamiltonian matrix in CI calculations, *J. Chem. Phys.* **159**, 071101 (2023). doi:10.1063/5.0168590.

[227] B. Krässig, M. Jung, D. S. Gemmell, E. P. Kanter, T. LeBrun, S. H. Southworth, and L. Young, Nondipolar asymmetries of photoelectron angular distributions, *Phys. Rev. Lett.* **75**, 4736–4739 (1995). doi:10.1103/PhysRevLett.75.4736.

[228] T. Mazza, M. Ilchen, A. J. Rafipoor, C. Callegari, P. Finetti, O. Plekan, K. C. Prince, R. Richter, M. B. Danailov, A. Demidovich, et al., Determining the polarization state of an extreme ultraviolet free-electron laser beam using atomic circular dichroism, *Nat. Commun.* **5**, 3648 (2014). doi:10.1038/ncomms4648.

[229] A. A. Lutman, J. P. MacArthur, M. Ilchen, A. O. Lindahl, J. Buck, R. N. Coffee, G. L. Dakovski, L. Dammann, Y. Ding, H. A. Dürr, et al., Polarization control in an x-ray free-electron laser, *Nat. Photon.* **10**, 468–472 (2016). doi:10.1038/nphoton.2016.79.

[230] E. Allaria, B. Diviacco, C. Callegari, P. Finetti, B. Mahieu, J. Viefhaus, M. Zangrando, G. De Ninno, G. Lambert, E. Ferrari, et al., Control of the polarization of a vacuum-ultraviolet, high-gain, free-electron laser, *Phys. Rev. X* **4**, 041040 (2014). doi:10.1103/PhysRevX.4.041040.

[231] E. Prat, A. Al Haddad, C. Arrell, S. Augustin, M. Boll, C. Bostedt, M. Calvi, A. L. Cavalieri, P. Craievich, A. Dax, et al., An x-ray free-electron laser with a highly configurable undulator and integrated chicanes for tailored pulse properties, *Nat. Commun.* **14**, 5069 (2023). doi:10.1038/s41467-023-40759-z.

[232] G. Perosa, J. Wätzel, D. Garzella, E. Allaria, M. Bonanomi, M. B. Danailov, A. Brynes, C. Callegari, G. De Ninno, A. Demidovich, et al., Femtosecond polarization shaping of free-electron laser pulses, *Phys. Rev. Lett.* **131**, 045001 (2023). doi:10.1103/PhysRevLett.131.045001.

Acknowledgements

First of all, I would like to thank Professor Dr. Santra, who kindly supervised my PhD thesis, for giving me the opportunity to write this work. I also want to thank Professor Dr.-Ing. Tropmann-Frick for being the co-supervisor, Prof. Dr. Pfannkuche for being the project panel chair, and Prof. Dr. Bari for being the DESY mentor. Additional thanks go to the members of the examination commission of my defense (whose names were not yet known to me when writing these lines) for kindly taking on this task. Further, I am also very grateful to Dr. Son for good discussions and for his advices and support in preparing and writing my publications.

Moreover, I gratefully acknowledge support by DASHH (Data Science in Hamburg - HELMHOLTZ Graduate School for the Structure of Matter) with Grant.-No. HIDSS-002 and from DESY (Hamburg, Germany), a member of the Helmholtz Association HGF.

Eidesstattliche Versicherung

Hiermit versichere ich an Eides statt, die vorliegende Dissertationsschrift selbst verfasst und keine anderen als die angegebenen Hilfsmittel und Quellen benutzt zu haben.

Sofern im Zuge der Erstellung der vorliegenden Dissertationsschrift generative Künstliche Intelligenz (gKI) basierte elektronische Hilfsmittel verwendet wurden, versichere ich, dass meine eigene Leistung im Vordergrund stand und dass eine vollständige Dokumentation aller verwendeten Hilfsmittel gemäß der Guten wissenschaftlichen Praxis vorliegt. Ich trage die Verantwortung für eventuell durch die gKI generierte fehlerhafte oder verzerrte Inhalte, fehlerhafte Referenzen, Verstöße gegen das Datenschutz- und Urheberrecht oder Plagiate.

Stade, November 18, 2024